The Dissertation Committee for Roman J. Shor
certifies that this is the approved version of the following dissertation:

The effect of well path, tortuosity and drillstring design on the transmission of axial and torsional vibrations from the bit and mitigation control strategies

Committee:

Eric van Oort, Supervisor

Behçet Açikmeşe, Co-Supervisor

Carlos Torres-Verdin

Kamy Sepehrnoori

Mark Dykstra

The effect of well path, tortuosity and drillstring design on the transmission of axial and torsional vibrations from the bit and mitigation control strategies

by

Roman J. Shor, B.A.; B.S.E.; M.S.E.; M.S.E.

DISSERTATION

Presented to the Faculty of the Graduate School of

The University of Texas at Austin

in Partial Fulfillment

of the Requirements

for the Degree of

DOCTOR OF PHILOSOPHY

THE UNIVERSITY OF TEXAS AT AUSTIN

May 2016

Dedicated to the patience and perseverance of all,
but most of all to my mother who always strived to give me the best
education she could.

Acknowledgments

To my advisors Eric van Oort and Behçet Açikmeşe for their guidance and support, Pradeep Ashok and Mitch Pryor for many insightful conversations, the entire Drilling and Rig Automation Team at The University of Texas at Austin and the members of the committee.

To Mark Dykstra for initially proposing extending an existing methodology to predict bit bounce to agitator placement optimization, which in turn led to the evolution of this dissertation, and for guiding me through many summers at Shell, along with Mark Anderson and John Runia and the entire Drilling Mechanics Technology team. Also to Jan Jette Blange and the entire team at Shell Research in Rijswijk.

To Ivo Stulemeijer for his role in the primary development stick-slip mitigation system evaluation methodology used in part in this dissertation and for countless hours discussing applications and field trials. To Sicco Dwars for taking me along, first to the deployment of SoftTorque, then through the development, field testing and deployment of ZTorque.

To Tore Butlin, Jim Woodhouse and the entire Dynamics and Vibrations Research Group at the University of Cambridge, for hosting me during my semester as a visiting student and for significantly furthering my understanding of the fundamentals of vibrations.

The author would like to thank the Shell International Exploration and Production Company for sponsoring this research, both at The University of Texas at Austin and at the University of Cambridge and also National Oilwell Varco (NOV) for providing field data essential for the verification the model described in this dissertation.

The effect of well path, tortuosity and drillstring design on the transmission of axial and torsional vibrations from the bit and mitigation control strategies

Publication No. _____

Roman J. Shor, Ph.D.
The University of Texas at Austin, 2016

Supervisors: Eric van Oort
Behçet Açikmeşe

As well designs become increasingly complicated, a complete understanding of drillstring vibrations is key to maximize drilling efficiency, to reduce drillstring dysfunction and to minimize drillstring, tool, and borehole damage. Torque and drag models exist that seek to quantify the effects of borehole inclination and tortuosity on static friction along the drillstring; however, the effects on dynamic friction remains poorly understood. This dissertation begins with a review of the past fifty years of work on drillstring dynamics models, an overview of the proposed control strategies and a summary deployed vibration mitigation applications within the drilling industry. Derivations from first principles of a series of computationally efficient axial and torsional drillstring models in both the frequency and time domains are then presented and verified with field data.

The transfer matrix approach is used to predict the severity of axial vibrations along the drillstring and is verified using a series of case studies using field data. Harmonic axial vibrations within drillstrings are either induced intentionally, in the case of axial oscillation tools midway along the drillstring, or unintentional, in the case of bit bounce. Two case studies of bit bounce are first evaluated to ensure model validity for a harmonic excitation at a the bit and the model is found to accurately predict bit bounce based on surface rotation rates. Induced axial oscillations, generated by axial oscillation tools, are then investigated to quantify friction reduction and drilling efficiency improvements. Optimal placement is found to depend on wellbore geometry, but is usually restricted to periodic regions of the drillstring. These optimizations are then verified using field trials and suggest that improved placement can result in 20% or more reduction in friction along the drillstring.

Two applications of torsional drillstring vibrations are then investigated – stick slip mitigation and drillstring imaging. The time domain form of the torsional drillstring model is used first to evaluate the effectiveness of three types of top drive controllers – stiff controllers, tuned PI controllers and impedance matching controllers – in mitigating stick slip oscillations. Then, the transfer matrix method is applied to evaluate the effect of wellbore geometry on drillstring mobility to conclude that higher order modes of stick slip may become dominant in non-vertical wellbores. The feasibility of drillstring imaging using torsional signals from surface is then investigated to identify inputs and methods that show promise in three setups of varying complex-

ity – a hanging beam, a laboratory drillstring model and a drilling rig. Two techniques show promise – white noise injection and model fitting of a step response – in identifying larger features, including drillstring length and BHA location. However, low sampling frequencies and low bandwidth inputs reduce the ability to image small features such as friction points along the wellpath.

Table of Contents

List of Tables

List of Figures

Chapter 1

Introduction

The upstream oil and gas industry is primarily concerned with the exploration for and extraction of hydrocarbons from formations deep below the earth's surface. Hydrocarbon reservoirs are typically found between 2,000 and 20,000 feet vertical depth, but newer discoveries in places like the Gulf of Mexico have also occurred at depths in excess of 30,000 feet (van Oort et al., 2013) or required extended reach wells with horizontal displacements over 30,000 feet (Allen et al., 1997). Drilling for these hydrocarbons involves the transmission of cutting force through miles of slender drillpipe – from the drilling rig at the surface to the drill bit, as shown in Figure 1.1. Drillstrings are composed of various diameters of drillpipe that snake along an often irregular and curving wellbore drilled through formations with heterogeneous lithology. Control inputs are generally limited to surface rotational speed, rotary torque, axial loading of the string and mud flow rate. Effective torque-on-bit and weight-on-bit transmission is key to efficient drilling but is greatly influenced by the dynamics of the moving drillstring in the borehole and by the formation properties themselves. Understanding drillstring dynamics has been key to improving drilling efficiency.

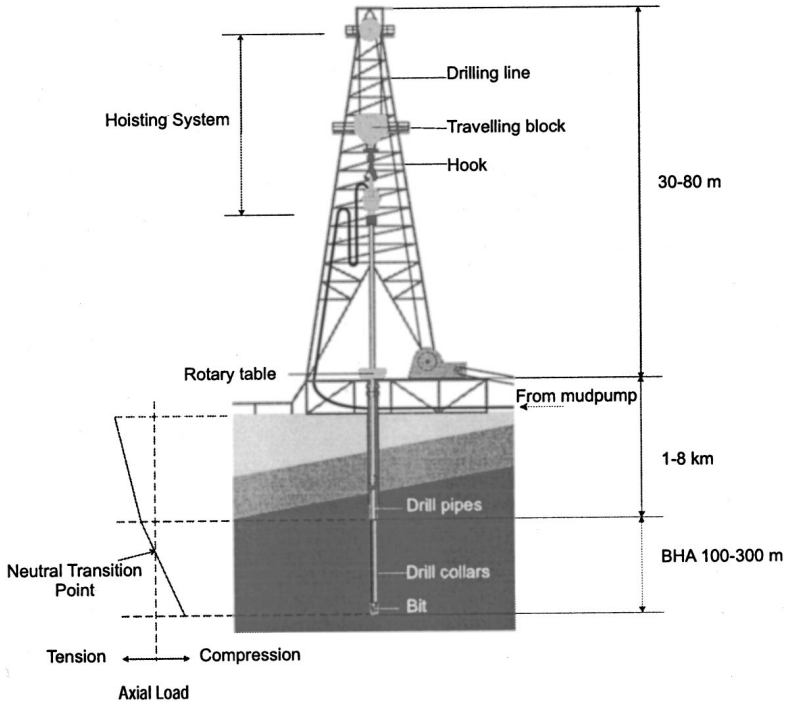

Figure 1.1: A traditional drilling rig and drillstring setup, as shown in (Leine et al., 2002).

This dissertation seeks to first survey the current state of drillstring dynamics modeling and of mitigation systems currently deployed in the field. Then a suite of drillstring vibration models based upon the damped wave equation are derived from base principles for both axial and torsional vibrations in both the frequency and time domains. Frequency domain models are implemented using the transfer matrix approach while the time domain solutions are implemented either through the use of finite difference models or through state-space models. These models are then applied to a series of problems,

including the characterization of the axial dynamic behavior of the drillstring subject to a harmonic input, an analysis of the effectiveness of surface control strategies, and a feasibility study of drillstring imaging using torsional reflectances. However, it is important to first understand the different types of drillstring vibrations and their effects on operations.

1.1 Categories of Drillstring Vibration

Sensing of drilling dysfunction (such as undesired vibrations) is typically limited to real-time surface data at a relatively low frequency (typically 0.5 - 1 Hz) but is occasionally available at higher sampling frequencies within particular systems, such as top drive control systems. Limited real-time downhole data is generally available but is primarily used for well steering operations, i.e. deviating the well from vertical towards a specific target zone. Current communication methods, relying on mud-pulse telemetry (Bonner et al., 1992), have limited bandwidth and potentially significant time delays. New technologies, such as wired drillpipe, have been deployed and provide high-frequency downhole data (Briscoe et al., 2013). Wired drillpipe now allows for the incorporation of downhole vibration sensors that can accurately characterize harmful excitations of the drillstring in real-time, allowing for real-time automated control but remains costly. These sensors are also widely deployed as parts of downhole dynamics recording devices, but this data can only be analyzed after the well has been drilled and the tool retrieved.

Classes of drillstring vibrations are typically characterized in industry by the resulting physical behaviors of the system and are related to three vibration modes. Torsional vibrations often manifest as **stick-slip** events. Lateral vibrations are typically associated with **whirl**. Axial vibrations occur due to bit-rock interaction and resulting **bit-bounce**, or from induced axial oscillations in efforts to reduce friction. Each of these is described in detail below.

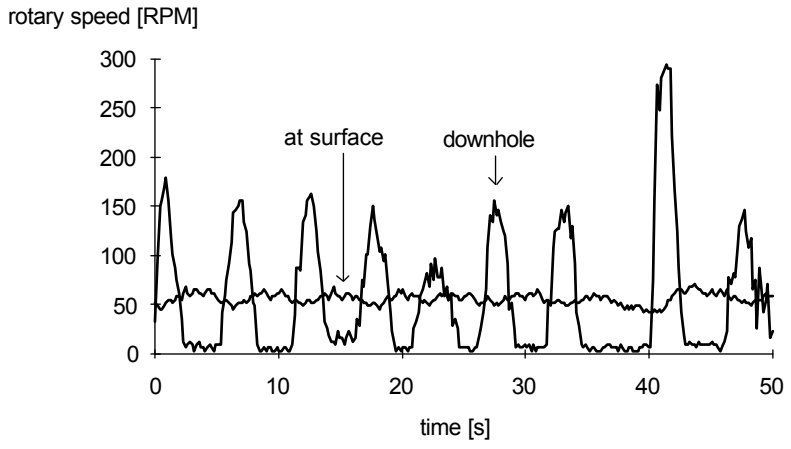

Figure 1.2: Typical stick-slip behavior, both at the surface and the bit, as shown in (Kriesels et al., 1999).

1.1.1 Stick-slip

Stick-slip events are visible at the surface as low frequency torque fluctuations (on the order of 2 – 10 seconds, an example is shown in Fig 1.2) and are caused by non-linear frictional forces at the bit or at the stabilizers coupled with insufficient cutting force, either through insufficient torque or

excessive weight-on-bit. A self-exciting limit cycle then occurs in the bit rotation – bit torque phase plane. When insufficient torque is applied at the bit to cut through the rock at a given weight-on-bit, the bit stalls and ceases rotation. As surface rotation continues, the drillstring will continue to twist and "store torque", which will subsequently be transferred to the bit. Once sufficient torque is available, the bit releases violently and rotates faster than the surface rotation until the additional twist in the drillstring is removed and torque at bit again falls below the cutting limit, stalling the bit once more. The cycle then repeats (Kriesels et al., 1999). High frequency torsional oscillations (HFTO) within the bottom hole assembly (BHA) have also been observed in field data, but consensus on their existence – an argument has been put forth that these oscillations are simply an artifact of sensor position – has not been reached and are thus outside the scope of this dissertation (Oueslati et al., 2013a; Baumgartner and van Oort, 2014; Jain et al., 2014; Hohl et al., 2016).

1.1.2 Lateral vibrations

Lateral, sometimes referred to as longitudinal, vibrations of rotating shafts typically manifest as a migration of the axis of rotation of the drillstring within the confines of a wellbore. This is referred to as drillstring whirl. Whirl is damaging to the drillstring and may cause failure or wear of bits and other bottom-hole assembly components (i.e. motors, monitoring-while-drilling/logging-while-drilling tools etc.) through prolonged and often violent contact with the wellbore wall. Forward whirl occurs when the drillstring

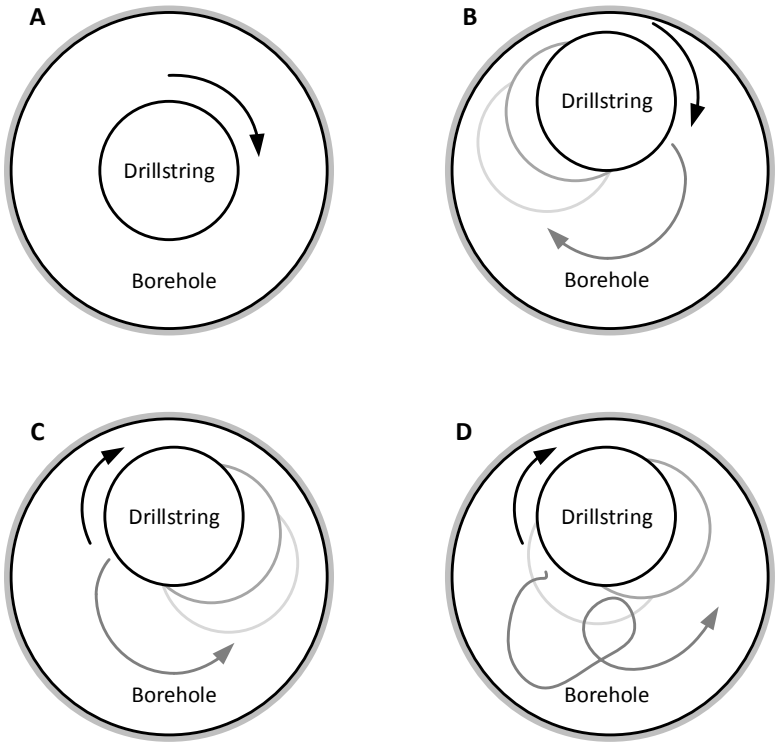

Figure 1.3: Drillstring whirl. (A) Ideal conditions, where the drillstring is centered in the borehole and is rotating clockwise. (B) Forward whirl, where motion of the drillstring around the wellbore and pipe rotation are both clockwise. (C) Backward whirl, where motion of the drillstring around the wellbore is counterclockwise. (D) Chaotic whirl where motion around the wellbore is erratic.

rotation and direction of axis rotation around the wellbore are prograde. Laboratory experiments (Aldred and Sheppard, 1992; Liao et al., 2012) and field experience (Brett et al., 1990; Vandiver et al., 1990) have shown that in forward whirl, contact occurs between the same spot on the borehole and the drillstring, leading to excessive wear (of the borehole and/or exposed drill-

string components) if the vibration is not mitigated. Backward whirl occurs when the two rotations are retrograde and there is no observed pattern in drillstring – wellbore contact. Chaotic whirl is neither prograde nor retrograde but involves erratic movement of the axis of rotation within the wellbore with high shock loads. Detection of whirl using low frequency surface sensors is extremely difficult due to high dampening of lateral drillstring vibrations in the borehole through interaction with the viscous drilling fluid, different drillstring elements, the borehole walls and harmonic modes (Swanson et al., 2005).

1.1.3 Axial vibrations

Axial vibrations of the drillstring are either random or harmonic and are either caused by bit-rock interaction or induced by downhole tools. During the rock cutting process, random axial motion originates from the bit and propagates through the drillstring and may be detected at surface in some cases as noise in the hookload measurement. This noise may excite natural modes of the drillstring to create standing waves, and in the case of tricone bites, developed into a tri-lobbed pattern which may be detected as a harmonic axial oscillation at three times rotary speed. However, in many cases axial vibrations of the drillstring are often difficult to detect on surface due to attenuation within the drillstring, especially in deviated wells where extended sections of the drillstring are supported by the borehole wall. Even when downhole motors drive the bit (and thus the drillstring does not rotate) axial vibration can be induced by downhole tools, such as axial oscillation tools (Barton et al.,

2011a), which are deployed in an attempt to reduce friction while sliding to improve toolface control and transmission of torque-on-bit and weight-on-bit. There are industry studies showing the benefits of incorporating oscillation tools into bottom hole assemblies (Alali and Barton, 2011; Alali et al., 2012), but since these tools cannot be deactivated once in the hole, they continually induce axial vibration even while rotating the drillstring.

1.2 Prior Work

Current drillstring models can be characterized into two basic categories: soft-string and stiff-string models. A soft-string model is a lumped mass model that assumes continuous drillstring-borehole contact. A stiff-string model explicitly calculates bending and may assume point wise contact with the borehole. A survey by Janwadkar in 2006 found that drill collars and heavyweight drillpipe obey the stiff string model, while ordinary drillpipe and coil tubing are well approximated by the soft string model (Janwadkar et al., 2006). Soft-string models are typically simpler and less computationally intensive than stiff-string models and lend themselves to real-time modeling and analysis.

The typical formulations of dynamics models are shown in Figures 1.4 - 1.7. Torsional vibrations are often explored as stiff string models using series of lumped inertial discs connected by torsional springs and dampers (Figure 1.4). Whirl is typically modeled as an inertial disc on a torsional transmission shaft that is allowed to move within the confines of a wellbore (Figure 1.5).

Lateral vibrations are often explored through either lumped mass models that allow the axis of rotation of each mass to move within the borehole or through soft string models that allow for bending of drillstring components (Figure 1.6). Current bit models are similar to the one presented by Germay et al. (Figure 1.7) (Germay et al., 2009).

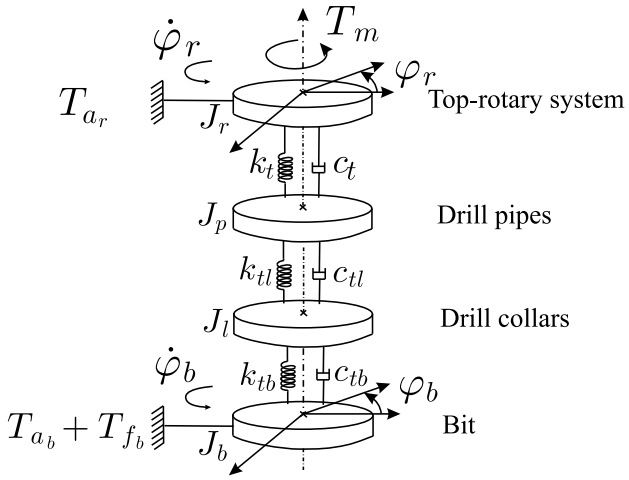

Figure 1.4: A typical lumped mass torsional model, as used in (Leine et al., 2002). Components of the drillstring are lumped into singular masses, typically representing the drillpipe and BHA, which then interact via springs and dampers, the properties of which are determined from drillstring properties or through tuning from field or experimental data.

Current drillstring models are either computationally efficient but make overly simplifying assumptions – often by ignoring wellbore geometry and dynamic system delays – or account for complex dynamic drillstring behaviors but result in computational complexity. This dissertation seeks to propose a

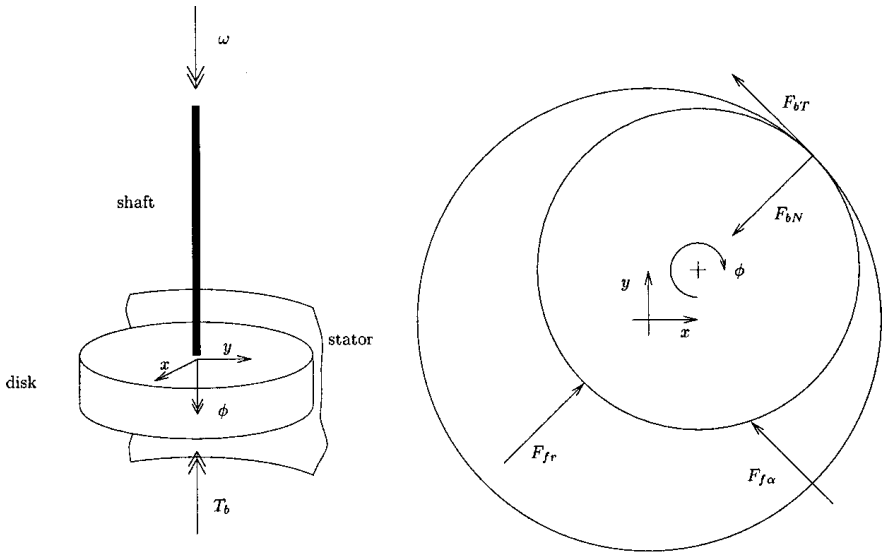

(*a*) Shaft, stator and disk.

(*b*) Fluid and contact forces on the disk.

Figure 1.5: A typical drillstring whirl model, as used in (Leine et al., 2002). In this case, an inertial disk is allowed to rotate within a confining wellbore with the drillstring modeled as an elastic spring or beam.

computationally efficient drillstring model which accounts for wellbore geometry and system transmission delays by viewing the drillstring as a waveguide.

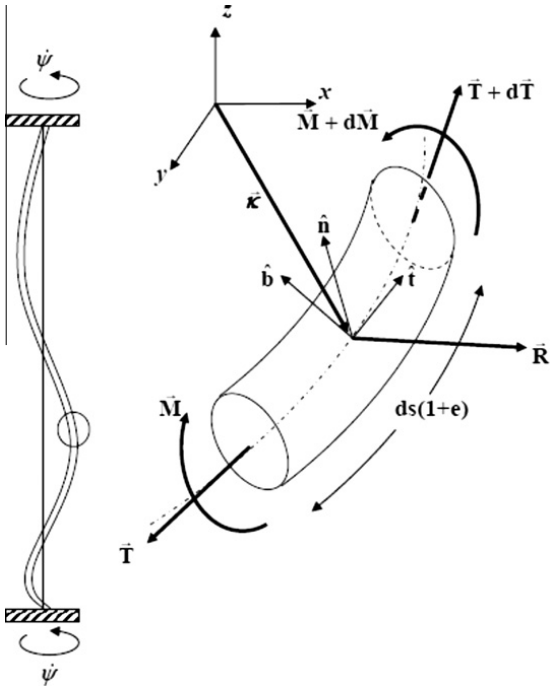

Figure 1.6: A stiff string model, allowing for drillstring component bending and shear, as used in (Chatjigeorgiou, 2013). Drillstring bending and shear are accounted for in an effort to simulate bucking and lateral motion.

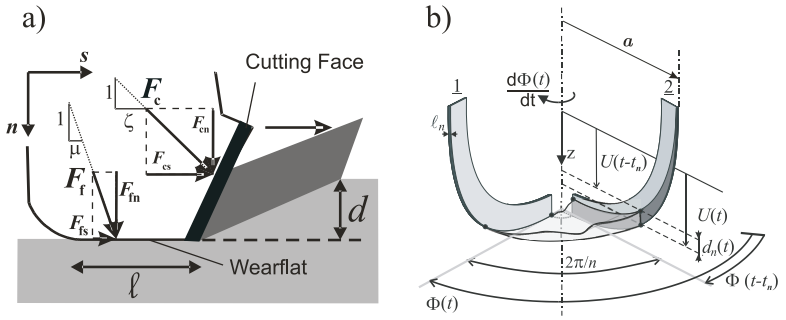

Figure 1.7: A PDC drag bit model, as developed by (Germay et al., 2009). The cutters are simplified as cutting blades to facilitate the simulation of cuttings and penetration rate.

1.3 Objectives and Contributions

This dissertation proposes two uncoupled drillstring models, one modeling harmonic axial vibrations in the drillstring and the other modeling torsional vibrations, both based upon the damped wave equation. These models are derived from first principles and the mechanics of each are verified with surface and downhole drilling data and scaled laboratory models. The axial model is then used to optimize the placement of axial oscillation tools and verified through a number of field trials. The torsional model is used first to compare the effectiveness of four types of top drive control systems, three of which incorporate active stick-slip mitigation, and secondly for an exploratory study of drillstring imaging.

The dissertation begins with a comprehensive literature survey, presented in **Chapter 2**, of the current state of drillstring dynamics modeling and an overview of currently deployed vibration mitigation control systems. A majority of this chapter has been previously presented as a paper in the ASME DSCC Conference in 2014 in San Antonio, TX (Shor et al., 2014).

A derivation from first principles of the drillstring model used in subsequent chapters is then presented in **Chapter 3**. The model allows for the distribution of damping along the drillstring in addition to allowing multiple harmonic force or displacement inputs to be present. Sources of damping are identified and quantified and solution methodologies in both the time and frequency domain are presented.

A comprehensive method to optimize the placement of axial oscillation tools with the drillstring is presented in **Chapter 4** and is verified using the results of several field trials showing improvements in steering abilities and well reach. Given an oscillation tool's design parameters and intended wellpath, locations within the drillstring are identified for optimal placement and friction reduction along the wellbore can be directly computed. A portion of this chapter was presented at the 2015 SPE/IADC Drilling Conference in London, United Kingdom (Shor et al., 2015a).

The torsional implementation of the model is then used to compare the effectiveness of four different top drive control strategies in **Chapter 5**. These four strategies include a stiff PI controller, a tuned PI controller, a second order tuned PI controller, and an idealized impedance matching controller. A portion of this chapter was presented at the 2015 International Conference on Engineering Vibration (ICoEV) in Ljubljana, Slovenia (Shor et al., 2015b).

A feasibility study of drillstring imaging, which utilizes torsional signals from surface to image features along the drillstring, is presented in **Chapter 6**. Through a series of experiments, at multiple scales and complexities, it is shown that it is possible to image features as small as 30ft within a drillstring if surface sampling frequency is in excess of 1000Hz and a small random square wave input is imposed over the commanded rpm signal. The research presented in this chapter was carried out as part of a joint research project with the University of Cambridge.

The dissertation concludes in **Chapter 7** with a brief summary of the work presented in the preceding chapters and highlights the major contributions. A proposed path forward and possible future work is also outlined.

1.4 Outline

This dissertation is laid out in seven chapters, some of which have been presented as independent conference papers and others of which are in preparation.

- *Chapter 2* presents a literature review of the current state of drillstring modeling as well as the models currently used for control applications.
- *Chapter 3* introduces the two drillstring models and derives each from first principles. Sources of damping within the drillstring are identified and their inclusion in the models discussed.
- *Chapter 4* applies the axial drillstring model first to bit bounce, to verify model mechanics, and secondly to the placement of axial oscillation tools. Optimal placement strategies are discussed and then verified with field trials.
- *Chapter 5* applies the torsional drillstring model to optimize controllers for model centric control to minimize stick slip. The effectiveness of a stiff PI controller, a tuned PI controller, a tuned second order PI controller and an idealized impedance matching controller are compared.

- *Chapter 6* applies the torsional drillstring model to the imaging of impedance changes within the drillstring. This feasibility study applies the concepts of wave reflection, signal processing and model fitting to map changes in three demonstration setups: a simple beam, a laboratory drillstring model and a drilling rig.

- *Chapter 7* summarizes the contributions of the this dissertation and presents the path forward, further work and conclusions.

- *Appendix A* lists the abbreviations and symbols used in this dissertation.

- *Appendix B* lists the papers published by the author and papers in preparation.

- *Appendix C* contains a summary of equations used for the minimum curvature method, used to interpolate grid points along a curving wellpath based on sparse survey data, used primarily in Chapter 4.

- *Appendix D* contains a summary of the algorithms used in the transfer matrix approach used in Chapter 4.

- *Appendix E* contains the Simulink^{TM} model for the time domain simulation and the torsional transfer matrix model for frequency domain analysis used in Chapter 5.

- *Appendix F* contains a summary of the signal processing code used in Chapter 6.

Chapter 2

Literature Review

In the following chapter, a comprehensive overview of the history of drillstring modeling and vibration detection is presented, which culminates in an assessment of the current state-of-the-art and the main challenges that still remain to be addressed. This review builds upon an earlier review paper by Patil and Teodoriu that looked specifically at torsional vibrations (Patil and Teodoriu, 2013) and was presented in 2014 at the ASME Dynamic Systems and Controls Conference (Shor et al., 2014).

Early efforts in drillstring dynamics modeling focused on understanding vibration patterns that were observed using surface sensors or during the early deployments of downhole sensing equipment. Models were simple and typically modeled the drillstring either as simple beams or as series of discrete masses connected by springs or dashpots. These models could not explain many phenomena observed but were sufficient for efforts in vibration control and mitigation to begin. These strategies either defined critical control parameter regions to avoid the onset of vibration or actively sought to mitigate specific forms of it, specifically torsional vibration. Development of advanced coupled models continued rapidly, but deployment of advanced con-

trol approaches in the field remains hampered by low data quality, both due to bandwidth limitations and expense, and reluctance of stakeholders to accept liability or change. Operators championing new technology have emerged and are driving the deployment of new and improved methods, but progress remains slow. Current work has focused on the development of coupled models and their use in control situations, but field testing and deployment has been limited but are slowly expanding. Future work will need to refine sensor and instrumentation requirements for successful deployment, provide validation and demonstrate tangible performance gain. The past development of drillstring dynamics modeling, current modeling approaches and examples of industry deployment will presented in following sections.

2.1 Evolution of Drillstring Modeling

Drillstring dynamics modeling began in the 1960s in efforts to understand downhole behavior and optimize performance. These models often had few degrees of freedom and made simplifying assumptions, including independence of vibration modes, perfectly vertical wellbores and abstraction of various drillstring components as simple lumped masses. As well designs became increasing complex, couplings between the different modes of vibration and interaction between the wellbore and drillstring had to be introduced to explain observed behaviors. The advent of downhole sensing and improved surface sensing allowed for the characterization of modes of vibration and led to continued development of dynamics models.

In the following sections the early efforts of drillstring dynamics models, advances in coupled models and recent applications that use vibrational models for improving drilling performance are explored.

2.1.1 Early Efforts

Efforts to understand drillstring vibrations began in 1960 with papers by Bailey and Finnie delving into the theory and verification of axial and torsional vibrations of a vertical drillstring (Bailey and Finnie, 1960; Finnie and Bailey, 1960). Their model consisted of continuous beam elements subject to longitudinal, or axial, and torsional vibration and described mathematically using the wave equation. Lateral motion of the drillstring was ignored. They concluded that accurate estimates of the boundary conditions at the bit and the surface were necessary to estimate the natural frequencies, but they also noticed an interaction between torsional and axial vibrations that they were not able to explain. It was not until 1984 that Dunayevsky et al. proposed a model that considered the coupling of axial and lateral vibrations for a drillstring confined within a wellbore (Dunayevsky et al., 1984). The occurrence of drillstring precession, or whirl, had been noted in experiments and a mathematical model was laid out that was used to determine rotary speeds to avoid it.

In 1985, Wolf et al. describe one of the earliest instances of downhole sensing of downhole vibrations where they applied a wired drill pipe with downhole vibration sensors for real-time sensing of downhole measurements

(Wolf et al., 1985). In the same year, Besaisow et al. proposed a surface vibration measurement system that proved effective at detecting drillstring vibrations in shallow vertical wells (Besaisow et al., 1985). The following year, Ho published a theoretic analysis of the effects of stabilizer placement in the bottom hole assembly and hole curvature to explain bit side forces in a static drillstring (Ho, 1986). Simultaneously, in an effort to understand observed periodic oscillations in surface torque, Shell Research developed a similar wired drillstring and recorded the downhole cyclic behavior of stick-slip that was not visible at the surface (Dwars et al., 2013).

As interest in understanding torsional vibrations increased, Halsey et al. presented a model that looked at torsional resonance and verified it using a test well (Halsey et al., 1986). They found a close correlation between predicted and observed frequency spectra. With the application of a correction factor to account for speed of torsional vibration propagation through the drillstring, they concluded that downhole torsional vibrations could be effectively measured at the surface. In 1987, Skaugen noted that bit-rock interaction adds additional quasi-random excitation to the system which, when taken into account, improves frequency domain analysis of torsional vibrations (Skaugen, 1987).

Advances in the understanding of axial vibrations also continued and were applied by Kaisi et al. in 1987 to model the axial response of drillstring in response to jarring – a drilling operation where a large impact force is applied at point(s) on the drillstring to free stuck pipe (Kalsi et al., 1987). In 1991,

Lee's Ph.D. thesis presented the most thorough investigation of axial vibrations in a drillstring up to that date, along with an examination of hydraulic interaction and the various sources of dampening. For a drillstring under harmonic disturbance, a framework for calculating dampening factors that accounted for friction – modeled as Coulomb friction, viscous dampening and material hysteresis – was presented. A simple transfer matrix approach was proposed for solving the frequency domain response of the drillstring. Comparing test rig data with modeled results, Lee determined that frictional forces were the dominant source of dampening in axial and torsional vibrations, especially in deviated wellbores (Lee, 1991). In 1993, Aarrestad and Kyllingstad proposed an extension to the surface boundary condition by splitting the surface equipment into two parts, being the stationary rig and suspended top drive. This significantly improved upon Lee's model, where the surface was modeled as a single mass spring damper system attached to a fixed boundary instead using two discrete masses (Aarrestad and Kyllingstad, 1993).

2.1.2 Coupled and Advanced Models

In the early 90's, it was becoming apparent that a full understanding of vibrations would require a coupling of the axial, torsional and lateral modes. In 1992, Aldred and Sheppard proposed a coupled lateral, torsional and axial vibration model (Aldred and Sheppard, 1992). They performed laboratory experiments that confined a section of pipe, mounted with a fixed motor and bearing within a circular bracket, thus modeling the drillstring – borehole

system. Using this configuration, they induced lateral motion showing that whirl is in fact self-sustaining and lateral motion continues once rotation has stopped until attenuation has been fully achieved. A study a few years later by Santos et al. in 1999 presented empirical evidence that excessive downhole vibration – especially whirl – could potentially lead to borehole damage (Santos et al., 1999).

Multiple degree-of-freedom models for rotating shafts have been used in rotor dynamics for decades and are well reviewed by Ishida (Ishida, 1994). These models allowed for the calculation of harmonics and critical speeds for inertial disks on rotating shafts fixed at one or two ends. A subsequent review by Swanson et al. in 2005 described the conditions and geometries of forward and backward whirl in rotating machinery (Swanson et al., 2005). The first application of these models was for models of drill collars between stabilizers in BHAs by Jansen in 1991 (Jansen, 1991). He noted that forward whirl was caused by a center-of-mass not located on the axis of rotation in the assembly and backward whirl was caused by friction between the stabilizers and borehole wall. A similar conclusion was reached by Vandiver et al. in 1990 when they ascribed the onset of whirl from the bending or buckling of the drill collars in a bottom hole assembly (Vandiver et al., 1990). A series of experimental studies by Dykstra et al. in 1994 and 1995 confirmed onset of whirl (Dykstra et al., 1994, 1995).

As extended reach, deviated and horizontal wells became a mainstay of the industry in the 1990s and 2000s, interest in understanding vibrations and

dampening in the tangent and horizontal sections increased. An analysis by Heisig in 2000 computed the natural frequencies of drillstrings in laterals using resolved FEM simulations (Heisig and Neubert, 2000). This allowed for the characterization of drillstring – borehole contact throughout the full lateral section, but was found to be computationally intensive. In 2002, Tikhonov et al. proposed a hybrid model that combines the bending beam model with the lumped mass model where external forces, such as borehole contact, are applied at the nodes between beams and internal forces are applied on the beams themselves, to achieve similar results as Heisig but with significantly faster computational time (Tikhonov and Safronov, 2002).

The interaction between whirl and stick-slip is explored in papers by Leine et al. in 2002 and Christoforou and Yigit in 2003 (Leine et al., 2002; Yigit and Christoforou, 1996, 2000; Christoforou and Yigit, 2003). Both papers assume vertical wellbores and model the drillstring as a single mode approximation of a continuous beam model that is allowed to rotate off-center within a circular wellbore. A self-exciting and stable cycle was confirmed, as observed in the field, of torque on bit and angular bit velocity. Mitigation was achieved with a simple PID controller in simulation. Mihajlovic et al. present additional modeling and experimental work of rotating unbalanced masses in 2007, further confirming the drillstring behavior under stick-slip and whirl (Mihajlović et al., 2007). Applied directly to a bottom hole assembly, Liao details several experiments in 2012 where two different whirl regimes are observed: periodic

bump and stick, or continuous rolling motion (Liao et al., 2012; Ghasemloonia et al., 2014).

The low attenuation of torsional vibrations within the drillstring, low inherent frequency and ease of detection at the surface meant that simple models could continue to be applied in studies of stick-slip. In a series of papers in 2007 and 2009, Navarro-Lopéz and Cortes presented a simple lumped mass model to look at stick-slip and used this model to create a sliding mode controller to mitigate its occurrence (Navarro-López and Cortés, 2007; Navarro-Lopez, 2009). As recently as 2011, Rudat et al. used a single degree of freedom model to investigate stick-slip (Rudat et al., 2011). Further developing these models in 2013, Nandakumar and Wiercigroch presented a modified two-degree of freedom lumped-mass model to look at stick-slip and bit bounce (Nandakumar and Wiercigroch, 2013). They noted that many previous models do not allow for sufficient dampening of axial and torsional vibrations within the drillstring due to material properties. Stick-slip mitigation approaches currently used by industry employ models similar to these and are discussed in later in this chapter.

2.1.3 Current Approaches and Accounting for Deviated Wells

In 2005, Khulief and Al-Naser incorporated elasto-dynamic properties into a FEM model that incorporated bending and strain of drillstring elements (Khulief and Al-Naser, 2005). With this model, the first three vibrational modes (previously only the first mode) were formulated. They also proposed

a reduced order model that was still able to capture lower frequency modes. In 2007, they extended their work and showed the development of a stable cycle between angular displacement and velocity during these stable stick-slip events (Khulief et al., 2007). A similar FEM model presented by Trindade et al. in 2005 showed BHA deformation under compression that is similar to that experienced in the field (Trindade et al., 2005). Moreover, rotation of this deformed BHA can lead directly to whirl due to an offset center of mass during rotation.

To further understanding of bit-rock interaction, Richard et al. in 2007 presented a detailed model for Polycrystaline Diamond Compact (PDC) bits (Richard et al., 2007). PDC bits are rapidly becoming the workhorses of the industry through almost universal applicability. They looked closely at cutter-rock interaction and cutter placement. When coupled with a simplistic lumped-mass torsional drillstring model, they were able to replicate both stick-slip limit cycles and bit bounce. Analysis of stick-slip with PDC bits is continued by Zamanian et al. in 2007 and Germay et al. in two papers in 2009 which contain detailed analyses of the stick-slip limit cycle (Zamanian et al., 2007; Germay et al., 2009). Accounting for high degrees of uncertainty due to heterogeneity of the formation, Ritto et al. in 2009 added explicit uncertainty to their bit-rock interaction model and determined that even small uncertainties give large variations in axial and torsional vibrations and, through coupling, on lateral vibrations as well (Ritto et al., 2009).

Bit-rock interaction models were expanded through work by Perneder et al. in 2012 to explain bit tilt and directional tendencies when drilling with PDC bits (Perneder et al., 2012). Kovalyshen presented an analytic model for bit whirl in 2013 that uses the time history dependent bit-rock interaction to excite the onset of whirl (Kovalyshen, 2013). By allowing the BHA to buckle under compression and provide some side force to the bit, bit whirl – and the resulting spiral wall cut – is observed, and forward or backward whirl in the BHA is excited. From the analytic model, he identified a region of stability as a function of bit rotary speed and rock strength. Depouhon and Detournay in 2014 determined a critical angular bit speed, below which stick-slip occurs but above which stable bit rotation degenerates into bit bounce or whirl (Depouhon and Detournay, 2014).

With a majority of wells drilled in the past twenty years being deviated or horizontal wells, special considerations had to be taken into account for wellbore deviation. In 2010, Hakimi and Mardi proposed using the differential quadrature method to determine the contact length of a drillstring and borehole to improve calculation of friction and dampening (Hakimi and Moradi, 2010). In 2011, Sahebkar et al. presented a drillstring model for an inclined well where drillstring– wellbore interaction is accomplished through a series of linear springs (Sahebkar et al., 2011). In 2012, Hu et al. presented a FEM model that allows for special curvature of the drillstring within a deviating wellbore and also allows for strain and bending within the individual

beam elements (Hu et al., 2012). They found rapid convergence with analytic solutions for simple cases that closely matched field case measurements.

In efforts to apply models used regularly in rotor dynamics, a series of papers in 2012 by Ghayesh and Ghayesh et al., and in 2013 by Chatjigeorgiou, used finite difference models of rotating beams under chaotic excitation (Ghayesh, 2012; Ghayesh et al., 2012; Chatjigeorgiou, 2013). These beams have fixed boundary conditions where rotation is applied to one end and friction to the other and a chaotic excitation is either applied along the beam or at the frictional end. Neither of these models was confined within a borehole, but both efforts are ongoing.

With the advent of high frequency – up to 1400 Hz – measurement of downhole vibrations, previously unobserved high frequency vibrations are now being observed. In 2013, Baker Hughes equipped a PDC bit with a high-frequency collar-mounted vibration sensor to investigate at-bit vibrations and their correlations with bit failure (Makkar et al., 2014). They recorded high frequency torsional vibrations, dubbed High Frequency Torsional Oscillations (HFTO), at frequencies much higher than stick-slip vibrations, and attributed these to natural frequencies of the bottom-hole assembly that are excited by drilling through harder formations (Oueslati et al., 2013b). Subsequent laboratory tests with single cutter bits seem to confirm the existence of these high-frequency torsional vibrations (Ledgerwood III and Tergeist, 2014). They were also noticed by Stroud et al. in 2013 with a similar vibration recording tool near the bit in a rotary steerable operation (Stroud et al., 2013). However,

work by Baumgartner et al. was able to replicate these high frequency signals as an artifact of sensor whirl around the borehole (Baumgartner and van Oort, 2014).

2.2 Industry Applications

Drilling rigs built through the 1980s, some still in use today, have simple brake and throttle interfaces that make them ill-suited for automated controls. Computerized control systems only began to appear in the late 1980s and early 1990s; one of the earliest is described by Sananikone et al. in a 1992 paper as a simple torque and RPM control system where rotary speed set points are maintained through torque control (Sananikone et al., 1992). Tonnesen presents a further refinement in 1995, in the form of the NOV smart chair, which is in wide use today (Tonneson et al., 1995). Torque measurements, necessary for control, were first achieved through costly strain gauges which were quickly replaced with current sensors, integrated to estimate torque, once electric top drive units were deployed (Sananikone et al., 1992).

Early computer control efforts, such as a system described in Young in 1969, ignored drillstring dynamics completely (Young, 1969). Dynamics was considered later on, such as by Skeem in 1979 in his analysis of drillstring dynamics during jarring operations following a stuck pipe event (Skeem et al., 1979). Real-time management of drilling parameters to avoid calculated natural vibration frequencies is now common, such as in a system described by Chen in 2003. Active vibration mitigation efforts have primarily been focused

on mitigating stick-slip due to its low inherent frequency and ease of detection using surface equipment. Industry applications include the STRS System deployed by Shell (Kriesels et al., 1999) and NOV (Kyllingstad and Nessjøen, 2009) and its descendants. A newly proposed DOSKIL system proposed by Canudas-de-Wit, 2008 adds real-time weight-on-bit control (Canudas-de Wit et al., 2008). Whirl remains a topic of interest, but due to poor transmission of lateral vibration signals to the surface it incredibly hard to detect it without downhole tools. Such tools now exist and, coupled with real-time high-frequency and high bandwidth downhole communication, now offer the opportunity for improved control purposes.

The SoftTorque Rotary System (STRS) is a system developed independently by Shell and NOV, now cross-licensed, that works directly with the control system of AC top-drives to detect and mitigate stick-slip conditions. Runia et al. describe the Shell variant in detail in their 2013 paper (Dwars et al., 2013). STRS was first developed in the 1980s and initially deployed in the 1990s on rigs with electrically driven kellies or top drives. The controller was a bolt-on black box that supplemented the analog control signal and is shown in Figure 2.1. It was effective in cancelling out first order vibration modes and was often able to cancel out adjacent modes, but it was unstable at low rotational speeds, which were commonly used during well steering operations, and in long strings or strings with multiple drillstring components. It became a standard drilling tool after extensive testing on DC electric drives in the early 1990s. Once newer rigs began to be introduced with digitally con-

trolled AC top drives that used variable frequency drives, the relatively long time delay in the analog SoftTorque systems and conflicts in control signals with the VFDs reduced STRS's effectiveness and led to a decline in use. A decade later, the system was revisited and re-implemented as an integrated component of the top drive control system that eliminated time delays and control signal conflicts. Now deployed on over sixty rigs, the STRS system has been shown to be an effective stick-slip mitigation system, an example operation of which is shown in Figure 2.2. Challenges remain, including the need to tune the system to individual top drive systems and continued instability in long drillstrings.

Kyllingstad and Nessjøen detailed the NOV variant, called SoftSpeed, in two papers in 2009 and 2010 as a simple tuned PI control loop built into the top drive control unit that is able to actively dampen both the first and second modes of stick-slip vibration by modeling the drillstring as a pendulum (Kyllingstad and Nessjøen, 2009, 2010). An earlier version of the system, presented in 2009, did not account for inertia of the drillstring and was shown to be ineffective for drillstrings over 5000 meters long in simulation. The second version, presented in the 2010 paper, adds tuning for drillstring inertia, and showed that the system could dampen the fundamental modes in long strings as well as the higher order modes. A follow-up paper in 2011 detailed the results of a field trial of the system and showed that with proper tuning, the system is able to actively dampen any stick-slip vibrations encountered (Nessjøen et al., 2011). Forster, in 2011, proposed using induced axial vibration

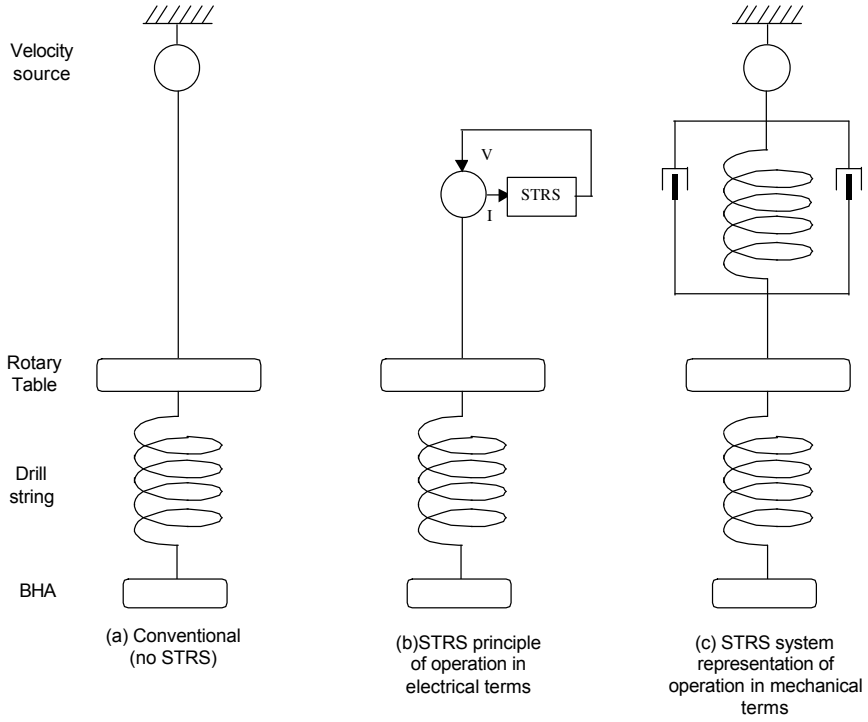

Figure 2.1: The STRS system model, as shown in (Kriesels et al., 1999).

near the bottom hole assembly to mitigate stick-slip (Forster, 2011) and a follow-on study published in 2014 showed improvements in rate of penetration as well as reduced incidents of stick-slip (Gee et al., 2014).

A new approach under development within Shell Research regards the drillstring as a transmission line for torsional waves and eliminates the need for tuning (Kreuzer and Steidl, 2010). By attempting to reduce the reflectivity of the surface boundary condition – the top drive – the incidence of standing torsional waves in the drillstring is greatly reduced (Dwars, 2015).

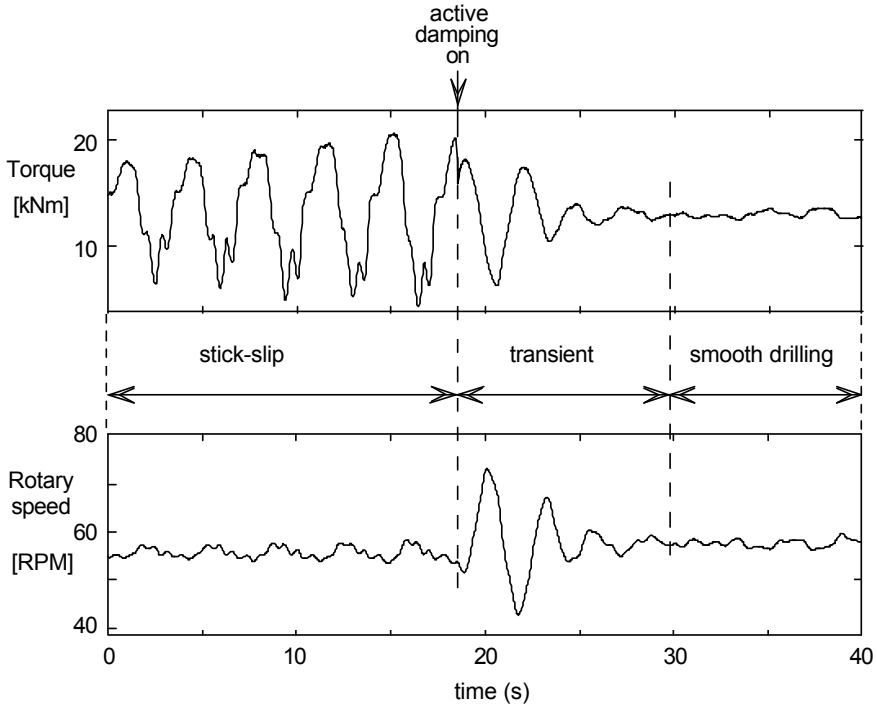

Figure 2.2: Function of STRS system during a drilling operations, as shown in (Kriesels et al., 1999).

Early field trials have shown promise in the system, but precise and high speed sensor measurements are required and poor sensor quality or delays degrade performance and can inject instabilities.

Other proposed systems have ranged from applications of Neural Networks (Dashevskiy et al., 1999; Rudat et al., 2011), non-linear control (Al-Hiddabi et al., 2003), sliding-mode control (Navarro-Lopez and Cortes, 2007; Navarro-Lopez and Licéaga-Castro, 2009), H-infinity control (Yilmaz et al., 2013), attractive ellipsoid method (Saldivar and Mondié, 2013), passive non-

linear energy sink downhole tools (Viguié et al., 2009) or time-delayed shock absorbers (Chatterjee and Mahata, 2009).

2.3 Conclusions of the Literature Review

Early drillstring dynamics models were primarily developed as aids to drilling engineers and rig designers to help understand downhole behaviors and to provide guidelines to improve drilling operations. These models made simplifying assumptions but were still able to determine critical speeds to avoid based on drillstring design. Once downhole measurements were made available, the three basic modes of vibration were characterized: stick-slip, whirl and axial vibration.

Stick-slip occurs at frequencies of 0.1 - 0.5 Hz and is readily detectible at surface, so much of the modeling and control efforts since the 1980s has focused on identifying and actively mitigating stick-slip. Simple single degree of freedom models are able to simulate stick-slip and an entire suite of control algorithms has been proposed. This work has found an application in industry, as the Shell SoftTorque Reduction System and the NOV SoftSpeed System and has been shown to be effective.

Rather than propose another comprehensive, computationally intensive drillstring model which may be tuned to replicate field data, this dissertation will instead develop a computationally efficient method to characterize drillstring dynamics for optimization and control purposes. By treating the drillstring as a wave guide for both standing and traveling waves, both axial and

torsional waves may effectively modeled using the wave equation, and by incorporating a methodology to account for damping due to wellbore geometry, physical results are produced.

Chapter 3

Definition of Drillstring Models

The solution strategy for physical models may be broken up in two broad categories, time domain models and frequency domain models. In general, each of these categories can be transformed into the other, however, it is possible to make simplifying assumptions that reduce the complexity of each. A study of both shall be conducted, but shall begin with the derivation of the underlying model, the damped wave equation, from basic principles.

3.1 Derivation from First Principles

The dynamics of a thin walled tube may be approximated by Hooke's law in cylindrical coordinates if linear, elastic behavior is assumed. Along the outside of the tube, Hooke's law states

$$\epsilon_z = \frac{1}{E}\left(\sigma_z - \nu\left(\sigma_r + \sigma_\theta\right)\right) \tag{3.1}$$

$$\epsilon_r = \frac{1}{E}\left(\sigma_r - \nu\left(\sigma_z + \sigma_\theta\right)\right) \tag{3.2}$$

$$\epsilon_\theta = \frac{1}{E}\left(\sigma_\theta - \nu\left(\sigma_z + \sigma_r\right)\right) \tag{3.3}$$

where the axial, radial and hoop stresses are σ_z, σ_r, and σ_θ, E is Young's modulus and ν is Poisson's ratio. Shear is given by

$$\tau_{rz} = G\gamma_{rz} \tag{3.4}$$

$$\tau_{\theta z} = G\gamma_{\theta z} \tag{3.5}$$

$$\tau_{r\theta} = G\gamma_{r\theta} \tag{3.6}$$

where the shear strains are γ, the shear stresses are τ and G is the shear modulus.

For the remainder of the dissertation, the following simplifying assumptions will be made to allow the drillstring to be simplified as a one dimensional wave guide

- The radial strain due to a difference in fluid pressure from the inside of the drillpipe to the annulus will be assumed to be negligible and will be taken to be zero.
- The radial and hoop strain due to axial stress will be assumed to be much smaller than axial strain and thus be negligible and taken to be zero.
- Only rotational shear strain is taken into account and shear strain due to bending is ignored.
- Axial and torsional components are entirely decoupled along the drillstring.

Thus, the simplified form of Hooke's law becomes

$$\sigma_z = E\epsilon_z \tag{3.7}$$

$$\tau_{\theta z} = G\gamma_{\theta z} \tag{3.8}$$

Since these equations are identical in form, the resulting damped wave equation is equivalent for both axial and torsional waves. In the following sections, strain is taken to be $\epsilon_z = \frac{\partial u}{\partial z}$ and shear strain is taken to be $\gamma_{\theta z} = \frac{\partial \phi}{\partial z}$, where u and ϕ are axial and torsional displacement, respectively. For the remainder of this dissertation, $\sigma = \sigma_z$, $\epsilon = \epsilon_z$, $\tau = \tau_{\theta z}$ and $\gamma = \gamma_{\theta z}$.

3.1.1 Damped Wave Equation

The wave equation for axial or torsional motion of a drillstring may be derived from first principles assuming a linear response of the system. Beginning with simplified form of Hooke's law in Equation 3.7

$$\frac{F}{A} = \sigma = E\epsilon = E\frac{\partial u}{\partial z} \tag{3.9}$$

where F is axial force, A is cross sectional area and u is displacement as a function of axial position, z and time, t.

An incremental change in force due to the acceleration of an incremental mass is given by Newton's law

$$\frac{\partial F}{\partial z} = \rho A\frac{\partial^2 u}{\partial t^2} \tag{3.10}$$

Equations 3.9 and 3.10 may be combined into a single equation

$$\frac{\partial}{\partial z}\left(EA\frac{\partial u}{\partial z}\right) = \frac{\partial F}{\partial z} = \rho A\frac{\partial^2 u}{\partial t^2} \tag{3.11}$$

$$\frac{\partial^2 u(z,t)}{\partial t^2} = \left(\frac{\rho}{E}\right)\frac{\partial^2 u(z,t)}{\partial z^2} \tag{3.12}$$

which gives the one dimensional undamped wave equation

$$\frac{1}{v^2}\frac{\partial^2 u(z,t)}{\partial t^2} = \frac{\partial^2 u(z,t)}{\partial z^2} \tag{3.13}$$

Axial and torsional wave velocity is not dependent on frequency, thus the wave velocity for axial, v_a, and torsional, v_t, are given by

$$v_a = \sqrt{\frac{E}{\rho}} \tag{3.14}$$

$$v_t = \sqrt{\frac{G}{\rho}} \tag{3.15}$$

Damping may be added to Equation 3.10 as a term that removes a velocity dependent component from the incremental force

$$\frac{\partial F}{\partial z} = \rho A\frac{\partial^2 u}{\partial t^2} - C\frac{\partial u}{\partial t} \tag{3.16}$$

which gives the damped wave equation

$$\frac{1}{v_a^2}\frac{\partial^2 u(z,t)}{\partial t^2} + c\frac{\partial u}{\partial t} = \frac{\partial^2 u(z,t)}{\partial z^2} \tag{3.17}$$

where

$$c = c(z,t) = \frac{C}{EA} \tag{3.18}$$

is the damping coefficient, which may be a function of distance and time. This coefficient may be modeled a number of ways, a thorough review of which is given by Lee in his thesis (Lee, 1991). A discussion of the forms of damping considered in this dissertation will be given in a subsequent section.

An equivalent construct may be derived for torsional waves if Equation 3.8 is combined with the following relationship between angular acceleration and the moment of inertia

$$\frac{\partial \tau}{\partial z} = \rho J \frac{\partial^2 \phi}{\partial t^2} \tag{3.19}$$

to give

$$\frac{1}{v_t^2}\frac{\partial^2 \phi(z,t)}{\partial t^2} + c\frac{\partial \phi}{\partial t} = \frac{\partial^2 \phi(z,t)}{\partial z^2} \tag{3.20}$$

where $\phi(z,t)$ is the angular displacement as a function of axial position, z, and time, t.

3.2 Frequency Domain Modeling

The wave equation may be modeled in the frequency domain through the application of the Fourier transform and using an elegant simplification where only the response of the system to a single induced frequency is examined. This method generates a transfer matrix which establishes a relationship between the displacement and force across a discretized simulation node.

3.2.1 Transfer Matrix Method

The one dimensional damped wave equation, Equation 3.17, can be solved if a zero displacement boundary condition is assumed at $z = 0$ and a

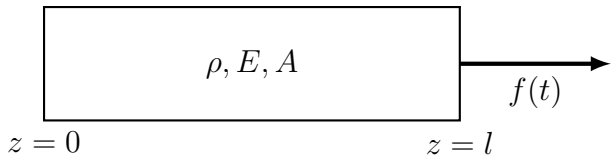

Figure 3.1: Simple beam of length l modeled using the one dimensional wave equation.

unit harmonic input $f(t) = e^{i\omega t}$ is assumed at $z = l$, as shown in figure 3.1. These boundary conditions may be summarized as

$$\frac{\partial u(z=0)}{\partial z} = 0 \tag{3.21}$$

$$EA\frac{\partial u}{\partial z}(z=l) = e^{i\omega t} \tag{3.22}$$

Equation 3.17 may be solved by applying the Fourier Transform, $u(z,t) \rightarrow \mathcal{U}(z,\omega)$ to obtain

$$\frac{\rho}{E}\frac{\partial^2 u(z,t)}{\partial t^2} + \frac{C}{EA}\frac{\partial u}{\partial t} = \frac{\partial^2 u(z,t)}{\partial z^2} \tag{3.23}$$

$$-\omega^2 \mathcal{U}(z,\omega) + i\omega\frac{C}{EA}\mathcal{U}(z,\omega) = \frac{\partial^2 \mathcal{U}(z,\omega)}{\partial z^2} \tag{3.24}$$

$$-\left(\frac{\omega^2\rho}{E} - \frac{i\omega C}{EA}\right)\mathcal{U}(z,\omega) = \frac{\partial^2 \mathcal{U}(z,\omega)}{\partial z^2} \tag{3.25}$$

$$\tag{3.26}$$

which is simplified to the equation

$$-k^2 \mathcal{U}(z,\omega) = \frac{\partial^2 \mathcal{U}(z,\omega)}{\partial z^2} \tag{3.27}$$

where

$$k^2 = \frac{\omega^2\rho}{E} - i\frac{C\omega}{EA} \tag{3.28}$$

This differential equation has the general solution

$$\mathcal{U}(z,\omega) = c_1 \sin(kz) + c_2 \cos(kz) \tag{3.29}$$

and the boundary conditions, Equations 3.21 and 3.22, become

$$\frac{\partial \mathcal{U}(0,\omega)}{\partial z} = 0 \tag{3.30}$$

$$EA\frac{\partial \mathcal{U}(l,\omega_0)}{\partial z} = \delta(\omega - \omega_0) \tag{3.31}$$

At frequency $\omega = \omega_0$, the boundary condition at $x = l$ becomes

$$\frac{\partial \mathcal{U}(l,\omega)}{\partial z} = \frac{1}{EA} \tag{3.32}$$

Applying the boundary condition given by Equation 3.30 gives $c_1 = 0$. Equation 3.32 can then be used to solve for c_2:

$$\frac{\partial \mathcal{U}(l,\omega)}{\partial z} = c_2 k \sin(kl) = \frac{1}{EA} \tag{3.33}$$

$$c_2 = \frac{1}{EAk\sin(kl)} \tag{3.34}$$

which gives the final solution

$$\mathcal{U}(z,\omega) = -\frac{\cos kz}{EAk \sin kl} \tag{3.35}$$

Now, this assumes a beam of length l with the two force boundary conditions, $f(t)$ at $z = l$ and 0 at $z = 0$. For a subcomponent of the system, a force balance needs to conducted, as shown in Figure 3.2 and can be expressed as

$$\begin{pmatrix} \mathcal{U}_l \\ F_l \end{pmatrix}_n = \begin{pmatrix} \mathcal{U}_u \\ F_u - F_e \end{pmatrix}_{n-1} \tag{3.36}$$

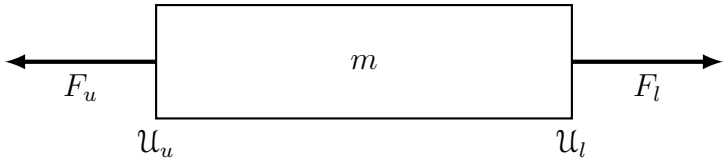

Figure 3.2: Force balance across a simple beam element.

where $F_e = f(t)$ is the external excitation force.

To calculate the transfer matrix, the change in displacement, from $z = 0$ to $z = l$ based upon a unit force at $z = l$ is given by

$$z = 0 \qquad \mathcal{U}(0,\omega) = -\frac{1}{EAk\sin kl} \tag{3.37}$$

$$z = l \qquad \mathcal{U}(l,\omega) = -\frac{\cos kl}{EAk\sin kl} = \mathcal{U}(0,\omega)\cos kl \tag{3.38}$$

For a unit force from $z = 0$, the boundary conditions must be swapped but give the same (but negative) solution

$$z = 0 \qquad \mathcal{U}(0,\omega) = \frac{\cos kl}{EAk\sin kl} = -\mathcal{U}(l,\omega)\cos kl \tag{3.39}$$

$$z = l \qquad \mathcal{U}(l,\omega) = \frac{1}{EAk\sin kl} \tag{3.40}$$

Therefore, for an arbitrary force from either $z = 0$ or $z = l$, the displacements at $z = 0$ and $z = l$ can be computed using

$$\begin{pmatrix} \mathcal{U}_{z=0} \\ \mathcal{U}_{z=l} \end{pmatrix} = \begin{pmatrix} \frac{\cos kl}{EAk\sin kl} & -\frac{1}{EAk\sin kl} \\ \frac{1}{EAk\sin kl} & -\frac{\cos kl}{EAk\sin kl} \end{pmatrix} \begin{pmatrix} F_{z=0} \\ F_{z=l} \end{pmatrix} \tag{3.41}$$

from which the transfer matrix can be determined by solving for $\mathcal{U}_{z=l}$ and $F_{z=l}$ given that $\mathcal{U}_{z=0}$ and $F_{z=0}$ are known:

$$\mathcal{U}_{z=0} = \frac{\cos kl}{EAk\sin kl}F_{z=0} - \frac{1}{EAk\sin kl}F_{z=l} \tag{3.42}$$

$$\mathcal{U}_{z=l} = \frac{1}{EAk\sin kl}F_{z=0} - \frac{\cos kl}{EAk\sin kl}F_{z=l} \tag{3.43}$$

Equation 3.42 may be rearranged to find $F_{z=l}$

$$F_{z=l} = -\left(EAk\sin kl\right)\mathcal{U}_{z=0} + \left(\cos kl\right)F_{z=0} \tag{3.44}$$

and using equations 3.43 and 3.44, $\mathcal{U}_{z=l}$ may be found

$$\begin{aligned}
\mathcal{U}_{z=l} &= \frac{1}{EAk\sin kl}F_{z=0} - \frac{\cos kl}{EAk\sin kl}F_{z=l} && (3.45)\\
&= \frac{1}{EAk\sin kl}F_{z=0} && (3.46)\\
&\quad - \frac{\cos kl}{EAk\sin kl}\left(-\left(EAk\sin kl\right)\mathcal{U}_{z=0} + \left(\cos kl\right)F_{z=0}\right) && (3.47)\\
&= \frac{1-\cos^2 kl}{EAk\sin kl}F_{z=0} + \left(\cos kl\right)\mathcal{U}_{z=0} && (3.48)\\
\mathcal{U}_{z=l} &= \left(\cos kl\right)\mathcal{U}_{z=0} + \left(\frac{\sin kl}{EAk}\right)F_{z=0} && (3.49)
\end{aligned}$$

which may be written in matrix notation as

$$\begin{pmatrix}\mathcal{U}\\F\end{pmatrix}_{z=l} = \begin{pmatrix}\cos kl & \frac{\sin kl}{EAk}\\ -EAk\sin kl & \cos kl\end{pmatrix}\begin{pmatrix}\mathcal{U}\\F\end{pmatrix}_{z=0} \tag{3.50}$$

giving an elegant method to compute the displacement and force at one end of a beam given the displacement and force at the other. This can be further transformed using the transformation $k = i\gamma$ to give

$$\begin{aligned}
\mathcal{U} &= -\frac{\cos kz}{EAk\sin kl} = -\frac{\cos i\gamma z}{EAi\gamma\sin i\gamma l} = -\frac{\cosh\gamma z}{EA\gamma\sinh\gamma l} && (3.51)\\
\gamma &= \sqrt{\frac{iC\omega}{EA} - \frac{\omega^2\rho}{E}} = \sqrt{\frac{i\omega}{E}\left(1\omega\rho + \frac{C}{A}\right)} && (3.52)
\end{aligned}$$

and using the transformation $EAk = i\omega Z_0$ to give

$$Z_0 = \frac{EA}{i\omega}k = A\sqrt{\frac{E^2}{(i\omega)^2}\frac{i\omega}{E}\left(i\omega\rho + \frac{C}{A}\right)} = A\sqrt{\frac{E}{i\omega}\left(i\omega\rho + \frac{C}{A}\right)} \tag{3.53}$$

which results in the elegant transfer matrix

$$\begin{pmatrix} \mathcal{U} \\ F \end{pmatrix}_n = \begin{pmatrix} \cosh \gamma L & \frac{\sinh \gamma l}{i\omega Z_0} \\ i\omega Z_0 \sinh \gamma l & \cosh \gamma L \end{pmatrix} \begin{pmatrix} \mathcal{U} \\ F \end{pmatrix}_{n-1} \tag{3.54}$$

where

$$\gamma = \sqrt{\frac{i\omega}{E}\left(1\omega\rho + \frac{C}{A}\right)} \tag{3.55}$$

$$Z_0 = A\sqrt{\frac{E}{i\omega}\left(i\omega\rho + \frac{C}{A}\right)} \tag{3.56}$$

3.2.2 Mass-Spring-Damper Equivalent System

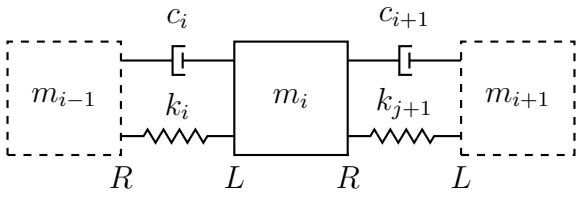

Figure 3.3: Element i within a mass-spring-damper system.

Similarly, a transfer matrix may be built for a mass-spring-dashpot system described by the general differential equations

$$m\frac{d^2u}{dt^2} = -ku - c\frac{du}{dt} \tag{3.57}$$

First, for a spring, from Newton's second law, the force across the spring is given by

$$m_i\mathcal{U}_i'' = F_i^R - F_i^L \tag{3.58}$$

and when subject to harmonic motion, the acceleration is given by $\left(\frac{d^2z}{dt^2}\right)_i = \omega^2\mathcal{U}_i$, so

$$F_i^R = -\omega^2 m_i\mathcal{U}_i + F_i^L \tag{3.59}$$

Assuming that there is zero strain across mass i, $\mathcal{U}_i = \mathcal{U}_i^R = \mathcal{U}_i^L$, giving the matrix:

$$\begin{pmatrix} \mathcal{U} \\ F \end{pmatrix}_i^R = \begin{pmatrix} 1 & 0 \\ -\omega^2 m_i & 1 \end{pmatrix} \begin{pmatrix} \mathcal{U} \\ F \end{pmatrix}_i^L \tag{3.60}$$

Similarly, if transmission of force is assumed between nodes, then the change in displacement may be calculated

$$F_{i-1}^R = F_i^L \tag{3.61}$$

$$\mathcal{U}_i^L - \mathcal{U}_{i-1}^R = \frac{F_{i-1}^R}{k_i} \tag{3.62}$$

which gives the transfer matrix

$$\begin{pmatrix} \mathcal{U} \\ F \end{pmatrix}_i^L = \begin{pmatrix} 1 & \frac{1}{k_i} \\ 0 & 1 \end{pmatrix} \begin{pmatrix} \mathcal{U} \\ F \end{pmatrix}_{i-1}^R \tag{3.63}$$

Combining these two matrices

$$\begin{pmatrix} \mathcal{U} \\ F \end{pmatrix}_i^R = \begin{pmatrix} 1 & 0 \\ -\omega^2 m_i & 1 \end{pmatrix} \begin{pmatrix} \mathcal{U} \\ F \end{pmatrix}_i^L \tag{3.64}$$

$$= \begin{pmatrix} 1 & 0 \\ -\omega^2 m_i & 1 \end{pmatrix} \begin{pmatrix} 1 & \frac{1}{k_i} \\ 0 & 1 \end{pmatrix} \begin{pmatrix} \mathcal{U} \\ F \end{pmatrix}_{i-1}^R \tag{3.65}$$

$$= \begin{pmatrix} 1 & \frac{1}{k_i} \\ -\omega^2 m_i & 1 - \frac{\omega^2 m}{k} \end{pmatrix} \begin{pmatrix} \mathcal{U} \\ F \end{pmatrix}_{i-1}^R \tag{3.66}$$

If a velocity dependent damper is placed in parallel with the spring, then Equation 3.62 will change to

$$\mathcal{U}_i^L - \mathcal{U}_{i-1}^R = \frac{F_{i-1}^R}{k_i + i\omega c} \tag{3.67}$$

which gives the spring-damper transfer matrix

$$\begin{pmatrix} \mathcal{U} \\ F \end{pmatrix}_i^L = \begin{pmatrix} 1 & \frac{1}{k_i + i\omega c} \\ 0 & 1 \end{pmatrix} \begin{pmatrix} \mathcal{U} \\ F \end{pmatrix}_{i-1}^R \tag{3.68}$$

and when combined with the mass matrix, gives the final form of the mass-spring-damper transfer matrix

$$\begin{pmatrix} \mathcal{U} \\ F \end{pmatrix}_n = \begin{pmatrix} 1 & \frac{1}{k+i\omega c} \\ -\omega^2 m & 1 - \frac{\omega^2 m}{k+i\omega c} \end{pmatrix} \begin{pmatrix} \mathcal{U} \\ F \end{pmatrix}_{n-1} \tag{3.69}$$

3.2.3 Solution Methodology

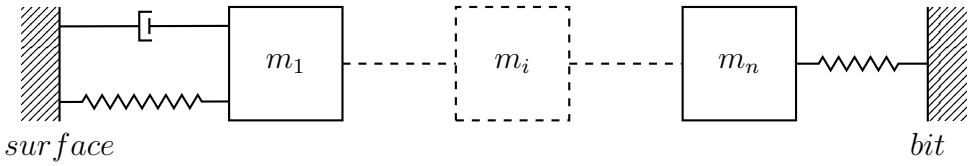

Figure 3.4: Drillstring Model including the surface and bit boundary conditions.

A 2×2 transfer matrix for a system provides two equations for a system of four unknowns, thus requiring two known boundary conditions – zero displacement boundaries at the surface and the bit. The surface equipment is modeled as a spring, representing the cables suspending the topdrive, and a damper, representing the damping from the mass of the topdrive itself. Bit-rock interaction is modeled through the use of a simple spring, with the spring constant representing the elastic axial interaction of the bit and rock but not the rock cutting process. The drillstring itself is composed of n beam elements, each defined by the drillpipe's damping factor – discussed in the next section – and physical properties, and characterized by a transfer matrix $\mathcal{A}_i$.

Given the two known boundary conditions, the other two unknown conditions may be computed by assembling the transfer matrix for the en-

tire drillstring. This is simply the product of all the transfer matrices of the drillstring components

$$\begin{pmatrix} \mathcal{U} \\ F \end{pmatrix}_{bit} = \mathcal{A}_n \begin{pmatrix} \mathcal{U} \\ F \end{pmatrix}_{n-1} \tag{3.70}$$

$$= \mathcal{A}_n \mathcal{A}_{n-1} \begin{pmatrix} \mathcal{U} \\ F \end{pmatrix}_{n-2} \tag{3.71}$$

$$... \tag{3.72}$$

$$= \prod_{1}^{n} \mathcal{A}_i \begin{pmatrix} \mathcal{U} \\ F \end{pmatrix}_{surface} \tag{3.73}$$

$$\begin{pmatrix} \mathcal{U} \\ F \end{pmatrix}_{bit} = \mathcal{A} \begin{pmatrix} \mathcal{U} \\ F \end{pmatrix}_{surface} \tag{3.74}$$

A harmonic displacement or force input can then be assigned at one of the two boundaries and the response of entire system efficiently computed. However, this is only simple if the excitation is at the boundary. If the excitation, or excitations, are input somewhere within the drillstring, then the process is complicated unless an augmented transfer matrix is introduced.

3.2.4 Augmenting the Transfer Matrix

The 2×2 transfer matrix is a powerful tool to investigate the transmission of displacement and force through a system, but it does not easily allow for input of arbitrary additional harmonic displacements or forces within the system, as would be experienced in the case of an induced axial oscillator. For this case, an external harmonic force or displacement may be input in the system through the use of an augmented transfer matrix. A similar method was used by Ceasu et al. to add point forces while assembling transfer matrices

to describe rotating shafts (Ceasu et al., 2010). This method builds on this to include both harmonic forces and displacements, all within a single matrix.

Beginning with a 2×2 transfer matrix $\mathcal{A}$, the relation between $\mathcal{U}_n$ and $\mathcal{U}_{n-1}$ and F_n and F_{n-1} are given by

$$\mathcal{U}_n = \mathcal{A}_{11}\mathcal{U}_{n-1} + \mathcal{A}_{12}F_{n-1} \tag{3.75}$$

$$F_n = \mathcal{A}_{21}\mathcal{U}_{n-1} + \mathcal{A}_{22}F_{n-1} \tag{3.76}$$

An external force input, $F_{external}$, and an external displacement input, $\mathcal{U}_{external}$ may be added directly to the respective equations if they are assumed to be constant, harmonic, point sources. of the forms

$$u_{external}(t) = u_0 \cos(\omega_0 t + \phi) \tag{3.77}$$

$$F_{external}(t) = f_0 \cos(\omega_0 t + \phi) \tag{3.78}$$

where ω_0 is the harmonic frequency and ϕ is the phase. Applying the Fourier transform at frequency $\omega = \omega_0$ gives

$$\mathcal{U}_{external}(\omega) = \pi u_0 \tag{3.79}$$

$$\mathcal{F}_{external}(\omega) = \pi f_0 \tag{3.80}$$

and then adding to the respective equations gives

$$\mathcal{U}_n = \mathcal{A}_{11}\mathcal{U}_{n-1} + \mathcal{A}_{12}F_{n-1} + \mathcal{U}_{external} \tag{3.81}$$

$$F_n = \mathcal{A}_{21}\mathcal{U}_{n-1} + \mathcal{A}_{22}F_{n-1} + \mathcal{F}_{external} \tag{3.82}$$

which may be written in a 3×3 matrix form as

$$\begin{pmatrix} \mathcal{U} \\ F \\ 1 \end{pmatrix}_n = \begin{pmatrix} \cosh \gamma L & \frac{\sinh \gamma L}{i\omega Z_0} & \mathcal{U}_{external} \\ i\omega Z_0 \sinh \gamma L & \cosh \gamma L & \mathcal{F}_{external} \\ 0 & 0 & 1 \end{pmatrix} \begin{pmatrix} \mathcal{U} \\ F \\ 1 \end{pmatrix}_{n-1} \tag{3.83}$$

If there is no external input that node n, these can be set to zero and the transfer matrix behaves in an identical manner to a 2×2 matrix.

3.3 Time Domain Modeling

The damped wave equation may be solved in the time domain using the finitie difference method or a simplified form with an n-DOF mass-spring-damper system to find the state space solution. The finite difference method is presented first followed by the state-space solution.

3.3.1 Steady State Solution

In the case of the damped axial wave equation, the final time domain solution is the sum of the steady state solution – which solves for the effects of the constant force due to gravity, and the dynamic solution – which solves for the effects of transient forces on the drillstring. To account for gravity, the damped wave equation needs to be modified

$$\frac{\partial^2 u(z,t)}{\partial t^2} = v^2 \frac{\partial^2 u(z,t)}{\partial z^2} - c\frac{\partial u(z,t)}{\partial t} + g \tag{3.84}$$

with the boundary conditions

$$u(z,0) = 0 \tag{3.85}$$

$$u(0,t) = 0 \tag{3.86}$$

$$u(L,t) = u_0(t) \tag{3.87}$$

where v is the wave velocity and the c is the damping coefficient due to friction

$$v^2 = \frac{E}{\rho} \tag{3.88}$$

$$c = \frac{\mu F_n}{\rho A} \tag{3.89}$$

The steady state solution does not depend on time, t, and is given by

$$v^2 \frac{\partial^2 s(z)}{\partial z^2} = -g \tag{3.90}$$

which, once proper boundary conditions are applied and including drillstring buoyancy is given by

$$s(z) = \frac{z}{EA}\left[w\left(L - \frac{z}{2}\right) - Ap(L)\right] \tag{3.91}$$

for an untapered string, where w is the weight per unit length, L is the length of the drillstring, A is the cross sectional area, and $p(L)$ is the mud pressure at depth L. For a tapered string, the solution is simply the piecewise summation of the various components

$$s(z) = \Sigma_i \frac{z}{EA_i}\left[w\left(L_i - \frac{z}{2}\right) - Ap(L_i)\right] \tag{3.92}$$

For the remaining solutions, the steady state solution is neglected and only the transient component computed. The complete solution may be assembled as the sum of the steady state solution and the transient solution.

3.3.2 Finite Difference Solution

The dynamic solution may be solved using a centered finite difference approach. The first and second derivatives are approximated using the central differences

$$\frac{\partial^2 u(z,t)}{\partial t^2} \approx \frac{u_i^{n+1} - 2u_i^n + u_i^{n-1}}{\Delta t^2} \tag{3.93}$$

$$\frac{\partial^2 u(z,t)}{\partial z^2} \approx \frac{u_{i+1}^n - 2u_i^n + u_{i-1}^n}{\Delta z^2} \tag{3.94}$$

$$\frac{\partial u(z,t)}{\partial t} \approx \frac{u_i^{n+1} - u_i^n}{\Delta t} \tag{3.95}$$

where i is the discretization in space, z, and n is the discretization in time, t.

When substituted into the partial differential equation for the axial damped wave equation, gives

$$\frac{u_i^{n+1} - 2u_i^n + u_i^{n-1}}{\Delta t^2} = v^2 \frac{u_{i+1}^n - 2u_i^n + u_{i-1}^n}{\Delta z^2} - c\frac{u_i^{n+1} - u_i^n}{\Delta t} + g \tag{3.96}$$

and simplifying

$$u_i^{n+1} = \frac{1}{1 + c\Delta t}\left(\left(\frac{v\Delta t}{\Delta z}\right)^2 \left(u_{i+1}^n - 2u_i^n + u_{i-1}^n\right) + 2u_i^n - u_i^{n-1} + c\Delta t u_i^n + g\Delta t^2\right) \tag{3.97}$$

The wave propagation velocity is constant for all elements, but the damping factor c can be a function of depth.

Discretization in the spatial domain, z, is chosen to be equal to joint length, $\Delta z = 30ft$. Discretization in the time domain must smaller than the time step necessary for a wave to propagate across an element, thus $\Delta t < \frac{\Delta z}{v}$

and is chosen to be $\Delta t = \frac{\Delta z}{2v}$. Future work may include optimization of the time step to improve performance and accuracy.

In the torsional case, the finite difference approximation is given by

$$\phi_i^{n+1} = \frac{1}{1 + c\Delta t}\left(\left(\frac{v\Delta t}{\Delta z}\right)^2 \left(\phi_{i+1}^n - 2\phi_i^n + \phi_{i-1}^n\right) + 2\phi_i^n - \phi_i^{n-1} + c\Delta t\phi_i^n\right) \tag{3.98}$$

3.3.3 State Space Solution

An alternative solution methodology in the Laplace domain may be given by the state space solution of the approximation of the wave equation – a series of mass-spring-dampers, as shown in Figure 3.5, which obey the following equation

$$m\frac{d^2u}{dt^2} = -ku - c\frac{du}{dt} \tag{3.99}$$

where, m is the mass of each element, $k = \frac{EA}{L}$ is the axial spring constant or $k = \frac{GJ}{L}$ is the torsional spring constant, and c is the damping between elements.

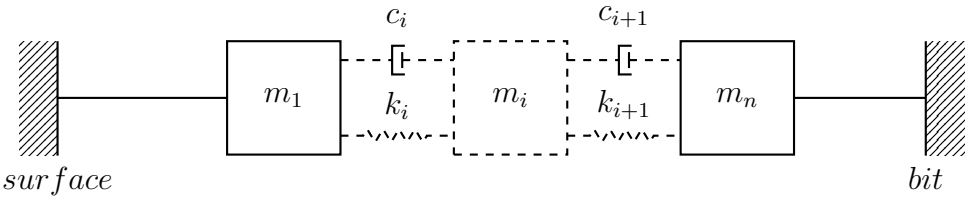

Figure 3.5: Drillstring model consisting of a series of mass-spring-dampers and arbitrary surface and bit boundary conditions.

For a n-DOF model, the motion of each mass may be described using

$$m_i\ddot{u}_i = -k_{i-1}\left(u_i - u_{i-1}\right) - u_i\left(u_i - u_{i+1}\right) - c_i\dot{u}_i \tag{3.100}$$

and the transfer function may be obtained for an axial displacement source at the bit and a zero displacement boundary condition at the rig. Therefore, $u_1, ..., u_{n-1}$ represent the motion of the $n-1$ drillstring elements and u_n is an ideal velocity source. This system can then be expressed as a series of n second order differential equations in the form $M\ddot{\tilde{u}}+C\dot{\tilde{u}}+K\tilde{u} = k_1 e_1 \phi_1$, where $e_1 \in \mathbf{R}^n$ is the standard basis vector, $\tilde{u} = [u_1, u_2, ..., u_n]$ is the new state vector with the axial displacements of n lumped masses and the M, C and K matrices are the mass, damping and spring matrices defined as

$$M = \begin{bmatrix} m_1 & & \\ & \ddots & \\ & & m_n \end{bmatrix} \qquad C = \begin{bmatrix} c_1 & & \\ & \ddots & \\ & & c_n \end{bmatrix} \tag{3.101}$$

$$K = \begin{bmatrix} k_1 + k_2 & -k_2 & & \\ ... & -k_{i-1} & k_{i-1} + k_i & -k_i \\ & & \ddots & \\ & & & \ddots \\ & & -k_n & k_n \end{bmatrix} \tag{3.102}$$

Applying the Laplace transform and rearranging gives the transfer function of the plant which will be used in the subsequent control section.

$$\tilde{\Phi}(s) = (Ms^2 + Cs + K)^{-1} k_1 e_1 \frac{1}{s} U(s), \qquad Y(s) = e_7^\top \tilde{\Phi}(s) s \tag{3.103}$$

$$G(s) = \frac{Y(s)}{U(s)} = k_1 e_7^\top (Ms^2 + Cs + K)^{-1} e_1 \tag{3.104}$$

This construct may be used in both the frequency domain, for control system design and system response, and in the time domain to analyze

transient behavior. In the case of this dissertation, a commercial ODE solver, Matlab ODE 45, is used to compute the inverse transform to the time domain.

3.4 Sources of Damping

Damping within the drillstring system comes from various sources and needs to be accounted for. The broad categories of damping, as described by Lee in his dissertation, are:

- *Material hysteresis*: internal damping within the steel structure itself can either be described as a velocity, hence frequency dependent, damping term or as a complex damping factor in the steel properties, E or G, themselves.

- *Friction with the borehole*: this velocity dependent term can be modeled in a variety of ways, including Coulomb friction, valid if the velocity profile crosses zero in a cycle, and Streibeck fricton.

- *Viscous friction with the borehole fluids*: enforcing the no-slip condition between the borehole fluid and the drillpipe body necessitates the addition of damping, which may be estimated through the addition of a small mass to the moving drillpipe.

- *Radiation of energy into the formation*: the near wellbore formation is able to absorb energy from vibration through the cross coupling of lateral modes of vibration with the axial and torsional ones considered.

3.4.1 Structural Damping

Damping within structures can also be expressed by using the complex Young's Modulus, $\tilde{E}$, which is given by

$$\tilde{E} = E(1 - \eta i) \tag{3.105}$$

Where η is the structural damping coefficient and is simply twice the viscous damping ratio, ζ, which can be measured for materials and typically varies between 0.03 and 0.05 for steel (Han, et al., 2013). In this dissertation, a value of $\eta = 0.04$ is used.

3.4.2 Equivalent Viscous Damping

Friction in an oscillating system can be modeled with an equivalent viscous damping coefficient, as shown in Figure 3.6. The work done by a damper per cycle in a harmonically forced system can be calculated using

$$W_d = \int F_d dx \tag{3.106}$$

Given that friction force is velocity dependent, $F_d = C\frac{dx}{dt}$, and $dx = \left(\frac{dx}{dt}\right) dt$. For harmonic motion with cyclic displacement amplitude X at steady state $x = X\sin(\omega t - \phi)$, the equation becomes

$$W_d = \int F_d dx = \int \left(C\frac{dx}{dt}\right) \cdot \left(\frac{dx}{dt}dt\right) \tag{3.107}$$

$$= C\omega^2 X^2 \int_0^{\frac{2\pi}{\omega}} \cos^2(\omega t - \phi) dt \tag{3.108}$$

$$= \pi C \omega X^2 \tag{3.109}$$

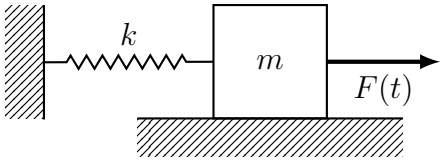

(a) Oscillating mass with sliding friction coefficient μ.

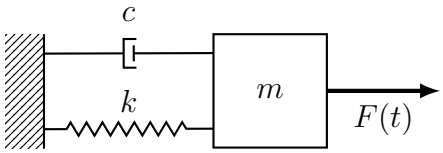

(b) Equivalent system with damper element c modeling the action of friction.

Figure 3.6: Modeling friction as an equivalent damper.

Rearranging the derivative of the steady state displacement equation

$$\dot{x} = \omega X \cos(\omega t - \phi) \tag{3.110}$$

$$= \pm\omega X \sqrt{\cos^2(\omega t - \phi)} \tag{3.111}$$

$$= \pm\omega X \sqrt{1 - \sin^2(\omega t - \phi)} \tag{3.112}$$

$$= \pm\sqrt{X^2 - x^2} \tag{3.113}$$

and applying in the force dampening equation

$$F_d = C\dot{x} = \pm C\omega\sqrt{X^2 - x^2} \tag{3.114}$$

gives

$$\frac{F_d^2}{X^2} = C^2\omega^2\left(1 - \frac{x^2}{X^2}\right) \tag{3.115}$$

which may be rearranged as

$$\left(\frac{F_d}{C\omega X}\right)^2 + \left(\frac{x}{X}\right)^2 = 1 \tag{3.116}$$

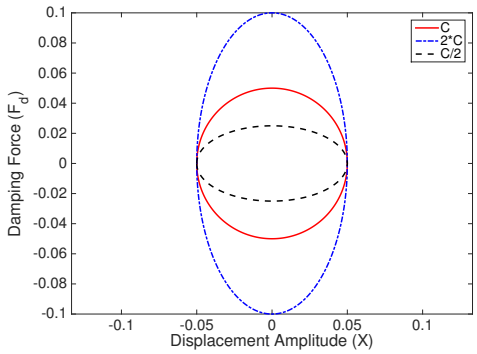

(a) Varying damping coefficient C.

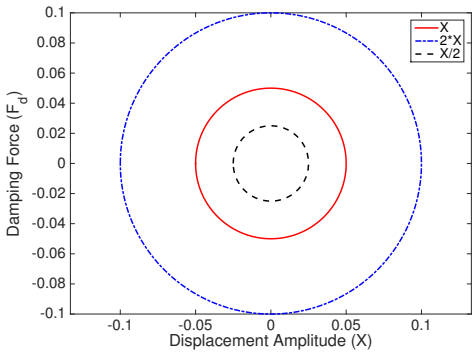

(b) Varying displacement amplitude X.

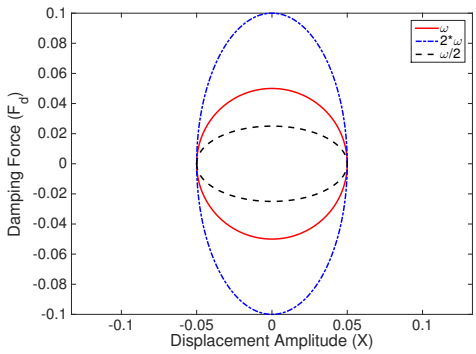

(c) Varying harmonic frequency ω.

Figure 3.7: For a normalized case, where $C = 1$, $X = 1$, $\omega = 1$, the parameters are varied in turn to demonstrate the effects on damping force. Total energy dissipated by damping is defined the area of the inscribed circle.

giving the equation of an ellipse. The area within the ellipse is equal to the energy dissipated by the viscous dampening.

As shown in Figure 3.7, doubling the damping coefficient C or frequency ω only doubles the area inscribed in the ellipse, while doubling the displacement amplitude X quadruples the area.

The equivalent viscous dampening coefficient can then be written as

$$W_d = \pi C_{eq} \omega X^2 \tag{3.117}$$

and rearranging

$$C_{eq} = \frac{W_d}{\pi \omega X^2} \tag{3.118}$$

gives a form that relates the equivalent damping, the energy dissipated and displacement. This will be combined with Coulomb friction in the next section to give an estimate of damping coefficient.

3.4.2.1 Coulomb Friction

Equivalent friction in an oscillating system can be modeled through the use of an equivalent viscous damping coefficient through, in this case, Coulomb friction. A frictional force is a damping force, so the amount of work done per cycle by damping, W_d, can be given by

$$W_d = 4 \int F_d dx = 4\pi c \omega X^2 \tag{3.119}$$

where F_d is the damping force, c is the coulomb damping, X is cyclic displacement amplitude.

Now, by noting that the work done by a damping force is also the force times distance, the equivalent damping factor can be found

$$C_c = \frac{4F_c}{\pi \omega X} = \frac{4\mu F_n}{\pi \omega X} \tag{3.120}$$

which is maximal at small displacements

$$\lim_{x \to 0} \frac{4\mu F_n}{\pi \omega X} \to \infty \tag{3.121}$$

3.4.3 Radiation into the drilling fluid

Drilling fluids add mass to the system and can be modeled using the following damping coefficient, as done by Lee (1991).

$$m' = 2\pi(r_0 + r_i)\sqrt{\frac{\rho_m \mu}{2\omega}} \tag{3.122}$$

$$c_m = 2\pi(r_0 + r_i)\sqrt{\frac{\rho_m \mu \omega}{2}} \tag{3.123}$$

where ρ_m and μ are the density and viscosity of the drilling mud, which is assumed to be an incompressible Newtonian fluid, r_0 and r_i are the outer and inner drillstring radii, and ω is the rotating frequency in radians per second. The effect of vibration radiating into the near-wellbore rock formation has been shown to several orders of magnitude smaller than other damping factors, and will not be considered in this model.

3.4.4 Curve Trajectory and Torque and Drag Modelling

Wellbores are no longer simple vertical holes and have tortuosity. Torque and drag due to friction with the wellbore walls needs to be taken into account and is is not constant along the drillstring. Given a wellbore survey, the path of the drillstring is interpolated using the minimum curvature method, as described in (Sawaryn, et al., 2003) and presented in Appendix A. Once the inclination of each of the drillstring elements is known, the torque and drag can then be calculated be calculated.

Torque and drag loss due to drag along the borehole wall can approximated by the following equations, as presented by Johancsik et al., for each

drillpipe element.

$$F_n = \sqrt{(F_t \Delta\alpha \sin\theta)^2 + (F_t \Delta\theta + W \sin\theta)^2} \tag{3.124}$$

$$\Delta F_t = W \cos\theta \pm \mu F_n \tag{3.125}$$

$$\Delta M = \mu F_n r \tag{3.126}$$

where F_n is the normal force of the drill string on the borehole wall, W is the weight of the segment, F_t is the tensional force, r is the borehole radius, θ is the vertical deviation and α is the horizontal angle. A closed form solution only exists when α is constant or W is zero. Error in the calculation increases as segment size increases, but is still within 1% if segments of 100 ft or less are used (Johancsik, et al., 1984).

F_n can then be used as the estimate for normal force in the calculation of the Coulomb friction factor, C_c, previously described.

Chapter 4

The Transfer Matrix Approach Applied to Axial Drillstring Vibrations

4.1 Introduction

Over the years, there has been agreement over the fact that drillstring vibrations are generally detrimental and should be understood and controlled. Shock absorbing subs have been deployed to damp shocks coming from the bit and systems have been introduced to control stick-slip oscillations, a low frequency torsional vibration. Bottom hole assemblies (BHAs) have been tuned to mitigate vibrations and to define critical speeds for operator to avoid. Others have deployed axial oscillation tools (AOTs) to induce vibrations in efforts to reduce torque and drag in deviated wells. In all cases, a clear understanding of drillstring dynamics is crucial, as is the formulation of a model that can efficiently predict downhole dynamics.

Using the transfer matrix approach, is possible to examine the drillstring dynamic response to a harmonic input, either at a boundary or within the drillstring itself. This chapter presents a series of case studies analyzing model performance in comparison to field data with various input conditions. First, periodic inputs are simulated at the bit, particularly due to bit-bounce,

in a series of historic studies aimed at eliminating or minimizing bit-bounce. Then high frequency downhole and surface data are analyzed to investigate other forms of harmonic input, including stick-slip and bit chatter. Finally, the placement and effect of AOTs is investigated, which have been used for friction reduction, but placements and configurations have largely been due to empirical evidence (Robertson et al., 2004; Clausen et al., 2014; Gee et al., 2015). A series of case studies are then presented utilizing instrumented drillstrings.

4.2 Literature Review

Drillstring dynamics models range from lumped mass systems modeling single vibration types – axial, torsional or lateral – to coupled models allowing for interaction of the vibrational modes. The simplest models are just inertial masses modeling the BHA with a spring and damper for the drillstring (Navarro-López and Cortés, 2007; Rudat et al., 2011). These have been shown to be effective in some applications of bit bounce or stick-slip, but often only correctly model the first mode of vibration (Kyllingstad and Nessjøen, 2009; Dwars et al., 2013). Higher order modes have been captured through the addition of multiple lumped masses (Navarro-Lopez and Cortes, 2007; Nandakumar and Wiercigroch, 2013) or through the application of Timoshenko beam theory (Ghayesh, 2012; Chatjigeorgiou, 2013), but these models rapidly become computationally intensive. An in-depth review of the current state of drillstring modeling can be found in Chapter 2 as well as in two recent review papers (Shor et al., 2014; Ghasemloonia et al., 2014).

Early axial vibration models, such as the one by Aarrestad et al., modeled shock absorbers as spring and dashpot systems, and induced vibrations as a sinusoidal input oscillating at three times the rotation rate at the bit, simulating the three lobed pattern commonly associated with roller cone bits (Aarrestad et al., 1986). Various forms of damping were assumed, including viscous damping from the fluid in the wellbore, friction with the wellbore wall, and losses to the shock absorber or the boundaries (bit or rig). Similar models have been used for torsional vibration modeling, such as stick-slip modeling (Brett, 1992). Stick-slip frequency has been shown to be a function of BHA length rather than bit-rock interaction, rotary speed and bit type (Chen et al., 2003). Tool joints have been found to play a role in higher frequency vibrations and less so in low frequencies (Drumheller and Knudsen, 1995).

The propagation of axial waves in beams, investigated through a series of articles by Drumheller in the 1980s and 1990s, details the transmission and attenuation of sound waves within drillstrings. The pass and stop bands for signals over 100 Hz was found to be highly dependent on the drillstring length and compositions and presence of tool joints, but is not affected by drillstring rotation (Drumheller and Knudsen, 1995). A series of experiments was conducted in a successful effort to validate the acoustic model, both in a scale laboratory model and in the field (Drumheller, 1989) and to estimate attenuation (Drumheller, 1993). Compressional waves are reflected when changes in impedance are encountered, but by matching the impedance, the wave is transmitted rather than reflected, a technique used by Drumheller to install

acoustic repeaters in the drillstring (Drumheller, 2002) or in torsional vibration mitigation (Dwars et al., 2013). Previous uses of the transfer matrix approach include (Paslay and Bogy, 1963; Khan, 1986; Clayer et al., 1990; Han et al., 2013).

Appropriate boundary conditions are explored by Clayer et al., who find that modeling the rig as a mass-spring-damper system agrees well with measurements, but significant uncertainty arises from the bit (Clayer et al., 1990). A similar approach looks at the drillstring elements as sources of impedance (Zamudio et al., 1987; Booer and Meehan, 1993; Reid and Rabia, 1995). A similar method is used to investigate torsional vibrations by relating surface conditions to the bit (Ertas et al., 2013). A model that couples axial, torsional and lateral vibrations using transfer matrices introduces the idea of implementing structural damping through the use of the complex Young's Modulus (Han et al., 2013). A similar technique was used by Rao for modeling attenuation of acoustical signals through submerged pipes by using a complex wave number (Rao, 1991).

A similar model was presented recently that is able to model vibration in the drillstring within a vertical wellbore (Ghasemloonia et al., 2014) and is widely used in other industries where rotating shafts are present (Chahr-Eddine and Yassine, 2014). Harmonic point forces have been included recently in transfer matrix models for shaft design problems (Ceasu et al., 2010). This model extends those capabilities to the arbitrary wellbore through the use of

viscous damping and also proposes a single three-by-three transfer matrix to allow for arbitrary harmonic force and displacement inputs.

4.3 Axial Oscillation Tools

Tools which induce axial or torsional vibrations in drillstrings have been referred to by a variety of names, including Drilling Agitator Tools (DATs) (Baez and Barton, 2011; Barton et al., 2011b), Axial Oscillation Tools (AOTs) (Alali et al., 2012), Pressure Pulse Friction Reducing Tools (PPFRTs) (McCormick and Chiu, 2011), and Axial Oscillation Generator Tools (AGTs) (Newman et al., 2009; Alali and Barton, 2011) in literature. They have typically been deployed while drilling deviated or horizontal wells to reduce friction and improve weight transfer to bit in slide drilling scenarios with downhole motors. Almost universally, they consist of a power section, typically a PWM mud motor, and an oscillation section. These range from rotating masses to pressure pulse generators. The focus for the remainder of this chapter will be on these latter tools due to a series of field trials utilizing them.

4.3.1 Tool Design

Agitation tools considered herein typically consist of consist of three assemblies: the power section, the valve assembly and the oscillating system. The power section is a mud motor that consists of a rotor inside a stator in the form of a Positive Displacement Motor (PDM). The choice of mud motor impacts the agitation frequency of the assembly. The valve, placed below

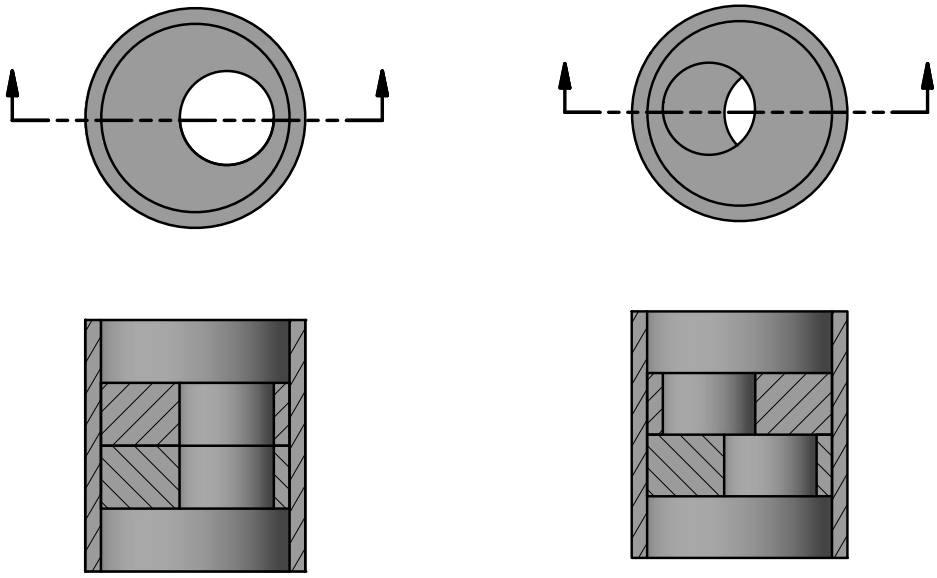

(a) The open areas of the rotor and stator are aligned, maximizing flow area.

(b) The open areas of the rotor and stator are malaligned, minimizing flow area.

Figure 4.1: Two views of a simplified representation of the rotor and stator in the valve assembly of an agitator unit which generates a pressure pulse within the drillpipe.

the power section, creates pressure pulses that propagate axially. Pulses are typically generated in the 12 to 19 Hz range and are converted to mechanical motion by the oscillating assembly (Alali et al., 2012; Alali and Barton, 2011). While running agitator tools in the drill string, maximum observed axial acceleration was 4.5g, greater than the 3g observed in an offset well without agitator tools. Average acceleration forces were equivalent at 2g (Alali and Barton, 2011; Barton et al., 2011a).

Shock absorbers and shock subs were developed over fifty years ago and have been often deployed to reduce axial vibrations in drillstrings, especially in hard formations. Mathematical models describing them have existed since at least 1970 (Kreisle and Vance, 1970; Parfitt and Abbassian, 1995). A series of experiments in the late 1990s showed that axial vibration amplitude decreases across the shock sub, but axial vibrations below the shock absorber and at the bit remained the same as without the shock absorber (Warren et al., 1998). Their dynamic behavior is well understood and for the majority of currently available shock subs, the effective spring rate is constant over frequency – something that was not true in the late 1980s (Skaugen and Kyllingstad, 1986; Aarrestad et al., 1986).

Multiple patents have been filed with downhole agitator designs (Hopf and Co, 2011; Seutter et al., 2012). A small scale laboratory experiment verified that AOTs mitigate stick slip problems and that the stick slip regime may be broken by application of a force greater than applied WOB. Also, the higher the applied frequency, the greater the effectiveness of the AOT

on breaking stick slip static friction (Forster, 2011), but also the higher the attenuation of the vibration.

4.3.2 Field Experience

A study from the Haynesville pointed to a savings of $65,000 per well drilled with a DAT in the BHA, with 35% higher ROP in the lateral section and a 30% improvement in the build section. In the Eagle Ford, the addition of a DAT during a problematic lateral drilling operation increased ROP threefold. In the Barnett Shale, the use of DAT was shown to increase both footage and ROP by 30% (Baez and Barton, 2011). Shell has successfully used agitators to dramatically increase rate of penetration in horizontal sections and has stressed the importance of pre and post well planning to optimize well design (Dykstra et al., 2001; Falodun et al., 2005). Current practices in the Permian Basin and in Appalachia include running AOTs to achieve longer laterals and to improve steering abilities. Field experience has shown an inability to steer in a horizontal well on a subsequent trip without an AOT to finish the remaining 1000 feet of a well.

4.3.3 Alternatives to AOTs

A widely used class of alternatives to AOTs are systems which slowly rotate the drillpipe from surface in an oscillatory manner to reduce friction in deviated or horizontal sections of the wellbore during sliding operations. These systems incorporate a control loop which rotates the top drive, either for a

known number of revolutions or until a set value of reactive torque is reached, first in one direction and then the other, with the goal of rotating the entire drillstring up to the bent motor assembly. These systems often include control systems to maintain toolface – bent motor housing orientation – to effectively steer. The two widely used systems, Canrig's Rock-It and Schlumberger's Slider, are presented in two papers detailing the performance improvements from several series of field trials (Gillan et al., 2011; Maidla et al., 2009). These systems have the advantages of being surface controlled and thus only be activated when needed during drilling operations, of not inducing additional downhole vibrations during drilling (or pumping) operations, and are coupled with steering control systems. However, they do have a maximal reach, limited by the make up torque of connections during reverse rotation. AOTs have the additional benefit of documented reductions in stick-slip, but are active during all operations – not just steering – and do increase maximal shock loads experienced by downhole tools (Clausen et al., 2014; Alali et al., 2012).

4.4 Model Formulation

The dynamic axial and torsional response of a drillstring in a curved wellbore is modeled through application of the transfer matrix approach. This produces a frequency domain solution in milliseconds that allows detailed sensitivity studies to optimize BHA tuning and for determining the optimal placement of AOTs.

4.4.1 Transfer Matrix Approach

A continuous system can in general be simplified as a series of discrete elements bounded by nodes. The forces and displacements at one node are related to those at an adjacent node through a transfer function that is affected by material and geometric properties. More specifically, the drillstring can be idealized by combinations of beam elements and mass-spring-damper elements. The derivations of the transfer matrices for similar elements have been presented elsewhere (Lee, 1991; Ertas et al., 2013; Han et al., 2013). Full derivations can be found in the preceding chapter but relevant formulas are reprinted below.

4.4.1.1 Beam Element

The general solution to the one dimensional wave equation that describes propagation of a harmonic excitation at angular frequency along a beam, including distributed viscous damping, can be solved in close-form with suitable boundary conditions to yield the following transfer matrix relating the displacement and force between two adjacent nodes, n and $n-1$

$$\begin{pmatrix} \mathcal{U} \\ F \end{pmatrix}_n = \begin{pmatrix} cosh(\gamma L) & \frac{sinh(\gamma L)}{i\omega Z_0} \\ i\omega Z_0 sinh(\gamma L) & cosh(\gamma L) \end{pmatrix} \begin{pmatrix} \mathcal{U} \\ F \end{pmatrix}_{n-1} \tag{4.1}$$

The coefficient γ and Z_0 are defined as:

$$\gamma = \sqrt{\frac{i\omega}{E}\left(i\omega\rho + \frac{C}{A}\right)} \tag{4.2}$$

$$Z_0 = A\sqrt{\frac{E}{i\omega}\left(i\omega\rho + \frac{C}{A}\right)} \tag{4.3}$$

where $\mathcal{U}$ and F are the displacements and forces of nodes that define an element of length L, cross sectional area A, Young's modulus E, density ρ, damping coefficient C and oscillation frequency ω.

4.4.1.2 Mass-Spring-Damper Element

The second order ordinary differential equation governing oscillation of a mass-spring-damper with a harmonic excitation can be solved with appropriate boundary conditions to yield a similar transfer matrix

$$\begin{pmatrix} \mathcal{U} \\ F \end{pmatrix}_n = \begin{pmatrix} 1 & \frac{1}{k+i\omega c} \\ -\omega^2 m & 1 - \frac{\omega^2 m}{k+i\omega c} \end{pmatrix} \begin{pmatrix} \mathcal{U} \\ F \end{pmatrix}_{n-1} \tag{4.4}$$

where m is the mass, k is the spring constant and c is the damping coefficient.

4.4.2 Accounting for Damping

Within a vertical wellbore, the primary sources of damping are viscous damping due to interaction with the drilling fluid, energy loss due to material hysteresis, and radiation of energy into the formation. All three of these effects can be modeled using velocity-dependent terms in the governing equations. Damping due to radiation of energy into the near-wellbore rock formation is an order of magnitude smaller than these effects and will be ignored (Lee, 1991). A damping value of has been used for vertical wells based on experimental published results from field experiments (Dareing and Livesay, 1968).

Once the borehole deviates from vertical, drillstring-borehole wall contact must be considered. This interaction is considerably different than drillstring-fluid interaction, and is typically modeled using a Coulomb friction approach

(Johancsik et al., 1984; Sheppard et al., 1987). During a vibration cycle, the energy loss results from a frictional force acting over the cumulative displacement rather than a loss depending on velocity. This poses no great difficulty for models that solve the vibration problem in the time domain (Dykstra, 1996; Kieschnick et al., 2013), but the current model is focused on solutions in the frequency domain. The model overcomes this difficulty using an equivalent viscous damping coefficient that yields the same energy loss during a vibration cycle by summing the cumulative work done by friction during a cycle (Thomson, 1996). The expression for Coulomb damping then, is given by

$$C = \frac{4F_c}{\pi\omega X} = \frac{4\mu F_n}{\pi\omega X} \tag{4.5}$$

where F_c is the contact force, which is the normal force, F_n multiplied by the friction coefficient μ, and assumed displacement magnitude X. Normal force may be calculated from hole inclination and an estimation of borehole contact. The friction coefficient is not well quantified and varies with formation and drilling fluid, but can be estimated using approaches employed in torque and drag models (Johancsik et al., 1984; Hu et al., 2012; Tikhonov et al., 2014). The displacement magnitude may be varied to tune the model to match field predictions but is closely related to the displacement at the excitation source, be it bit bounce or induced oscillations. In this model, the friction coefficient, μ will be varied along the wellbore, with a different value used for the drillstring within casing and within open hole.

4.4.3 Excitation Sources within the Drillstring

Most transfer matrix models that have been described in the literature assume a harmonic input at one end, the effect of which is transferred between nodes via the transfer matrices. Boundary conditions are enforced by solving for the forces at the boundaries based on either the force or displacement assumed at the harmonic input node. The current model, shown in Figure 3.4, expands this by allowing the excitation source to be placed anywhere within the drilling system, as shown in Figure 4.2.

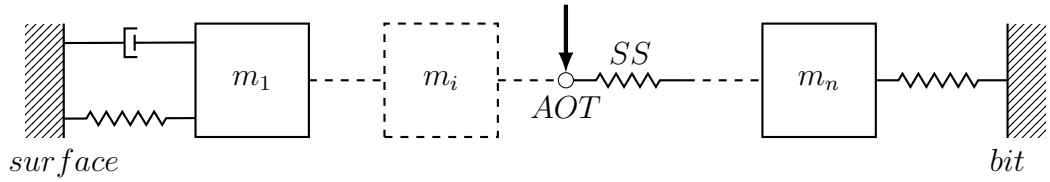

Figure 4.2: Drillstring model with fixed displacement boundaries and an oscillation source somewhere within the string (here shown as AOT + shock sub).

The general solution approach is the same, but with a three by three augmented transfer matrix

$$\begin{pmatrix} \mathcal{U} \\ F \\ 1 \end{pmatrix}_n = \begin{pmatrix} \cosh\gamma L & \frac{\sinh\gamma L}{i\omega Z_0} & \mathcal{U}_{external} \\ i\omega Z_0 \sinh\gamma L & \cosh\gamma L & \mathcal{F}_{external} \\ 0 & 0 & 1 \end{pmatrix} \begin{pmatrix} \mathcal{U} \\ F \\ 1 \end{pmatrix}_{n-1} \tag{4.6}$$

where the external displacement is zero and the external force is given by

$$F_{ext} = |F|e^{i\omega t} \tag{4.7}$$

and the magnitude of the exerted force at the axial oscillator is given by the pressure drop across a nozzle for a Newtonian fluid (Robinson, 2010) multiplied

by the open area of the shock absorber

$$\Delta P = \frac{\rho_{mud} \times Q^2}{12032 \times C_d \times A^2} \tag{4.8}$$

$$F_{ext} = \Delta P \times SS_{openarea} \tag{4.9}$$

where A is the flow area for flow through a nozzle, Q is the flow rate and C_d is the nozzle efficiency, values of which typically range between 0.9 and 0.95.

Displacement at the excitation source must remain continuous to retain model physicality. A jump discontinuity is introduced in the force, with magnitude equal to the force exerted at the node. Enforcing these conditions at the excitation node and zero displacements at the boundary, allows the response along the entire drillstring to be obtained.

4.5 Visualizing Excitation and Optimizing Placement

Once the boundary conditions are determined, the response – the displacement and force of each node – of the entire drillstring may be determined. These computed responses are complex, so it is necessary to understand their meanings.

The input in to the model – the harmonic oscillation either at the bit or at the axial oscillation tool – is assumed to be a real amplitude oscillating at a specified frequency, ω. A complex number can be regarded equivalently – as a having an amplitude and a phase. Within the model, there can be both standing waves, those that whose peaks and troughs do not move, and traveling waves, those that do move. Figure 4.3 shows sample output from the

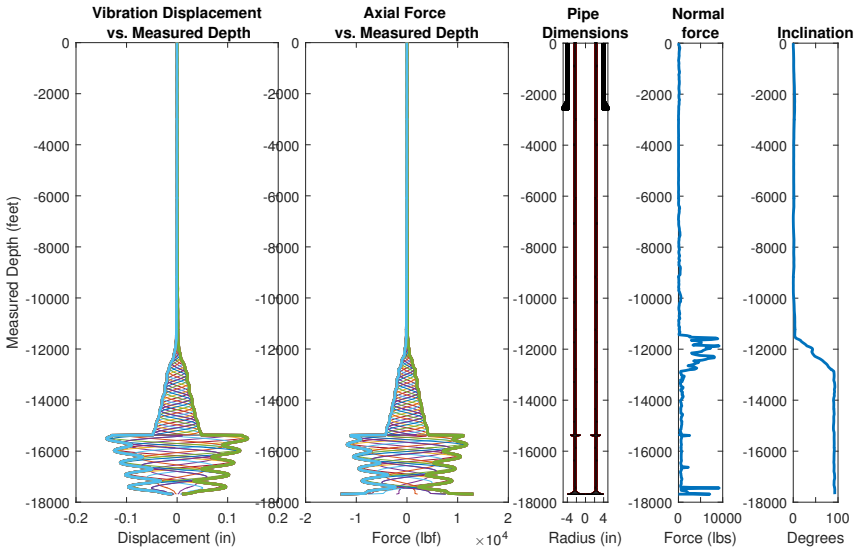

Figure 4.3: Model output: from left to right: (1) displacement and (2) force at each node along the drillstring, (3) dimensions of the drillstring, (4) computed normal force along the drillstring due to hole inclination and tension and (5) hole inclination.

transfer matrix model. The first two plots show the displacement and force along the drillstring, both as an amplitude – the green and blue curves – and as traveling waves – those curves between the positive and negative amplitudes.

Displacement amplitude along the drillstring is useful to compute accelerations along the drillstring due to the harmonic input using the familiar formula

$$\frac{d^2x}{dt^2} = \omega^2 \mathcal{U} \tag{4.10}$$

Force amplitude along the drillstring is useful to compute the percentage of the drillstring experiencing sufficient force to overcome static friction. Static friction along the wellbore is simply the coefficient of static friction, μ_s,

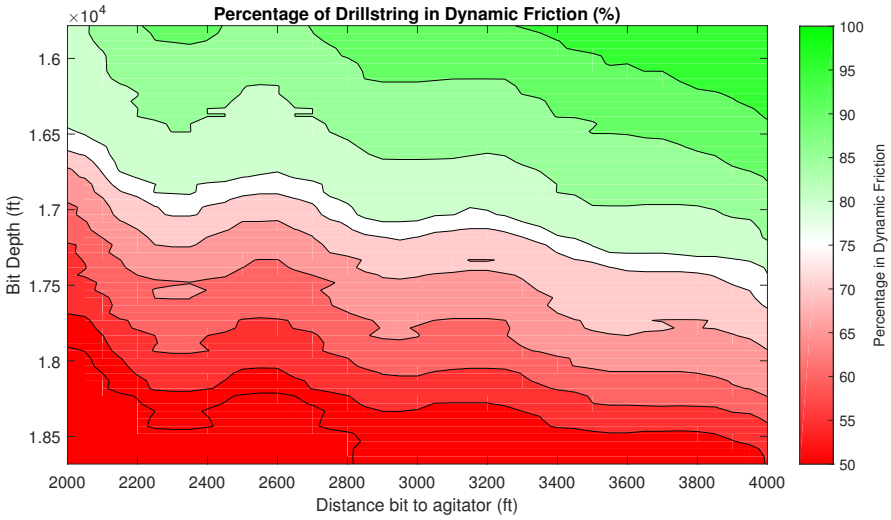

Figure 4.4: Optimizing the location of the axial oscillation tool.

multiplied by the normal force at each node, which has already been computed. Thus, if

$$|F_{calc}| >= \mu_s F_n \tag{4.11}$$

then the node is considered to be experiencing dynamic friction rather than static friction. Tool placement may be optimized by iterating through a series of depths of interest – usually along the lateral section of a well – and for a range of agitator - bit distances and computed the percentage of drillstring experiencing dynamic friction. Example output is shown in Figure 4.4 which shows graphically regions where dynamic friction is maximized.

4.6 Verification of Model Mechanics

4.6.1 Validation with analytic solutions

The analytic solution is known for the axial vibration of a uniform rod fixed at one end which is a close approximation for a vertical wellbore with the string off bottom. The system can be described using the general equation

$$\frac{\partial F}{\partial z} = EA\frac{\partial^2 u}{\partial z^2} = \rho A\frac{\partial^2 u}{\partial t} \tag{4.12}$$

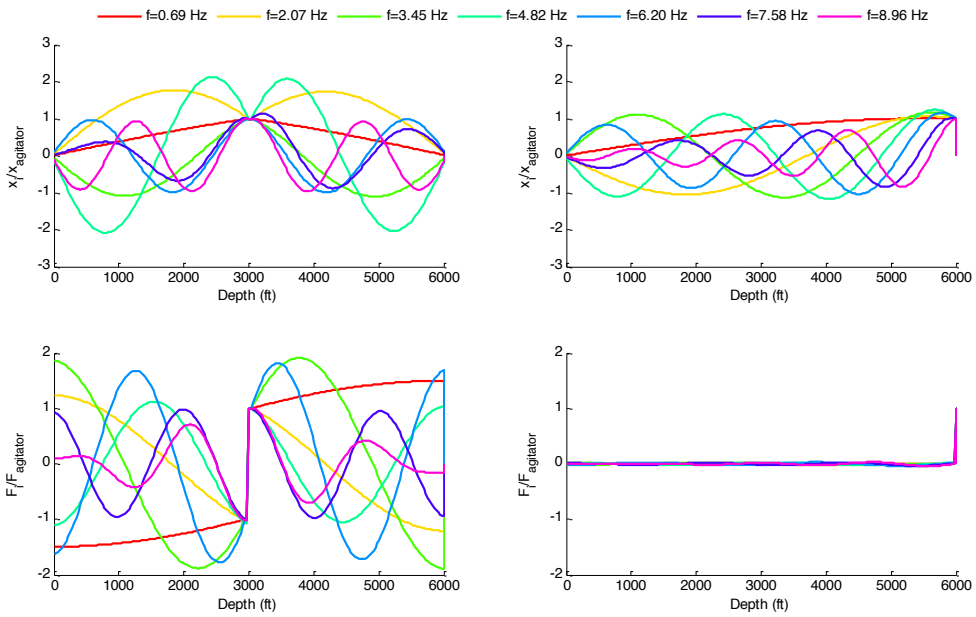

Figure 4.5: The normalized displacements and forces for a simple drillstring in a perfectly vertical wellbore with an agitator placed either halfway (right plots) or at the bit (left plots) agitating at the first 7 natural frequencies as calculated analytically.

where ρ is the mass density, A is the cross sectional area and u is the displacement. Solving this by separation of variables gives

$$u = \Sigma_{n=1}^{\infty} \left(C_n \sin \frac{\omega_n z}{v^2} + D_n \cos \frac{\omega_n z}{v^2} \right) \cos \left(\omega_n t + \Omega_n \right) \tag{4.13}$$

where $v^2 = \frac{\rho}{E}$. Applying the following boundary conditions 1. $u = 0$ at $z = 0$ 2. $u' = 0$ at $z = l$ Gives a natural frequency of

$$\omega_n = \left(n + \frac{1}{2} \right) \pi \sqrt{\frac{E}{\rho l^2}} \tag{4.14}$$

Running the model with $n \in \{0, 1, 2, 3, 4, 5\}$with the harmonic excitation location either at the center or at a boundary and applying equivalent spring reactions at both boundaries, the anticipated node shapes are formed, as shown in Figure 4.5.

4.6.2 Comparison with a commercial code implementation

ViBounce is an internal drillstring dynamics code used with Shell which was developed in the late 1980s and early 1990s and first deployed in 1992. Today it exists as the bit bounce prediction portion of the Shell IDM Kernel. ViBounce serves as the original inspiration for the axial vibration code, albeit in a simplified vertical wellbore with constant damping, and has been shown to be effective at predicting bit bounce. Several case studies, compiled with the assistance of Mark Dykstra, have been published as part of an investigation into axial drillstring vibration, segments of which are reproduced in the following sections (Shor et al., 2015a).

Tricone bits are known to be prone to bit bounce and generate a harmonic oscillation input at the bit, the frequency of which can be quantified as

$$\omega = RPM \cdot \frac{2\pi \cdot 3}{60} = RPM \cdot \frac{\pi}{10} \tag{4.15}$$

The transfer matrix solution relating the surface and the bit is given by

$$\begin{pmatrix} a_{11} & a_{12} \\ a_{21} & a_{22} \end{pmatrix} = \prod_{bit}^{surface} A_i \tag{4.16}$$

and given a surface impedance of

$$z_0 = k_{surf} + s_{mass}\omega^2 \tag{4.17}$$

the bit impedance can be computed using

$$z_{bit} = \frac{a_{11} + a_{12}z_0}{a_{21} + a_{22}z_0} \tag{4.18}$$

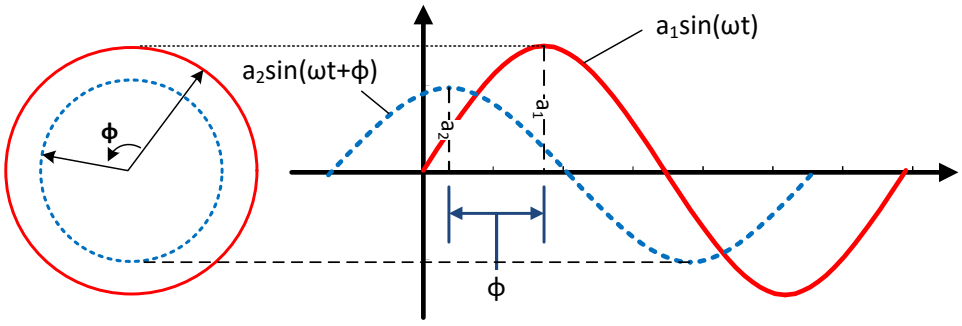

Figure 4.6: The phase difference between two sinusoid curves, ϕ. If $\phi > 90^o$, then both curves are increasing for a period of time. If these two curves are taken to be torque and rpm, then energy is injected into the system if both are increasing.

Component	Length (ft)	OD (in)	ID (in)	Number of Joints	OD of Joints (in)	Weight per Foot (lbf)	Spring Constant (lbf/in)
Drill Pipe	3000	5	4	95	5	24.03	0
Drill Pipe	5000	5	4.276	159	5	17.93	0
Heavy Weight Drill Pipe	90	5	2.875	2	5	44.68	0
Drill Pipe	300	6.5	2.875	9	6.5	90.74	0
Shock Sub	7.2	8.25	2.8125	0	8.25	0	7.50×10^4
Drill Pipe	90	6.5	2.875	2	6.5	90.74	0
Bit	0	8.5	0	0	0	0	2.85×10^6

Table 4.1: Drillstring components used in the ViBounce comparison case

Parameter	Value
Weight of surface equipment (lbs)	35,000
Number of lines	10
Diameter of lines (in)	1.5

Table 4.2: Additional model parameters

The phase difference between the displacement and force at the bit can then be computed from the angle the bit impedance makes in the complex plane

$$\phi = \tan^{-1} \frac{Im(z_{bit})}{Re(z_{bit})} \tag{4.19}$$

The phase plot generated by the current model is compared with the phase plot generated by a commercial code used at Shell, ViBounce, to ensure the models agree and the results are shown in Figures 4.7 and 4.8, based on the parameters listed in Tables 4.1 and 4.2.

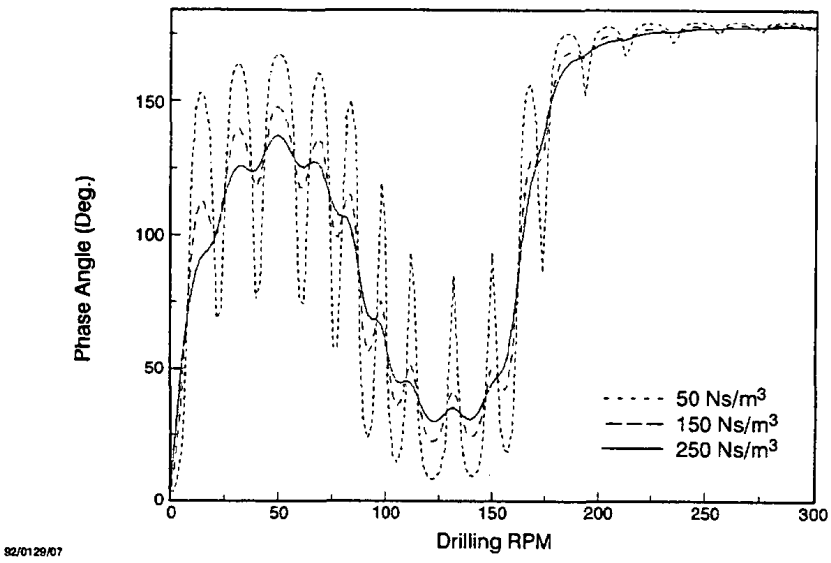

(a) Phase diagram for the example drillstring in Table 4.1, as presented in the 1992 ViBounce report.

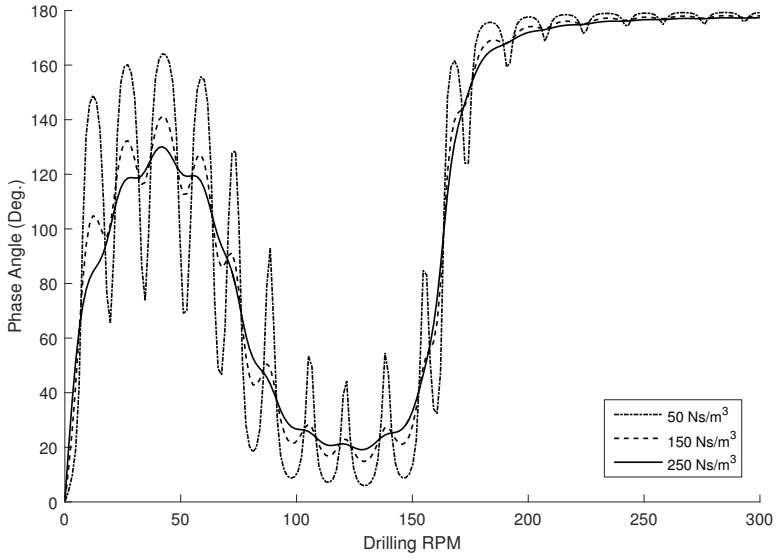

(b) Phase diagram for the same drillstring as generated by the base matlab implementation.

Figure 4.7: Computed phase angle vs drilling rpm for the demonstration case presented in the 1992 ViBounce report for three different values of constant damping along the drillstring.

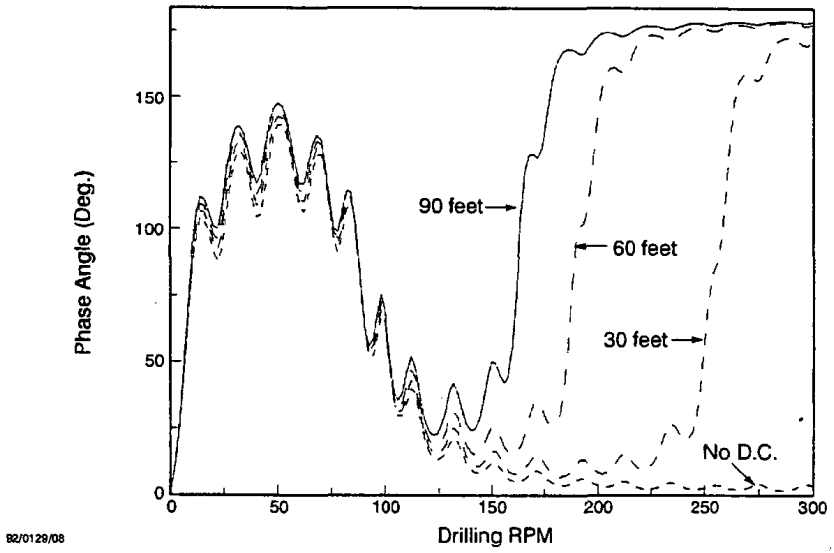

(a) Phase diagram for the example drillstring in Table 4.1, as presented in the 1992 ViBounce report.

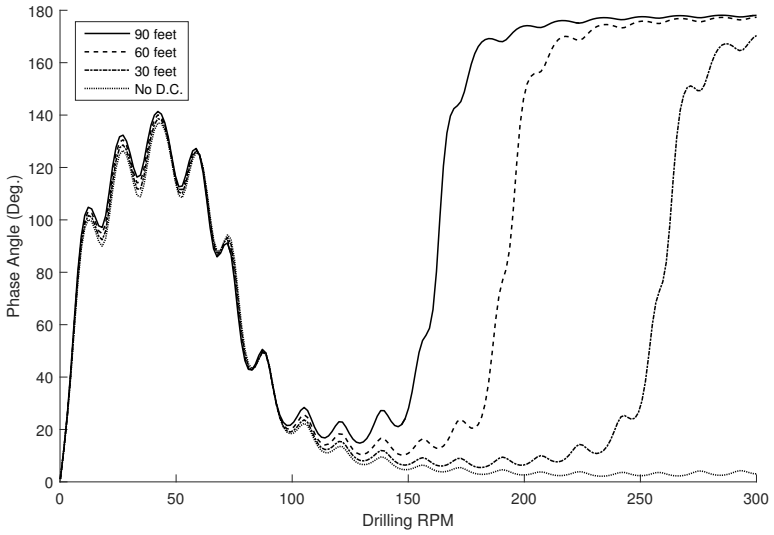

(b) Phase diagram for the same drillstring as generated by the base matlab implementation.

Figure 4.8: Computed phase angle vs drilling rpm for the demonstration case presented in the 1992 ViBounce report with three different length drill collars between the bit and shock absorber.

4.7 Model Application 1: Diagnosis and Prevention of Roller Cone Bit Bounce

Roller cone bits (RC bits) have an exhibited tendency to generate axial vibrations and has been well studied in the past (Wolf et al., 1985; Macpherson et al., 1993). The rolling cones lead to cyclic engagement and disengagement of milled teeth or inserts on each cone, generating axial vibration energy which may excite natural frequencies in the drillstring. As shown in Figure 4.9, downhole measurements of forces and motions in the bottom hole assembly have shown that dynamic axial loads can reach several times the nominal weight-on-bit indicated at the surface (Deily et al., 1968; Wolf et al., 1985), and that during these situations the bit can lift off the hole bottom and come crashing back down, a phenomenon referred to as *bit bounce*. Impact loads of this magnitude can cause catastrophic failure of inserts, and strings of bit failures led to the development of axial dynamics models in attempts to predict and mitigate its occurrence.

Bit bounce is often associated with resonance – situations where the frequency of the axial vibration input of the bit-rock interaction coincides with a natural frequency of axial vibration in the drillstring. Field measurements have shown that the primary excitation frequency for roller cone bits is 3N, where N is the bit rotation speed. One approach for avoiding bounce is to compute the axial natural frequencies of the drilling system and try to avoid rotation speeds that would cause 3N to coincide with one of these natural frequencies. The natural frequencies depend on the boundary conditions at the

bit and the surface (Clayer et al., 1990), and a common approach is to treat the bit as free at the bit-rock interface and fixed at the surface (Deily et al., 1968). This model is different in that it focuses on the phase difference between the harmonic force input and resulting displacement at the bit (Nicholson, 1986; Kriesels et al., 1999). This angle is related to the energy transfer between the excitation and the response (Den Hartog, 2013), and if greater than a threshold value the trilobed bottomhole pattern may form in competent rock.

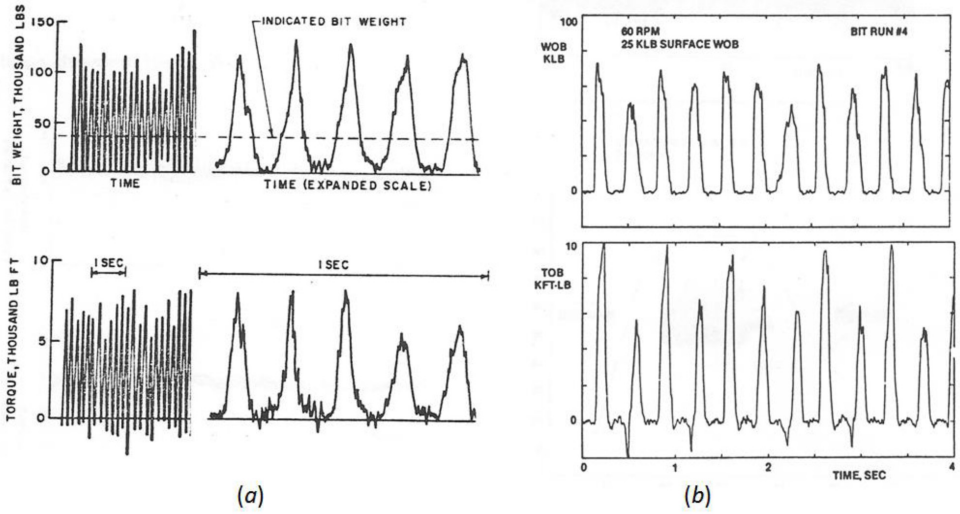

Figure 4.9: Examples of downhole measurements of weight- and torque-on-bit showing sequential loading and unloading, or 'bounce'. Peak loads during bounce events can be several times the nominal weight-on-bit indicated at the surface. (3a from (Deily et al., 1968); 3b from (Wolf et al., 1985)).

Presented below are summaries of two case studies compiled with the help of Mark Dykstra and previously published (Shor et al., 2015a).

4.7.1 Case Study 1: Offshore Australia

During a drilling campaign in Northwest Australia in the Browse Basin, severe axial vibration was observed at surface while drilling a 17.5" vertical hole section through a hard calcareous claystone with a tricone bit. The drilling rotary rate was low – 35-40 RPM – and an attempt to increase RPM resulted in observedly higher vibrations. After drilling 22 meters at an average penetration rate of 1.32 m/h, the bit was pulled with significant damage. An analysis was conducted using the model with the drillstring as it had been run, with results shown in Figure 4.11a, predicts severe bit bounce within the operating window.

(a) Photos of the first bit showing significant damage.

(b) Photos of the second bit showing little damage.

Figure 4.10: Photos of the drillbits after drilling, the first exhibited severe axial vibration while the second used the optimized drillstring design as recommended by the drilling team.

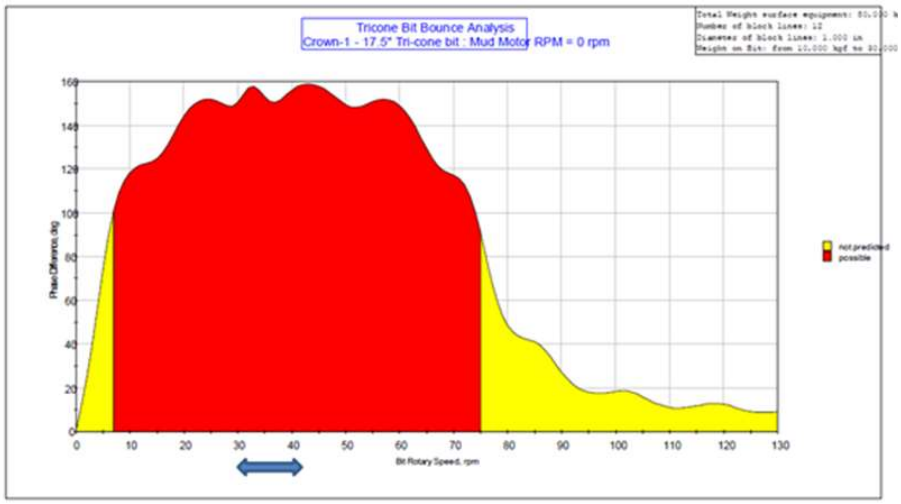

(a) Phase diagram for the original drillstring which exhibited severe axial vibrations in Austria.

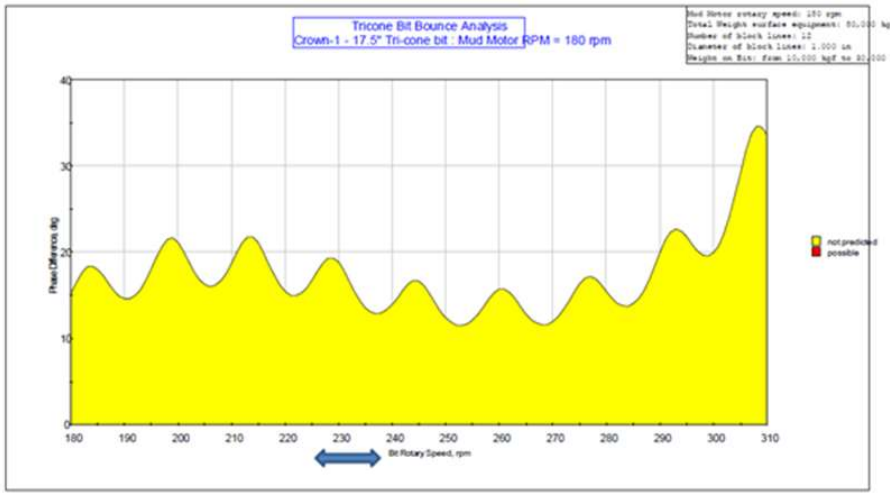

(b) Phase diagram for the second drillstring which included a downhole motor in Australia, showing no predicted axial vibration in the operating window.

Figure 4.11: Phase diagrams for the original and revised drillstrings run in Australia, the first exhibited severe axial vibrations while the second did not.

To increase downhole RPM, a 9.625" motor was added to the BHA for the next run, and a bit design with a more robust cutting structure was used to decrease the likelihood of insert breakage. Much less vibration was reported and performance was improved and agrees with the predictions, shown in Figure 4.11b. A visual inspection of both bits, shown in Figure 4.10 shows clear damage to the first one, caused by severe bit bounce, while the second exhibits very little wear. The additional 200 RPM provided by the motor shifted the excitation frequency such that the phase angle was below the threshold over a wide range of surface rotary speeds.

4.7.2 Case Study 2: Onshore New Mexico

In a drilling campaign in New Mexico, USA, significant axial vibration was encountered when drilling a shallow 14.75" vertical hole section through hard, interbedded sequences of clastics and carbonates. The phase diagram showed that significant bit bounce would likely be encountered throughout the interval, especially as the formations transitioned from hard rock to soft rock. A shock absorber was added near the bit which significantly improved the operating window. However, it is noted that shock absorbers are not the solve all for axial vibrations problems – by simply shifting the shock absorber further away from the bit, the phase diagram becomes worse than without one at all. The reader is referred to the paper for full details (Shor et al., 2015a).

4.8 Model Application 2: High-frequency Vibration Analysis

Further validation is demonstrated by comparing model predictions to high-frequency measurement of vibration data; the vibrations measured here result from the drilling process with no additional excitation purposely applied to the string. Two cases are presented, one focusing on high-frequency downhole data, and the other on surface vibration data. In the first case, the sensing location is near the bit within the BHA, and thus the frequency peaks are dominated by BHA resonance and bit-rock interaction. In the second case, the frequency peaks are dominated by the drillstring and are much more dependent on the drillstring length.

4.8.1 Case Study 1: High-frequency downhole vibration data

In the last few years it has become increasingly common to use commercially available memory-based downhole vibration data loggers to gain greater understanding of drilling processes and dysfunctions. The compact size of these tools allows strategic placement at various locations of interest along the string with minimum impact on drilling operations.

Two sets of memory-based downhole vibration data, acquired using different commercially available Dynamic (or/and Downhole) Data Recorders (DDR) tools, are utilized in the field examples presented in the following two sections: one recording continuous high-frequency data (presented here), and one with records of processed data only (presented in the next section). Both

tools allow for detailed post-well analysis, however only the high-frequency data set allows for spectral analysis.

A dataset containing continuous 50Hz downhole data recorded by a commercial DDR device (Desmette et al., 2005) was obtained as part of a drilling optimization effort in the Permian basin. The dataset focuses on a 8" vertical section and was analyzed to determine the frequency content of the axial and torsional vibrations experienced during the drilling process.

The frequency spectrum maps shown in Figure 4.12 and Figure 4.13 were obtained by calculating the Fast Fourier Transforms (FFTs) of data extracted from the 50 Hz downhole time histories every 50 feet. Low frequency (1 - 3 Hz) peaks that appear in the torsional data are likely due to bit-rock interaction since a majority of the section was drilled with a bit speed of approximately 120 RPM (i.e. 2 Hz). Higher frequency peaks, between 12 Hz and 15 Hz for the axial accelerometer and near 11 Hz for the torque sensor, are due to structural resonances in the BHA. As illustrated in Figure 4.12, this higher frequency content is highly correlated to formation lithology. By comparing the formation tops with the frequency intensity mapping, the Bushy Creek and Upper Avalon Carbonates can easily be picked out.

Applying the model over a range of frequencies for an input force applied at the bit, it is also possible to construct frequency intensity maps. The predicted results shown in this manner, using carefully selected bit spring constants to characterize the various formations, are displayed in Figure 4.12. Not

only the model is able to reproduce the lithology contrast observed in the field data, but also the values of the peak frequencies match well the field.

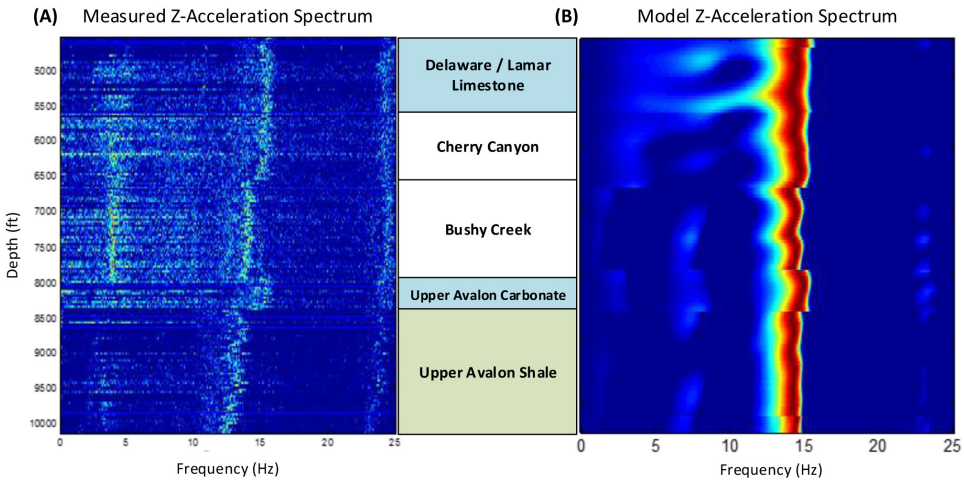

Figure 4.12: The frequency spectrum of the continuous downhole RPM (A), showing resonance frequencies for depths from 4,500 feet to 10,000 feet. Low frequency peaks are associated with the rotary drilling operations – peaks are integer multiples of bit rotation frequency, while higher frequency peaks are due to the first BHA resonance coupled with a changing bottom condition – the bit-rock interaction. Model predictions are shown (B) show a frequency match at 13-15 Hz with proper choice of bit-rock interaction parameter – the spring stiffness.

This downhole data will be contrasted with surface data in the next section and will show the dependence of the frequency spectrum on sensor location. For a sensor located near the bit, the spectrum is dominated by the resonances of the BHA and bit-rock interaction. The BHA remains constant during the duration of a bit run, thus frequency shifts indicate formation changes and can be used to identify formation tops (Al-Shuker et al., 2011; Esmaeili et al., 2012). Moving the sensing location away from the BHA will

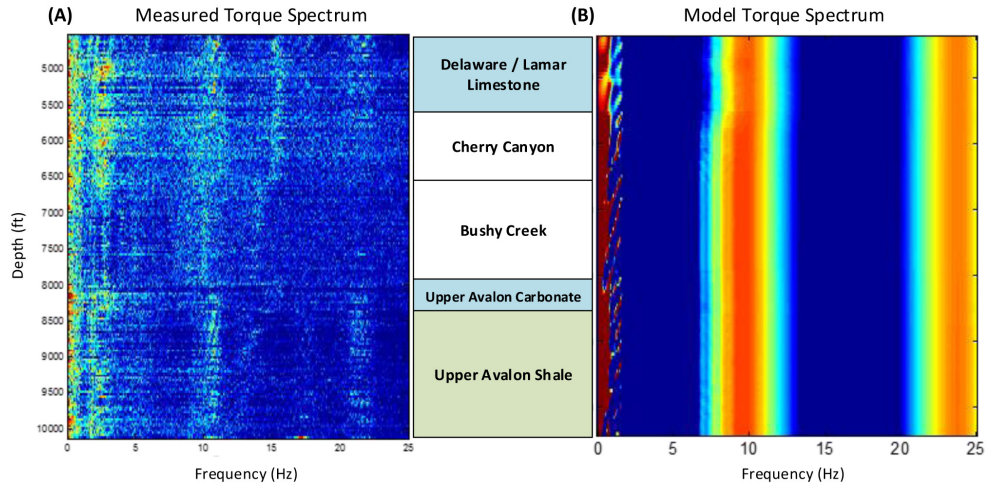

Figure 4.13: In contrast, the power spectrum of downhole torque (A) shows a steady downhole resonance around 11 Hz as well as lower frequency resonance related to bit ration. The predicted frequency spectrum (B) shows a frequency match at 10 Hz.

shift the resonance frequencies recorded to those dominated by the drill pipe and will thus evolve with depth.

4.8.2 Case Study 2: High frequency surface vibration measurements

Surface drilling data are typically recorded at 0.1-1 Hz, but the underlying sensors typically sample at much higher rates and compute statistics that are recorded. State-of-the-art top drives currently deployed have the ability to record rotary speed and torque at frequencies up to 200 Hz and have been used for stick-slip mitigation (Kyllingstad and Nessjøen, 2009; Dwars et al., 2013). One such dataset contained RPM and torque data sampled at 200Hz for two depth intervals of a 16" section of a difficult well.

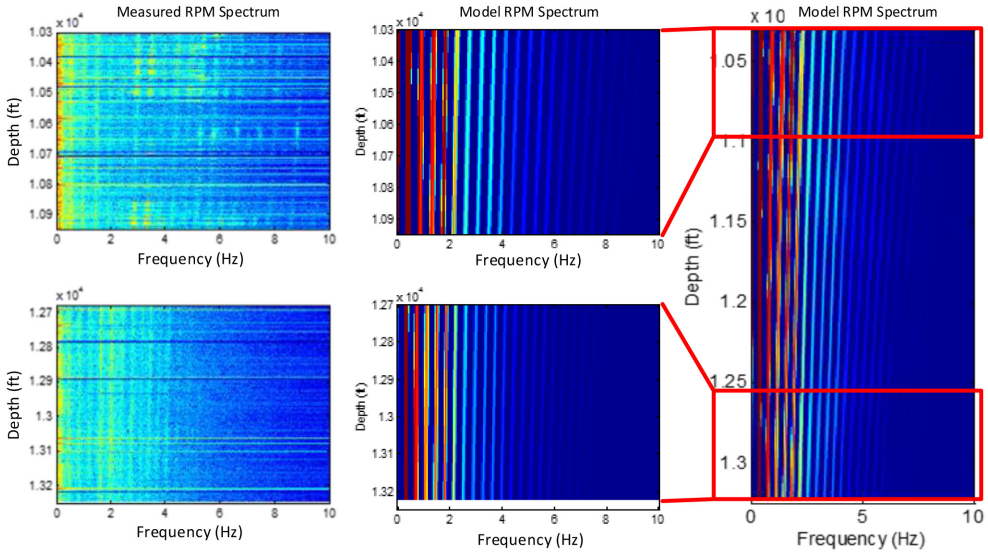

Figure 4.14: Surface frequency content from topdrive data (left) and corresponding simulation data (center and right).

Unlike the downhole data presented in the previous example, where the data was dominated by the resonances of the BHA and did not evolve with depth, this data set shows a clear evolution. The resonances are dominated by the length of drill pipe and shift to lower frequencies as hole depth increases. Presented in Figure 4.14 are the frequency spectra of two different depth intervals of data – at 10300 feet and 12700 feet – recorded at 200 Hz. Only the first 10 Hz are shown due to the high amount of noise and loss of signal in the higher frequencies. A clear evolution with depth is seen, with predominant frequency content shifted towards the lower range. No evidence is seen to indicate any effect of formation lithology, supporting the claim that the drill pipe dominates the frequency response at the surface. The corresponding results

from the simulation are shown to the right and display a similar evolution of frequency with depth.

These two examples show that care must be taken when analyzing high frequency vibration data and that resonances of both the drill pipe and the BHA must be considered. Drillpipe resonances are dominated by its evolving length, while the BHA resonance is both a function of its composition as well as the lithology of the formation being drilled.

4.9 Model Application 3: Axial Oscillation Tool Effectiveness and Placement

Axial oscillation tools are sometimes added to drillstring designs in efforts to reduce the effects friction between the drillstring and the borehole by inducing axial oscillations whenever circulating. Frictional torque and drag within the wellbore are detrimental to the transmission of torque and weight from the surface to the bit, especially while sliding during geosteering operations, and significantly reduce the efficiency of the drilling process and limit the reach of deviated wells.

4.9.1 Case Study 1: Horizontal well with an axial oscillation tool and multiple measuring subs

For this model application, a set of downhole data was used derived from an instrumented drillstring with multiple DDRs inserted at different locations along the string, on a well for which the BHA picked up after kick-off

accommodates an AOT. This setup allowed for the comparison of a BHA without an AOT higher in the hole with another BHA with an AOT in the lower section. Survey data was also included in the set of data.

When continuous high-frequency data is not available, as in this case, a great deal of useful downhole information can still be gathered using processed a.k.a. reduced data (also referred to as statistical data). Examples of DDR devices offering such capability are found in the literature (Barton et al., 2009; McCarthy et al., 2009; Hoffmann et al., 2012). These devices typically process high-frequency raw data downhole and store reduced values such as average, minimum, maximum, standard deviation and RMS values calculated over a predefined time window. The processed vibration data was obtained from a pair of DDR devices included in the string at two different locations, one in an upper location, and one closer to the bit, as shown in Figure 4.15. The device closer to the bit is located right above the AOT when the AOT is present. In the figures that follow, these two DDRs are referred to as the upper and lower DDR, where the latter is one closer to the bit and just above the AOT when present.

The primary goal for the analysis is to evaluate the model by focusing on the attenuation of axial drilling and AOT-induced vibrations along the string. A secondary goal is to contrast the cases with and without an AOT in the string, and compare with expected behavior from rough estimates and field data previously published. To assess the attenuation of axial vibration along the string, a convenient parameter to examine is $Z_{U/L}$, the ratio of the

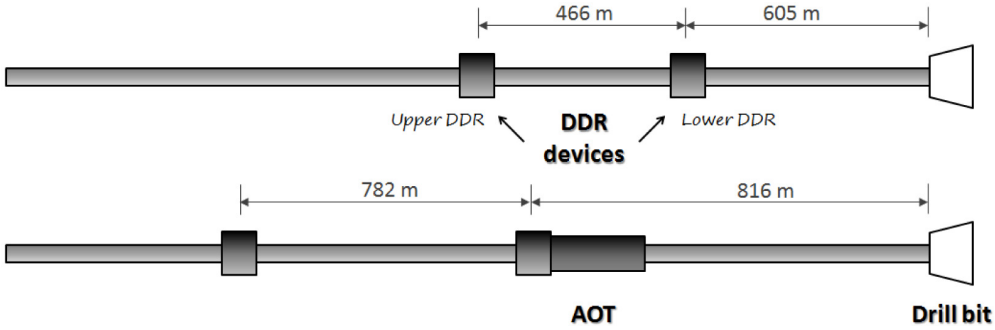

Figure 4.15: Location of data loggers in the field case examined, with AOT (lower drawing) and without AOT (upper drawing).

axial acceleration measured by the upper AOT to that measured by the lower AOT, expressed in RMS, and corrected from biases in the data. The RMS ratio can be expressed as

$$Z_{U/L} = \frac{\left(A_{RMS}^{corrected}\right)_{Upper\,AOT}}{\left(A_{RMS}^{corrected}\right)_{Lower\,AOT}} \tag{4.20}$$

The recording tools were run after the well was landed in the target formation in the lateral section. Since the DDR devices were upstring from the bit, early in the run they are still located in the vertical portion of the well while the bit is making hole in the lateral section. As drilling progresses the DDR devices enter the build section first and later on the lateral. Therefore, the inclination of the hole and thus the inclination of the recording tools themselves changes during the run. Because the DDR devices employed to gather the data use DC-coupled accelerometers, the recorded axial acceleration therefore contains a component due to gravity that varies with inclination. That fact

needs to be taken into account while analyzing the measured axial acceleration. Before the attenuation of axial vibration can be calculated, the effect of gravity, as well as any additional calibration offsets, must be removed. As seen in the raw data, shown in Figure 4.16, a clear correlation between hole inclination and average axial acceleration exists, as well as an offset in the data themselves. The workflow utilized to find the corrected RMS axial acceleration is presented in Figure 4.17.

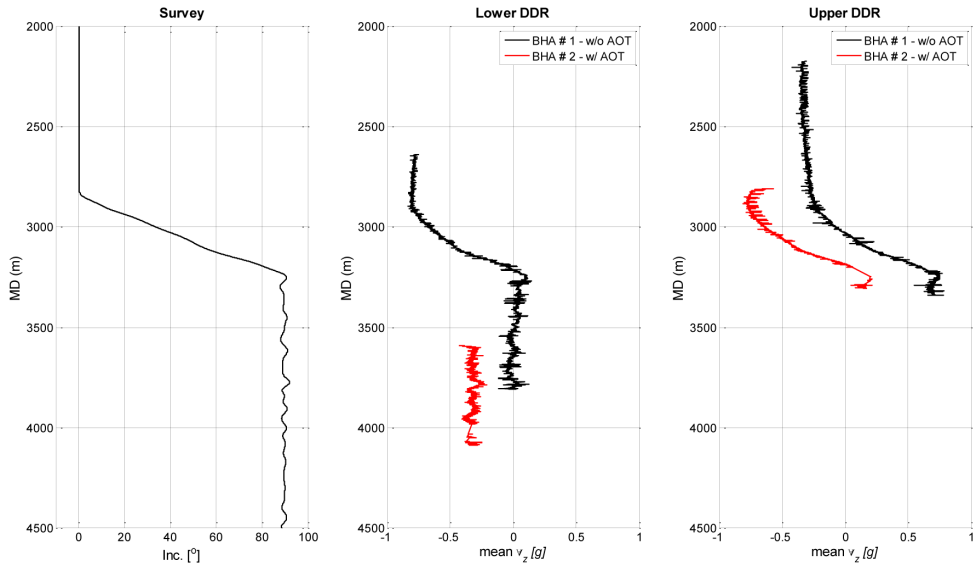

Figure 4.16: Comparison between inclination depth profile and axial acceleration at the sensors location. Data showing both slide and rotate drilling with no distinction.

The data were originally sampled as high frequency bursts of 400 Hz of 10 s duration, and then continuously processed in the memory-based device to calculate the reduced data set stored in memory while discarding the original high frequency data. The data set provided for analysis in this paper con-

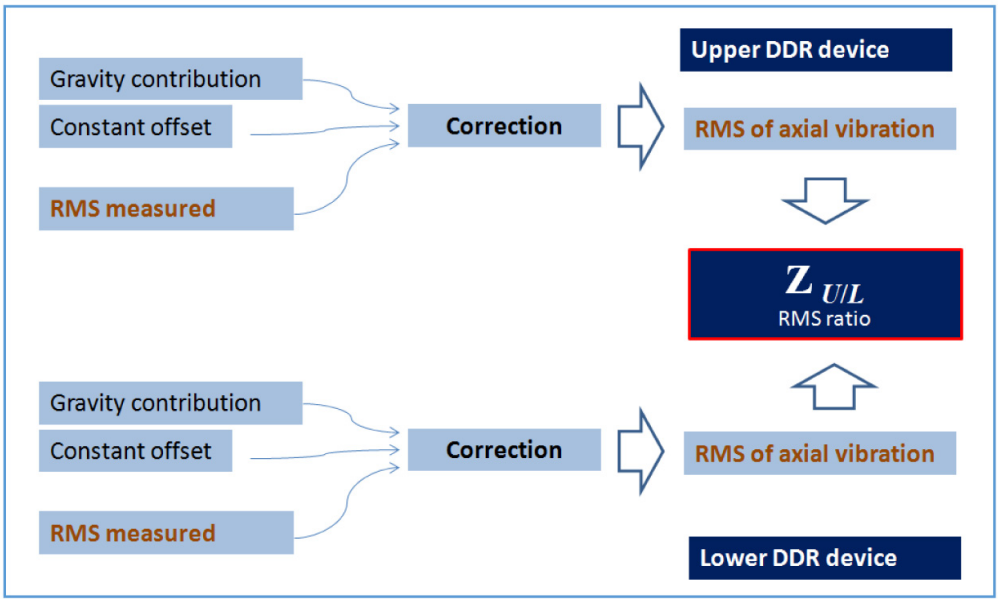

Figure 4.17: Axial vibration attenuation assessment - data processing workflow.

tained RMS values, mean values, minimum and maximum values for the axial acceleration for each of the two DDR devices. Due to the length of sampling window (much longer than an oscillation cycle), the expected value for average axial vibration should be directly correlated with hole inclination and gravity. For a sensor in the vertical section, average accelerations should be near 1 g, and 0 g for one in the lateral. A cursory glance at the raw data Figure 11 shows that each DDR can be characterized by an individual offset (mismatch with the expected value) that needs to be quantified. For the purpose of this analysis, the offset is assumed to be constant for the duration over which data are sampled and analyzed by the DDR, and includes a contribution due to gravity as well as a calibration offset. As true calibration bias is unknown, the

bias is estimated here by assuming it corresponds fully to the departure of the mean vibrations (corrected for gravity effects) from zero.

The corrected RMS axial vibration data are presented in Figure 4.18 and Figure 4.19 (corrected according to the scheme previously discussed) as a function of Measured Depth (MD) for both cases, with and without AOT as well as the attenuation between DDRs. All data presented here were collected while the bit is on bottom and making hole, and while circulating. Red data points indicate slide drilling while blue data points indicate drilling while rotating. Axial vibrations are higher while rotating and lower while sliding due to higher attenuation due to borehole friction. The primary reason attenuations shown in Figure 4.18 are lower than those in Figure 4.19 is due to the smaller distance between the two DDRs in the first BHA than in the second BHA.

Comparing vibration levels with and without AOT, a small change (on the order of 0.5 g) in RMS axial vibration is observed at 4400 feet, when the AOT is first placed in the hole, with higher magnitude when the AOT is present. Published results (Barton et al., 2009) also conclude that the AOT doesn't introduce significant vibration level (while still increasing performance) even when a shock sub is used; note that the location where the data were recorded is unknown making a direct comparison with the data presented here difficult. It is interesting to compare these results with a rough theoretical estimate. A typical AOT will oscillate with a displacement of 1/2 to 3/8 inch at an angular frequency , which is typically between 16 Hz and 20 Hz

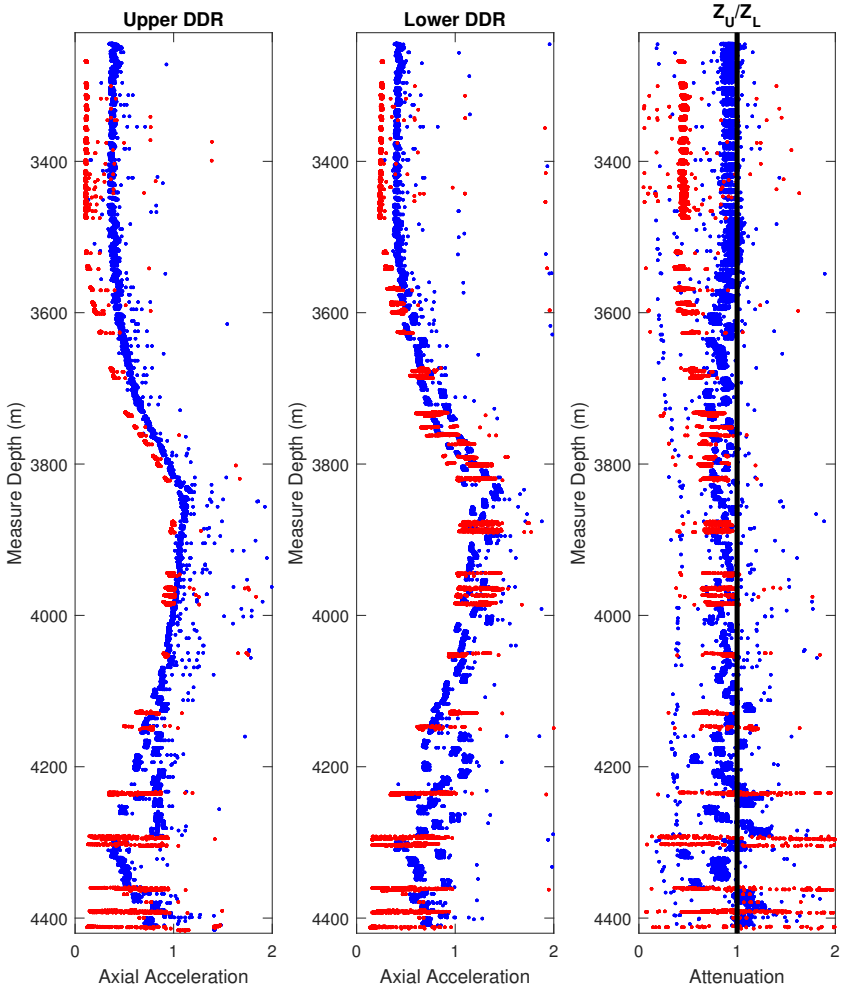

Figure 4.18: Corrected axial accelerations, at the upper DDR (left), the lower DDR (center) and the attenuation between DDRs (right) for the BHA without an AOT. Red points indicate slide drilling, blue points indicate drilling while rotating.

(McCarthy et al., 2009). Assuming harmonic acceleration, the typical AOT would generate a steady state axial acceleration amplitude on the order of 0.25

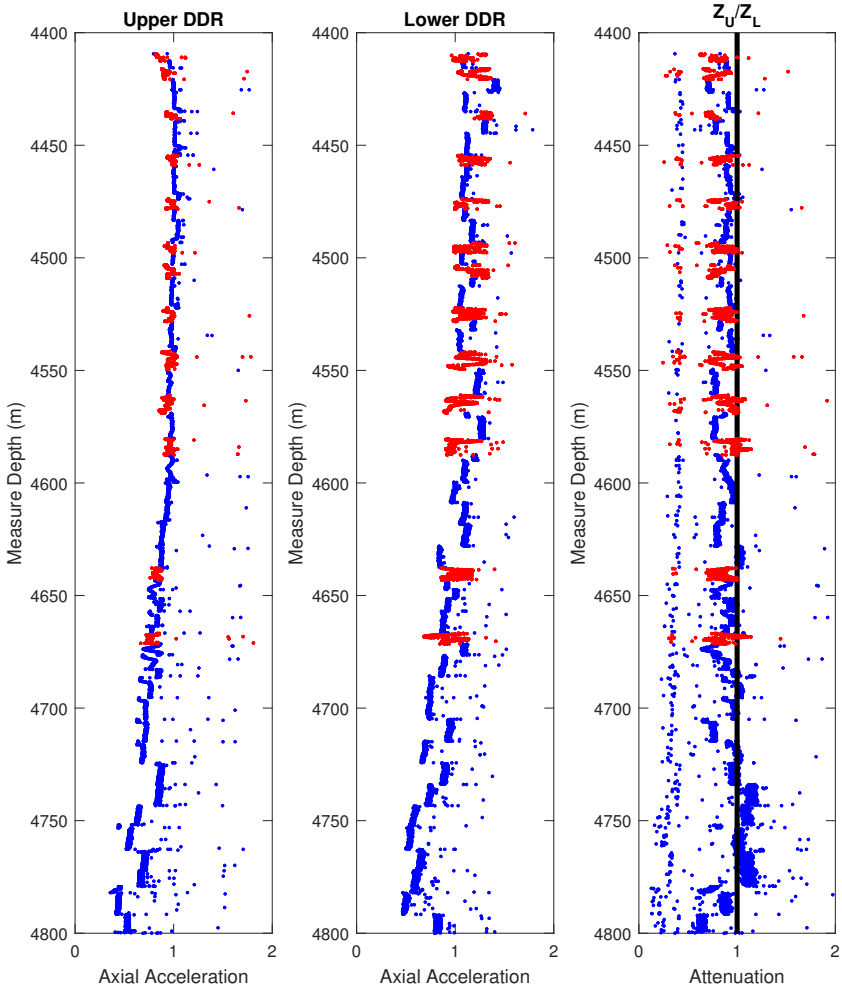

Figure 4.19: Corrected axial accelerations, at the upper DDR (left), the lower DDR (center) and the attenuation between DDRs (right) for the BHA with an AOT. Acceleration magnitude is overall somewhat higher than that experienced in the BHA without an AOT. Red points indicate slide drilling, blue points indicate drilling while rotating.

g to 0.5 g. This increase in RMS axial vibration is indeed seen in the data – at a MD around 4,400 m, when the BHAs are swapped, the RMS axial force increases by 0.5g, from a range of 0.5g to 1g to 1g to 1.5g, as can be seen in Figure 4.18 and Figure 4.19.

The field results in Figure 4.19 can be compared directly to the attenuation predicted by the model in Figure 4.20, where the attenuation due to a range of damping coefficients is shown. The model most accurately predicts the decreasing trend in attenuation seen in the field data between 0.3 and 0.5, but does not capture the elevated axial accelerations due to drilling inputs, as expected. Since these data sets are being collected in the lateral section, the coefficient of friction used for Coulomb friction can be tuned to match the result. Coulomb friction is inversely proportional to harmonic displacement, so a displacement value of 0.5 inch yields an attenuation that is similar to the 0.3-0.5 level shown in the data.

Downhole sensors only record vibrations at a single point and cannot provide insight into the dynamics of the entire drillstring. The model being presented explicitly calculates the displacement and force at each simulation node, chosen as a joint of drillstring, and can be visually presented to understand the complete drillstring response. Presented in Figure 4.21 and 4.22 are the responses of the drillstring at different bit depths for the field example just described. Subfigures 4.21a through 4.22b show the evolution of the displacement and force as the bit moves from the vertical 4.21a, through the build (4.21b and 4.22a), into the lateral 4.22b. The wellbore geometry is presented

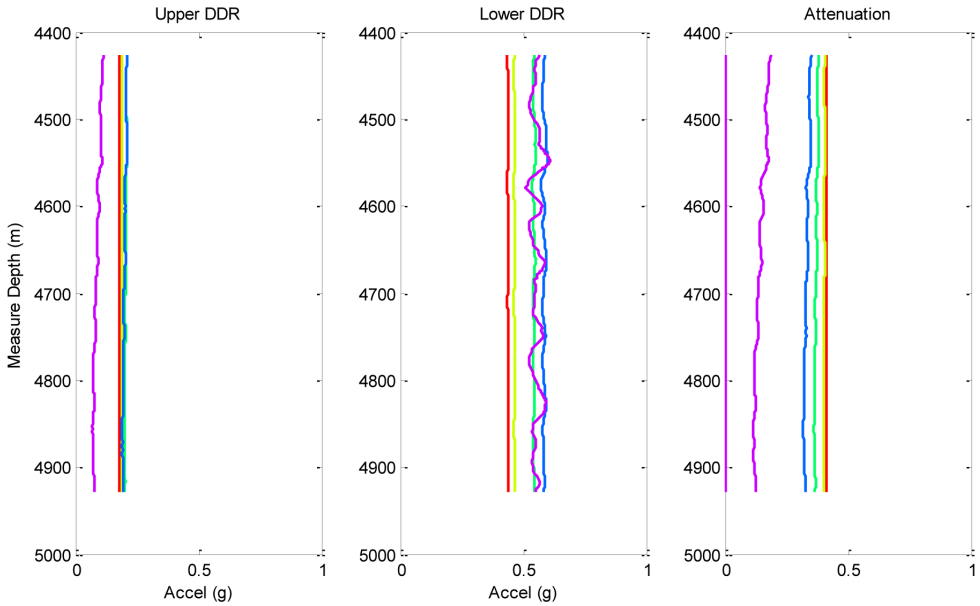

Figure 4.20: Attenuation predicted by the model with a range of frictional damping coefficients, ranging from low (red), as calculated by Coulomb friction (red) to high friction (violet). The blue, green, and yellow are in order of increasing friction.

in the inset 3D figure, with the location of the AOT highlighted in green and the drillstring in red. Displacement magnitude, in inches, is presented in the first vertical plot, followed by force normalized to the exerted force at the AOT, drillstring composition, with dimensions in inches, computed normal force on each stand of drillpipe in pounds and wellbore inclination in degrees.

In agreement with intuition, attenuation of the vibration increases once the AOT enters the lateral section due to the higher normal force which results in higher Coulomb friction. This is apparent both above the AOT and below the AOT due to the placement of the shock-absorber above the AOT, the

magnitude of vibration is higher below the AOT than above for all segments of the well. When it comes to understanding effects of AOT placement along the string, the main advantage a model such as the one presented here over scrutiny of measured data is that the same analysis can be conducted at the design and planning stage by using simulations. Previous models have only calculated effective friction coefficients; this model, on the contrary, can predict attenuation through the drillstring and can be used to tune tool placement for optimum effect (Newman et al., 2009). As shown in Figure 4.23, the location of the AOT within the borehole has a dramatic effect on attenuation of the vibration and poor placement of the AOT may severely limit its performance.

This step change, the movement from an effective friction coefficient to the simulation of distributed drillstring response, will allow for highly tuned BHAs in future wells that maximize the effect of the AOT based on the desired well trajectory and formations lithology. This will improve drilling efficiency and allow for the drilling of even longer laterals without the need for new or larger equipment.

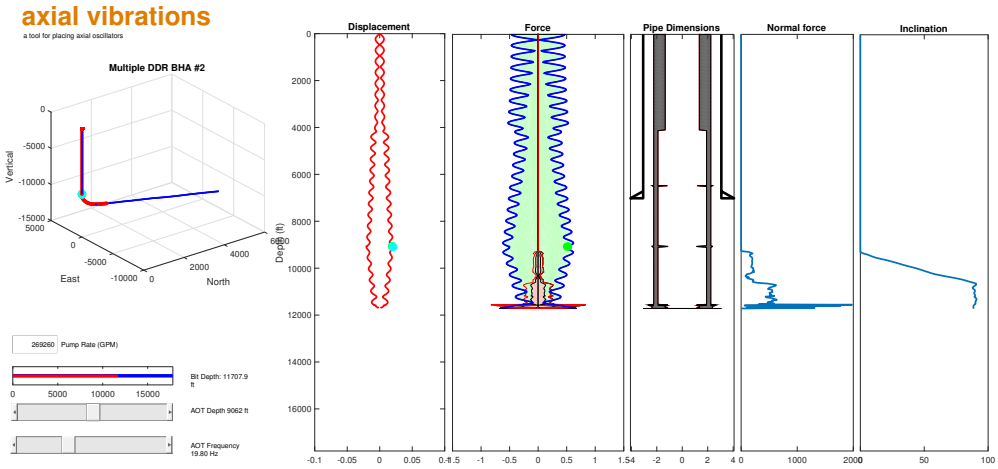

(a) Predicted dynamic response with the AOT above the curve.

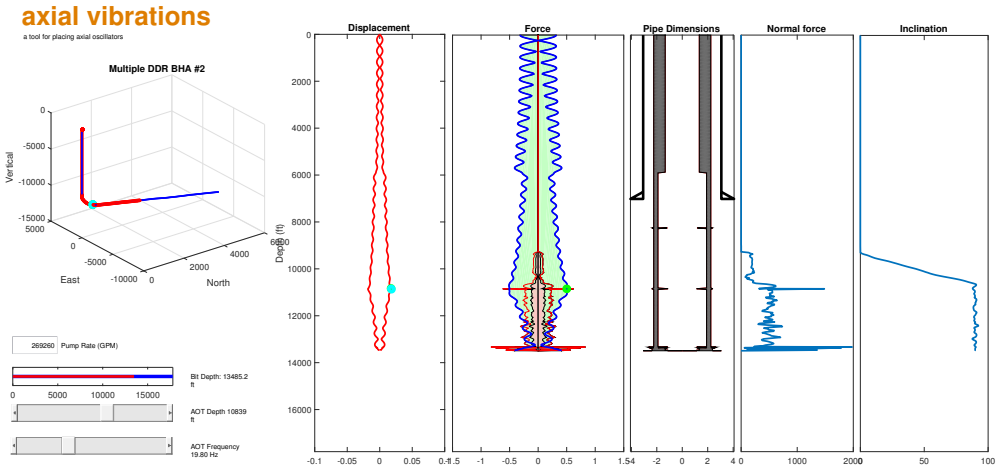

(b) Predicted dynamic response with the AOT entering the curve.

Figure 4.21: Model predictions for the dynamic response of the drillstring in the case of the AOT with DDRs for the AOT transiting the curve. Vibration amplitude in the vertical section is high while being rapidly damped towards the bit through the curve. Wellpath is shown in the inset plot in each, followed by displacement magnitude in inches, normalized force magnitude, drillstring dimensions in inches, normal force per stand in pounds and hole inclination.

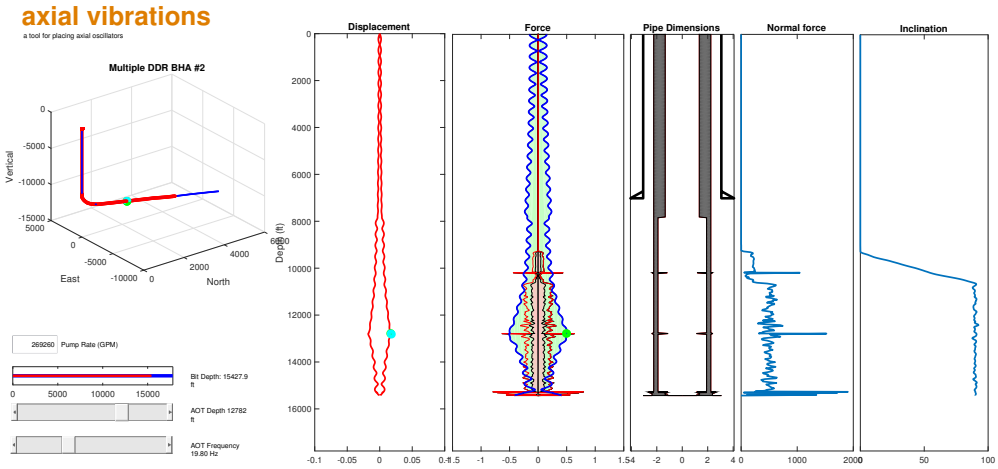

(a) Predicted dynamic response with the AOT having entered the lateral.

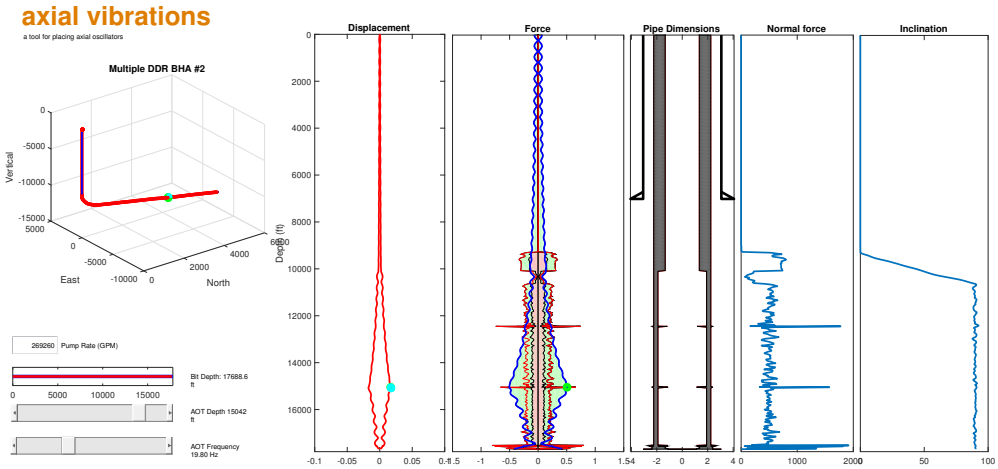

(b) Predicted dynamic response with the AOT midway through the lateral.

Figure 4.22: Model predictions for the dynamic response of the drillstring in the case of the AOT with DDRs for the AOT in the horizontal section. Vibration amplitude in the vertical lessens as the AOT moves further down the horizontal as damping due to friction increases. Wellpath is shown in the inset plot in each, followed by displacement magnitude in inches, normalized force magnitude, drillstring dimensions in inches, normal force per stand in pounds and hole inclination.

4.9.2 Case Study 2: Horizontal well with an axial oscillation tool and a continuous downhole dynamics recorder

A series of wells have been drilled with axial oscillation tools with continuous, low frequency, downhole dynamics recorders in the continental United States. Each well is drilled with a bent downhole motor below an MWD-LWD capable of recording 0.1 Hz axial and lateral acceleration data from a pair of DC coupled accelerometers. 10 second averaged acceleration and peak value during those 10 seconds are recorded and loaded from memory once the tool returns to surface.

In one of these wellbores, placement was optimized using the transfer matrix model already described. Based on the projected wellpath and bottom hole assembly, a tool position of 2317 feet behind the bit was chosen. The

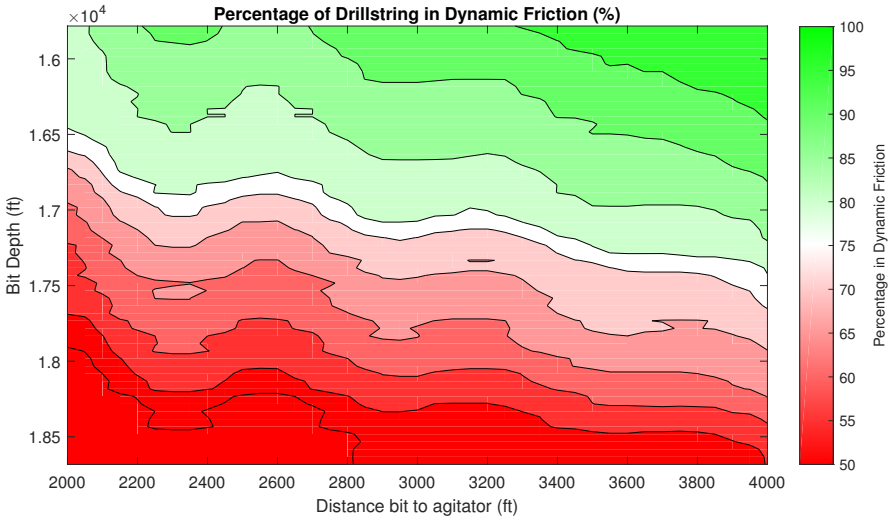

Figure 4.23: Optimizing the location of the axial oscillation tool.

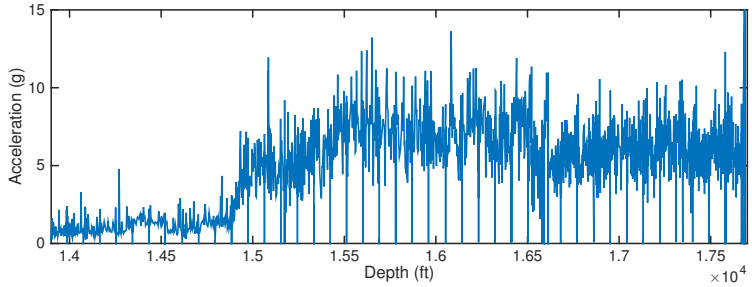

(a) Depth based average axial acceleration data from the downhole data recorder.

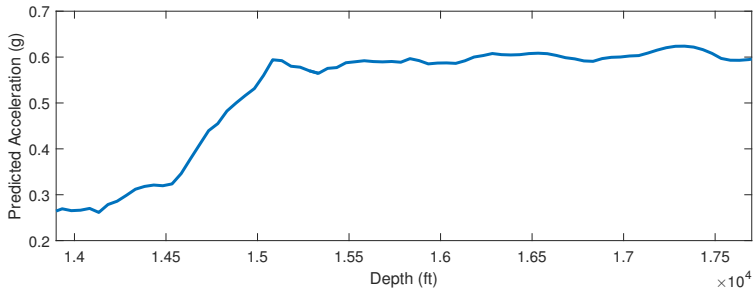

(b) Predicted average axial acceleration due to the axial oscillator at the location of the data recorder.

Figure 4.24: As the AOT transits the curve, acceleration magnitude at the bit increases in both the field data as well as in the model prediction.

expected reduction in friction along the drillstring due to tool placement is shown in Figure 4.23.

Once the well was drilled and an after action report prepared, an interesting phenomenon was observed where axial vibrations began to increase dramatically once the bit was approximately 2000 feet down the lateral section and then peaked at 2300 feet. Upon investigation, it was realized that this was the precise depth at which the axial oscillation tool was transiting the curve of the well and then exiting into the lateral. The model predicts that axial

vibrations will not travel far past the curve due to high normal forces, and thus high frictional damping, along the curve. Comparing the predicted axial vibrations with those recorded by the drilling dynamics recorder, a similarity is observed.

4.10 Conclusions

The case studies presented herein have shown that the transfer matrix model with equivalent viscous damping can predict drillstring response over a broad range of frequencies. The model allows the oscillation source to be placed at an arbitrary point in the drillstring for evaluation of axial oscillation tools in drillstrings. The predicted phase response of force and displacement at the bit correlates well with the likelihood of bounce and has demonstrated that the use of downhole motors – by shifting frequency of excitation – and the use and placement of shock absorbers reduce the incidence of bounce if properly chosen. The dependence of the drillstring dynamic response on bit-rock interaction and formation properties was verified, and by updating the bit boundary condition to reflect formation boundaries, the model correctly predicted the excitation frequencies that resulted in drillstring resonance. High frequency surface vibration data sets were also analyzed and the model also predicted similar resonance peaks. It was also demonstrated that surface measurements are highly influenced by drillstring resonance responses, while measurements near the bit were dominated by the resonances of the BHA. Since downhole measurement is limited to a small number of discrete measurement

points, the model's ability to predict displacement and force throughout the drillstring allows for tuning of BHA design and tool placement. The examples presented included visualization of the effect of axial oscillation tools throughout the entire drillstring at any measured depth as well as the response after a shock absorbing tool was moved to a new location. Similarly, drillstrings can be designed to avoid resonance due to excitation frequencies that have been observed in offset wells, both axially and torsionally.

Chapter 5

Comparing Control Paradigms using a Control Centric Model for Torsional Drillstring Vibrations

The wave equation model previously described may be used to test the effectiveness of control strategies to minimize higher order torsional oscillations. Until recently, the models used to both develop and test controllers were simple single degree of freedom models which captured first order dynamics but were often neither able to capture the delay inherent in the system nor the higher order modes. These controllers worked in many scenarios in the field, but often failed once these higher modes began to appear – in long slender drillstrings or in complicated well geometries. This chapter will study the effectiveness of four different control schemes: a stiff PI controller, a tuned PI controller, a second order PI controller and an impedance matching controller.

5.1 Introduction

The underlying goal of control system design is to match an output, y, to a reference signal, r, while rejecting any disturbances to the system, d, and reducing the effect of noise, n, in sensor readings. In the basic control

system loop shown in figure 5.1, the frequency domain output $Y(s) = \mathcal{L}\{y(t)\}$ is given by the expression

$$Y(s) = S_s C_s P_s (R_s - N_s) + S_s P_s D_s \tag{5.1}$$

where the sensitivity S is given by

$$S_s = \frac{1}{1 + C_s(s) P_s(s)} \tag{5.2}$$

and $C_s(s)$ is the control system and $P_s(s)$ is the plant, as shown in Figure 5.1. In the frequency domain, the reference signal is $R_s(s) = \mathcal{L}\{r(t)\}$, the disturbance is $D_s(s) = \mathcal{L}\{d(t)\}$, and noise is $N_s(s) = \mathcal{L}\{n(t)\}$.

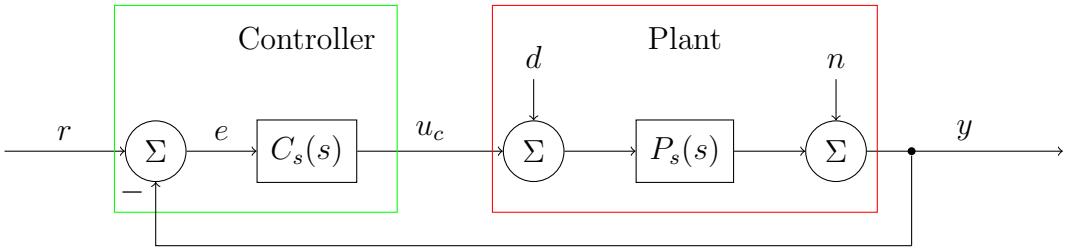

Figure 5.1: A basic feedback control loop, with r being the reference and y being the output, u is the controller output, d is the disturbance and n is the sensing noise. The frequency domain representations of the control system and the plant are $C_s(s)$ and $P_s(s)$, respectively.

The controller has two inputs, the reference signal r and the measured signal y, and one output signal, u_c. This output signal is fed into the plant, thus the role of the controller system is to generate an output which will cause the measured signal to approach the reference signal with minimal oscillation and maximum rapidity. The plant has three inputs, the controller output u_c, the disturbance d and external sensing noise n, and one output, y which

is the measured system state. Both of these system, the controller and the plant, may have additional inputs and outputs to monitor or modify internal variables.

5.2 Common Control System Components

Both the controller and the plant may be assembled from a basic library of components which will be briefly summarized here (Aström and Murray, 2010). All components are presented in the s-domain due to ease of representation and to facilitate the computation of the frequency response of a system.

5.2.1 PID Controller

A basic formulation of a controller is the proportional-integral-derivative (PID) controller which has one input, e, the error, or difference between the reference and the measured signals, and one output, u. This type of controller may be described in one of two ways in the s-domain:

$$C_s(s) = K_p + \frac{K_i}{s} + K_d s \tag{5.3}$$

where K_p is the proportional coefficient, K_i is the integral coefficient and K_d is the derivative coefficient. The second way, which is more convenient when poles and zeros of the system are analyzed to determine stability, is

$$C_s(s) = \frac{K_i + K_p s + K_d s^2}{s} \tag{5.4}$$

where the zeros of the system are given by

$$Z_c = \frac{-K_p \pm \sqrt{K_p - 4K_d K_i}}{2K_d} \tag{5.5}$$

and the pole of the system is at $s = 0$.

5.2.2 Filters and Delays

In the s-domain, filters and delays are compactly expressed as transfer functions. First order low pass filters, which broadly allow low frequency components of a signal to pass while filtering out high frequency noise, can be expressed as

$$LP(s) = \frac{1}{1 + \frac{2\pi f_{cutoff}}{s}} \tag{5.6}$$

where f_{cutoff} is the cutoff frequency. High pass filters are the exact opposite and thus allow high frequency components of a signal to pass while eliminating low frequency components. These are often used to remove signal bias or a constant offset, such as the force of gravity from an accelerometer. First order high pass filters can be expressed as

$$HP(s) = \frac{1}{1 + \frac{s}{2\pi f_{cutoff}}} \tag{5.7}$$

where f_{cutoff} is once again the cutoff frequency. Both low pass and high pass filters act both on the amplitude of the signals upon which they are applied, but also upon their phases. The same way a running average lags behind the signal it is averaging, so does a filtered signal. Thus, a 100 ms low pass filter will eliminate most noise within a 100 ms time window, it will also phase shift the signal by 100 ms. This frequency domain representation is widely used and has been shown to accurately model analog filters often used in the field (Oppenheim and Schafer, 2009).

Simple delays in signals which do not change the amplitude of the signal can be expressed in the frequency domain as

$$De(s) = e^{-s\tau} \tag{5.8}$$

where τ is the delay in seconds. These are often used to represent electronic or signal processing delays, such as measurements from encoders or other sensors.

5.2.3 Representing Real Components

Real systems may be modeled using the three components detailed in the previous section.

5.2.3.1 Variable frequency drives

The speed and torque of AC motors, such as those widely used in top drives, are controlled using variable frequency drives. These drives modulate the frequency and current of three phases of electrical current to accurately control motor speed and torque. A thorough review of the types of VFDs and their operation may be found on various manufacturer websites, but are well summarized in two theses (Jadric, 1998; Ozkentli, 2012).

The simplest model to describe a VFD in a plant model is as a low pass filter and a delay. All VFDs have a cutoff frequency above which commands will be ignored, and may be simplified as a low pass filter. The electronics within the VFD add an inherent pure delay into the system as well. Thus, a

VFD may be modeled as

$$VFD(s) = \frac{1}{1 + \frac{2\pi f_{cutoff}}{s}} e^{-t_{vfd}s} \tag{5.9}$$

where f_{cutoff} is the cutoff frequency of the VFD, or maximum change in signal that the VFD may follow, and t_{vfd} is the time delay of signal input to the motor output.

5.2.3.2 AC Motors

AC motors often have large moments of inertias which cause torque to decrease across a motor if it is accelerating. At steady state, the torque input into a motor is the same as its output, but during acceleration or deceleration, motor inertial torque must be considered (Gibbs, 1975). Thus, for systems which accelerate or decelerate frequently, the following simplified motor model may used

$$\tau_{inertia} = J_{td}\ddot{\phi} = sJ_{td}\dot{\phi} \tag{5.10}$$

where J_{td} is the top drive inertia and $\dot{\phi}$ is current rotary speed. This model ignores frictional and steady state motor torque, thus torque values reported by the model will be lower than expected. However, since this is a steady state error, the dynamic behavior of the system will not be affected.

5.3 Methodology

To design high-order, high performance controllers, an improved plant model, $P(s)$, is needed to ensure proper stability criteria are met. However,

this requires knowledge of physics of the plant, the drillstring in this case, which is hard to quantify. Existing systems model the drillstring as a lumped mass and torsional spring, as in the case of SoftTorque and SoftSpeed (Dwars et al., 2013; Kyllingstad and Nessjøen, 2009, 2010), or as a transmission line (Kreuzer and Steidl, 2010) and treat the wellbore geometry, bit rock interaction, and friction as disturbances to the system. Many of these can be estimated, both during the drilling process or prior during the well planning process, and their incorporation into the plant model would allow for improved controller design.

The overall model is shown in Figure 5.2 and is comprised of a controller block, a VFD block, a motor block, a drillstring model and an optional observer. Prior work in this area has almost entirely left out the effects of the VFD and motor on system performance by assuming a perfect system. In reality, especially when control is attempted at frequencies higher than 1 Hz, motor inertia and signal filtering become critical. At oscillation frequencies over 2 Hz, VFD delays must also be accounted for.

The mathematical model of the drillstring is reviewed first, both in time and frequency domains, and includes a discretized implementation as both the damped wave equation and a mass-spring-damper system. The mass-spring-damper simplified model is then be compared to a simple laboratory setup to verify model mechanics. Further verification of model mechanics is performed in the subsequent chapter where the model is used to image the drillstring.

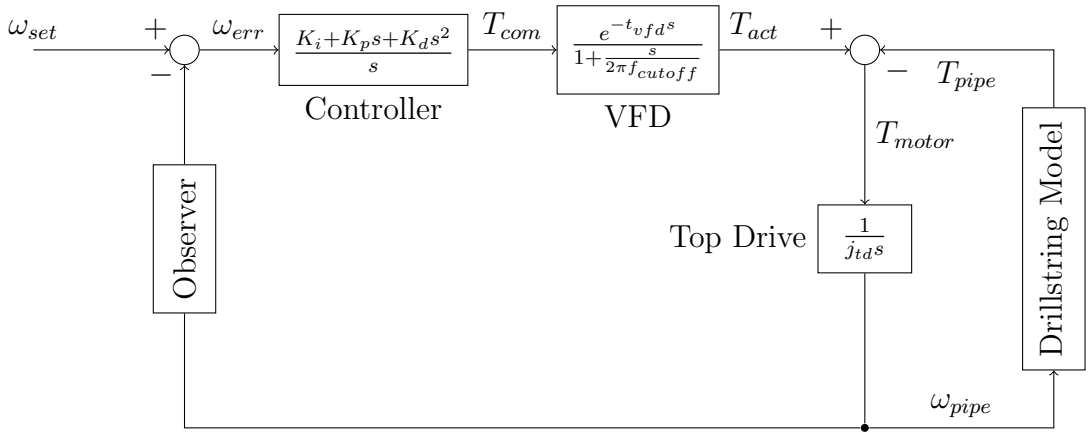

Figure 5.2: Control Diagram for a PID controller, VFD and top drive. T_{pipe} is an output and ω_{pipe} is the input of a drillstring model. An observer may be inserted which may improve system performance.

5.3.1 Mathematical Model

Two drillstring models are systematically compared: a time domain implementation of the wave equation and a frequency domain simplification as a n-DOF mass-spring-damper model. The wave equation is solveable in the time domain which allows for a time varying speed input from surface and a non-linear friction boundary from the bit. This gives an opportunity to investigate controller operation with a time varying speed setpoint. The wave equation can be simplified as an n-DOF mass-spring-damper model with the proper constants. This type of model is easily expressed in the frequency domain and allows for rapid characterization of the control system to step, unit and harmonic inputs.

The drillstring is modeled using the one dimensional damped wave equation and incorporates complexities using boundary conditions and dis-

tributed damping. As described by Lee (Lee, 1991), the primary sources of damping are: viscous damping from the borehole fluid, material hysteresis, radiation of energy into the formation, and frictional damping. All of these except for friction can be considered constant along a drillstring. Friction between the drillstring and wellbore is a function of borehole inclination, tortuosity of the wellbore, the existence of ledges or other points of wellbore contact, and the drillstring design, namely the placement of stabilizers.

The angular displacement of the drillstring, ϕ, may be described using

$$\frac{1}{v_t^2}\frac{\partial^2\phi}{\partial t^2} = \frac{\partial^2\phi}{\partial z^2} - \frac{C(x,t)}{GJ(x)}\frac{\partial\phi}{\partial t} \tag{5.11}$$

where $v_t^2 = \frac{G}{\rho}$ is the wave velocity, C is the damping and J is the moment of inertia. The general model consists of n beam elements, each described by the wave equation, bounded by a surface impedance, representing the top drive, and a bit boundary, representing bit-rock interaction.

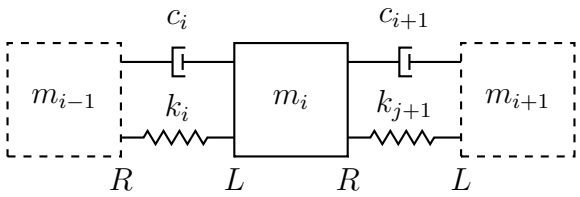

Figure 5.3: Mass-spring-damper equivalent system.

This model may be simplified further, as shown in Figure 5.3, by abstracting each mass element as a mass-spring-damper which obeys the following equation

$$m\frac{d^2\phi}{dt^2} = -k\phi - c\frac{d\phi}{dt} \tag{5.12}$$

In this case, m is the moment of inertia of each element, $k = \frac{GJ}{L}$ is the torsional spring constant, and c is the damping between elements.

For a n-DOF model, the motion of each mass may be described using

$$m_i\ddot{\phi}_i = -k_{i-1}\left(\phi_i - \phi_{i-1}\right) - \phi_i\left(\phi_i - \phi_{i+1}\right) - c_i\dot{\phi}_i \tag{5.13}$$

and the plant transfer function may be obtained, assuming a free bit end condition and an ideal velocity source at the top drive.

For a seven lumped mass model presented here, the states are the angular displacements of the top drive and the seven lumped masses representing the drillpipe and the bit, $\phi = [\phi_1, \phi_2, ..., \phi_8]$ with an ideal velocity source $\dot{\phi}_1 = u$. The system can be expressed as a series of seven second order differential equations in the form $M\ddot{\tilde{\phi}} + D\dot{\tilde{\phi}} + K\tilde{\phi} = k_1 e_1 \phi_1$, where $e_1 \in \mathbf{R}^7$ is the standard basis vector, $\tilde{\phi} = [\phi_2, \phi_3, ..., \phi_8]$ is the new state vector with the angular displacements of seven lumped masses and the M, C and K matrices are the inertia, damping and spring matrices defined as:

$$M = \begin{bmatrix} I_1 & & \\ & \ddots & \\ & & I_7 \end{bmatrix} \quad C = \begin{bmatrix} c_1 & & \\ & \ddots & \\ & & c_7 \end{bmatrix} \quad K = \begin{bmatrix} k_1 + k_2 & -k_2 & & \\ -k_2 & k_2 + k_3 & -k_3 & \\ & & \ddots & \\ & & -k_7 & k_7 \end{bmatrix} \tag{5.14}$$

Applying the Laplace transform and rearranging gives the transfer function of the plant which will be used in the subsequent control section.

$$\tilde{\Phi}(s) = (Ms^2 + Cs + K)^{-1} k_1 e_1 \frac{1}{s} U(s), \qquad Y(s) = e_7^\top \tilde{\Phi}(s) s \tag{5.15}$$

$$G(s) = \frac{Y(s)}{U(s)} = k_1 e_7^\top (Ms^2 + Cs + K)^{-1} e_1 \tag{5.16}$$

This construct may be used in both the frequency domain, for control system design and system response, and in the time domain to analyze transient behavior.

5.3.2 Bit Torque Model

A simplified bit model is used and utilizes a Stribeck friction curve to model rock-bit interaction as a non-linear relation between bit speed and torque. At zero speed, reactive bit torque is high, but then drops rapidly once bit rotation begins before increasing linearly with rotational speed. This model has been shown to give a good approximation of bit behavior without needing to account for the complexities of cutter-rock interaction and is an improvement over a Coulomb friction law (Reckmann et al., 2007; Navarro-Lopez and Cortes, 2007). The Stribeck curve is approximated as

$$\tau_{bit} = \frac{a}{|\omega_{bit}|} + b \cdot |\omega_{bit}| + c \tag{5.17}$$

for bit speeds greater than some ω_{cutoff}, otherwise $\tau_{bit} \to \infty$ as $\omega_{bit} \to 0$.

The Stribeck curve used in the control simulations presented later in this chapter is shown in Figure 5.4.

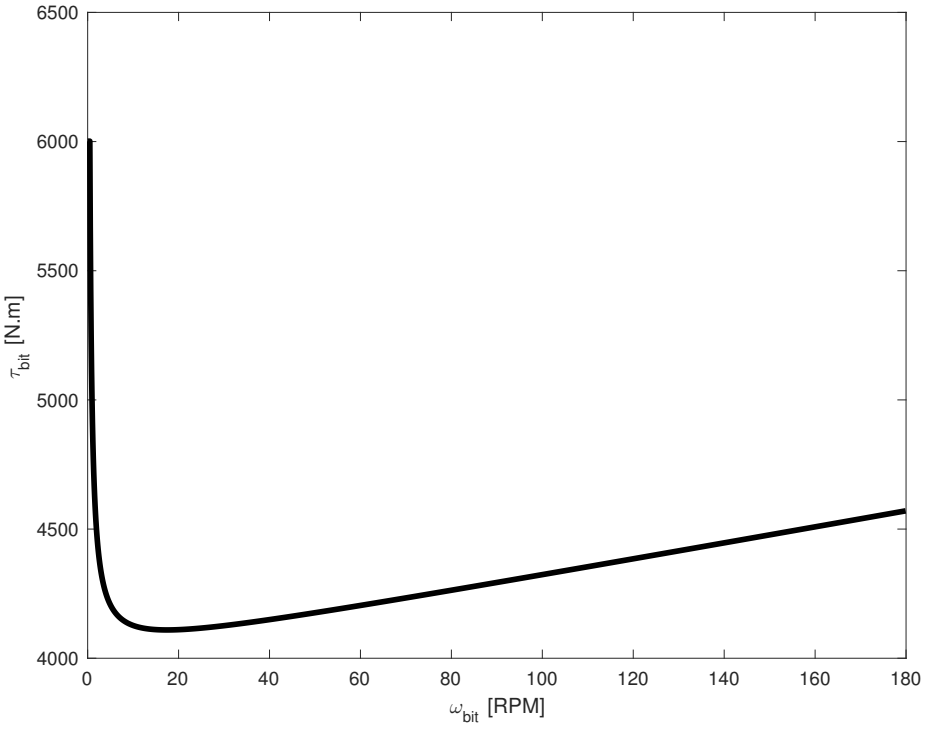

Figure 5.4: Stribeck curve used for the control simulations.

5.3.3 Bit Boundary Condition

The bit boundary condition in the drillstring model is modeled as a rotating inertial mass which obeys the following force balance:

$$\tau_{BHA} = J_{BHA}\ddot{\phi} + \tau_{bit} \tag{5.18}$$

where τ_{BHA} is the torque exerted on the BHA by the drillstring, τ_{bit} is the reactive bit torque as computed by the Stribeck friction law, J_{BHA} is the BHA inertia, and $\ddot{\phi}$ is the acceleration of the BHA. Solving for angular velocity, $\dot{\phi}$

of the BHA gives

$$J_{BHA}\ddot{\phi} = \tau_{BHA} - \tau_{bit} \tag{5.19}$$

$$\ddot{\phi} = \frac{\tau_{BHA} - \tau_{bit}}{J_{BHA}} \tag{5.20}$$

and then applying a centered finite difference approximation, the angular position of the bit may be found

$$\frac{\phi_{bit}^{t+1} - 2\phi_{bit}^{t} + \phi_{bit}^{t-1}}{\Delta t^2} = \frac{\tau_{BHA} - \tau_{bit}}{J_{BHA}} \tag{5.21}$$

$$\phi_{bit}^{t+1} = \frac{\tau_{BHA} - \tau_{bit}}{J_{BHA}}\Delta t^2 + 2\phi_{bit}^{t} - \phi_{bit}^{t-1} \tag{5.22}$$

5.4 Experimental Setup

Many laboratory models described in literature (Leine et al., 2002; Kreuzer and Steidl, 2010; Liao et al., 2012) are single degree of freedom models that model the BHA as a single large inertial mass (typically a disk) and the drillstring as a torsional spring (typically a long slender rod). These models are effective at modeling first order dynamics, but do not take complexities of complex drillstring designs or non-vertical wellbores into account. A seven degree of freedom model is constructed as a proof of concept for a much larger 30 degree of freedom model designed and built by another student in the research group which emulates a 2km drillstring and is detailed in other papers. These models are based upon a model designed by Shell Research (Dwars, 2015) that distributes the inertial masses along the drillstring, but expands on its capabilities by allowing for distributed damping to emulate borehole contact. n

inertial masses, the size of which can be varied to match different sections of a BHA, are fixed to a steel rod that acts as a torsional spring between each of the masses. Torsional waves can then be generated, either at the top drive or at the bit and wave propagation can be observed and recorded at each inertial mass.

This chapter details a seven-DOF benchtop prototype of the laboratory model that is able to simulate a 320 meter (950 ft) drillstring by using a series of 2.54 cm diameter inertial masses attached to a rubber rod. The masses act to delay a torsional wave that would otherwise travel at 25 m/s down to an effective velocity of 3.3 m/s. Measurement of angular displacement at four points is achieved using rotating stripped disks and photo sensors, giving an estimate of angular velocity.

The seven degree of freedom mass-spring-damper model described in the previous section is next compared with the velocity distributions generated by the benchtop model to ensure model fidelity.

5.5 Model Analysis

A sinusoidal input is placed at bit boundary in the desktop model and velocities are computed from the reflectance values of the photo sensors. The initial wave propagation may be used to compute propagation delay and once the sinusoidal input ceases, the decay of the oscillations may give a damping factor. Of note, the simple encoder discs do not allow for differentiation between forward and reverse motion, so only the absolute value of velocity may

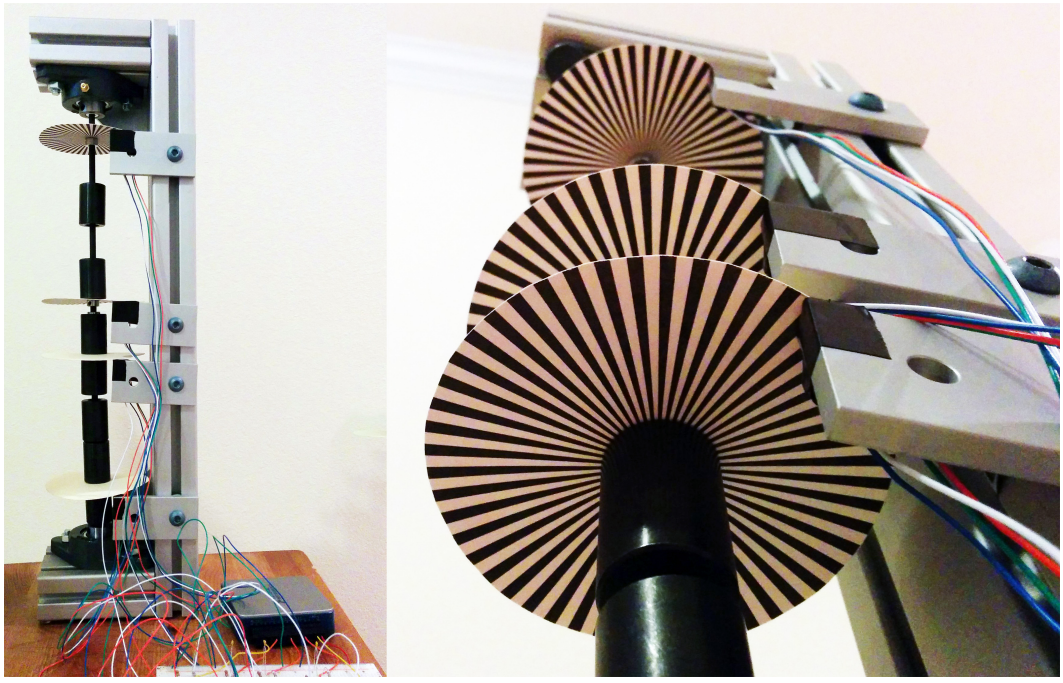

Figure 5.5: The desktop prototype model showing the full model, sensing and data acquisition (right) and the stripped disks and photo sensors used as rudimentary encoders (left).

be computed from the transit time of a light or dark stripe. Lateral motion is not accounted for in the model physics, but does not affect angular velocity measurements since sensor radial position does not affect the angular width of a stripe.

The analytic derivation of the spring constants and mass inertial elements from material constants gives a close approximation of the physical behavior, and as expected, the damping constants, which are constant within the model, require some tuning to match the decay of the observed wave be-

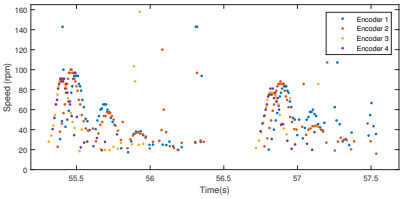

(a) Half period sinusoidal input at the bit.

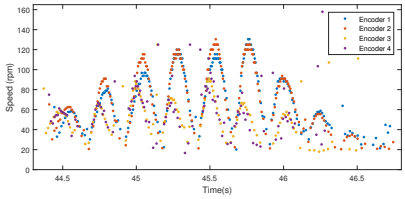

(b) Two period sinusoidal excitation from the bit boundary.

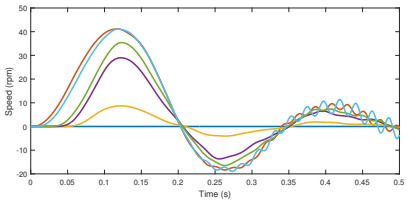

(c) Modeled half period sinusoidal excitation from the bit boundary.

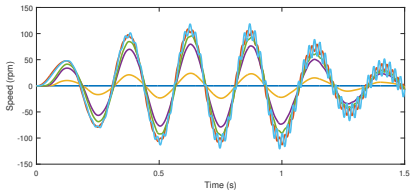

(d) Modeled four period sinusoidal excitation from the bit boundary.

Figure 5.6: Model output (top) and model results (bottom).

havior. Consistent behavior of the model, either after a unit cycle or a repeated oscillation cycle indicates that damping may be estimated from the behavior of the top node within a true drillstring. A series of controller were demonstrated using this seven lumped mass mathematical model and show that loop shaping methods may be used to successfully damp out oscillations from a step response (Shor et al., 2015b).

5.6 Comparing Controllers

The performance of a series of controllers will be compared in this section with the drillstring configuration shown in Table 5.1 and the rig and control system parameters shown in Table 5.2. These values are representative

of a small top drive, such as those built by NOV and Canrig and a typical digital VFD setup, as manufactured by Siemens or ABB.

Component	Length (ft)	OD (in)	ID (in)	Damping (η)
Drill Pipe	4000	5	4.5	0.01
Heavy Weight Drill Pipe	800	6	4.5	0.02
Drill Collar	200	8	2	0.1

Table 5.1: Drillstring components used in the controller comparison cases

Parameter	Value	Unit
Top Drive Motor Inertia	1200	N.m
PI Controller Delay	0	ms
VFD Cutoff Frequency	200	Hz
VFD Delay	0	ms
VFD Torque Limiter	40000	N.m
Encoder Low Pass Filter	4	ms
Additional Speed Low Pass Filter	0	ms
Sensor Delay	2	ms

Table 5.2: VFD and motor parameters for the control scenarios

Bit-rock interaction is accomplished using the stribeck curve to simulate static and dynamic torque behavior with the parameters shown in Table 5.3.

Parameter	Value	Unit
a	100	$(N \cdot m)(s^{-1})$
b	30	$(N \cdot m)(s)$
c	4000	$N \cdot m)$

Table 5.3: Stribeck parameters used for the bit-rock friction model: $\tau_{bit} = \frac{a}{|\omega_{bit}|} + b \cdot |\omega_{bit}| + c$

5.6.1 Stiff PID Controller

The simplest control methodology for a top drive is a control paradigm typically known as a stiff speed controller, where torque is modulated to ensure constant rotary speed. This is the simplest controller to implement and is the most convivial to the driller – the top drive spins at exactly the speed commanded. However, this creates a stiff boundary condition at the surface and allows standing waves to develop – exhibited as stick-slip behavior. The control system is shown in Figure 5.7.

Two stiff PI controllers are shown in Figures 5.8 and 5.9 for two scenarios – the bit off bottom and the bit on bottom – which exhibit large torsional oscillations at the bit while surface rotary speed remains constant.

In the off-bottom case, shown in Figure 5.8, the bit is treated as a free boundary condition which allows for both positive and negative torque to experienced at the BHA as the bit fluctuates from 0 to 120 rpm while the

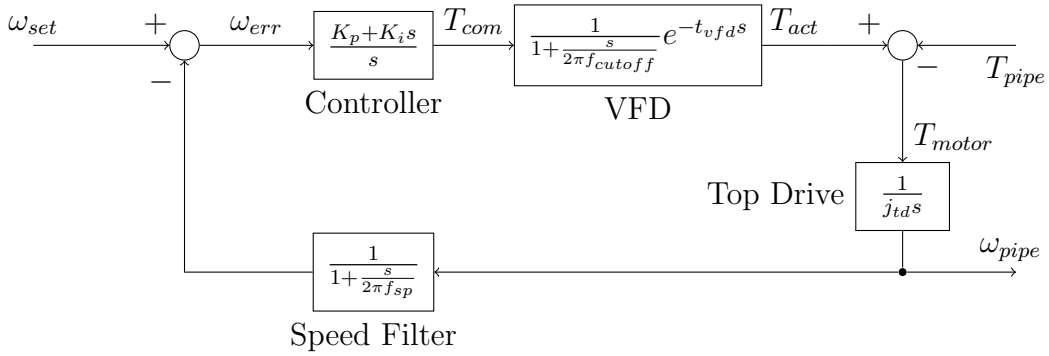

Figure 5.7: Control Diagram for a PID controller, VFD and top drive. T_{pipe} is the output of the drillstring model and ω_{pipe} is the input of a drillstring model.

surface is maintained at 60 rpm. This type of behavior has been observed in many cases in the field when the drillpipe is first rotated after a connection.

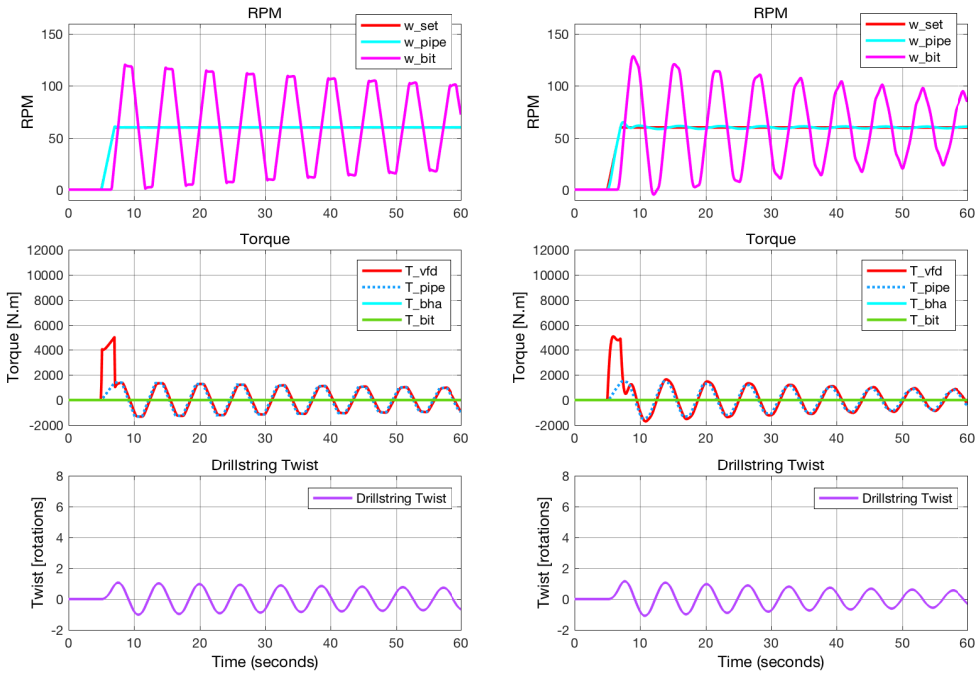

(a) $K_p = 38000$ and $K_i = 100000$. (b) $K_p = 3800$ and $K_i = 10000$.

Figure 5.8: Step response of the system with a stiff PI Controller and the bit off bottom.

With the bit on bottom and obeying the Stribeck curve, shown in Figure 5.9, the bit boundary becomes a nonlinear torque boundary. Momentary sticking is observed – seen as zero bit rotation – as well as peak bit rpms of 120, similar to the bit off bottom case. The second mode of stick slip, the embedded higher frequency oscillation in the rpm and torque, is also clearly visible. Of note is the change in stick slip frequency, shifting from a higher frequency when the bit is free to a lower frequency when the bit is on bottom.

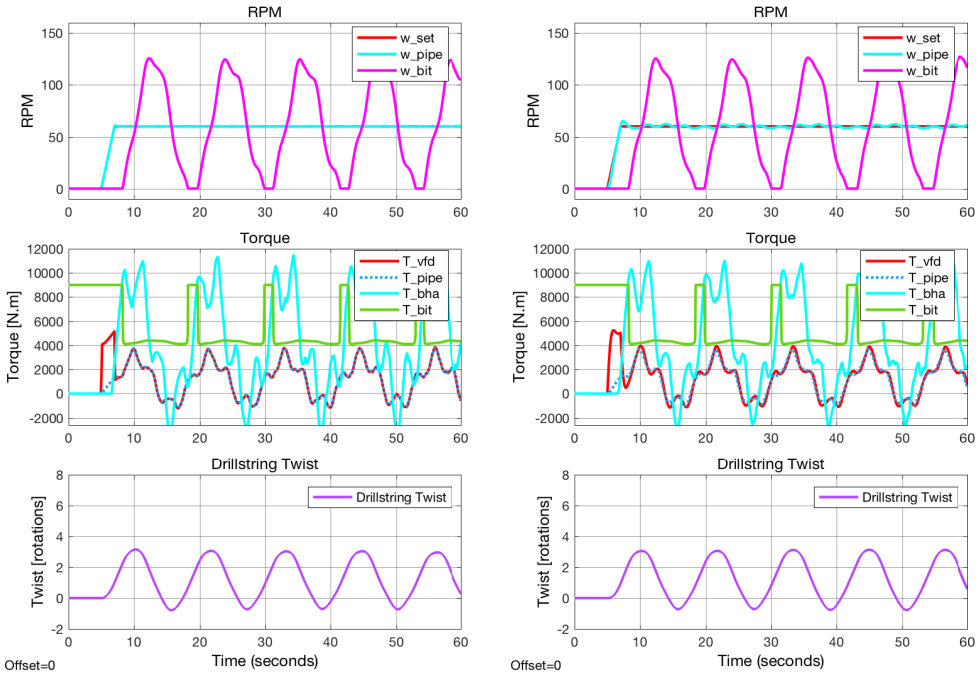

(a) $K_p = 38000$ and $K_i = 100000$. (b) $K_p = 3800$ and $K_i = 10000$.

Figure 5.9: Step response of the system with a stiff PI Controller and the bit on bottom.

5.6.2 Tuned PI Controllers

The PI controller may be tuned to have a zero at the frequency of the first mode of stick slip, which is roughly equal to one over the one way travel time of a wave from the surface to the bit, but can also be computed analytically – as shown in a later section. For a 5000 ft drillstring, this is 1.56 seconds or 0.64 Hz. By placing a zero at this frequency, waves traveling from the bit to the surface at this frequency are ignored and not allowed to develop into standing waves. For a free boundary condition, this methodology quickly attenuates any standing waves, as shown in Figure 5.10.

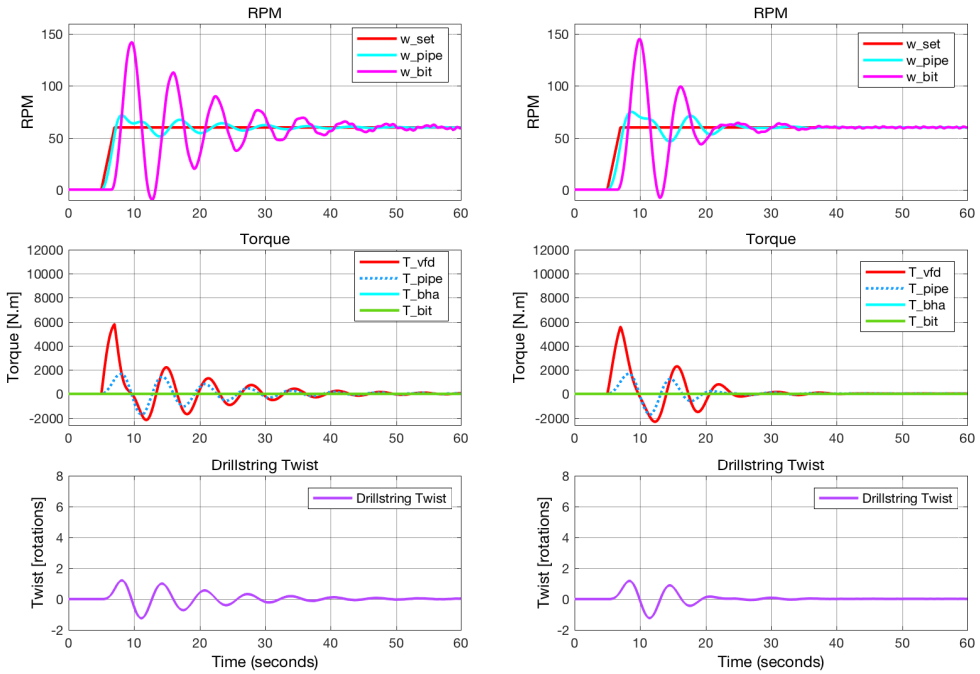

(a) $K_p = 1350$ and $K_i = 2107.6875$. (b) $K_p = 850$ and $K_i = 1327.0625$.

Figure 5.10: Step response of the system with a tuned PI Controller and the bit off bottom.

With the bit on bottom, as shown in Figure 5.11, it becomes apparent that the tuned PI controller only attenuates the first mode of stick slip as the second order continues without any attenuation in amplitude. Also since the frequency of stick-slip has shifted, the tuned PI controller which was effective for a free bit is much less effective.

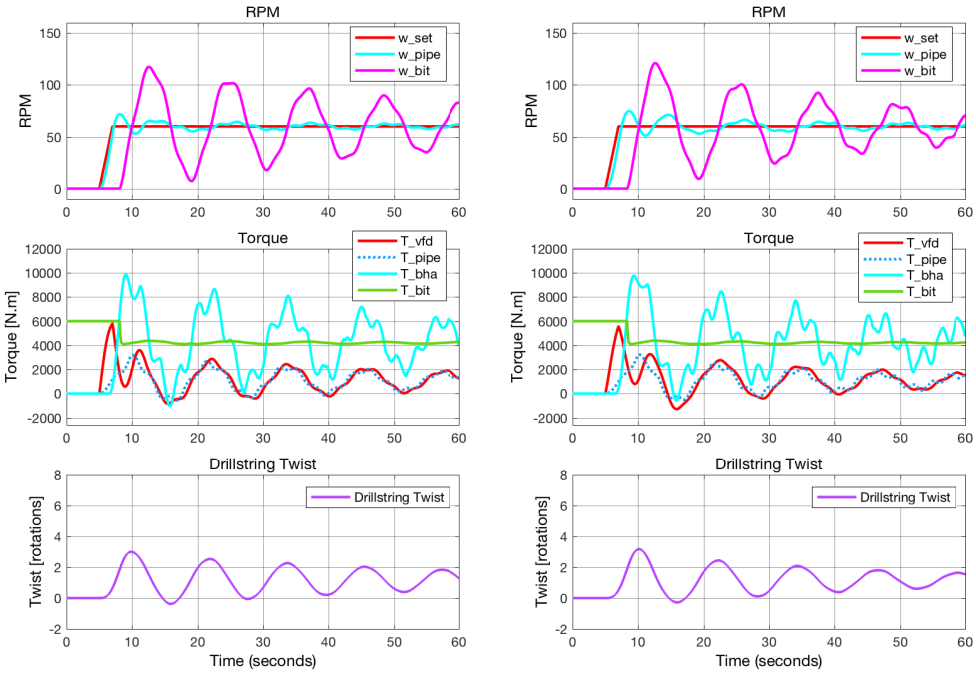

(a) $K_p = 1350$ and $K_i = 2107.6875$. (b) $K_p = 850$ and $K_i = 1327.0625$.

Figure 5.11: Step response of the system with a tuned PI Controller and the bit on bottom.

Changing the tuning frequency to one closer to the frequency exhibited by the bit on bottom, the bit oscillations decay quicker, as shown in Figure 5.12. Oscillations also damp faster in the case with the smaller K_p value acts as a 'softer' system and thus reduces the amount of twist in the drillstring faster.

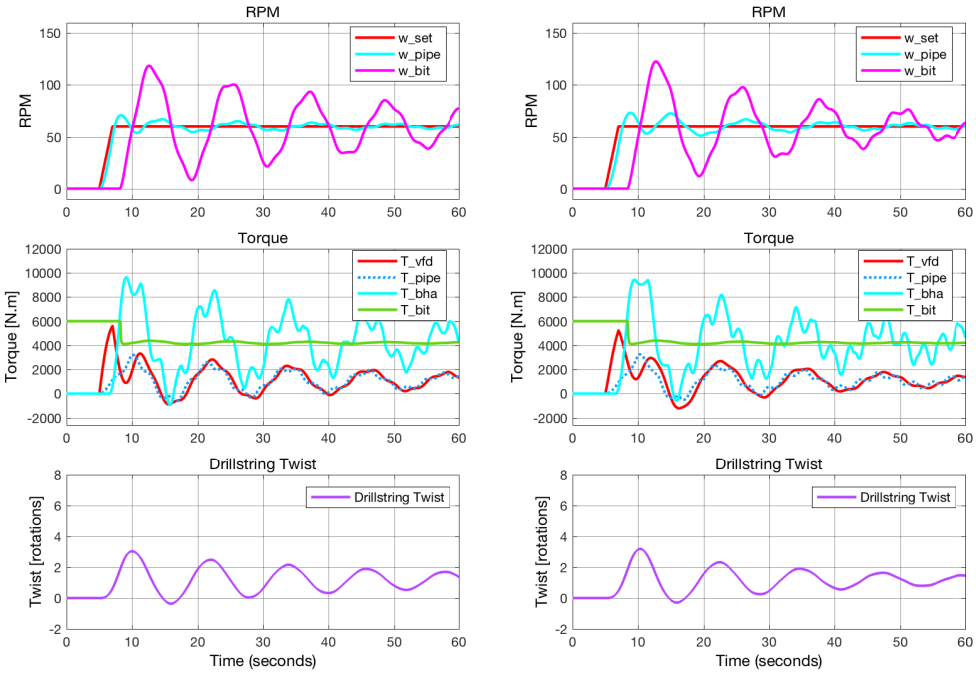

(a) $K_p = 1350$ and $K_i = 1686.15$. (b) $K_p = 850$ and $K_i = 1061.65$.

Figure 5.12: Step response of the system with a modified tuned PI Controller and the bit on bottom.

5.6.3 Second Order PI Controllers

A second order PI controller may be designed to extend the functionality of the first order PI controllers in the previous section. In the case, the C_s block is replaced with

$$C_s = c_f \cdot \frac{a_1 s + a_2}{s} \cdot \frac{b_1 s + b_2}{s} \tag{5.23}$$

and performance is significantly improved, as shown in Figure 5.13

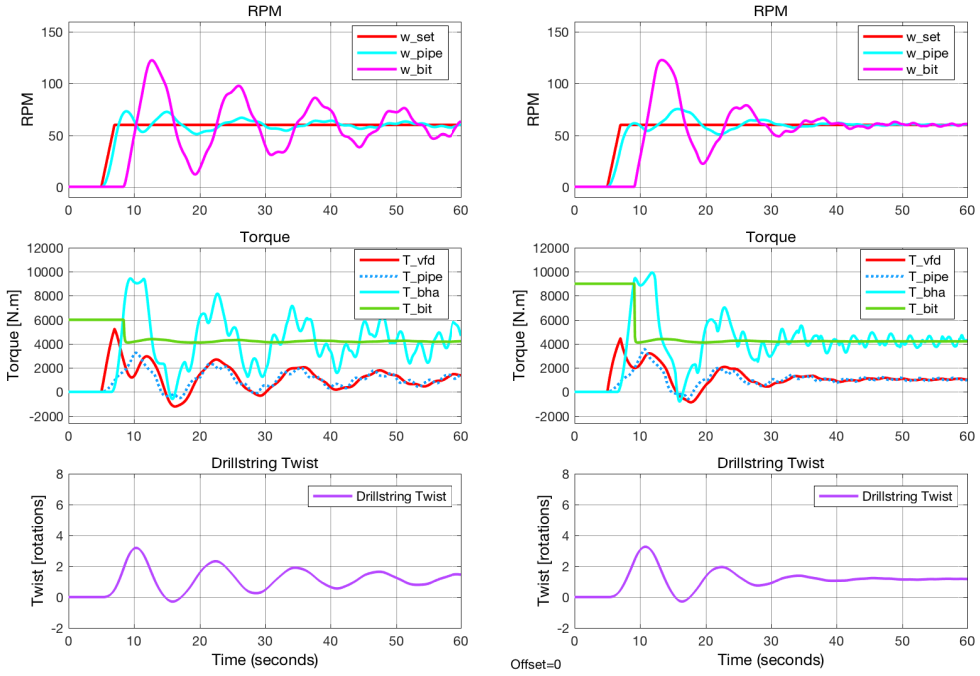

(a) Tuned first order PI controller with $K_I = 850$ and $K_i = 1061.65$.

(b) Tuned second order PI controller with $c_f = 100$, $a_1 = 4, a_2 = 0.1, b_1 = 3$ and $b_2 = 1$.

Figure 5.13: Step response of the system with a tuned first order and second order PI controller.

5.6.4 Impedance Matching Controllers

A new method has recently been proposed which describes the surface of a drillstring as a reflective boundary which allows standing waves to develop. By changing the reflectivity of this boundary, less energy is stored in the drillstring and standing waves are disrupted. The approach is described at length in literature but a summary is presented here (Dwars, 2015).

A concept familiar to those who work with seismic data, radar, sonar or non-destructive testing is acoustic impedance. A wave, be it acoustic or electromagnetic, travels through a medium until a change in material properties is encountered – density, viscosity, stiffness, inertia, etc – and is then partially transmitted and partially reflected. The ratio between transmission and reflection is given by ratio in impedance contrast across the boundary. Impedance, the ratio between the change in either displacement or velocity and change in force, is a material property that gives the amount of effort necessary to place the medium in motion. For a rotating pipe, this is simply the ratio of rotational velocity to torque and is computed directly from the wave equation:

$$Z = \frac{\Delta\omega}{\Delta\tau} = \frac{\frac{\partial\omega}{\partial t}}{\partial\tau}\partial z = \frac{\partial\omega}{\partial\tau} \cdot \frac{\partial z}{\partial t} = \rho J_p \cdot c = J_p\sqrt{\rho G} \tag{5.24}$$

The top drive may attempt to match the impedance of the drillpipe connected to it by modulating its rotational velocity given the amount of torque transmitted from the drill pipe. During perfect impedance matching, 100% of wave energy from the bit is transmitted across the top drive and none

is reflected. At 50% matching, half the energy is transmitted and half reflected. In reality, this is only true for a band of frequencies. At lower frequencies, this behavior is undesirable since the driller setpoint must be observed. At high frequencies, this ambition is impossible due to signal filtering and delays.

Impedance matching is accomplished through the addition of an observer consisting of a high pass filter, a low pass filter and an impedance gain, as shown in Figure 5.14. The controller must eventually match the set point, so only higher frequency noise from the bit is used to impedance match, thus a high pass filter is used with a slow time constant (on the order of seconds). Noise within the torque signal itself must be filtered, otherwise the top drive will be unable to match the signal, thus a low pass filter is also used. This filtered torque signal is then converted into an rpm setpoint by multiplying it by the target impedance and then applying the percent matching desired.

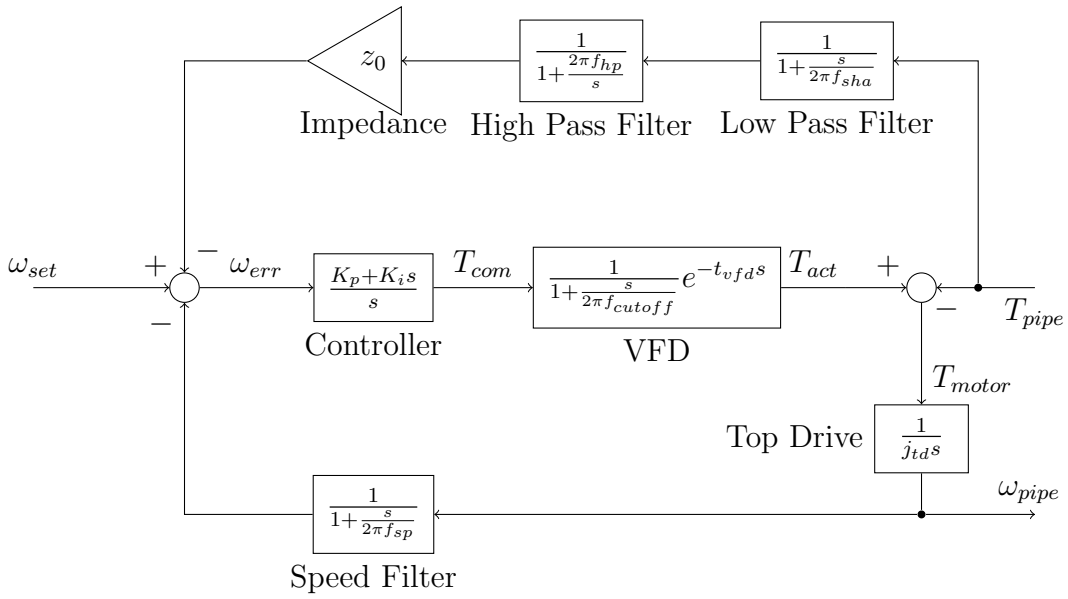

Figure 5.14: Control Diagram for an Impedance Matching PI controller, VFD and top drive. T_{pipe} is the output of the drillstring model and ω_{pipe} is the input of a drillstring model.

With 50% or 100% impedance matching, stick-slip oscillations attenuate almost immediately, however, high frequency noise becomes visible due to the delays inherent in the system from sensing, filtering and control delay, as shown in Figure 5.15. In a later section, the source of this noise will be quantified, however, due to the design of the system, it is particularly difficult to eliminate without eliminating most filter and delays, which is sometimes not possible due to the nature of the hardware.

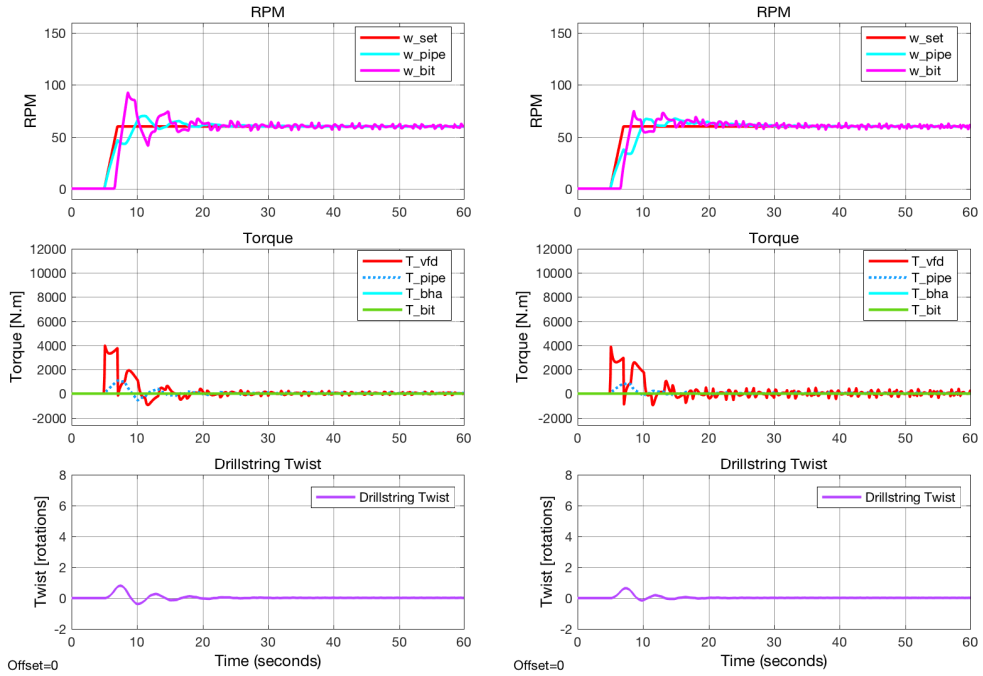

(a) 50% impedance matching. (b) 100% impedance matching.

Figure 5.15: Step response of the system with a stiff PI controller and 50% and 100% impedance matching with the bit off bottom.

By lowering the impedance matching target, attenuation takes longer, but has the benefit of removing much of the high frequency behavior. Even a 25% impedance matching controller outperforms a tuned PI controller, as shown in Figure 5.16.

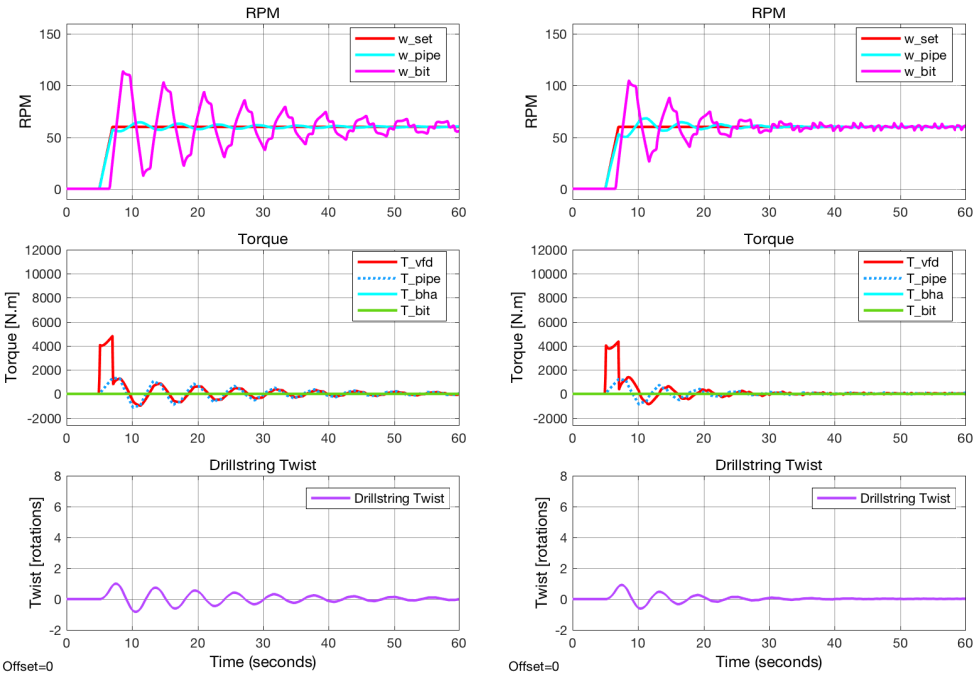

(a) 10% impedance matching. (b) 25% impedance matching.

Figure 5.16: Step response of the system with a stiff PI controller and 10% and 25% impedance matching with the bit off bottom.

Since an impedance matching controller is not tuned to a specific frequency, and is rather matched to the impedance of a connected drillpipe, performance remains robust with the bit on bottom. In this case, some of the high frequency noise is removed from the system due to energy being dissipated at the bit boundary, however low steady state noise remains in the torque signal, as shown in Figure 5.17.

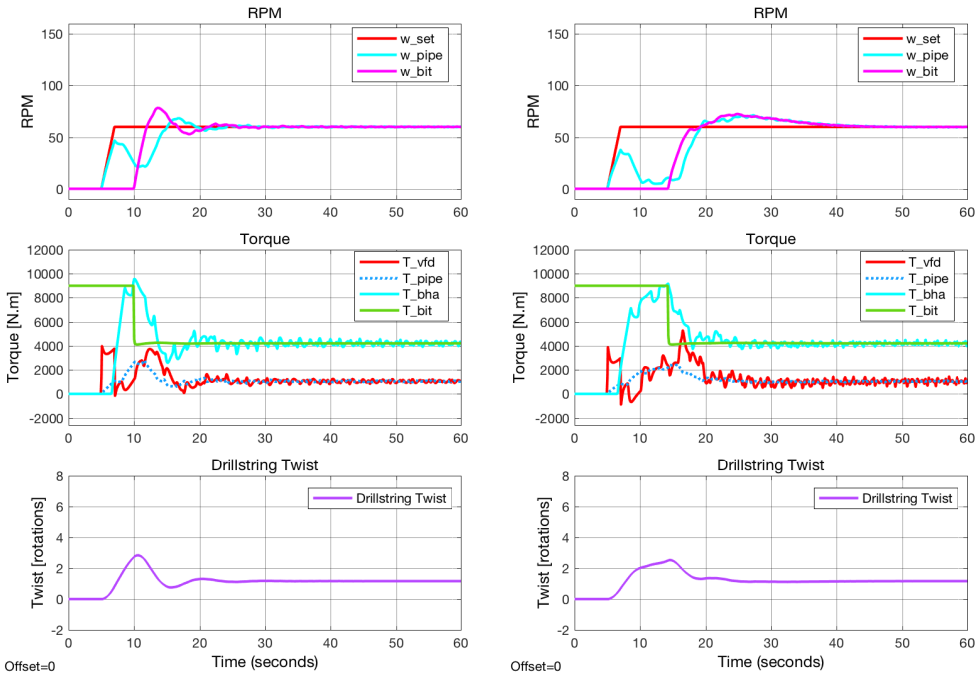

(a) 50% impedance matching. (b) 100% impedance matching.

Figure 5.17: Step response of the system with a stiff PI controller and 50% and 100% impedance matching and the bit on bottom.

On bottom, the 10% impedance matching controller outperforms the tuned PI controller and only is outperformed by the second order PI controller. Increasing matching to 25% eliminates this advantage, as shown in Figure 5.18. High frequency noise is no longer visible and thus presents a robust system which is able to mitigate stick-slip yet not inject high frequency noise. A quantification of this noise will be presented in a later section.

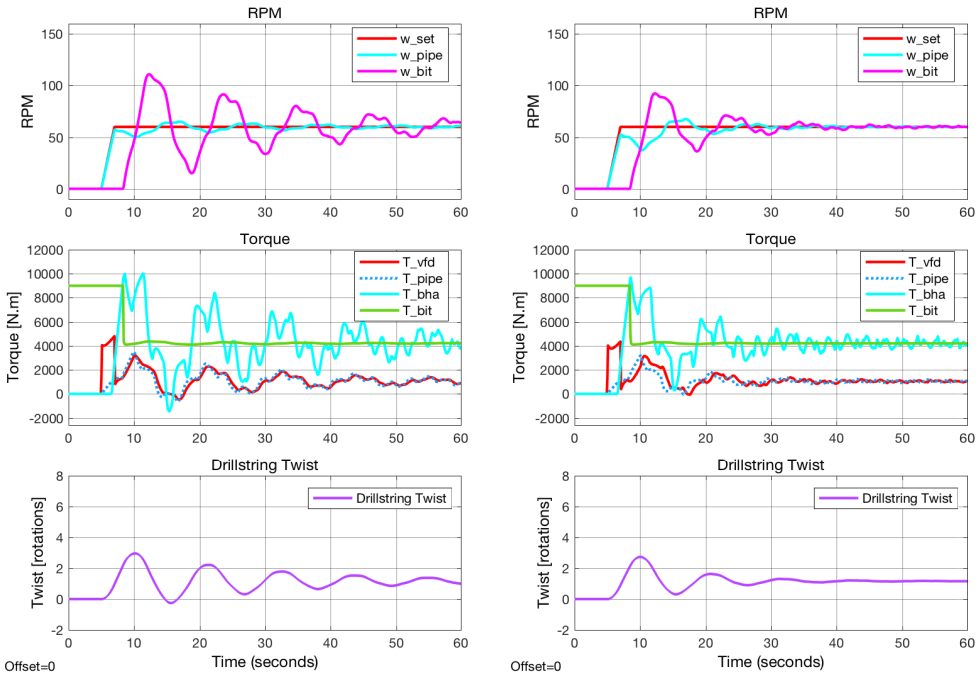

(a) 10% impedance matching. (b) 25% impedance matching.

Figure 5.18: Step response of the system with a stiff PI controller and 10% and 25% impedance matching and the bit on bottom.

5.6.5 Comparing Controllers

Broadening the simulation to 120 seconds of drilling time, the effectiveness of these four control methods can be directly compared.

A stiff PI Controller, shown in Figure 5.19, gives clear stick slip while maintaining a constant surface RPM. The continued stick cycle verifies model behavior and presents a torque curve that looks similar to those experienced in the field.

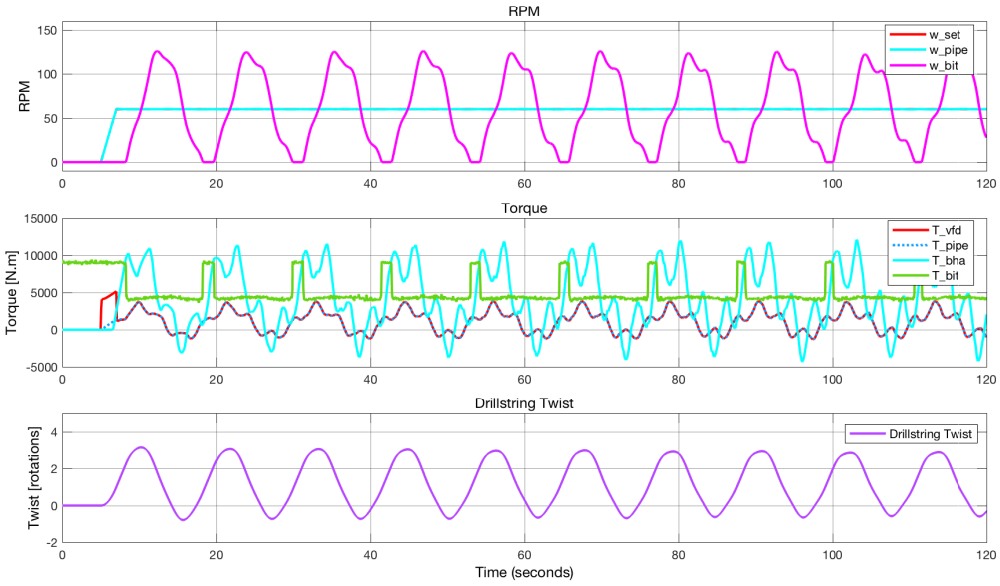

Figure 5.19: Stiff PI Controller with a $K_p = 38000$ and a $K_i = 100000$ showing clear stick slip.

A tuned PI Controller, shown in Figure 5.20, mitigates stick slip over 90 seconds by absorbing energy at the tuned frequency by modulating the top drive rpm at a set frequency (shown in light blue).

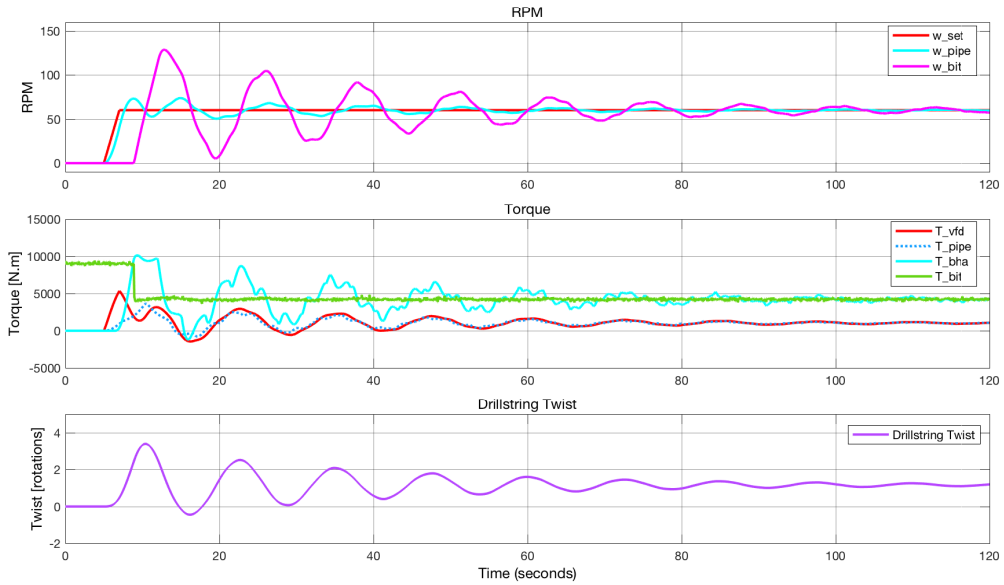

Figure 5.20: Tuned PI Controller with a $K_p = 850$ and a $K_i = 1061.65$ showing stick slip mitigation.

A second order tuned PI Controller, shown in Figure 5.21, mitigates stick slip over 40 seconds. The first mode is damped after three cycles, but the higher order mode is still visible for many more cycles – the tuned controller is only tuned to a single frequency.

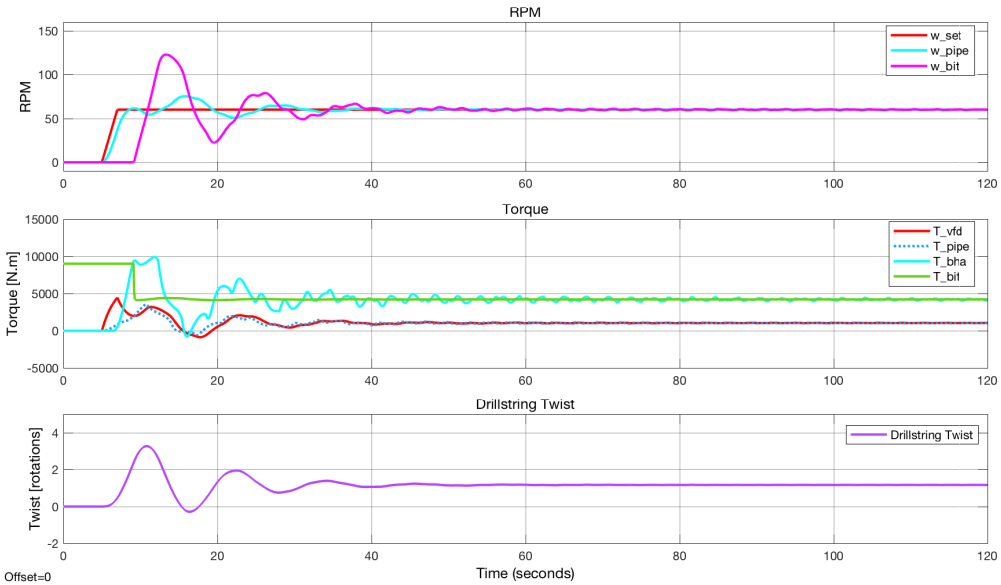

Figure 5.21: Tuned PI Controller with a $c_f = 100$ showing stick slip mitigation.

Performance of a first order PI can be matched with just 10% impedance matching at the surface controller, as shown in Figure 5.22. The second order PI controller can be matched with a 25% impedance matching controller, as shown previously.

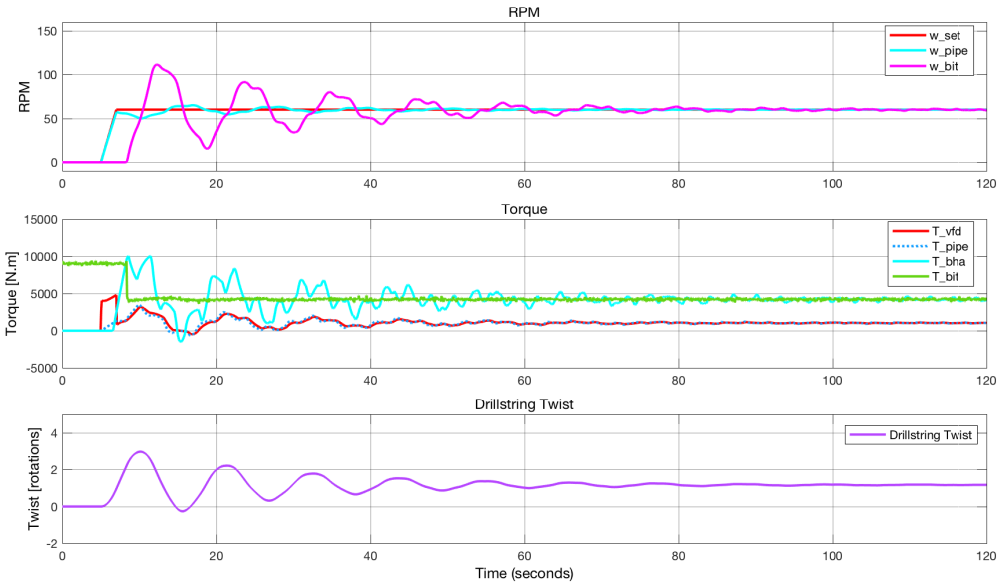

Figure 5.22: Impedance matching with 10% matching and a stiff PI Controller with a $K_p = 38000$ and a $K_i = 100000$ showing equivalent stick slip mitigation to a tuned PI Controller.

Performance can be greatly improved with just 50% impedance matching at the surface controller, as shown in Figure 5.23. Higher frequency noise injection in to the T_{vfd} signal is minimal and attenuates over time.

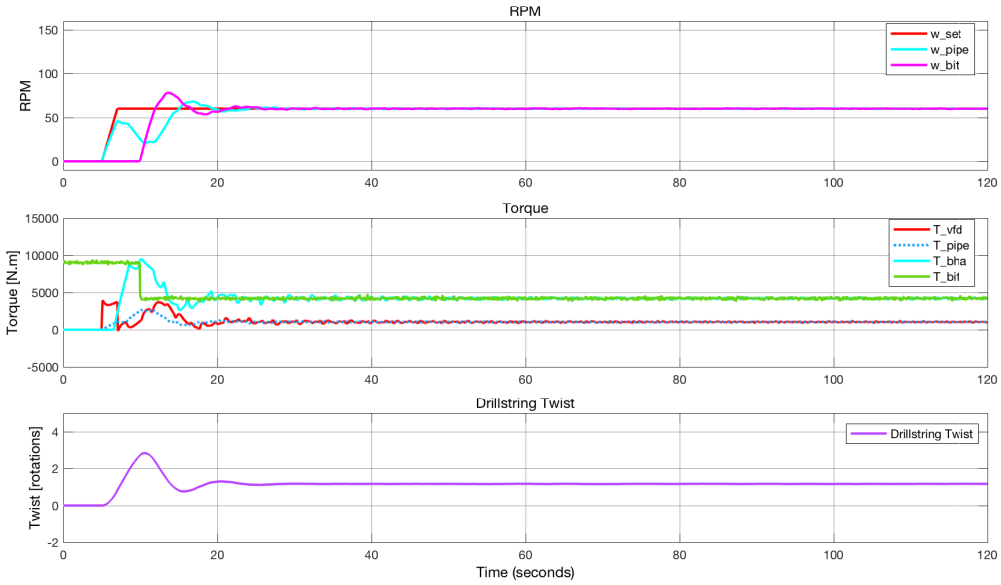

Figure 5.23: Impedance matching with 60% matching and a stiff PI Controller with a $K_p = 38000$ and a $K_i = 100000$ showing improved stick slip mitigation to a tuned PI Controller.

Performance can be improved further with 100% impedance matching at the surface controller, however, noise injection remains and does not attenuate with time, as shown in Figure 5.24. The source of this noise is shown in the next section.

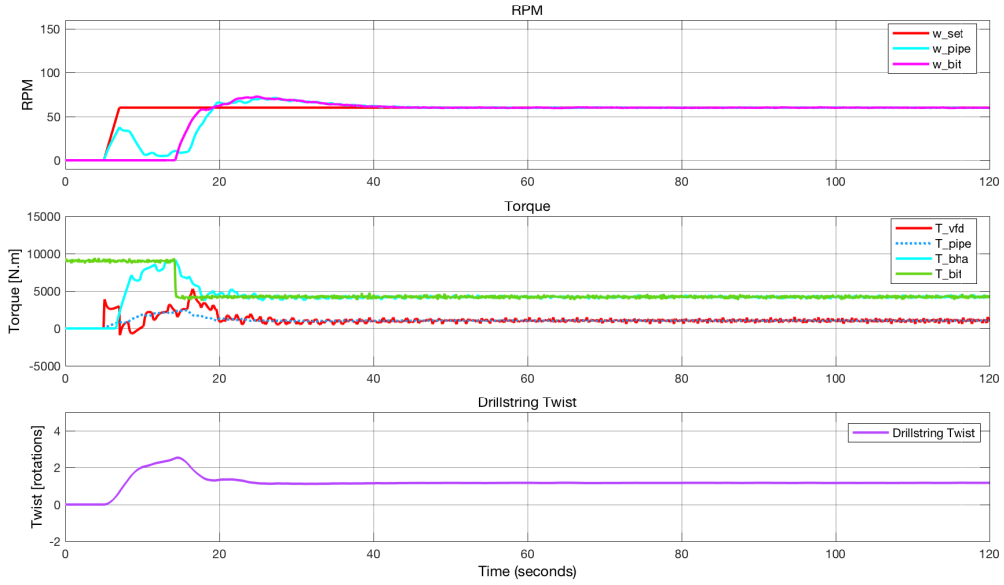

Figure 5.24: Impedance matching with 100% matching and a stiff PI Controller with a $K_p = 38000$ and a $K_i = 100000$ showing improved stick slip mitigation to a tuned PI Controller.

5.7 System Functionality

5.7.1 Top Drive Controller Impedance

The theory behind impedance matching may be applied to quantify the effectiveness of any top drive control system. The ability of the top drive to absorb and not reflect energy from the bit may be computed through the s-domain analysis of the control system components to give a system impedance as a function of frequency. By decoupling the drillstring model from the top drive and controller, the top drive impedance may be computed as the ratio of pipe speed, ω_{pipe}, to pipe torque, τ_{pipe}.

Using the simplified control system schematic in Figure 5.25, the transfer function for the system may be assembled:

$$\omega_{pipe} = \frac{1}{B_s}\left(-T_{pipe} - A_s D_s C_s \omega_{pipe}\right) \tag{5.25}$$

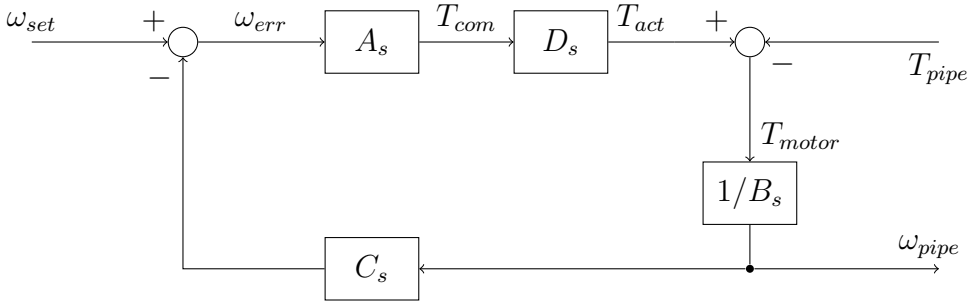

Figure 5.25: Control Diagram for a PID controller, VFD and top drive. T_{pipe} is the output of the drillstring model and ω_{pipe} is the input of a drillstring model.

Rearranging the equation and multiplying through by B_s

$$\omega_{pipe}\left(1+\frac{D_s A_s C_s}{B_s}\right) = -\frac{T_{pipe}}{B_s} \tag{5.26}$$

$$\omega_{pipe}\left(B_s + D_s A_s C_s\right) = -T_{pipe} \tag{5.27}$$

The impedance of the top drive, Z_{td} is simply the ratio of speed over torque:

$$Z_{td} = \frac{\omega_{pipe}}{T_{pipe}} = -\frac{1}{B_s + D_s A_s C_s} \tag{5.28}$$

and the top drive reflectivity, given the impedance of the connected drill pipe is z_0, is

$$R = \left|\frac{Z_{td}+z_0}{Z_{td}-z_0}\right|^2 \tag{5.29}$$

The sensitivity of the system is given by

$$S_s = -B_s \cdot Z_{td} = \frac{1}{1+\frac{D_s A_s C_s}{B_s}} \tag{5.30}$$

or is simply a function of the open loop gain:

$$OLG = \frac{D_s A_s C_s}{B_s} \tag{5.31}$$

In the case of the impedance matching controller, shown in Figure 5.26, a similar method may be used.

The transfer function of the system may be assembled as

$$\omega_{pipe} = \frac{1}{B_s}\left(-T_{pipe} + A_s D_s\left(-z_0 H_s L_s T_{pipe} - C_s \omega_{pipe}\right)\right) \tag{5.32}$$

$$\begin{aligned} &= -\frac{D_s A_s (z_0 HL)}{B} T_{pipe} \\ &\quad - \frac{D_s A_s C_s}{B_s}\omega_{pipe} - \frac{T_{pipe}}{B_s} \end{aligned} \tag{5.33}$$

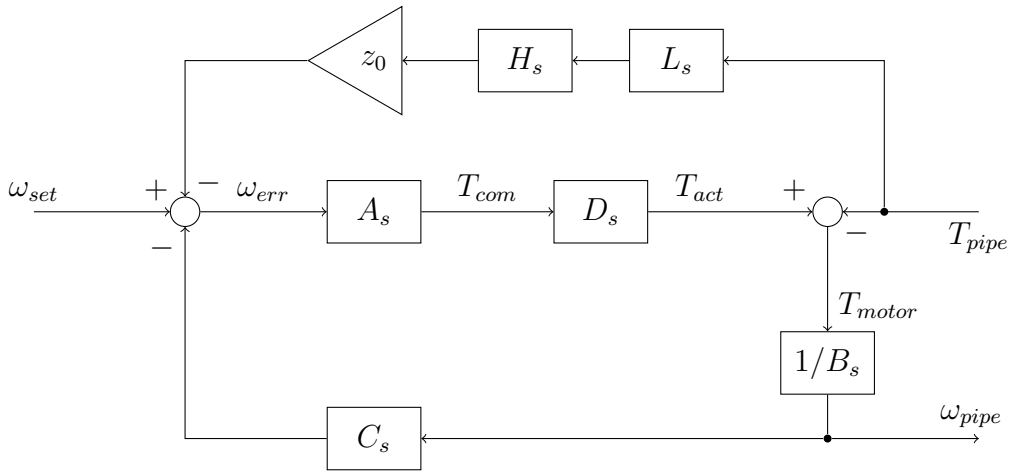

Figure 5.26: Control Diagram for an Impedance Matching PI controller, VFD and top drive. T_{pipe} is the output of the drillstring model and ω_{pipe} is the input of a drillstring model.

Rearranging the equation and multiplying through by B_s

$$\omega_{pipe}\left(1+\frac{D_sA_sC_s}{B_s}\right)=T_{pipe}\left(-\frac{D_sA_s(z_0H_sL_s)}{B_s}-\frac{1}{B_s}\right) \tag{5.34}$$

$$\omega_{pipe}\left(B_s+D_sA_sC_s\right)=T_{pipe}\left(-D_sA_s(z_0H_sL_s)-1\right) \tag{5.35}$$

The top drive impedance, Z_{td} is the ratio of speed over torque, which gives:

$$Z_{td}=\frac{\omega_{pipe}}{T_{pipe}}=-\frac{1+D_sA_s(z_0H_sL_s)}{B_s+D_sA_sC_s} \tag{5.36}$$

and system sensitivity is once again a function of the top drive impedance:

$$SS_{td}=-B_s\cdot Z_{td}=\frac{1+D_sA_s(z_0H_sL_s)}{1+\frac{D_sA_sC_s}{B_s}} \tag{5.37}$$

The reflectivity and sensitivity of each of the top drive controller may then be plotted for the frequency range f desired, where the Laplace variable s is given by

$$s=2\pi if \tag{5.38}$$

5.7.2 Drillstring Dynamic Response

The frequency response of the drillstring may be computed using the same transfer matrices as were used in Chapter 4, but with the appropriate constants for torsional rather than axial vibration. The transfer matrix, A_i,

$$\begin{pmatrix} \phi \\ \tau \end{pmatrix}_n = \begin{pmatrix} \cosh \gamma L & \frac{\sinh \gamma L}{i\omega Z_0} \\ i\omega Z_0 \sinh \gamma L & \cosh \gamma L \end{pmatrix} \begin{pmatrix} \phi \\ \tau \end{pmatrix}_{n-1} \tag{5.39}$$

where

$$\gamma = \sqrt{\frac{i\omega}{G}\left(i\omega\rho + \frac{C}{I_p}\right)} \tag{5.40}$$

$$Z_0 = I_p \sqrt{\frac{G}{i\omega}\left(i\omega\rho + \frac{C}{I_p}\right)} \tag{5.41}$$

with shear modulus G, polar moment of inertia I_p, density, ρ, and damping C, can be computed for each element within the drillstring and then combined into a drillstring transfer function, A,

$$\begin{pmatrix} \phi \\ \tau \end{pmatrix}_{surface} = \prod_1^n \mathcal{A}_i \begin{pmatrix} \phi \\ \tau \end{pmatrix}_{bit} \tag{5.42}$$

$$= \mathcal{A} \begin{pmatrix} \phi \\ \tau \end{pmatrix}_{bit} \tag{5.43}$$

The response of $\phi_{surface}$ and $\tau_{surface}$ are known at the top drive over the s-domain given a particular controller design, thus the behavior of the drillstring at the bit can be computed

$$\phi_{bit} = \mathcal{A}_{11}\phi_{surface} - \mathcal{A}_{12}\tau_{surface} \tag{5.44}$$

$$\tau_{bit} = -\mathcal{A}_{21}\phi_{surface} + \mathcal{A}_{22}\tau_{surface} \tag{5.45}$$

and the impedance of the drillstring is given by

$$Z_{ds} = \frac{\phi_{bit}}{\tau_{bit}} \tag{5.46}$$

$$= \frac{\mathcal{A}_{11}\phi_{surface} - \mathcal{A}_{12}\tau_{surface}}{-\mathcal{A}_{21}\phi_{surface} + \mathcal{A}_{22}\tau_{surface}} \tag{5.47}$$

$$= \frac{\mathcal{A}_{11}\frac{\phi_{surface}}{\tau_{surface}} - \mathcal{A}_{12}}{-\mathcal{A}_{21}\frac{\phi_{surface}}{\tau_{surface}} + \mathcal{A}_{22}} \tag{5.48}$$

$$= \frac{\mathcal{A}_{11}Z_{td} - \mathcal{A}_{12}}{-\mathcal{A}_{21}Z_{td} + \mathcal{A}_{22}} \tag{5.49}$$

Plotting the magnitude of Z_{ds} against frequency gives the drillstring mobility where structural modes appear as peaks. In the following series of plots, Figures 5.27 to 5.30, the evolution of these structure modes is shown for four different wellbore geometries at four different bit depths.

1. 4000 m vertical section to a 400 m build section to a horizontal lateral
2. 2000 m vertical section to a 400 m build section to a horizontal lateral
3. 2000 m vertical section to a 400 m build section to horizontal, then at 3000 m drop over 200 m to 45^o tangent
4. 2000 m vertical section to a 400 m build section to horizontal, then at 3000 m drop over 400 m back to vertical

In the following figures, Figures 5.27 through 5.30, the wellpath, plotted as horizontal displacement vs true vertical depth, is shown in the left subplot. In the right subplots, drillstring impedance, Z_{ds}, or drillstring mobility, is

plotted as a function of frequency. In the lower right subplot, the y axis is plotted on a linear scale, while the upper right subplot plots the y-axis on a log scale. This is done to show the prominence of the peaks while also showing the frequency response of the drillstring.

At a bit depth of 2000 meters, all four wellpaths coincide, as shown in Figure 5.27. The first structural mode is dominant and the higher modes are 20 times lesser. In this case, stick slip is primarily first mode and this is a case where a tuned PI controller may function effectively.

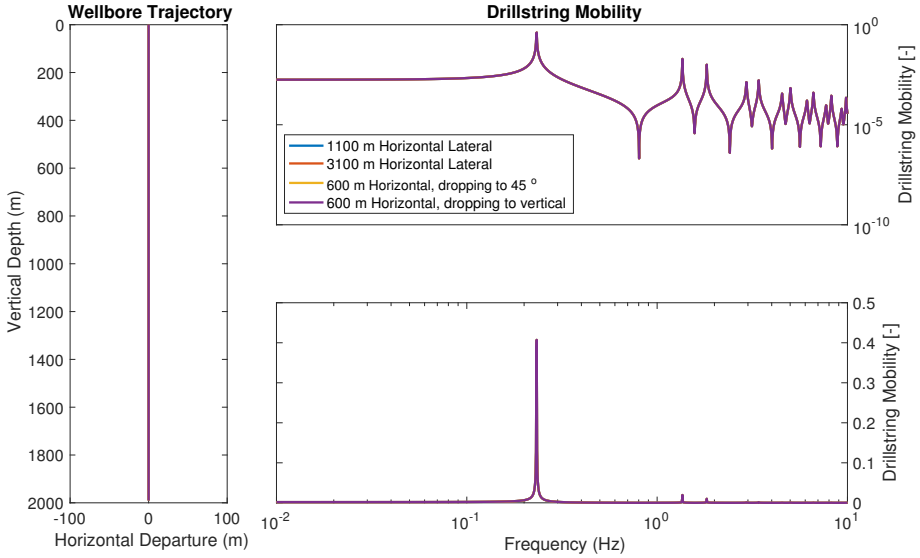

Figure 5.27: With the bit at 2000 meters, the wellpaths for the four wells are identical and the first mode is pronounced.

At a bit depth of 3000 meters, the four wellpaths have split into two groups, one group continuing vertically, the other landing into a lateral, as shown in Figure 5.28. The vertical wells continue to have a dominant first mode. The horizontal wellpaths have higher modes that are equal to or greater than the first mode, so these cases, higher order stick slip may expected with frequencies around 1-5 Hz, but peak magnitude is significantly reduced. In this case, the tuned PI controller will still function effectively in the vertical well, but will face difficulty, should stick-slip arise in the horizontal well, since higher modes are significant.

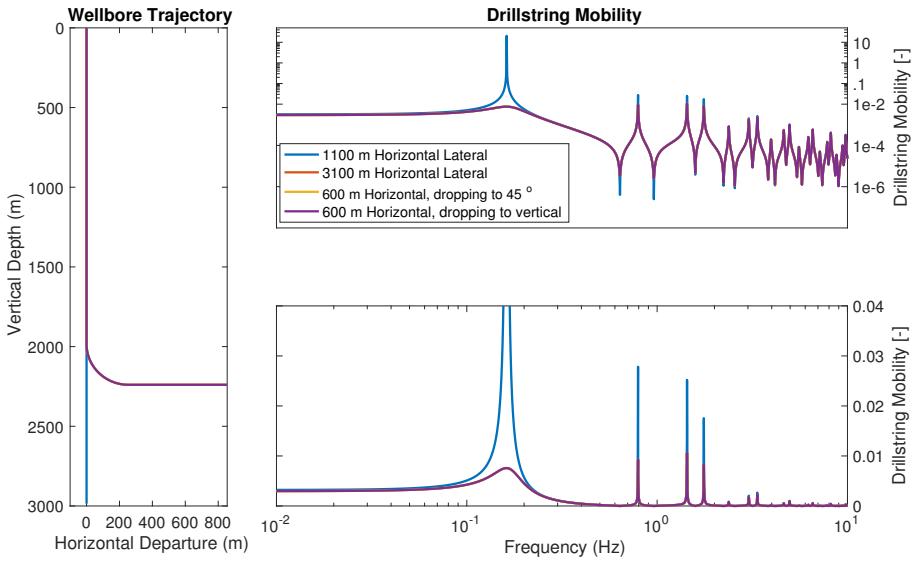

Figure 5.28: With the bit at 3000 meters, the wellpaths for the four wells have split into two groups – a horizontal well and a vertical well – and the first mode remains pronounced, especially in the vertical well.

At a bit depth of 4000 meters, all four example wellpaths have diverged, as shown in Figure 5.29. The vertical wellpath continues to have a dominant first mode, but the second mode is becoming significant. A tuned PI controller will no longer be as effective, since the first and second modes are of similar magnitude. In the horizontal well, the first several modes are of equal magnitude, while in the well which drops back to vertical, the first mode as well as the second, fourth and fifth modes are significant.

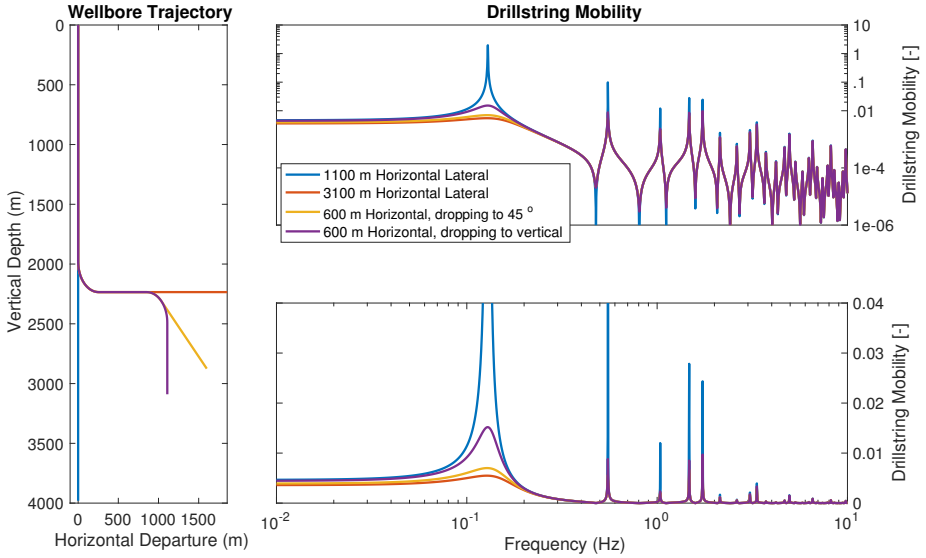

Figure 5.29: With the bit at 4000 meters, the first mode remains dominant for the vertical well. For the S-shaped well dropping to vertical, the first mode is dominant but higher order modes are of comparable magnitude. In the horizontal and S-shaped well dropping to a tangent, the first mode is significantly reduced.

At a bit depth of 5000 meters, the first mode of the well dropping back to horizontal is significant, along with several modes between 2 and 3 Hz, as shown in Figure 5.30.

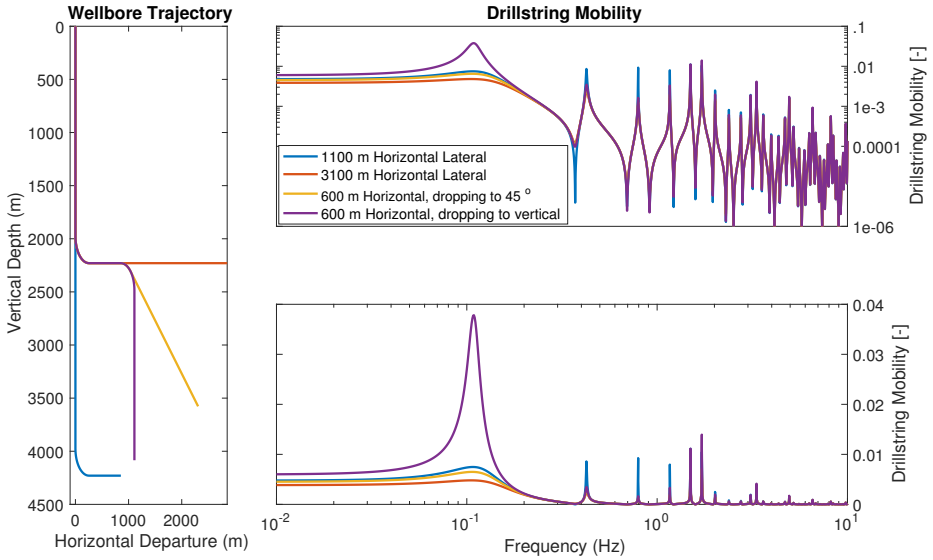

Figure 5.30: With the bit at 5000 meters, the first mode is significant for the S-shaped well dropping to vertical. In the deep horizontal well, the first mode is entirely damped out, but the second mode becomes dominant. In the other two case, all modes are reduced.

5.7.2.1 Evolution with Measured Depth

As can be seen in the previous section, there is an evolution in frequency of the structural modes as the drillstring length increases – as bit depth increases. This can be be visualized directly in the form of a spectrogram, which in this case, is easily assembled by stacking a series of drillstring mobilities at a sequence of depths. With the same drillstring used for each wellpath, the frequency evolution remains similar, however the magnitude of the resulting modes changes.

For a vertical well, shown in Figure 5.31, the first mode occurs at a lower frequency as depth increases and remains the most significant. The

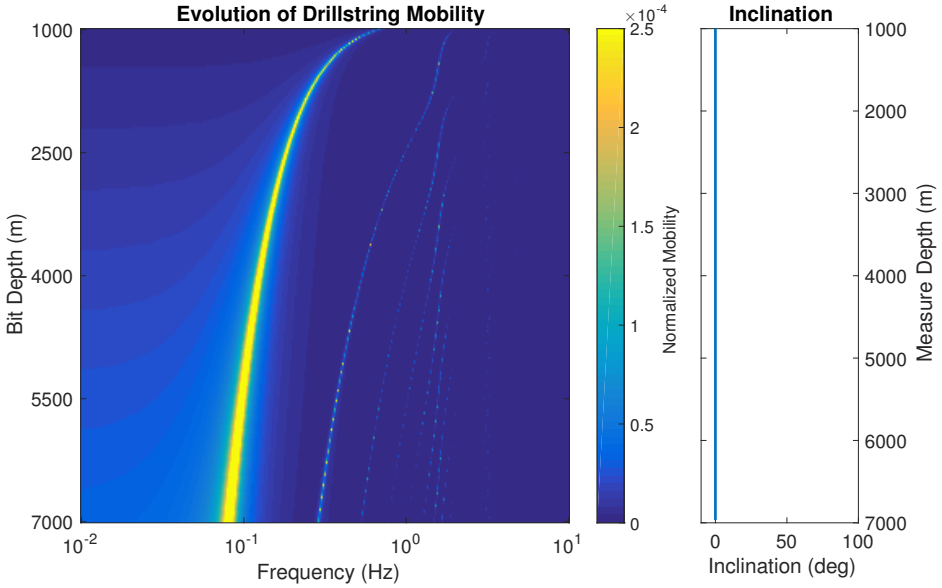

Figure 5.31: For a vertical wellbore, the evolution of the first mode of stick-slip is apparent and higher modes are nondominant.

second mode also shifts to a lower frequency with increasing depth and also increases in magnitude with depth, thus it can be expected that both the first and second modes of stick slip appear in vertical wells over 4000 meters while primarily the first mode will appear in wells less than 4000 meters with this drillstring.

For a shallow horizontal well, as shown in Figure 5.32, the first structural mode is significant through the vertical section and into the first part of the lateral before being damped out significantly. The second mode then becomes of the same magnitude as the first mode through the length of the lateral and may give rise to higher frequency stick slip.

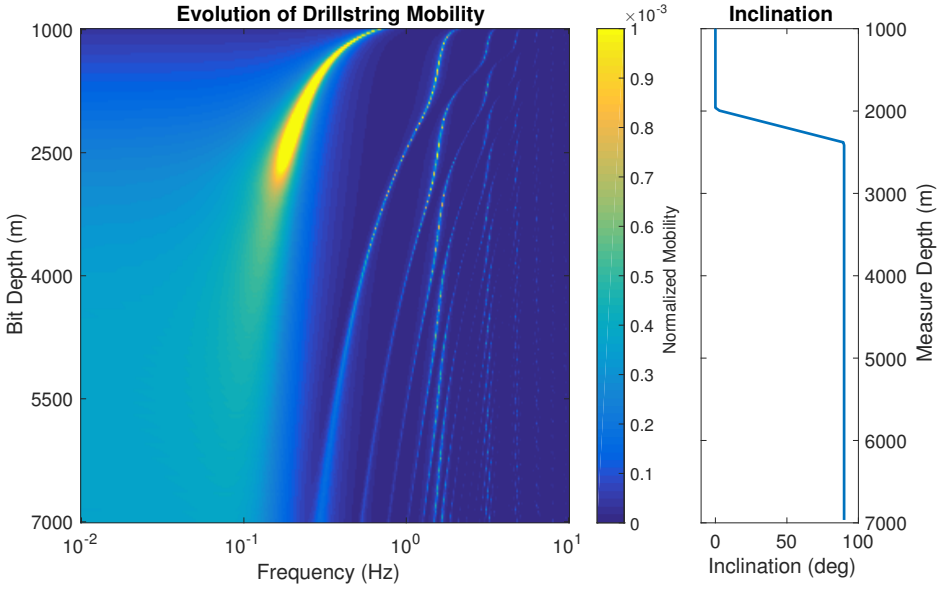

Figure 5.32: For a shallow horizontal well, the first mode of stick-slip is rapidly damped once in the lateral, and the second mode becomes the dominant mode.

In a deeper horizontal well, as shown in Figure 5.33, the first structural mode is significant once again throughout the vertical before being completely damped out in the horizontal. The second mode is also well damped.

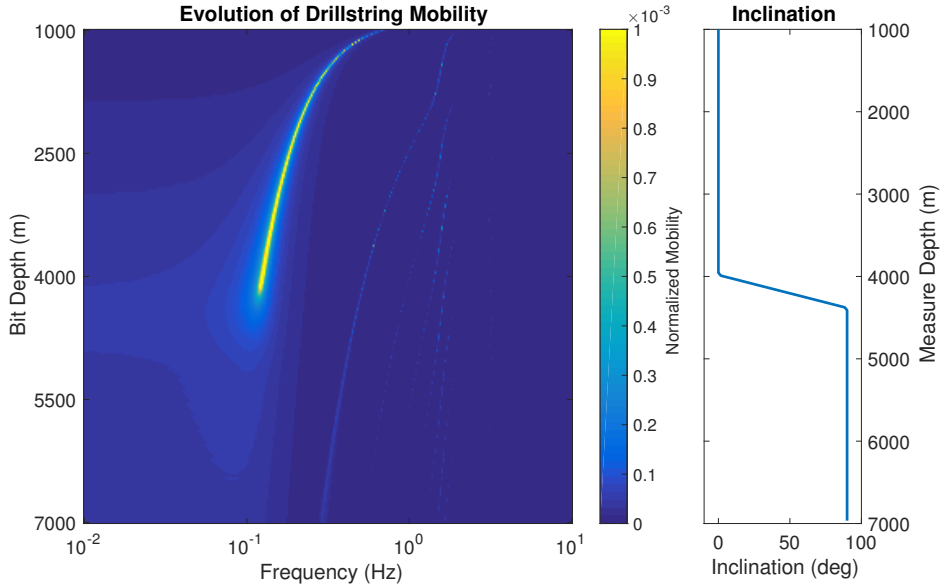

Figure 5.33: For a deeper horizontal well, the first mode of stick-slip is damped in the horizontal section, and higher order modes do not become dominant.

In the well dropping to a 45^o tangent, as shown in Figure 5.34, the first mode remains significant in the vertical section of the well, is damped slightly in the horizontal and then remains present throughout the tangent section due to continued friction with the wellbore wall.

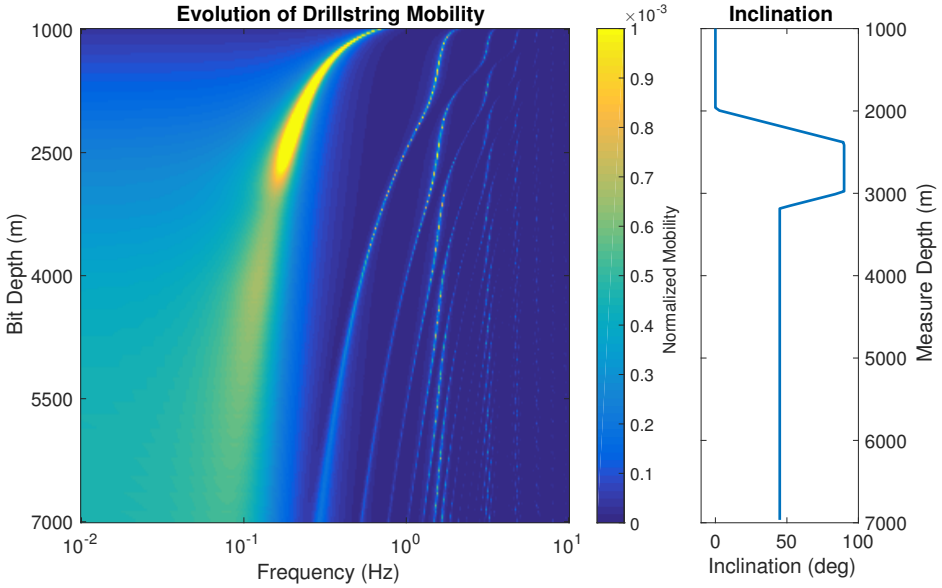

Figure 5.34: For a shallow S-shaped well dropping to a 45^o tangent, the first mode becomes reduced while the second and third modes become significant.

In the well dropping back to vertical after a short horizontal section, as shown in Figure 5.35, the first mode briefly diminishes in the horizontal section before coming back with a vengeance in the second vertical section. This type of wellpath is expected to generate significant stick slip, which has been observed in the field in wells with slender drillstrings and intermediate horizontal or tangent sections.

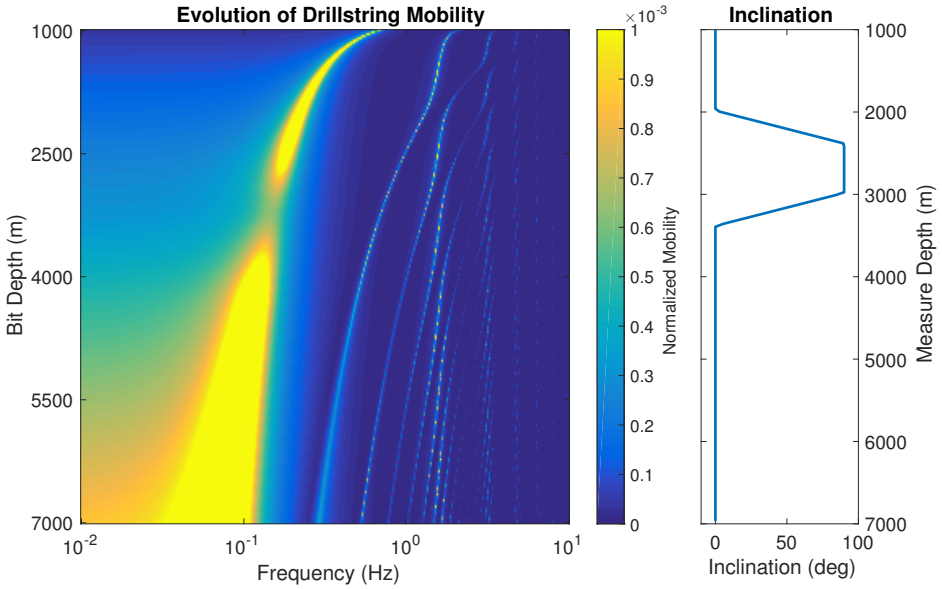

Figure 5.35: For an S-shaped well dropping back to vertical, the first mode becomes broad and remains dominant.

5.7.3 Controller Assessment

Understanding the structural modes of the drillstring within the wellbore in question allows the effectiveness of the various control strategies to be fully understood. Tuned controllers must be retuned for each depth to ensure the target frequency is that of the first structural mode, but these controllers fall victim to higher order modes once they appear. Untuned controllers maintain their performance throughout the life of the well and thus increase in effectiveness as the bit gets deeper and the frequency of structural modes lessens. This effectiveness is explored visually in the following two sections.

5.7.3.1 PI Controllers

PI controllers are either designed to reject all disturbance – or be stiff – and return the system to the setpoint, or can be tuned to a specific frequency. This behavior is clearly shown in the reflectivity plots. Based on the values chosen for K_I and K_p, the control system dampens a specific range of frequencies. Thus, a PI controller may be tuned to dampen the first structural mode and eliminate first order stick slip, but since the second mode lies outside the tuned band, higher order modes continue undamped, as shown in Figure 5.36.

The top drive sensitivity is another measure that characterizes the controller behavior. At low frequencies, sensitivity is low before approaching 1 at the tuned frequency. When sensitivity is low, the reaction of the top drive to a disturbance from the drillstring – a change in pipe torque – is small. When

sensitivity is 1, there is a reaction of equal magnitude from the top drive as the disturbance from the drillpipe. In the case of the second order PI controller, sensitivity is greater than 1 at the targeted frequency since controller aggression is higher. If sensitivity is greater than 2, problems may arise from controller activity.

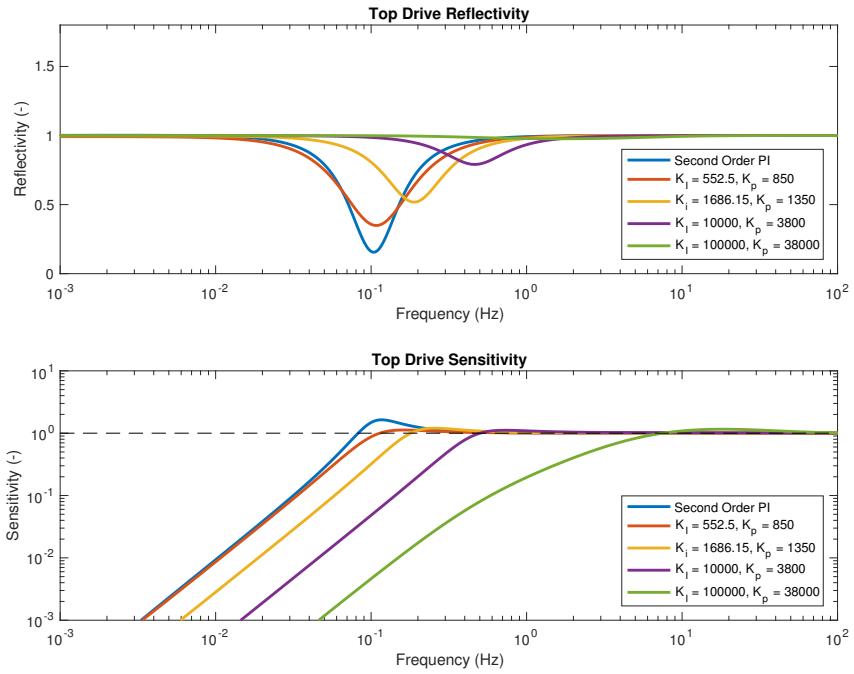

Figure 5.36: Top drive reflectivity and sensitivity of the PI controllers shown in this section.

5.7.3.2 Impedance Matching Controller

Impedance matching controllers have a much wider bandwidth of frequencies where top drive reflectance is less that one, however, this broader functionality comes at the cost of a much higher system sensitivity in the frequency band of interest as well as reflectivities higher than one at higher frequencies, as shown in Figure 5.37.

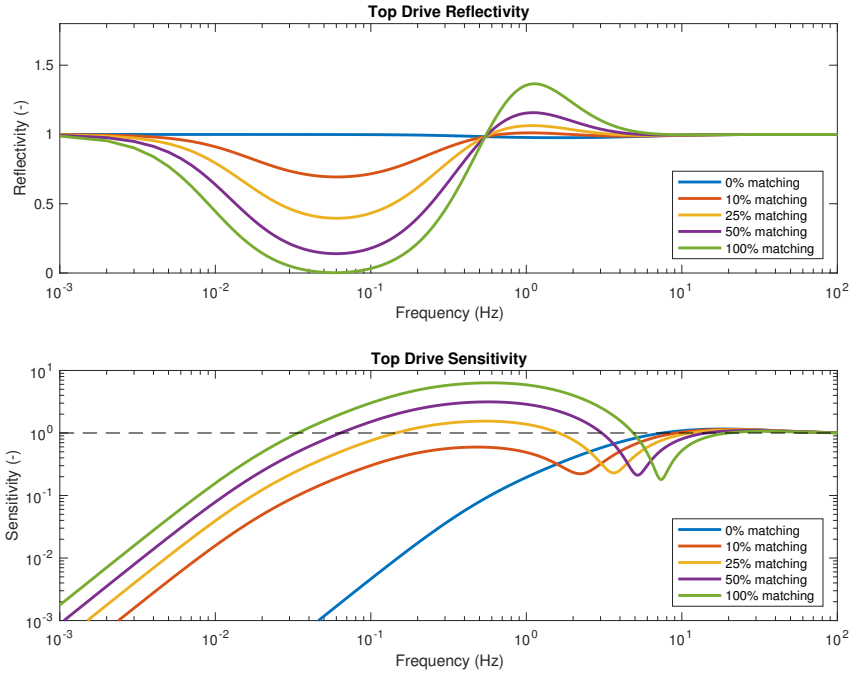

Figure 5.37: Top drive reflectivity and sensitivity of the impedance matching controllers shown in this section.

The high frequency noise which appears in the torque signal of the impedance matching simulations is a direct product of the high sensitivity

and reflectivity higher than one. As it was shown in the time domain plots, the 10% and 25% matching systems injected little or no high frequency noise into the T_{vfd} signals, which comes from their respective reflectivities remaining near 1 above a frequency of 0.5 Hz and their sensitivities remaining below 2. In the case of 50% matching, high frequency noise is seen since the reflectivity of the system has a maximum of 1.2 at 1 Hz, the frequency at which the noise is seen. It attenuates over time since the damping within the drillstring is greater than the injection of energy at the top drive. This is not true for the 100% damping case with its peak of 1.45 at 1 Hz.

5.8 Conclusion

The chapter presented the framework necessary to evaluate the performance of stick-slip mitigation controllers, both in the time domain to visualize performance, and in the frequency domain, to evaluate controller bandwidth. Previous work did not consider the delays inherent in the drillstring system, did not model higher structural modes or did not take into account wellbore trajectory. By combining an understanding of the reflectivity of the top drive due to control system operation with the dynamics of the drillstring, it is possible to first evaluate and then improve the function of installed or proposed control systems.

5.9 Further Work

The effectiveness of proposed or deployed stick-slip mitigation systems can be thoroughly assessed, both the time and frequency domains in varied wellbores using the methods presented in this chapter. This presents the possibility of

- tuning a control system to mitigate the expected drillstring modes based on a proposed wellpath, which may be different from a vertical wellpath.
- comparing different installed controllers on a drilling rig to choose the one best suited to the current wellpath and drillstring.
- quantifying the behavior of a newly proposed system and evaluating designer claims by comparing the performance envelope with existing and idealized control systems.

Chapter 6

A Feasibility Study in Drillstring Imaging

6.1 Introduction

Borehole surveys present a sparse view of borehole geometry that give an indication of tortuosity and borehole quality, but cannot give an detailed view of contact points along a borehole. In areas of low dogleg severity (DLS), these points represent areas of increased friction, leading to a reduction of torque and weight on bit transfer. In areas of high DLS, especially if the radius of curvature is small, these points present regions of the wellbore prone to problems, including increased chances of hang ups of both drillpipe and casing. To avoid placing additional equipment in the drillstring, there is a desire to implement solutions from the surface that have the capability to image these contacts using torsional signals sent from surface.

This chapter begins with a literature review of methods used in a variety of industries to conduct imaging of features using various types of waves, including the use of pressure or acoustic waves for seismic imaging, non-destructive testing and sonar. Algorithms used within the radar and medical communities are also reviewed, specifically for the benefits of signal filtering

and feature detection. Detection limits, feature contrast and signal to noise ratios are also presented as they pertain to imaging and feature detection.

Three broad groups of methods are investigated: a direct mapping of time to space, estimation of the system transfer function, and model based inversion. The first method allows for the characterization of reflections in the space axis without the need for a priori knowledge of the system through the use of signal processing techniques of wave reflections. The second attempts to estimate the transfer function of the system and then applies a band limited impulse to estimate the impulse response. The third generates a best fit model of the data by fitting the response to a model based on the wave equation. The advantages and disadvantages of each are discussed while being applied to three setups: transverse and axial waves in a hanging steel beam, torsional waves in a laboratory simulation, and drilling operations on a land based drilling rig.

Direct mapping from time to space is shown to be effective in the simple system of a simple hanging steel beam. Dispersion compensation of flexural waves presents the clearest image due to varied wave velocities of flexural waves presenting the widest bandwidth input. Axial waves in the beam also show a clear image, but are limited by the spatial resolution limit imposed by the Nyquist criteria and by the input bandwidth. System transfer function estimation shows promise, especially when applied to datasets with injected white noise. Model inversion is shown to produce accurate data fits and plausible

impedance maps, but is only as good as the models being fitted, and requires a priori knowledge of boundary conditions and system properties.

6.2 Literature Review

Reflections of pressure, acoustic or electromagnetic waves are used in many applications to image the internal structure of objects and materials. These applications range from seismic imaging of subsurface geologic features to nondestructive testing of structures, buildings or machinery. Other applications include ultrasound medical imaging of internal organs and sonic imaging, both through air using ultrasonics or underwater. All these applications carry a vast literature of methods and best practices to improve signal quality and feature detection. A broad overview will be presented in this literature review but several methods will be highlighted and then applied in the following sections.

One class of methods used for feature detection is the direct mapping of the time axis for a reflected signal to a spatial axis through the use of the estimated wave velocity. In homogeneous media, this is a simpler task since wave velocity is constant, but in nonuniform media the task becomes increasingly complex. In simplified systems, direct mapping can be used for ultrasonic imaging of small scale soil models, such as those presented by Lee and Santamarina and Coe and Brandenberg, or through phase shift analysis as presented by Gazdag et al. (Lee and Santamarina, 2005; Coe and Brandenberg, 2010; Gazdag, 1978). Pulse inversion, as presented by Shen et al.,

can be used to image non-linearities in media through the use of two inputs: a positive gaussian pulse followed by the inverted pulse to image the odd numbered modes of a system (Shen et al., 2005). Image resolution may also be improved through the uses of filtering to improve the signal to noise ratio, but coded inputs also help. Chirp signals may used to improve image contrast, as presented by Santosa and Vogelius while match filtering may used in conjunction with a pseudo random input to detect reflections within noise (Santosa and Vogelius, 1990).

A second class of methods uses model fitting of the system response based on the system input, or simply model inversion. This method is often used in seismic imaging since both the impedance contrasts between stratigraphic layers as well as wave velocities need to be estimated. A series of methods for one dimensional inversion based on a single emitter and receiver are presented in a review paper by Newton (Newton, 1981). More advanced inversion may be conducted through the application of Gaussian processes, as presented in a comprehensive book by Rasmussen and Williams, or through Bayesian system identification, as presented by Green and Worden, to improve model fitting (Rasmussen and Williams, 2006; Green and Worden, 2014).

The detection capabilities of all these methods are limited by the bandwidth of the inputs used, the sensing frequency, the impedance contrasts themselves and feature spacing. These will be discussed at length in the following sections, but overviews may be found in reviews written by Cheney and Isaacson, as applied to electrical and conductive impedance imaging, by Smith

and Webb, as applied to medical imaging, and by McCan and Forde and by Drinkwater and Wilcox, as applied to non-destructive testing (Cheney and Isaacson, 1992; Smith and Webb, 2011; McCann and Forde, 2001; Drinkwater and Wilcox, 2006).

6.3 Theory

In this section, the wave velocity of axial, torsional and flexural waves will be derived from first principles and then applied to quantifying resolvable feature size and impedance contrast.

6.3.1 Wave Velocities

The drillstring is assumed to have a constant density, shear modulus and Young's modulus along its length. This allows wave velocity to be constant and reduces model complexity.

6.3.1.1 Transverse or flexural waves

Transverse waves in a beam have different group and phase velocities, with the group velocity being twice the phase velocity. This can easily be shown by derivation if we assume that the wave equation has a solution of the form $u = \bar{u}e^{i(\omega t - \beta z)}$ and the system conforms to the Euler-Bernoulli beam model.

$$EI\frac{\partial^4 u}{\partial z^4} + \rho A\frac{\partial^2 u}{\partial t^2} = 0 \tag{6.1}$$

$$(EI\beta^4 - \rho A\omega^2)\bar{u} = 0 \tag{6.2}$$

Which gives the dispersion relation

$$\omega = \beta^2 \sqrt{\frac{EI}{\rho A}} \tag{6.3}$$

Now, the group velocity, v_g, and phase velocity, v_p, may be calculated from the dispersion relation as

$$v_g = \frac{d\omega}{d\beta} = 2\beta \sqrt{\frac{EI}{\rho A}} = 2\sqrt{\omega} \left(\frac{EI}{\rho A}\right)^{\frac{1}{4}} \tag{6.4}$$

$$v_p = \frac{\omega}{\beta} = \beta \sqrt{\frac{EI}{\rho A}} = \sqrt{\omega} \left(\frac{EI}{\rho A}\right)^{\frac{1}{4}} \tag{6.5}$$

6.3.1.2 Axial and torsional waves

Following from the derivation of the wave equation in Chapter 3, the wave velocities of axial, v_a, and torsional, v_t, waves are given by

$$v_a = \sqrt{\frac{E}{\rho}} \tag{6.6}$$

$$v_t = \sqrt{\frac{G}{\rho}} \tag{6.7}$$

where G is the shear modulus, E is Young's modulus, and ρ is the density of the material.

6.3.2 Resolvable Features

Given the velocity for a wave and the sampling frequency, the maximumly resolvable feature is given by the Nyquist criteria for spatial resolution

$$l_{feature} = 2 \cdot c_{wave} \cdot \Delta t_{sample} \tag{6.8}$$

For the setups considered in this writeup, the relevant parameters are

- Flexural waves in 7.2 meter beam sampled at 50kHz ($c_{wave} < 2436.2ms^{-1}$): < 0.097 m
- Axial waves in a 7.2 meter beam sampled at 50kHz ($c_{wave} = 5188.7ms^{-1}$): 0.208 m
- Torsional waves measured at 100Hz at the drilling rig ($c_{wave} = 3202.6ms^{-1}$): 64.05 m
- Torsional waves measured at 125Hz on the laboratory drillstring setup ($c_{wave} = 3202.6ms^{-1}$): 51.24 m of simulated length

This assumes that the input has sufficient bandwidth to excite all frequencies, which necessitates a square wave or pulse with sharp edges. This is not possible in many situations, due to ramp limitations on motor acceleration, so the spatial resolution is reduced to the bandwidth of the input.

6.3.2.1 Feature contrast

The ability to image changes in impedance is dependent on the contrast in impedances across the interface. Taking the reflectivity to be

$$\Gamma = \frac{z_1 - z_2}{z_1 + z_2} \tag{6.9}$$

and taking $z_2 = az_1$, the reflectivity as a function of impedance contrast may be plotted and is shown in Figure 6.1.

Which means for an impedance contrast of 100% ($z_2 = 2z_1$ or $z_2 = \frac{1}{2}z_1$), the reflectivity is only $\Gamma = \frac{1}{3}$, such as for the transition from 16.25 lb/ft 5" drillpipe to 25.6 lb/ft 5" drillpipe.

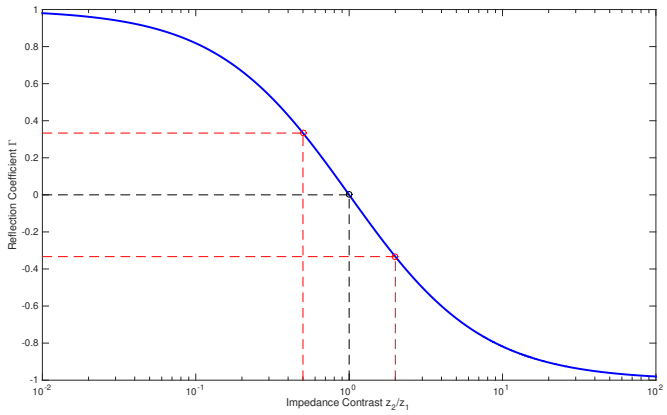

Figure 6.1: Reflectivity as a function of impedance contrast. Red dashed lines indicate a 100% change in impedance across an interface.

6.3.2.2 Sensor location

On drilling rigs deployed in the field, rotary speed is either measured with a spindle-mounted encoder or using the variable frequency drive. Torque is typically measured using a current integration algorithm in the variable frequency drive. From this setup, pipe rotary speed is equal to top drive rotary speed due to a stiff system. However, measured torque does not equal pipe torque due to the inertia of the top drive itself. An estimate of pipe torque is given by

$$\tau_{pipe} = \tau_{vfd} - J_{td}\ddot{\phi} = \tau_{vfd} - j\omega J_{td}\dot{\phi} \tag{6.10}$$

This inertial torque has a frequency dependent behavior, and thus the interface between the drillstring and the top drive inherently has a reflectivity coefficient.

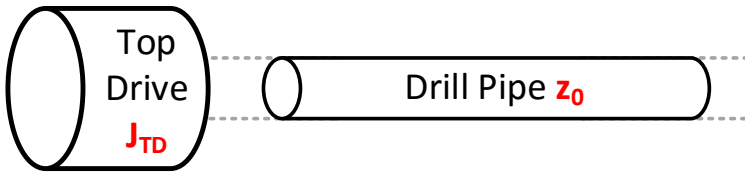

Figure 6.2: Top drive and drill pipe interface.

Taking the impedance of an element to be:

$$z = \frac{\dot{\phi}}{\tau} \tag{6.11}$$

The reflection coefficient, Γ, can be calculated using:

$$\Gamma = \frac{z_0 - z_{td}}{z_0 + z_{td}} = \frac{z_0 - \frac{1}{j\omega J_{td}}}{z_0 + \frac{1}{j\omega J_{td}}} \tag{6.12}$$

However, this formulation for motor torque only applies at high frequencies since steady state torque, needed to overcome friction in the system, is not included. If a simplified velocity dependent friction is included, the top drive impedance becomes

$$\tau_{td} = j\omega J_{td}\dot{\phi} + \tau_{fric}\dot{\phi} \tag{6.13}$$

At high frequencies, the motor impedance is dominated by the motor inertia, thus reducing the transmittance of high frequency signals to the torque sensor which is located above the top drive in the variable frequency drive. Example

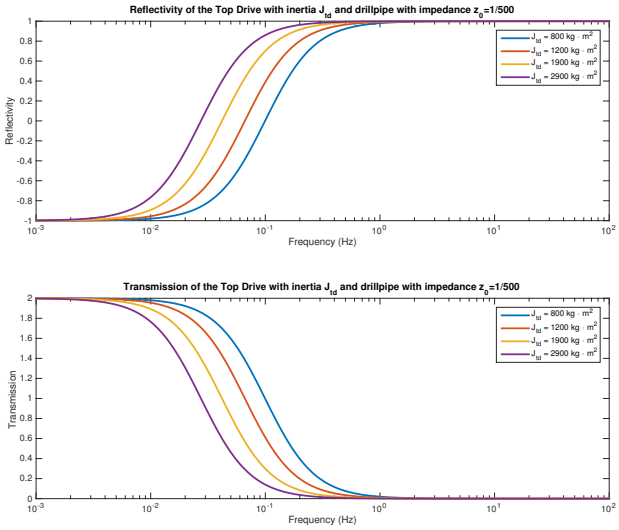

(a) Reflectivity and Transmissivity due to top drive inertia

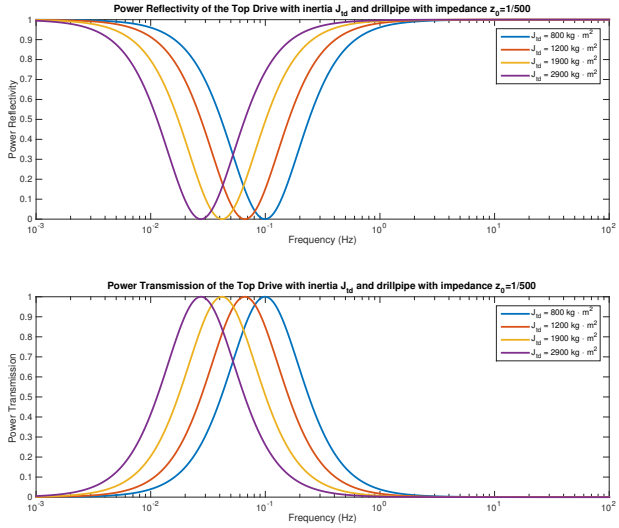

(b) Power Reflectivity and Transmissivity due to top drive inertia

Figure 6.3: Reflectivity and Transmissivity of the top drive considering just inertial torque for a variety of top drive inertias (6.3a and 6.3b.)

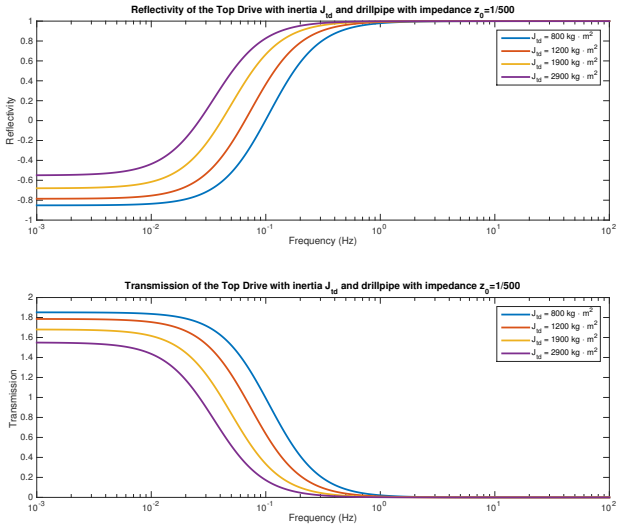

(a) Reflectivity and Transmissivity due to top drive inertia with a velocity dependent frictional torque.

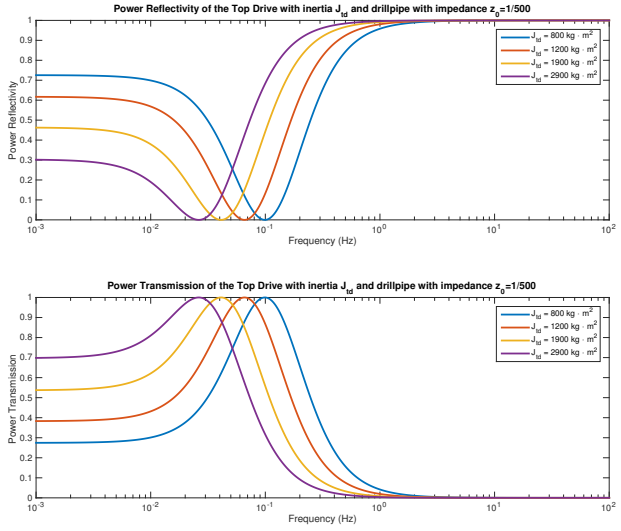

(b) Power Reflectivity and Transmissivity due to top drive inertia with a velocity dependent frictional torque.

Figure 6.4: Reflectivity and Transmissivity of the top drive considering just inertial torque for a variety of top drive inertias with a simplified velocity dependent friction (6.4a and 6.4b).

reflection and transmission coefficients for a drill pipe with an impedance of 1/500 and a range of top drive inertias is presented in Figure 6.3. High frequency signals will be reflected, and the cut-off frequency is lower the larger the inertia of the top drive.

6.4 Methods

Two groups of methods are described in the following section: a direct time-space mapping and a model based inversion method.

6.4.1 Space-time mapping

Direct mapping of the temporal axis to a spatial axis allows for the a system to imaged directly without any a priori knowledge of the configuration. However, resolution is limited to the bandwidth of the input without the application of filtering. Low pass, band pass and match filtering will be discussed and applied.

6.4.1.1 Transverse Waves

For transverse waves traveling in a beam, high frequency waves will arrive first, followed by the the slower low frequency waves. Dispersion compensation, as presented by Wilcox, can then be used to resolve reflections off of impedance changes by normalizing arriving waves based on their frequency Wilcox (2003). The general procedure may be described as:

1. Obtain signal $y(t)$, which is the response of the system as measured by an accelerometer

2. Compute the FFT $Y(\omega) = \mathcal{F}(y(t))$ of the signal

3. Linearly resample $Y(\omega) \rightarrow H(k)$ based on a remapping of ω to k, each frequency's phase velocity to determine the mapping into the wave number domain for space

4. Compute the group wave velocity, $c_g(\omega)$ of each ω in $Y(\omega)$.

5. Multiply $H(k)$ with v_g to determine wave amplitude.

6. Apply the reverse FFT $h(x) = \mathcal{F}^{-1}(H(k))$ to find the space mapped wave response

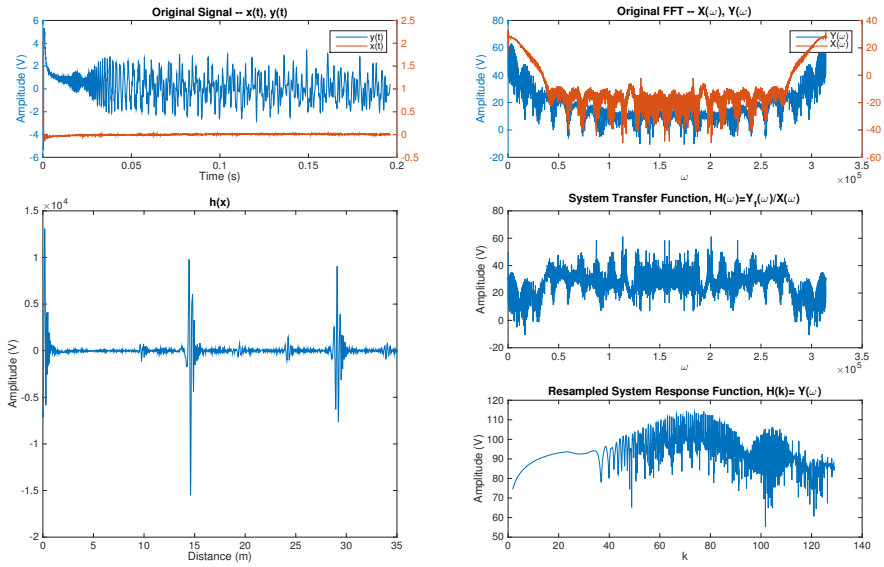

Figure 6.5: Visualizing the steps for dispersion compensation for flexural waves, showing (clockwise from the top for each subfigure), the input $x(t)$ and output $y(t)$, their respective FFTs, $X(\omega)$ and $Y(\omega)$, the system transfer function $H(\omega) = Y(\omega)/X(\omega)$, the remapping of $Y(\omega) \rightarrow H(k)$ and the space mapped wave response $h(x)$.

6.4.1.2 Axial and Torsional Waves

The procedure to transform time based signals is as follows:

1. Obtain signals $x(t)$, the input into the system and $y(t)$ which is the response of the system as measured
2. Compute the wave velocity, v_a or v_t
3. Rescale the time axis of $x(t)$ and $y(t)$ to a distance axis by multiplying by v_a or v_t

For problems with heterogeneous media, wave velocity changes as a function of distance; however, in this case, the wave velocity within steel is assumed to be constant.

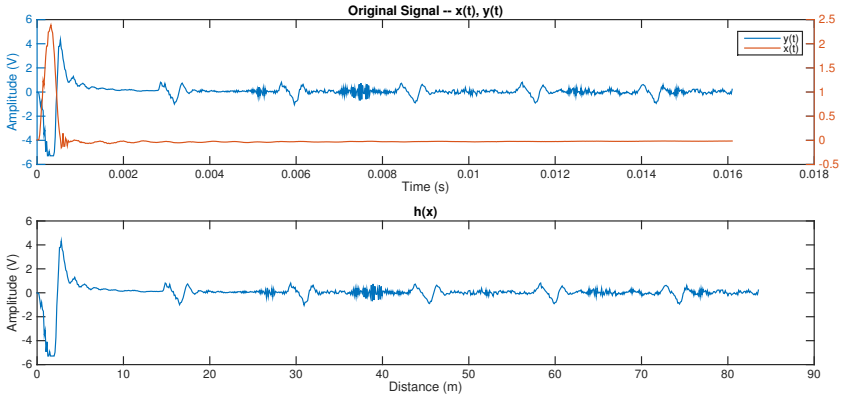

Figure 6.6: Direct time-space mapping of axial and torsional waves, in the case of constant wave velocity, simply involves rescaling the time axis to a spatial axis.

6.4.1.3 Filtering

Several filtering methods may be used to improve signal quality. Those used in the following sections are detailed below.

- Matched Filtering – the optimal linear filter for maximizing the signal to noise ratio, it is the correlation of the input signal, or template, with the unknown signal

    1. Let $x_r(t)$ be the time reversed, truncated version of the original input $x(t)$, truncated to just the input pulse
    2. Compute $y_f(t)$ as $y(t)$ filtered with $x_r(t)$

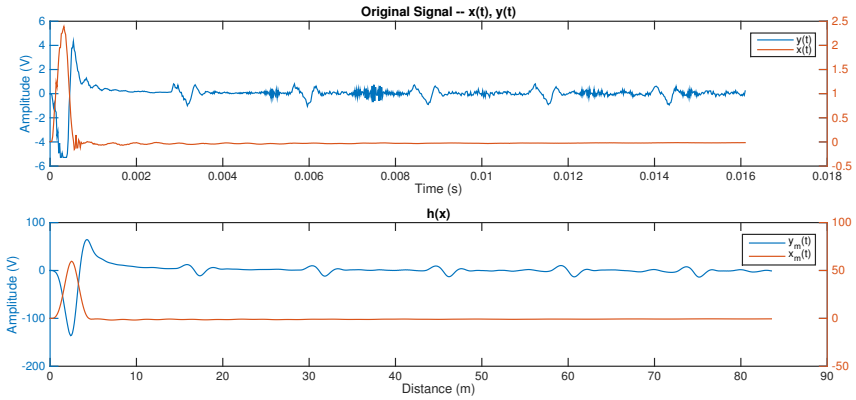

Figure 6.7: Direct time-space mapping of axial and torsional waves may be improved by matched filtering.

- Post Filtering

  1. Compute the FFTs $X(\omega) = \mathcal{F}(x(t))$ and $Y(\omega) = \mathcal{F}(y(t))$ of the signals
  2. Compute the transfer function $H(\omega) = Y(\omega)/X(\omega)$
  3. Multiply $H(\omega)$ with the FFT, $X_f(\omega)$ of a filter.
     - *Gaussian input*: A smooth gaussian input of width σ may be simulated by the frequency domain function

$$X_f = e^{-\frac{1}{2}(\sigma\omega)^2} \tag{6.14}$$

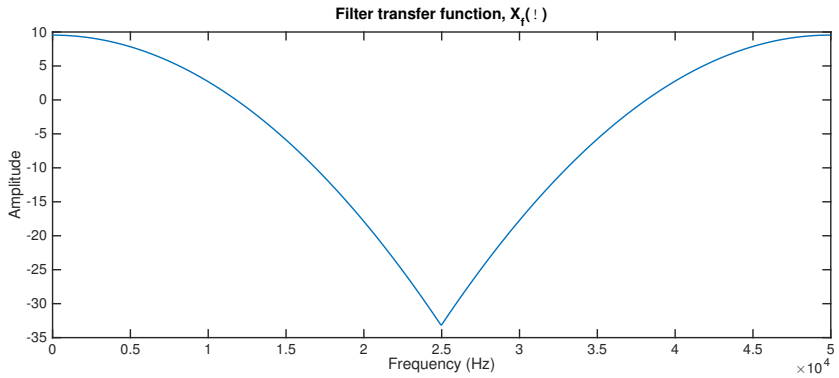

Figure 6.8: Frequency domain representation of a gaussian input.

     - *Butterworth filter*: A low pass filter may designed with a cutoff frequency f_{cutoff} with order n.

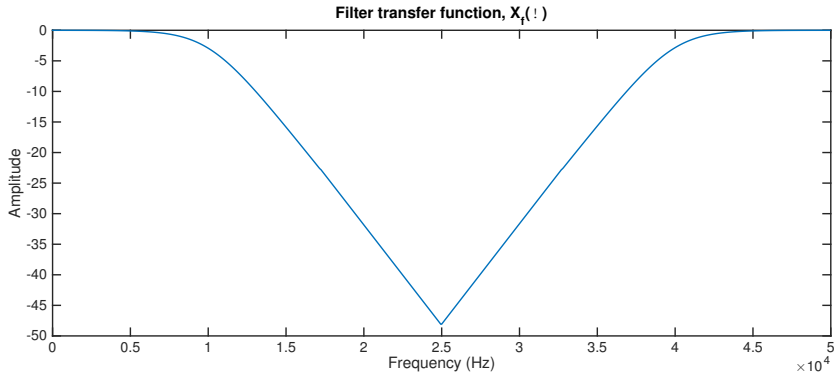

Figure 6.9: Frequency domain representation of a second order low pass Butterworth filter.

- *Impulse response*: The impulse response of the system may be simulated by setting $X_f(\omega) = 1$, but this amplifies high frequency noise

4. Apply the reverse FFT $h(x) = \mathcal{F}^{-1}(H_i(\omega))$ to find the space mapped wave response

6.4.2 Transfer Function Estimation

The transfer function of the system can be estimated and then be used to generate a step response curve. If the system is assumed to be time invariant and linear, then it can be treated as a black box and estimated from the Fourier transform of the input and the output.

$$H(\omega) = \frac{Y(\omega)}{X(\omega)} \tag{6.15}$$

and the inverse Fourier transform $h(t) = \mathcal{F}^{-1}(H(\omega))$ gives the estimated step response.

This method only works if the input signal contains sufficient bandwidth to provide a good estimate of $H(\omega)$ and works particularly well for chirp inputs.

6.4.3 Inversion Methods

In inverse problems, observed data is fit to a model via an error minimization technique. A modular method is implemented which allows for components to be replaced with ease.

6.4.3.1 Time domain fitting

Drumheller presents a modified form of the wave equation which may be used to model a structural transmission line with spatially varying impedance (Drumheller, 1989). The familiar wave equation

$$\frac{\partial^2 u(z,t)}{\partial t^2} = v^2 \frac{\partial^2 u(z,t)}{\partial z^2} \tag{6.16}$$

may be transformed by introducing the change of variables $z \to m$ from distance to mass:

$$m = \int_0^z \rho(\zeta) \cdot A(\zeta) d\zeta \tag{6.17}$$

$$\frac{\partial^2 u(m,t)}{\partial t^2} = Z^2 \frac{\partial^2 u(m,t)}{\partial m^2} \tag{6.18}$$

where $\rho(x)$ is the density, $A(x)$ is the cross sectional area, and $Z = \rho A c$ is the impedance.

A simple finite difference scheme may be applied to solve the equation numerically, where

$$\left(\frac{\partial u}{\partial t}\right)_j^{n+\frac{1}{2}} = \frac{u_j^{n+1} - u_j^n}{\Delta t} \tag{6.19}$$

$$\left(\frac{\partial^2 u}{\partial t^2}\right)_j^n = \frac{1}{\Delta t}\left(\left(\frac{\partial u}{\partial t}\right)_j^{n+\frac{1}{2}} - \left(\frac{\partial u}{\partial t}\right)_j^{n-\frac{1}{2}}\right) = \frac{u_j^{n+1} - 2u_j^n + u_j^{n-1}}{\Delta t^2} \tag{6.20}$$

Spatial discretization may be achieved using a similar transform as earlier, where Δr is the discretization in m:

$$\Delta r_{j+\frac{1}{2}} = \rho_{j+\frac{1}{2}} a_{j+\frac{1}{2}} \Delta x_{j+\frac{1}{2}} \tag{6.21}$$

Substituting these into modified wave equation and rearranging, the following finite difference solution is obtained:

$$u_j^{n+1} - u_j^{n-1} = \frac{2\Delta r_{j+\frac{1}{2}}}{\Delta r_{j+\frac{1}{2}} + \Delta r_{j-\frac{1}{2}}} u_{j+1}^n + \frac{2\Delta r_{j-\frac{1}{2}}}{\Delta r_{j+\frac{1}{2}} + \Delta r_{j-\frac{1}{2}}} u_{j-1}^n \tag{6.22}$$

Normalized impedance may also be used with the following substitution

$$\Delta r_{j+\frac{1}{2}} = \frac{Z_{j-\frac{1}{2}} \cdot \Delta x}{c_{j-\frac{1}{2}}} \tag{6.23}$$

and given a time discretization Δt, it follows that $\Delta z = v\Delta t$ to ensure compatibility. The inversion procedure is then as follows:

1. For an input force $x(t)$, the output acceleration $y(t)$ at point z_0 is recorded at sampling frequency f for times $t \in [0, t_1]$

2. A finite grid of time and space is generated with time discretization $\Delta t = 1/f$ and spatial discretization $\Delta z = v\Delta t$. Normalized impedance $Z(z)$ is initialized as an array of 1's.

3. Minimize L_2 error, e, between modeled system response $\hat{y}(t)$ for $t \in [0, t_1]$ based on forcing $x(t)$ at $z = 0$ and distributed impedances $Z(x)$ and the measured system response $y(t)$.

$$|e|_2 = \sqrt{y_i^2 - \hat{y}_i^2} \tag{6.24}$$

6.5 Experimental Results

Data was collected from a series of experimental setups with varying degrees of sensing quality and system complexity. The simplest system was a hanging steel beam located at the University of Cambridge which allowed for the study of axial and flexural waves. A laboratory drill string simulator at the Shell Research campus in Rijswijk allowed for torsional waves to be studied in a controlled environment. Data from the NAM T700 drilling rig was also used as a case study for field deployment.

6.5.1 Beam Experiment

A 7.2 meter beam, freely suspended in air from the ceiling, as shown in Figure 6.10, allows for the study of axial and flexural vibrations in a free-free beam. The system is instrumented with three accelerometers – two transverse accelerometers, mounted at 1.5 cm and 520 cm from end where the beam is excited, and one axial accelerometer mounted on the excitation end.

Data was recorded at 50kHz in all cases and operational amplifiers were used to amplify the accelerometer signals prior to data collection.

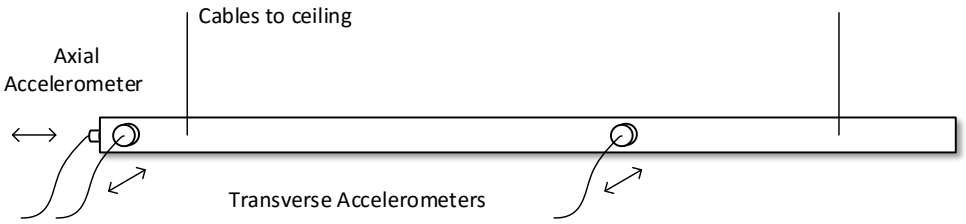

Figure 6.10: Schematic of the hanging beam experiment.

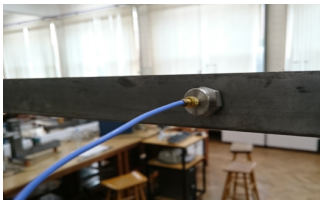

(a) Mounted transverse accelerometer two thirds of the way down the beam.

(b) Instrumented hammer with three varied stiffness tips and a force transducer.

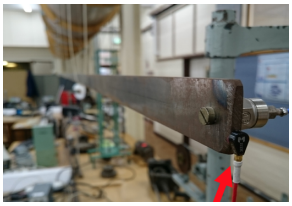

(c) Impact end of beam with the mounted axial and transverse accelerometers.

Figure 6.11: Components of the hanging beam experiment.

6.5.1.1 Effect of impulse length

The length of the input pulse was varied by changing the stiffness of the hammer tip by using a different material: rubber, nylon and metal. The shorter the impulse, the wider its bandwidth and the higher quality the reflections, as shown in Figure 6.12. Use of the rubber tipped hammer resulted in a pulse longer than the round trip travel time for an axial wave, while the nylon and metal tips progressively increased input bandwidth and allowed the returning wave to increase in contrast.

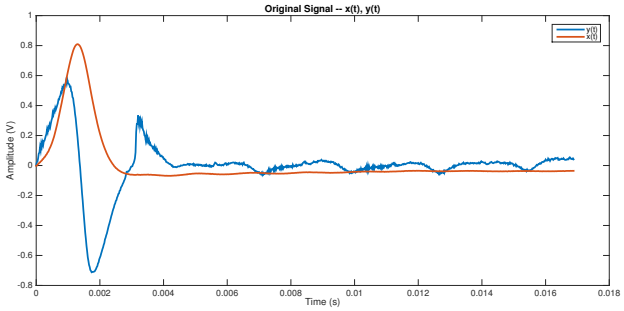

(a) Force input (red) and axial acceleration output (blue) for a rubber tipped hammer blow.

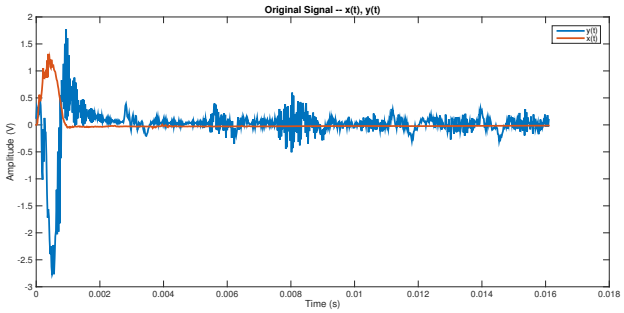

(b) Force input (red) and axial acceleration output (blue) for a nylon tipped hammer blow.

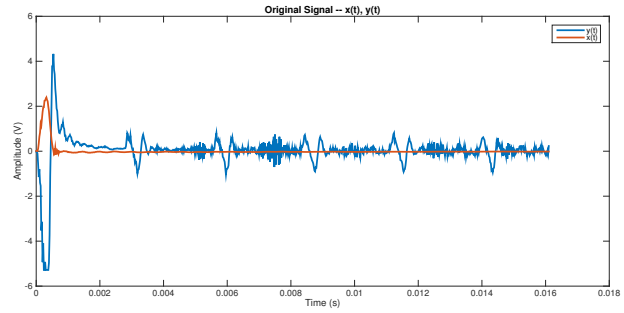

(c) Force input (red) and axial acceleration output (blue) for a metal tipped hammer blow.

Figure 6.12: Changing the hammer tip material changes the length and character of the impulse.

6.5.1.2 Direct time-space mapping

Two different waves are investigated – flexural waves and axial waves. Flexural waves are slower and exhibit dispersion, so were included in the investigation to mimic torsional waves seen in field data. Results are shown in figure 6.13 and clearly show beam length as well as the location of the midpoint accelerometer. Applying a matched filter further improves the S:N ratio.

Figure 6.13 shows (clockwise from the top for each subfigure), the input $x(t)$ and output $y(t)$, their respective FFTs, $X(\omega)$ and $Y(\omega)$, the system transfer function $H(\omega) = Y(\omega)/X(\omega)$, the remapping of $Y(\omega) \rightarrow H(k)$ and the space mapped wave response $h(x)$.

Axial waves travel faster with a wave speed that is not dependent on frequency, so the same dispersion method cannot be used. Additional noise is added to the system due to coupling between axial and flexural waves since the beam is not perfectly straight. This can be seen as high frequency noise that appears in the signal at multiples of 5/3 of the axial round trip time ($5/3 \approx c_a/c_f$).

Figure 6.14 shows (clockwise from the top for each subfigure), the input $x(t)$ and output $y(t)$, their respective FFTs, $X(\omega)$ and $Y(\omega)$, the filtered signal $y_f(t)$ and its FFT, $Y_f(\omega)$, the system transfer function $H(\omega) = Y(\omega)/X(\omega)$, the application of the filter transfer function $X_f(\omega)$ to the system transfer function $H_f(\omega) = H(\omega) \cdot X_f(\omega)$ and the space mapped wave response $h(z)$.

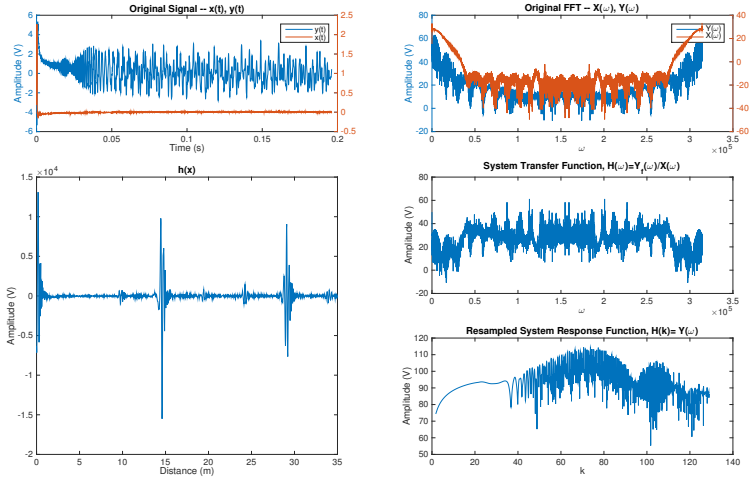

(a) Dispersion compensation for a flexural wave in a beam without filtering applied.

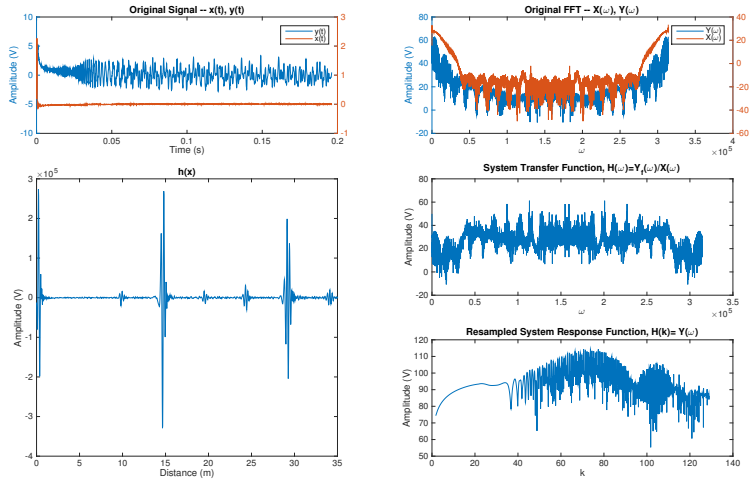

(b) Dispersion compensation for a flexural wave in a beam with input based matched filtering.

Figure 6.13: Visualizing the steps for dispersion compensation for flexural waves.

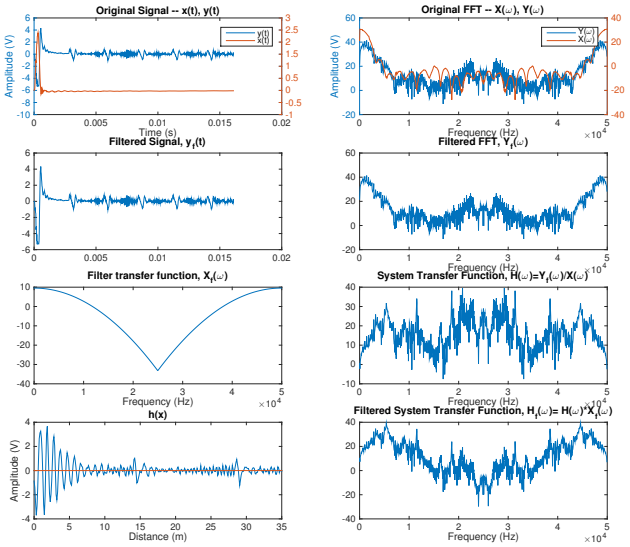

(a) Time-space mapping for an axial wave without matched filtering applied but with a gaussian input.

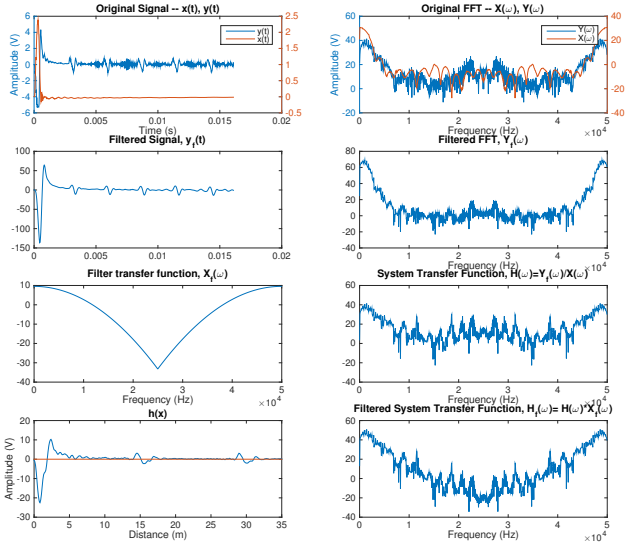

(b) Time-space mapping for an axial wave with matched filtering applied and with a gaussian input.

Figure 6.14: Visualizing the steps for dispersion compensation for axial waves.

6.5.1.3 System transfer function estimation

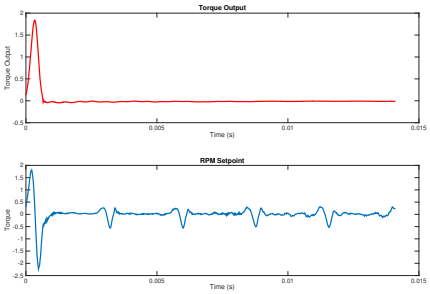

(a) Top plot shows force input (red) from the hammer, and the lower plot shows the axial acceleration output (blue) and axial acceleration output (blue) over a 0.014 second time period.

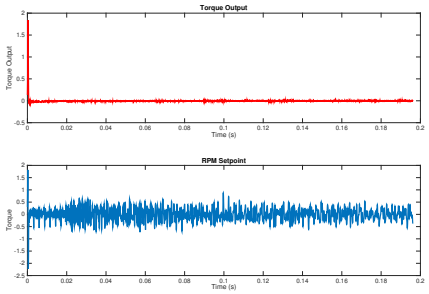

(b) Top plot shows force input (red) from the hammer, and the lower plot shows the axial acceleration output (blue) and axial acceleration output (blue) over a 0.195 second time period.

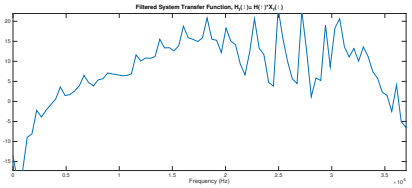

(c) Estimated system transfer function using just 0.014 seconds of data.

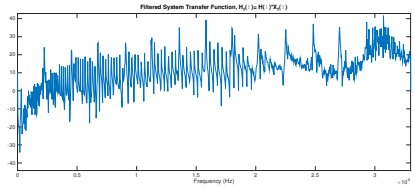

(d) Estimated system transfer function using 0.195 seconds of data.

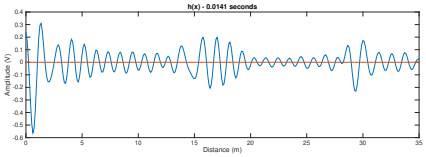

(e) Inverse transform of the system transfer function using just the lower frequency data displayed shows a periodic structure of the beam.

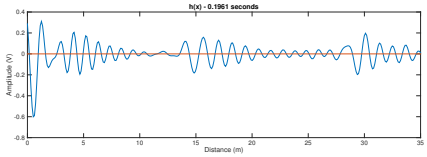

(f) The inverse transform of the system transfer function of a longer time period shows clearer periodicity of the beam end.

Figure 6.15: Estimating the system transfer function of the beam.

The hanging beam has significant cross coupling between axial and flexural waves which causes difficulties when estimating the transfer function for

axial waves, however, a reasonable estimate for beam length may be attained, as shown in Figure 6.15.

6.5.1.4 Impedance map inversion

Using Drumheller's wave equation modification to use element impedance, an impedance map may be fit to the data (Drumheller, 1989). Since the model does not account for the hammer - beam contact, only late time data, after the hammer is no longer in contact, may be used to fit the model. The greater the a priori knowledge of the system, the faster the fit is found and the higher the confidence may be placed in the fitting parameters. For example, if beam length is not know and is assumed to by 8 meters, as shown in Figure 6.16, the model fit finds a high impedance is necessary at 7.4 meters to fit the data reasonably. Using a priori knowledge about the beam length, as shown in Figure 6.17, the model converges to a minimum error faster and begins to reveal more information about the beam. Changes in impedance begin to appear in the region of 5 meters, where the accelerometer is located, as well as near the beginning of the beam, where the first accelerometer is placed, to match the higher frequency responses visible in the data.

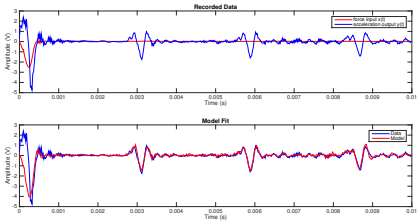

(a) Top plot shows force input (red) and axial acceleration output (blue) from experimental data, the bottom plot shows experimental axial acceleration in blue and the fitted model response in red.

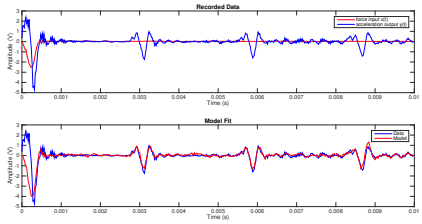

(b) Top plot shows force input (red) and axial acceleration output (blue) from experimental data, the bottom plot shows experimental axial acceleration in blue and the fitted model response in red.

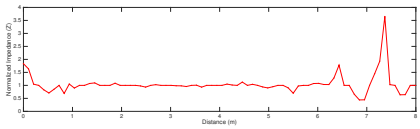

(c) Fitted impedance map of the beam with an original beam length guess of 8 meters. A high impedance at 7.3 meters is deduced.

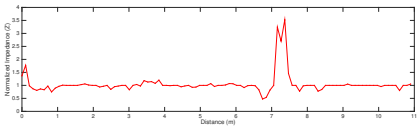

(d) Fitted impedance map of the beam with an original beam length guess of 11 meters. A high impedance at 7.1 meters is deduced.

Figure 6.16: Fitting the model without knowing the beam length.

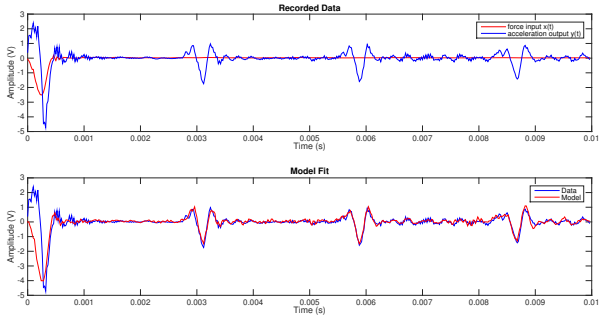

(a) Top plot shows force input (red) and axial acceleration output (blue) from experimental data, the bottom plot shows experimental axial acceleration in blue and the fitted model response in red.

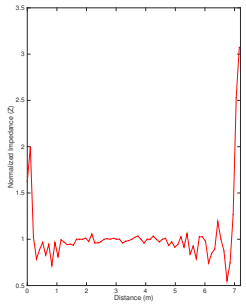

(b) Fitted impedance map of the beam that gives a good modeled response.

Figure 6.17: Fitting the model with a good initial guess of beam length. The impedance map shows a high impedance at the left end of the beam where the first accelerometer is placed and oscillation where the second one is located.

6.5.2 Zebra Drillstring Simulator

The Zebra setup is a drillstring simulator at the Shell Research Center in Rijswijk which simulates a 5750 meter drillstring as a series of lumped masses mounted on a slender steel rod. An AC motor provides rotary motion and is controlled via a compactRIO with an advanced experimental implementation of ZTorque.

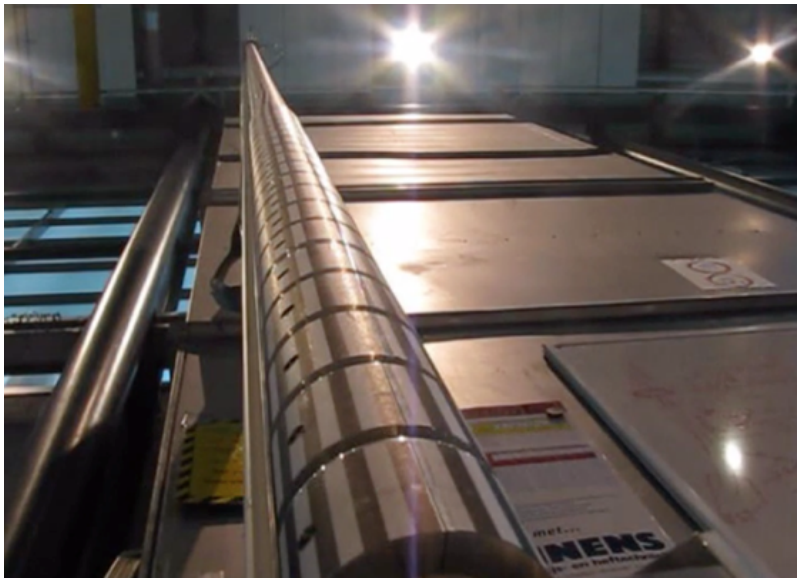

Figure 6.18: Look up along the Zebra simulator.

6.5.2.1 System transfer function estimation

This implementation allows for white noise injection of a specified amplitude and period range. Setpoint RPM including the white noise input is recorded at 125Hz and is synchronous with the torque signal. Example white noise data is shown in Figure 6.19.

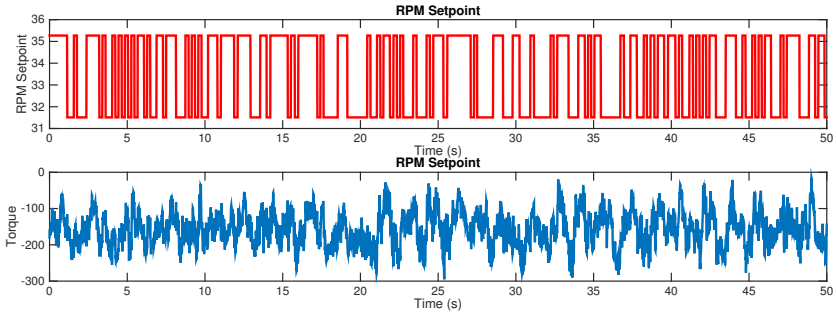

Figure 6.19: Injected white noise setpoint RPM and resulting torque. The white noise is +/- 2 RPM with a quasi random period of 0.1 to 2 seconds.

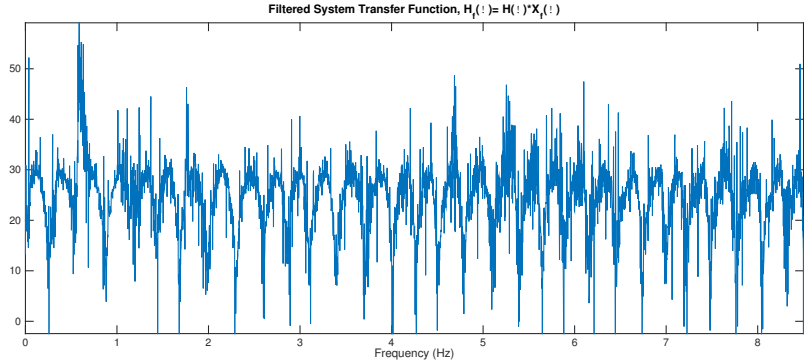

(a) System transfer function $H(\omega) = Y(\omega)/X(\omega)$ for 400 seconds of white noise data.

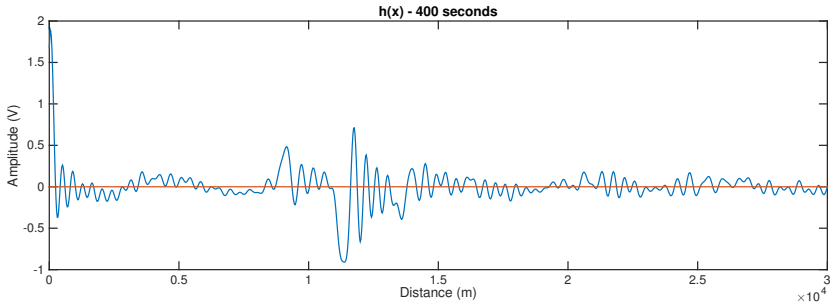

(b) Processed drillstring image using 400 seconds of data.

Figure 6.20: Recorded data and system transfer function.

Using the white noise injection as a broad bandwidth excitation input allows for the system transfer function to be reconstructed with clearly visible modal shapes, as seen in Figure 6.19b. The random phase of the input noise is compensated by this process, allowing the inverse FFT to show the impulse response. Taking only the low frequency modal data (up to 8.5Hz) and performing the inversion back to the spatial domain, the BHA and bit are clearly visible, as seen in Figure 6.19c. The first clear return at 9000 meters is due to the impedance contrast of the BHA, which begins at 4500 meters. The second return at 11500 meters is the end of the system, which correctly gives the 5750 meter drillstring length the Zebra is simulating. The third return at 14000 meters is the reflection of the wave within the BHA. As a longer and longer sampling window is used, secondary reflections will become more distinct and can already be seen at 22000 meters and 25000 meters.

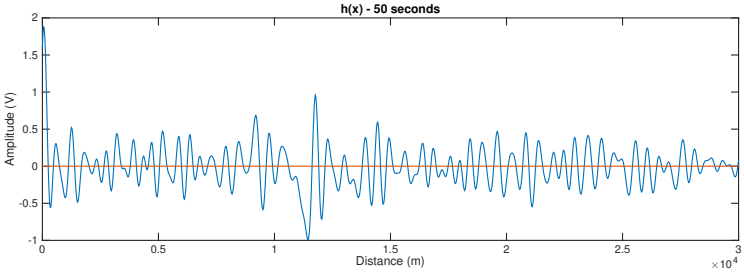

(a) Processed drillstring image using 50 seconds of data.

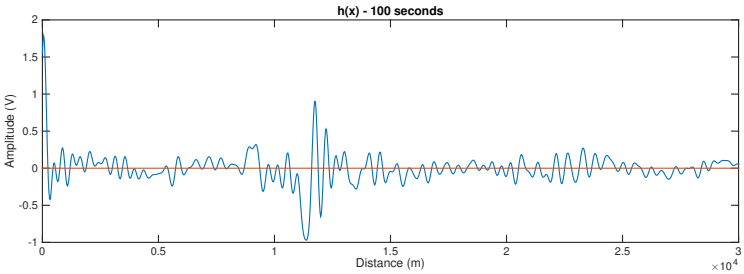

(b) Processed drillstring image using 100 seconds of data.

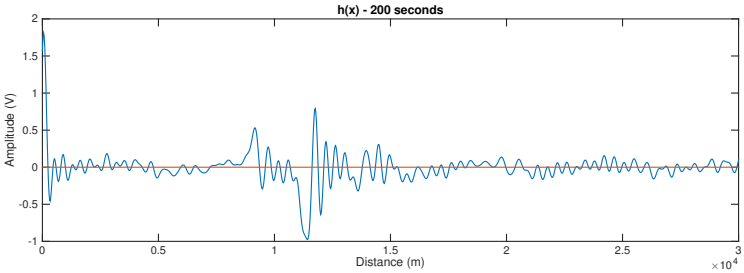

(c) Processed drillstring image using 200 seconds of data.

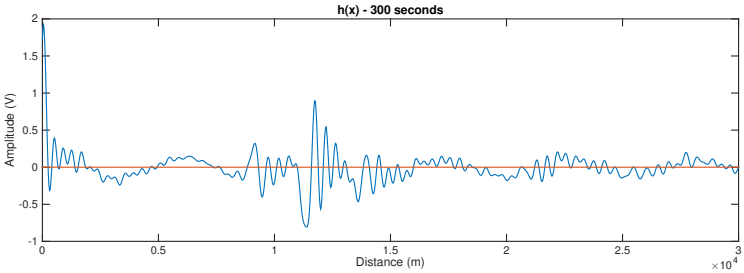

(d) Processed drillstring image using 300 seconds of data.

Figure 6.21: Processed drillstring images from injection of white noise into the surface rotary rate and the resulting impedance maps for different lengths of data.

The effects of sampling window length on feature resolution are shown in Figure 6.21. Using a short time window of 50 seconds gives the bit return but has a low signal to noise ratio. Moving to a 100 second sampling window improves this ratio and the BHA begins to appear. Continuing to extend the window continues to improve the signal to noise ratio until both the primary returns of the BHA and bit are seen as well as the second reflection from within the BHA.

Since a low pass filter of 8.5 Hz is used, the spatial resolution limited to 376 meters. The longer the sampling window, the wider the passband on the lowpass filter may be to maintain an adequate signal to noise ratio, so smaller features can still be identified. However, the passband is also limited by the bandwidth of the random noise input, 10 Hz in this case.

Using white noise on the Zebra setup shows promise for field deployment and is a builtin capability on Canrig implementations of Ztorque.

6.5.2.2 Using cross correlation

When injecting white noise, cross correlation between the rpm setpoint input and the torque out may also be used to identify reflections. The procedure is as follows

- Compute the FFTs of the input, $x(t) \rightarrow X(\omega)$, and the output, $y(t) \rightarrow Y(\omega)$
- Compute $H(\omega) = Y(\omega) \cdot \bar{X}(\omega)$ where $\bar{X}(\omega)$ is the complex conjugate

- Compute the iFFT and rescale the x axis to a distance axis.

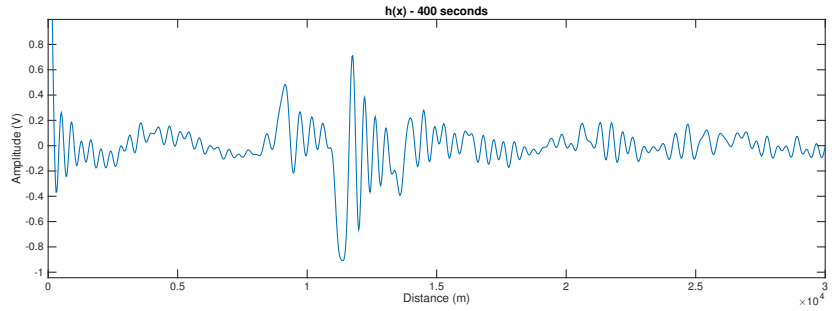

(a) Using the transfer function approach.

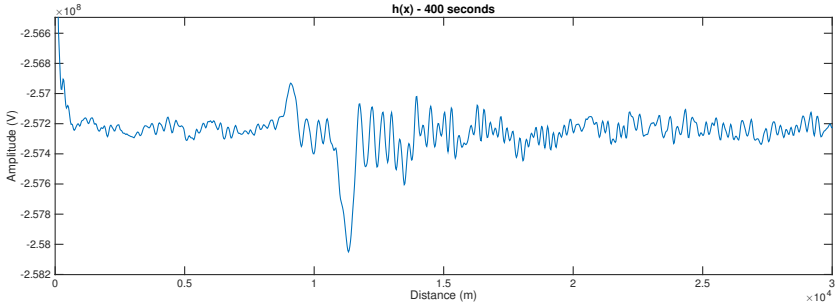

(b) Using cross correlation.

Figure 6.22: Reflection maps using the transfer function reconstruction and the cross correlation approach, both with 400 seconds of data.

Both transfer function estimation and cross correlation produce similar results which are both limited by the bandwidth of the random noise input, as shown in Figure 6.22.

6.5.2.3 Model inversion

Using Drumheller's time domain model with a free end at the bit, the impedance map may be fit to the data if the cost function is the difference in torque at the driving end and the displacement is the recorded rpm.

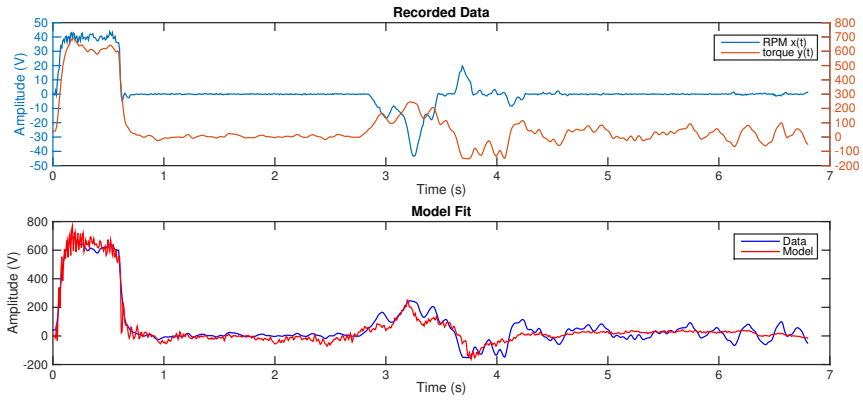

(a) Recorded data (top) and recorded torque (red) and modeled torque (blue).

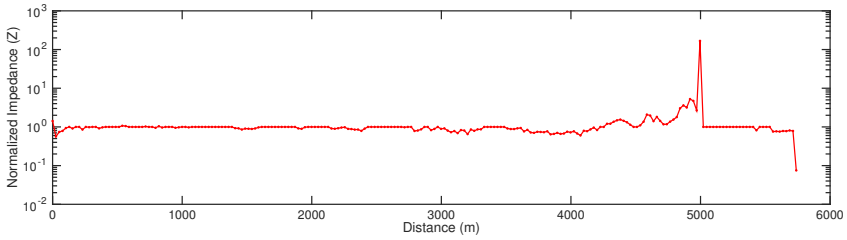

(b) Fitted impedance map generated.

Figure 6.23: Impedance map generated by model inversion using Drumheller's wave equation.

This shows the high impedance change at the BHA location.

6.5.3 NAM T700 Field Data

Field data was obtained from the drilling of a well by NAM on the T700 rig from normal drilling operations. The best candidates for imaging included data from

- Initial rotation after connection are made. This data gives the step response of the system from an rpm step. However, the step itself is gradual, lasting one to two seconds, thus blurring out much of the system response. Time-space mapping reveals little information, even with filtering, but inversion is possible due to the system being originally at rest. In early time, the bit can be assumed to be stuck, thus the system can be modeled as a fixed-fixed beam in torsion. Three examples of such events are shown in Figure 6.24.

- Injected square waves into drilling data. This data can be match filtered and then fed into the time-space mapping algorithm, but inversion is difficult due to the complexity of the system.

Injected white noise is also suggested as an input, but is not currently implemented on the rig and thus cannot be tested.

On each connection, a nearly identical procedure is followed to begin pipe rotation from standstill. This presents itself as a natural candidate for an imaging method since a borehole image may be obtained for each stand. The data does appear to show a low amplitude cyclic behavior during the first few rotations before the bit and BHA break free and begin rotating.

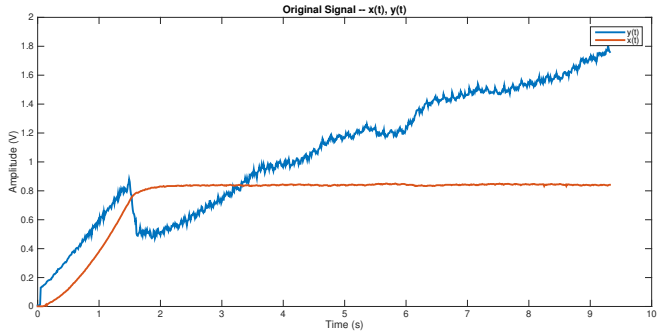

(a) Surface RPM (red) and surface torque (blue) for initial rotation.

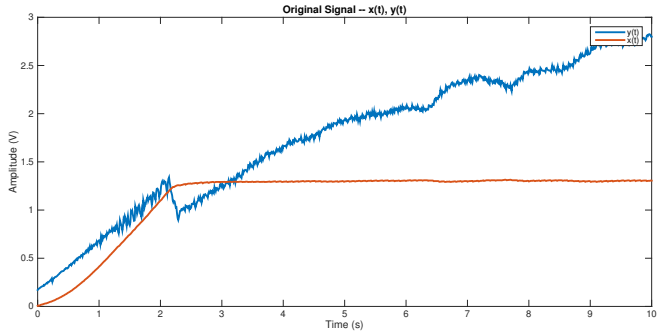

(b) Surface RPM (red) and surface torque (blue) for initial rotation.

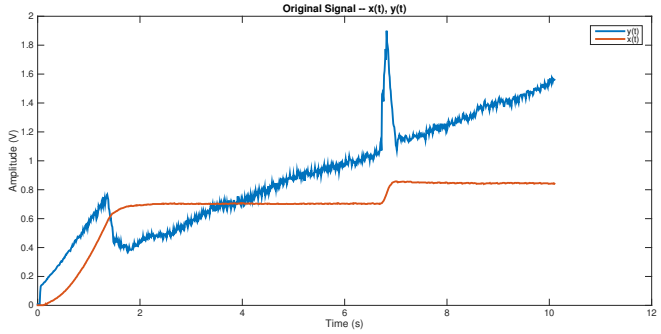

(c) Surface RPM (red) and surface torque (blue) for initial rotation.

Figure 6.24: Three examples of initial rotation after a connection is made, showing an RPM ramp and resulting torque curve. The bit and BHA are still stuck, thus the bit acts as a pinned end.

6.5.3.1 Time-space mapping

Torsional waves travel at a constant speed in drill pipe, allowing a direct temporal-spatial mapping to occur with the time axis simply scaled by the wave velocity. Additional filtering may improve imaging quality, however, the low bandwidth of the input hampers efforts.

The data shows a periodic signal during the initial start of rotation until the first slip event at the bit. However, even with filtering, the input bandwidth is scarcely sufficient to even image the end of the drillstring, as shown in Figures 6.25 and 6.26.

6.5.3.2 Model based inversion

Drumheller's wave equation is used to model the drillstring with two pinned ends. The bit is assumed pinned until enough torque is stored in the string to free it. At the surface, the recorded rpm signal, $x(t)$ is applied as displacement per time. Surface torque is computed as the twist of the uppermost element. Since the model does not include the top drive, this computed torque needs to corrected by adding an inertial torque component.

$$\tau_{measured} = \hat{\tau}_{model} + \dot{\Omega} J_{td} \tag{6.25}$$

Steady state friction may also be added to improve the model fit, as shown in Figure 6.27.

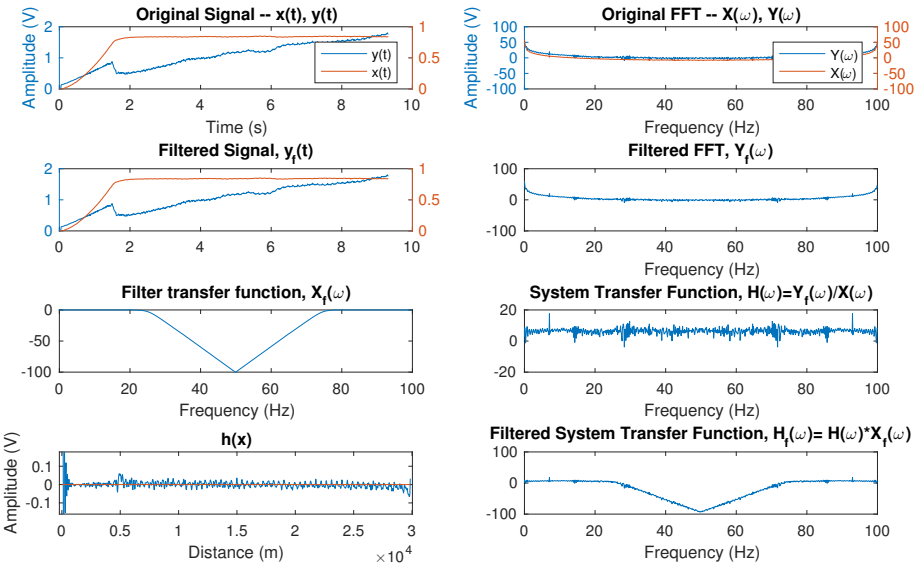

(a) Application of just a Butterworth low pass filter.

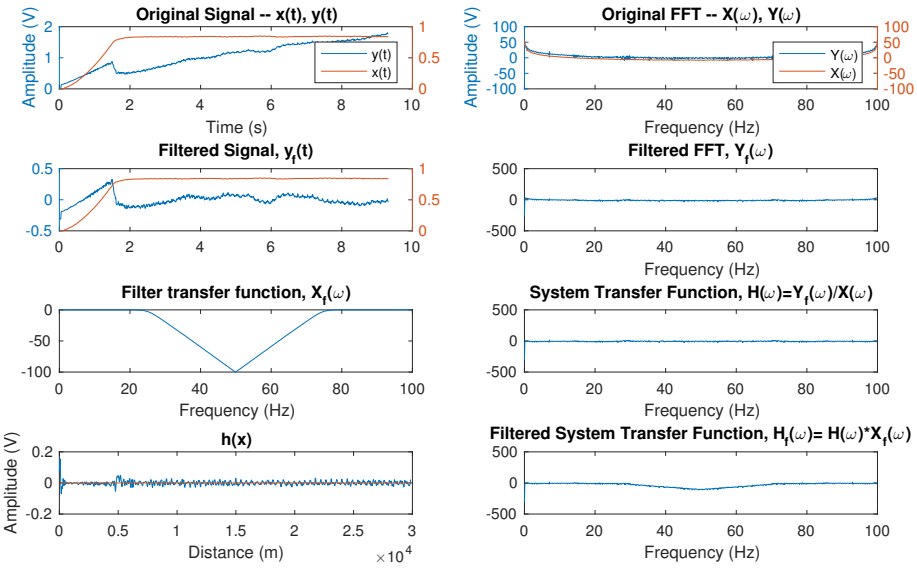

(b) Detrending the torque data before application of a Butterworth low pass filter.

Figure 6.25: Time-space mapping with a Butterworth low pass filter with original and detrended data with T700 data.

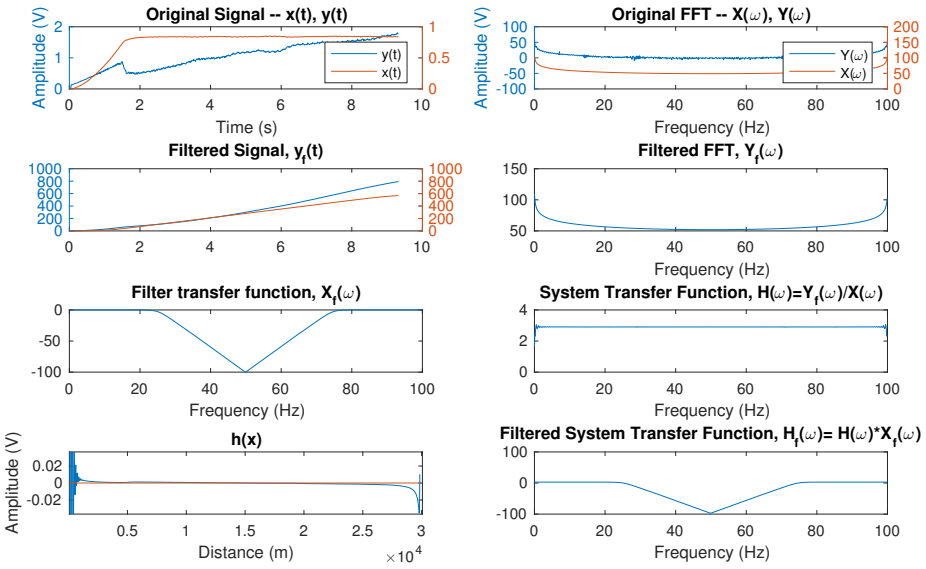

(a) Application of match filtering on the input and a butterworth low pass filter.

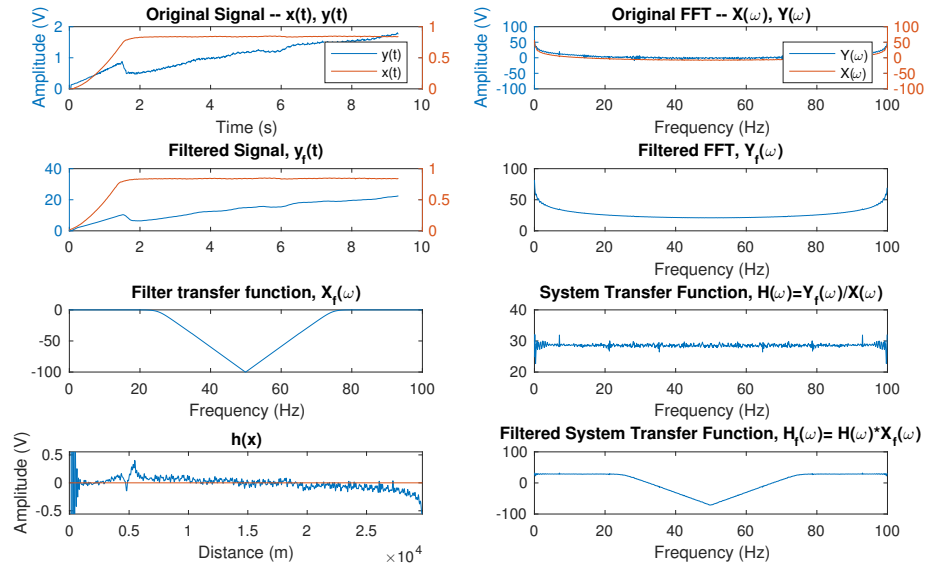

(b) Using the derivative of RPM, match filtered and low pass butterworth filtered.

Figure 6.26: Time-space mapping with a match filter and computed acceleration with T700 data.

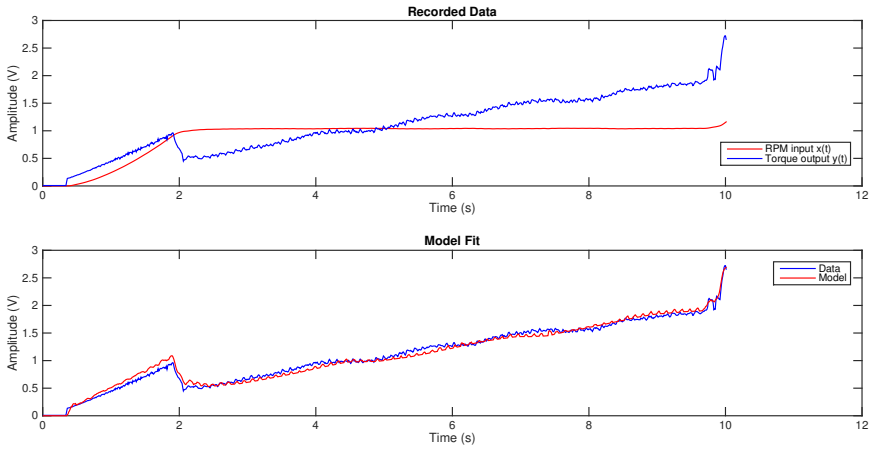

(a) Top plot showing the RPM setpoint (red) and torque (blue) for a start of rotation after a connection. The bottom plot shows the recorded torque (blue) and the model fitted torque (red), showing high agreement.

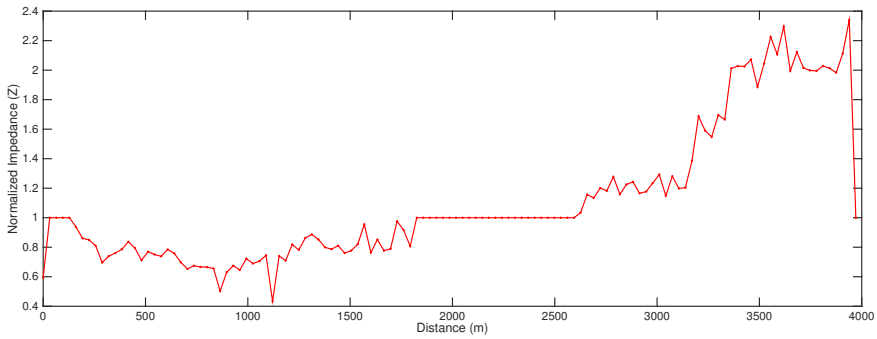

(b) Processed drillstring impedance map computed by the model to generate the best fit, showing an increase in impedance at 3200 m, which is near bit depth.

Figure 6.27: Fitting the wave equation model to field data shows a close model fit and a reasonable impedance map.

6.6 Conclusions

Three classes of methods are investigated as candidates processes for drillstring imaging: direct time-space mapping, system transfer function estimation, and model based inversion. Direct time-space mapping maps the response of a system to an input from the time domain to the spatial domain using the wave velocity within the system, which is constant over different frequencies for axial and torsional waves in steel pipe. Transfer function estimation augments this approach through frequency domain filtering and impulse response estimation to improve the resolution and contrast of features in the system. Model based inversion attempts to fit a spatial impedance map of a model based on the wave equation with assumed boundary conditions to the system response. Direct time-space mapping is an effective method only if a broadband system input is used, and match filtering can be used to remove artifacts due to the input. Transfer function estimation is used improve contrast and resolution, and is shown to be effective on the beam experiment with an impulse response and on the Zebra for a white noise input. It is not effective on the T700 data due to the low bandwidth of the input as well as a low signal-to-noise ratio for higher frequencies due to the large inertia of the top drive. Model based inversion is shown to be a powerful technique, but only if the model being fitted is a good approximation of the system and also has the ability to overfit the system. Drillstring length on the T700 is effectively estimated, however, BHA length could not be characterized effectively.

For systems with low noise, clean sensing and a high bandwidth input, direct time-space mapping is an effective technique, but is limited by Nyquist to a maximal resolution. Filtering and transfer function estimation are able to improve contrast of features and identify both the beam end in the hanging beam as well as both the BHA and bit in the Zebra. However, for complex systems, a white noise input has resulted in the best imaging results. This allows a broad bandwidth of excitation, and with long sampling windows, results in clear returns from features larger than those imageable by the highest frequency excited. Model inversion produces excellent results as well for datasets with impulse or step responses, regardless of input bandwidth. However, resulting impedance maps are only as good as the models used to fit the system. Once white noise injection is tested on a field drilling rig, it is expected that drillstring components will be readily visible and will show an evolution in depth as drilling proceeds. Resolved features which remain at constant depth for a range of bit depths can then be inferred as friction points along the drillstring and an exploration of this data is suggested as future work.

6.7 Further Work

- The use of white noise has been shown to be effective in the case of the Zebra experimental setup. White noise injection has been built into Canrig implementations of ZTorque but has not yet been tested in the field. Immediate future work will involve injecting white noise with a random period ranging from 0.1 to 2 seconds and several amplitudes to

investigate the minimum amplitude necessary for a sufficient signal to noise ratio.

- Model inversion has also been shown to be an effective technique. With the move towards realtime kernels within the drilling dynamics suite, it is recommended to implement the minimally sufficient model to allow for real-time impedance map estimation. This can be combined with real-time torque and drag estimation which will allow for the imaging of deviated and horizontal wells.

- The vibrating behavior of strings is known to be dependent on tension. There is a question whether applying a predetermined amount of torque to a string before applying an impulse or step function improves signal quality. This is especially relevant to the application in well abandonment, where it is desired to find the top of cement in the wellbore.

- Datasets containing data from torque and tension subs placed below the top drive can be used to verify the reflection effects of the top drive inertia and to evaluate the improvement of signal quality. If both torque and tension are recorded at high frequencies (greater than 100 Hz), it is possible to evaluate both axial and torsional signals and any cross coupling between them.

6.8 Recommendations

- Torque should be recorded using a torque and tension sub below the top drive to improve sensing abilities at higher frequencies. Even with a small top drive, torsional signal transmission to the VFD, where torque is traditionally measured, above 5 Hz approaches the ambient noise level. For the top drive on T700, distinguishing signals from noise becomes difficult above 1Hz

- Higher bandwidth inputs are necessary to allow for imaging of features

  - For an impulse or square wave input, ramp time needs to fast. For 10 Hz bandwidth, the ramp cannot be longer than 0.1 seconds. For 1 Hz, 1 second, and for 0.5 Hz, 2 seconds.

  - For white noise input, a range of periods from 0.1 seconds to 2 seconds gives a bandwidth of 0.5 - 10 Hz. This bandwidth is widened with smaller amplitude noise, but the signal to background noise ratio decreases.

- White noise injection shows the greatest promise for drillstring mapping, especially with longer sampling windows. The Zebra setup showed that even with a +/- 2 RPM amplitude white noise input, the bit and BHA could be distinguished in as little as 100 seconds.

- Repetitive rig activities, such as the start of rotation after a connection, may be used to fit a drillstring model to estimate system parameters

such as friction factors, but only if the model sufficiently describes the system. This could become part of a realtime kernel which estimates the torque and drag within a wellbore every stand.

Chapter 7

Conclusions and Recommendations

7.1 Conclusions

This dissertation presented a simple yet elegant drillstring model that has been shown to be effective in modeling harmonic axial drillstring vibrations and is useful for both the evaluation of control systems mitigating torsional oscillations as well for torsional drillstring imaging. The model was derived from first principles and then verified with both field and experimental data in both the axial and torsional cases. By abstracting the drillstring as a waveguide, the model presents a computationally efficient method of characterizing the drillstring dynamics, both at boundary conditions of interest or throughout the entire drillstring at high spatial resolution.

In the axial case, the transfer matrix implementation was used to optimize axial oscillation tool placement in drillstrings to maximize friction reduction while sliding. By modeling the oscillation source as an external harmonic force input, the dynamic response of the drillstring was computed and then compared with field data with multiple data recorders to verify vibration attenuation. Then, by comparing the dynamic force throughout the drillstring, friction reduction was computed as the fraction of the drillstring experiencing

sufficient dynamic force to overcome static friction. Tool placement could then be optimized by maximizing the friction reduction as a function of bit depth – the longer the lateral, the less of the drillstring is in motion.

In the torsional case, the model was first used to evaluate the functionality of four different top drive controllers and secondly for a feasibility study of drillstring imaging. By using the time domain implementation of the model, some of the features and drawbacks of each controller may be evaluated visually:

- stiff PI controllers do not attenuate any torsional oscillation – as they are designed to maintain rotary speed
- tuned PI controllers are successful at attenuating a single mode of stick-slip
- second order PI controllers improve upon the performance of tuned PI controllers
- impedance matching controllers successfully attenuate a wide band of modes but do inject some high frequency noise.

These features and drawback can then be quantified by comparing the reflectivity of the top drive – the ability of the top drive to absorb energy at certain frequencies – with the mobility of the drillstring within different wellbore geometries.

Finally, an exploration of drillstring imaging was conducted which evaluated the feasibility of imaging changes in the drillstring properties – both properties of the drillstring itself as well as interactions with the borehole – through a study of reflections in several experimental setups. It was concluded that model fitting shows promise in inferring impedance maps of the system. However, the best results were achieved through the injection of white noise into the rpm signal while drilling. When evaluating the system from rest – through the use of a step response – the use of signal processing and a transformation from time to space provided the best results, where spatial resolution was a function of both input bandwidth and sensing frequency.

7.1.1 Contributions of this Dissertation

- The *transfer matrix approach* with augmented 3×3 matrices is shown to be effective for modeling the effect of *axial oscillation tools* in drillstrings to improve weight on bit and torque on bit transfer in sliding situations in horizontal wells. Several case studies were presented that show agreement between the model and field measurements including several which use model predictions to optimize tool placement.

- An estimate of *friction reduction* is quantified from the drillstring response modeled using the transfer matrix approach which allowed for the *placement* of axial oscillation tools to be directly compared.

- An efficient method to quantify the effectiveness of stick-slip mitigation control from the top drive by computing the *drillstring mobility* using

a transfer matrix representation of the drillstring and an estimation of *damping* based on *wellbore trajectory*.

- The recommendation that *drillstring imaging* using torsional waves in a drillstring is *possible* and is best accomplished either using a *white noise* input to the rpm setpoint while drilling or by using a *wide bandwidth step input* and high frequency sensing while static.
  - While using white noise, either *transfer function reconstruction* or *cross correlation* may give clear images.
  - When using a step input, the resulting drillstring image is strongly affected by input bandwidth – i.e. the equivalent of a hammer blow – and by sensing frequency.

7.2 Recommendations

The transfer matrix model for axial vibrations should be used to verify and tune future deployments of axial oscillators in the field. By improving placement and increasing friction reduction, longer laterals are possible, increasing production per well and reducing the number of wells necessary. Improvements in steering due to improved toolface control will also reduce drilling times, improve wellbore quality and reduce tortuosity. Also, since the model allows for the placement of multiple oscillation sources to be evaluated, it opens up the possibility of continuing to extend the reach of laterals by reducing the friction both in the curve and lateral sections.

The operation of various stick-slip mitigation systems is well understood in simple wellbores, yet wellbore trajectory and ensuing changes in drillstring dynamics is not often considered. By optimizing the systems already installed on rigs to target prevailing drillstring modes based on well geometry, drilling performance may be improved without the need to upgrade the system.

Finally, since it has been shown that drillstring imaging using torsional waves is possible, it is recommended that field trials be conducted, both utilizing white noise injection while drilling and by hitting the drillpipe with the equivalent of a hammer while static.

7.3 Further Work

Much of the work presented in this dissertation is directly applicable to field applications, thus continued application to projects in the field is recommended.

- Evaluation of data from field trials with multiple oscillation sources needs to be compared to model predictions and performance quantified.
- Control systems from different vendors may be directly compared if all control system components are identified. These systems can then be tuned, if wellbore geometries are known, to target the prevalent modes of stick-slip.
- Data from any field trials pertaining to drillstring imaging needs to be evaluated and the quality of the drillstring image assessed.

Appendices

Appendix A

List of Symbols and Abbreviations

A.1 Symbols

Symbol	Meaning
i	$\sqrt{-1}$
t	time
z	spatial coordinate along measure depth
ω	frequency
s	Laplace variable
$u(x,t)$	axial displacement
$\phi(x,t)$	angular displacement
F	force
A	cross sectional area
E	Young's modulus
G	shear modulus
η	material damping factor
σ	stress
ϵ	strain
ρ	density
ρ_m	mud density
v	wave velocity
v_a	axial wave velocity
v_t	torsional wave velocity
$\mathcal{U}(x,\omega)$	axial displacement in the frequency domain
c	damping
C	element damping
k	spring constant
m	element mass
γ & Z_0	convenience functions in the transfer matrix
$\mathcal{A}$	transfer matrix

Symbol	Meaning
W_d	work done by damping
F_d	damping force
F_n	normal force
F_t	tensile force
μ	friction coefficient
S_s	Sensitivity
$C_s(s)$	control system
K_p	porportional gain
K_i	integral gain
K_d	derivative gain
$P_s(s)$	plant
$\tau_{inertia}$	inertial torque
τ_{td}	top drive torque
τ_{BHA}	BHA torque
J_{td}	top drive inertia
J_{BHA}	BHA inertia
f_{cutoff}	cut off frequency
f_{sp}	speed filter cut off frequency
t_{vfd}	time delay in a VFD
T_{motor}	motor torque signal
T_{pipe}	pipe torque signal
T_{vfd}	vfd torque signal
T_{comm}	commanded torque signal
ω_{pipe}	pipe angular velocity
ω_{set}	setpoint rpm
ω_{err}	difference between pipe rpm and setpoint rpm

A.2 Abbreviations

Abbreviation	Meaning
BHA	Bottom Hole Assembly
HFTO	High Frequency Torsional Oscillations
FEM	Finite Element Method
PID	Proportional, Integral and Derivative (control)
PI	Proportional and Integral (control)
PDC	Polycrystalline Diamond Compact (bit)
RC	Roller Cone (bit)
RPM	Rotations Per Minute
DC	Direct Current
AC	Alternating Current
VFD	Variable Frequency Drive
AOT	Axial Oscillation Tool
DDR	Dynamics (or Downhole) Data Recorder
RMS	Root Mean Square

Appendix B

Published Work

B.1 Published Conference Papers

1. Shor, R.J., Pehlivanturk, C., Acikmese, B., van Oort, E. **Propagation of Torsional Vibrations in Drillstrings: How Borehole Geometry Affects Transmission and Implications on Mitigation Techniques**. ICoEV 2015.

2. Shor, R.J., Dykstra, M.W. and Coming, M. **For Better or Worse: Applications of the Transfer Matrix Approach for Analyzing Axial and Torsional Vibration**. SPE/IADC Drilling Conference. 2015. (SPE-173121-MS).

3. Ashok, P., Ambrus, A., Shor, R.J. and van Oort, E. **Overcoming Barriers to Adoption of Drilling Automation: Moving Towards Automated Well Manufacturing**. SPE/IADC Drilling Conference. 2015. (SPE-173164-MS).

4. Shor, R.J., Pryor, M. and van Oort, E. **Drillstring Vibration Observation, Modeling and Prevention in the Oil and Gas Industry**. ASME Dynamic Systems and Controls Conference. 2014. (DSCC2014-6147).

B.2 Papers in Preparation

1. Shor, R.J., Dykstra, M.W., Panchal, N. and van Oort, E. **Drilling Longer Horizontals: Estimating Friction Reduction from Multiple Axial Oscillation Tools.** SPE/IADC Drilling Conference. 2017. (Abstract to be submitted)

B.3 Proposed Papers

1. Shor, R.J., Butlin, T., Dwars, S., Blange, J.J, and van Oort, E. **Imaging Drillstrings with Torsional Waves.** 2017 (conference / journal not decided)

2. Shor, R.J., Ackimese, B., and van Oort, E. **Evaluating Stick Slip Mitigation Control System Performance in Deviated and Horizontal Wells.** 2017 (conference / journal not decided)

Appendix C

Minimum Curvature Method

The input to the model is a series of survey points for a drilled or planned wellbore. The path is discretized and interpolated for use by the model using the minimum curvature approach commonly found in well planning best practices. An in depth approach to interpolating wellpath from survey points is presented in Sawaryn and Thorogood's work and is derived from the minimum curvature approach Sawaryn and Thorogood (2005). The relevant equations are described below. The reference frame of a survey point can be described in either the north-east-vertical frame or in the normal-tangential frame. For the N-E-V frame, we have

$$p = \begin{pmatrix} N \\ E \\ V \end{pmatrix} \tag{C.1}$$

$$dp = \begin{pmatrix} dN \\ dE \\ dV \end{pmatrix} = \begin{pmatrix} \sin\theta\cos\phi \\ \sin\theta\sin\phi \\ \cos\theta \end{pmatrix} \tag{C.2}$$

$$\theta = \tan^{-1}\left(\frac{\sqrt{dN^2 + dE^2}}{dV}\right) \tag{C.3}$$

$$\phi = \tan^{-1}\left(\frac{dE}{dN}\right) \tag{C.4}$$

In the normal-tangential reference frame, this equates to

$$h = \begin{pmatrix} \cos\theta\cos\phi \\ \cos\theta\sin\phi \\ -\sin\theta \end{pmatrix} \tag{C.5}$$

$$r = \begin{pmatrix} -\sin\phi \\ \cos\phi \\ 0 \end{pmatrix} \tag{C.6}$$

$$v = \begin{pmatrix} 0 \\ 0 \\ 1 \end{pmatrix} \tag{C.7}$$

where θ is the inclination and ϕ is the azimuth. Dogleg severity, β then can be calculated using

$$\alpha = 2\sin^{-1}\left\{\sqrt{\sin^2\left(\frac{\theta_2-\theta_1}{2}\right)+\sin\theta_1\sin\theta_2\sin^2\left(\frac{\phi_2-\phi_1}{2}\right)}\right\} \tag{C.8}$$

$$\beta = \frac{18000\cdot\alpha}{\pi\left(D_2-D_1\right)} \tag{C.9}$$

The position of the next survey point is given by

$$p_2 = p_1 + \frac{S_{12}f(\alpha)}{2}\begin{pmatrix} \sin\theta_1\cos\phi_1+\sin\theta_2\cos\phi_2 \\ \sin\theta_1\sin\phi_1+\sin\theta_2\sin\phi_2 \\ \cos\theta_1+\cos\theta_2 \end{pmatrix} \tag{C.10}$$

where

$$f(\alpha) = \frac{\tan(\alpha/2)}{\alpha/2} \tag{C.11}$$

is the shape factor and S_{12} is the arc length.

Given two survey points p_1 and p_2, a point p^* can be interpolated on subtended angle using

$$\alpha^* = \tan^{-1}\left(\frac{\sin\left(\phi_1-\phi^*\right)\sin\alpha\sin\theta_1}{\sin\left(\phi^*-\phi_2\right)\sin\theta_2+\sin\left(\phi_1-\phi^*\right)\sin\theta_1\cos\alpha}\right) \tag{C.12}$$

$$\theta^* = 2\tan^{-1}\left(\frac{A\pm\sqrt{A^2+B^2-C^2}}{B+C}\right) \tag{C.13}$$

where

$$A = \sin\theta_1 \cos\left(\phi^* - \phi_1\right) \qquad B = \cos\theta_1 \qquad C = \cos\alpha^* \tag{C.14}$$

If instead interpolation on inclination is desired, we have:

$$\alpha^* = 2\tan^{-1}\left(\frac{A \pm \sqrt{A^2 + B^2 - C^2}}{B + C}\right) \tag{C.15}$$

$$\theta^* = \tan^{-1}\left(\frac{\sin\theta_1 \sin\phi_1 \sin(\alpha - \alpha^*) + \sin\theta_2 \sin\phi_2 \sin\alpha^*}{\sin\theta_1 \cos\phi_1 \sin(\alpha - \alpha^*) + \sin\theta_2 \sin\phi_2 \sin\alpha^*}\right) \tag{C.16}$$

where

$$A = \sin\theta_1 \cos\left(\phi^* - \phi_1\right) \qquad B = \cos\theta_1 \qquad C = \cos\alpha^* \tag{C.17}$$

The position vector of the interpolated point p is then given by

$$p^* = p_1 + \frac{S_{12}(1 - \cos\alpha^*)}{\alpha^* \sin\alpha^*}(t_1 + t^*) \tag{C.18}$$

Other possible interpolation methods include solving with a defined position at target, a defined position and orientation at target, and using the minimum distance or closest approach methods Sawaryn and Thorogood (2005). The models developed by Sheppard et al., Johanscik et al., and Sawaryn and Thorogood were used effectively to improve well path planning to reduce drag force and torque. However, it was noted that accurate and high frequency (measured at least once for every stand of drill pipe) were required to generate meaningful data that could be acted upon (Brett, et al., 1989).

Appendix D

Transfer Matrix Algorithm

Included below is skeleton code which lays out the steps necessary to find the transfer matrix solution for a particular drillstring and wellbore.

```
%% Agitate
%  Runs the AOT Drillstring Dynamics Simulator
%
%  Author: Roman Shor
%  Institution: The University of Texas at Austin
%  (c) 2016

% Open loading window
splash;

% Load Excel Data
[survey, drillstring, parameters] = load_data;

% Calculate the Wellbore Path
% Using the Method of Least Curvature
wellpath = calc_path(survey);

% Discretize the Wellpath
% by adding intermediate points
nodes = discretize(drillstring);

% Interpolate the Wellpath
% based on a 30ft element length
[interpolated, nodes] = interpolate(nodes,survey,wellpath,
    parameters);

% Calculate the Torque and Drag
% to give a normal force for damping estimation
torque = calc_torque(survey,drillstring,parameters,wellpath,nodes,
    interpolated);
```

```
29
30 % Calculate the Drillstring Dynamics
31 % using the elements computed previously
32 dynamics = drillstring_dynamics(parameters,nodes,interpolated,
       torque);
33
34 % Plot the Data
35 plot_data(survey,wellpath,nodes,interpolated,torque,dynamics,
       parameters);
```

Appendix E

Torsional Drillstring Model Code

The torsional time domain drillstring model, solved using finite difference, is coupled to an s-Domain control system simulation in Mathworks Simulink^{TM}. This construct allows a non-linear bit model to be coupled to the drillstring model and control systems described in Chapter 5 of this dissertation.

The control system block is described either by Figure 5.26 for an impedance matching controller and Figure 5.25 for a PI controller. The bit model is an approximation using Stribeck friction and is described by Figure 5.4.

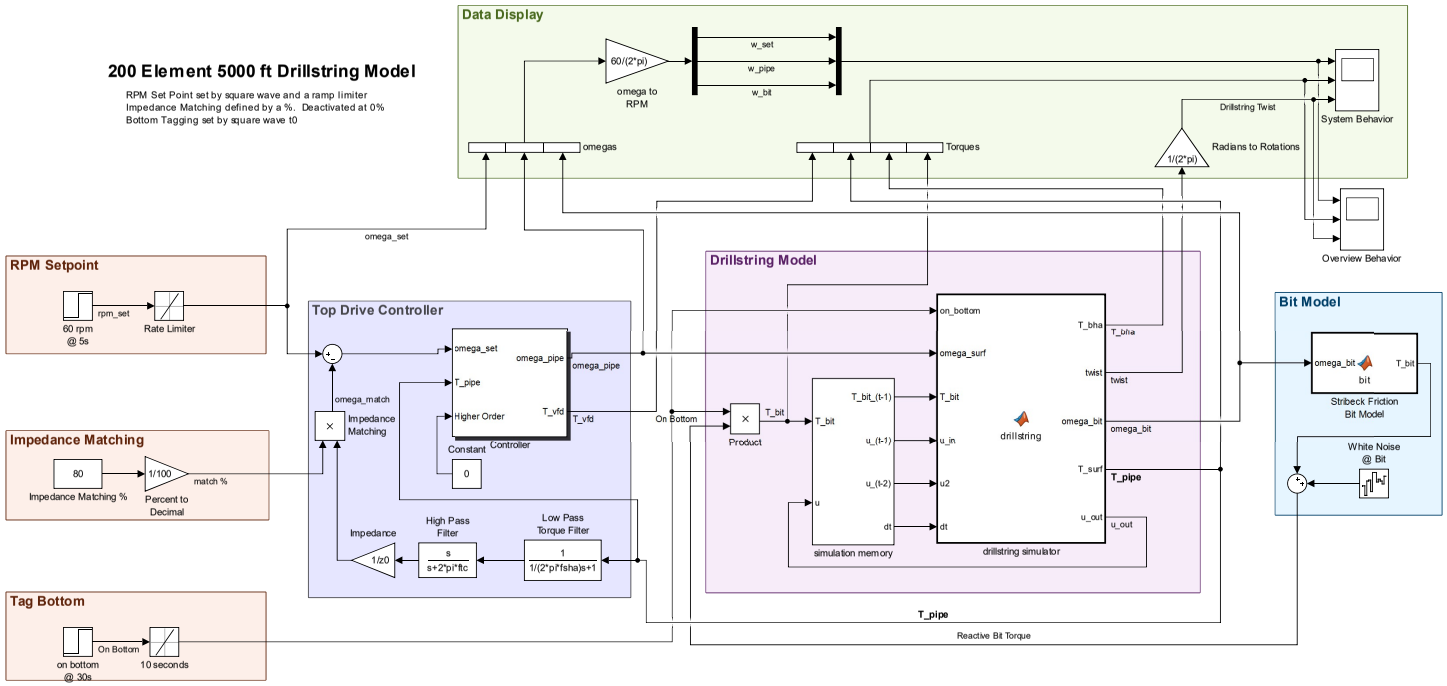

Figure E.1: Simulink Model used to model torsional vibrations in conjunction with a top drive controller and model.

Appendix F

Drillstring Imaging Algorithms

Included in this appendix is the basic code used to process the data for axial, flexural and torsional waves in the three setups used in this dissertation along with the filtering used.

```
%%
% Set of code to conduct time-space mapping
%
% Author: Roman Shor
% Institution: The University of Texas at Austin
% (c) 2016
%
% INPUT:
%   type:       'axial'
%               'flexural'
%               'torsional'
%
%   rig:        'beam'
%               'zebra'
%               'field'
%
%   prefilter:  'none'
%               'matched'
%               'detrend'
%               'derivative
%
%   postfilter: 'none'
%               'average'
%               'gaussian'
%               'lowpass'
%               'butter'
%
%   file:   data file of interest
%
```

```
30 %
31 %   time_space_mapping('flexural','beam','none','matched','file1.
       mat')
32 %   time_space_mapping('axial','beam','none','gaussian','file2.mat
       ')
33 %   time_space_mapping('torsional','field','derivative','none','
       file3.mat')
34
35
36 function time_space_mapping(type, rig, prefilter, postfilter,
       filename)
37
38
39 load(filename);
40
41 switch rig
42     case 'beam'
43         %% Beam parameters
44         E = 210E9;
45         I = 6.7E-10;
46         L = 7.2;
47         rho = 7.8E3;
48         A = 2.02E-4;
49         % get t1 and t2 for a specific filename
50         switch filename
51             % Files
52         end
53
54     case 'field'
55         %% Beam parameters
56         E = 210E9;
57         G = 80E9;
58         I = 6.7E-10;
59         rho = 7.8E3;
60         % get t1 and t2 for a specific filename
61         switch filename
62             % Files
63         end
64
65         freq = 100;
66         sample = round(freq*[t1 t2])+1;
67         yin = extracted.Torque_actual(sample(1):sample(end));
68         xin = extracted.RPM_encoder(sample(1):sample(end));
69         xb = flipud(xin);
70
```

```
71
72      case 'zebra'
73          %% Beam parameters
74          E = 210E9;
75          G = 80E9;
76          I = 6.7E-10;
77          rho = 7.8E3;
78          % get t1 and t2 for a specific filename
79          switch filename
80              %Files
81          end
82
83          freq = 125;
84          sample = floor(freq*[t1 t2])+1;
85          yin = ZT.Torque(sample(1):sample(end));
86          xin = ZT.RPM_SP(sample(1):sample(end));
87          xb = flipud(xin);
88  end
89
90  switch type
91
92      case 'axial'
93          sample = floor(freq*[t1 t2])+1;
94          yin = indata(sample(1):sample(end),2);
95          xin = indata(sample(1):sample(end),1);
96          xb = flipud(xin(1:25));
97          switch prefilter
98              case 'detrend'
99                  y = detrend(yin);
100             case 'none'
101                 y = yin;
102             case 'matched'
103                 y = filter(xb,1,detrend(yin));
104             case 'derivative'
105                 Nf = 50;
106                 Fpass = 5E3;
107                 Fstop = 10E3;
108
109                 d = designfilt('differentiatorfir','FilterOrder',
                        Nf, ...
110                     'PassbandFrequency',Fpass,'StopbandFrequency',
                            Fstop, ...
111                     'SampleRate',freq);
112
113
```

```
114                 xin = filter(d,xin);
115                 xin = [xin(Nf/2+1:end); xin(end-Nf/2+1:end)];
116                 xb = flipud(xin(1:25));
117                 y = filter(xb,1,yin);
118
119         end
120         N = length(y);
121         tmax = (N-1) / freq;
122         t = 0:1/freq:tmax;
123
124
125
126         %% Map to frequency
127         w = 2*pi*linspace(0,freq*(N-1)/N,N);
128         Y = fft(y);
129         X = fft(xin);
130         X1 = 3*exp(-0.5*(10/500000*w(1:end/2)).^2);
131         X1 = [X1 fliplr(X1)];
132
133
134         %% Map to space
135         w2 = w(1:floor(length(w)/2));
136         H = Y./X;
137         H(H>1E10) = 0;
138         cg = sqrt(E/rho);
139         Ht = H;
140         fprintf('Axial Velocity is %0.3f m/s and max resolution is
                %0.3f m\n',cg,2*cg/freq);
141         switch postfilter
142             case 'none'
143                 Xf = ones(size(H));
144
145             case 'average'
146                 B = 1/5*ones(5,1);
147                 H = filtfilt(B,1,H);
148                 Xf = ones(size(H));
149             case 'input'
150                 Xf = X;
151             case 'gaussian'
152                 Xf = X1';
153             case 'lowpass'
154                 cutoff = find(w>37.5E3,1,'first');
155                 Xf = ones(size(H));
156                 Xf(cutoff:end-cutoff) = 1E-6*Xf(cutoff:end-cutoff)
                        ;
```

```
157                 case 'butter'
158                     n = 2;
159                     f = 50;
160
161                     [zb,pb,kb] = butter(n,2*pi*f,'s');
162                     [bb,ab] = zp2tf(zb,pb,kb);
163                     [Xf,wb] = freqs(bb,ab,round(length(w)/2));
164                     Xf = [Xf' fliplr(Xf')]';
165                     H=H.*X;
166
167             end
168
169             H = H.*Xf;
170             Hp = [H zeros(size(H))];
171             h = ifft(Hp,'symmetric');
172
173             Nx = length(h);
174             x = linspace(0,cg*tmax,Nx);
175             k = w;
176
177         case 'flexural'
178             sample = round(freq*[t1 t2])+1;
179             yin = indata(sample(1):sample(end),2);
180             xin = indata(sample(1):sample(end),1);
181             y = yin;
182             N = length(yin);
183             tmax = (N-1) / freq;
184             t = 0:1/freq:tmax;
185
186             %% Map to frequency
187             w = 2*pi*linspace(0,freq*(N-1)/N,N);
188             Yin = fft(yin);
189             Y = Yin;
190             X = fft(xin);
191
192             %% Map to space
193             w2 = w(1:round(length(w)/2));
194             k = sqrt(w2)*(rho*A/E/I).^(1/4);
195             k_new = linspace(0,max(k),N);
196             w_new = interp1(k,w2,k_new);
197             H = interp1(w,Yin,w_new,'spline');
198             Xh = interp1(w,X,w_new,'spline');
199             Xf = Xh;
200             cg = 2*sqrt(w_new)*(E*I/rho/A).^(1/4);
201             H = cg.*H;
```

```
202         fprintf('Flexural Velcity ranges from %0.3f to %0.3f and
                resolution ranges from %0.3f to %0.3f m',...
203             min(cg), max(cg), 2*min(cg)/freq, 2*max(cg)/freq);
204         Hp = [H zeros(size(H))];
205         Xh = [Xh zeros(size(Xh))];
206         switch postfilter
207             case 'none'
208                 h = ifft(Hp,'symmetric');
209                 Xf = ones(size(Xf));
210             case 'matched'
211                 h = ifft(Hp,'symmetric');
212                 xh = ifft(Xh, 'symmetric');
213                 xb = flipud(xh(1:10));
214                 h = filter(xb,1,h);
215         end
216
217         Ht = Yin./X;
218         H = H(1:end/2);
219         Nx = length(h);
220
221         x = linspace(0,(Nx-1) / (k(end)*2/2/pi),Nx);
222
223
224     case 'torsional'
225
226
227         xi = xin;
228
229         switch prefilter
230             case 'none'
231                 y = yin;
232             case 'detrend'
233                 y = detrend(yin);
234             case 'matched'
235                 y = filter(xb,1,yin);
236                 xi = filter(xb,1,xin);
237             case 'derivative'
238                 Nf = 30;
239                 Fpass = 10;
240                 Fstop = 15;
241
242                 d = designfilt('differentiatorfir','FilterOrder',
                        Nf, ...
243                     'PassbandFrequency',Fpass,'StopbandFrequency',
                            Fstop, ...
```

```
244                     'SampleRate',freq);
245
246                 fc = 10;
247                 fs = freq;
248                 [b,a] = butter(1,fc/(fs/2),'high');
249                 xi = filter(b,a,xin);
250                 xi = [xin(Nf/2+1:end); xin(end-Nf/2+1:end)];
251                 xb = flipud(xin(129:148));
252                 y = filter(xb,1,yin);
253
254         end
255         N = length(y);
256         tmax = (N-1) / freq;
257         t = 0:1/freq:tmax;
258
259         %% Map to frequency
260         w = linspace(0,freq*(N-1)/N,N);
261         Yin = fft(yin);
262         Y = fft(y);
263         X = fft(xi);
264
265         %% Map to space
266         w2 = w(1:round(length(w)/2));
267         H = Y./X;
268         H(H>1E10) = 0;
269         cg = sqrt(G/rho);
270         Ht = H;
271
272         fprintf('Torsional Velocity is %0.3f m/s and max
                resolution is %0.3f m\n',cg,2*cg/freq);
273
274         switch postfilter
275             case 'average'
276                 B = 1/3*ones(3,1);
277                 H = filtfilt(B,1,H);
278                 Xf = ones(size(H));
279             case 'none'
280                 Xf = ones(size(H));
281             case 'input'
282                 Xf = X;
283             case 'gaussian'
284                 X1 = 3*exp(-0.5*(5/100*w(1:end/2)).^2);
285                 X1 = [X1 fliplr(X1)];
286                 Xf = [X1 X1(end)]';
287             case 'lowpass'
```

```
288                     cutoff = find(w>10,1,'first');
289                     Xf = ones(size(H));
290                     Xf(cutoff:end-cutoff) = 1E-12*Xf(cutoff:end-cutoff
                            );
291
292                 case 'butter'
293                     n = 5;
294                     f = 10;
295
296                     [zb,pb,kb] = butter(n,f,'s');
297                     [bb,ab] = zp2tf(zb,pb,kb);
298                     [Xf,wb] = freqs(bb,ab,floor(length(w)/2));
299                     Xf = [Xf' fliplr(Xf')]';
300                     if length(Xf) < length(H)
301                         Xf = [Xf; Xf(end)];
302                     end
303
304                 case 'xcorr'
305                     H = Y;
306                     Xf = conj(X);
307
308             end
309
310             H = H.*Xf;
311
312             Hp = [H zeros(size(H))];
313             Htp = [Ht zeros(size(Ht))];
314             h = ifft(Hp,'symmetric');
315
316
317             Nx = length(h);
318             x = linspace(0,cg*(t2-t1),Nx);
319             k = w;
320
321     end
322
323     %% Plot Results
324     %
325     %  Not included in this printout
326
327     end
```

Bibliography

Aarrestad, T. V. and Kyllingstad, A. (1993). Measurements and Theoretical Models on Rig Suspension and the Effect on Drillstring Vibrations. *SPE Drilling & Completion*, 8(03):201–206.

Aarrestad, T. V., Tonnesen, H. A., and Kyllingstad, A. (1986). Drillstring Vibrations: Comparison Between Theory and Experiments on a Full-Scale Research Drilling Rig. In *SPE/IADC Drilling Conference*. Society of Petroleum Engineers.

Al-Hiddabi, S. A., Samanta, B., and Seibi, A. (2003). Non-linear control of torsional and bending vibrations of oilwell drillstrings. *Journal of sound and vibration*, 265(2):401–415.

Al-Shuker, N., Kirby, C., and Brinsdon, M. (2011). The Application of Real Time Downhole Drilling Dynamic Signatures as a Possible Early Indicator of Lithology Changes. In *SPE/DGS Saudi Arabia Section Technical Symposium and Exhibition*. Society of Petroleum Engineers.

Alali, A., Akubue, V. A., Barton, S. P., and Gee, R. (2012). Agitation Tools Enables Significant Reduction in Mechanical Specific Energy. *SPE Asia Pacific Oil and Gas Conference and Exhibition*.

Alali, A. and Barton, S. P. (2011). Unique Axial Oscillation Tool Enhances Performance of Directional Tools in Extended Reach Applications. *Brasil Offshore Conference*.

Aldred, W. D. and Sheppard, M. C. (1992). *Drillstring Vibrations: A New Generation Mechanism and Control Strategies*. Society of Petroleum Engineers.

Allen, F., Tooms, P., Conran, G., Lesso, B., and Van de Slijke, P. (1997). Extended-Reach Drilling: Breaking the 10-km Barrier. *Oilfield Review*.

Aström, K. J. and Murray, R. M. (2010). *Feedback Systems*. An Introduction for Scientists and Engineers. Princeton University Press.

Baez, F. and Barton, S. P. (2011). Delivering performance in shale gas plays: Innovative technology solutions. *SPE/IADC Drilling Conference and Exhibition*.

Bailey, J. J. and Finnie, I. (1960). An Analytical Study of Drill-String Vibration. *Journal of Engineering for Industry*, 82(2):122–127.

Barton, S. P., Baez, F., and Alali, A. (2011a). Drilling performance improvements in gas shale plays using a novel drilling agitator device. *AADE National Technical Conference*.

Barton, S. P., Baez, F., and Alali, A. (2011b). Drilling performance improvements in gas shale plays using a novel drilling agitator device. *AADE National Technical Conference*.

Barton, S. P., Clarke, A. J., Garcia, A., Perez, D., Mora, G., and Carrion, C. (2009). *Improved Drilling Performance: Downhole Dynamic Logging Tools Break Paradigm in Ecuador*. Society of Petroleum Engineers.

Baumgartner, T. and van Oort, E. (2014). Pure and Coupled Drill String Vibration Pattern Recognition in High Frequency Downhole Data. *SPE Annual Technical Conference and Exhibition*.

Besaisow, A. A., Jan, Y. M., and Schuh, F. J. (1985). *Development of a Surface Drillstring Vibration Measurement System*. Society of Petroleum Engineers.

Bonner, S., Clark, B., Holenka, J., Voisin, B., and Dusang, J. (1992). Logging While Drilling: A Three-Year Perspective. *Oilfield Review*.

Booer, A. K. and Meehan, R. J. (1993). Drillstring imaging: an interpretation of surface drilling vibrations. *SPE Drilling & Completion*, 8(02):93–98.

Brett, J. F. (1992). The Genesis of Bit-Induced Torsional Drillstring Vibrations. *SPE Drilling Engineering*, 7(03):168–174.

Brett, J. F., Warren, T. M., and Behr, S. M. (1990). Bit whirl: A new theory of PDC bit failure. *SPE Drilling Engineering*.

Briscoe, M., Craig, A. D., and Jackson, T. A. (2013). The Evolution of Wired Drilling Tools: A Background History and Learnings from the Development of a Suite of Drilling Tools for Wired Drillstrings. *SPE/IADC Drilling Conference*.

Canudas-de Wit, C., Rubio, F. R., and Corchero, M. A. (2008). D-OSKIL: A New Mechanism for Controlling Stick-Slip Oscillations in Oil Well Drillstrings. *Control Systems Technology, IEEE Transactions on*, 16(6):1177–1191.

Ceasu, V., Craifaleanu, A., and Dragomirescu, C. (2010). Transfer Matrix Method for Forced Vibrations of Bars. *U.P.B Sci. Bull.*, 72(2).

Chahr-Eddine, K. and Yassine, A. (2014). Forced axial and torsional vibrations of a shaft line using the transfer matrix method related to solution coefficients. *Journal of Marine Science and Application*, 13(2):200–205.

Chatjigeorgiou, I. K. (2013). Numerical simulation of the chaotic lateral vibrations of long rotating beams. *Applied Mathematics and Computation*.

Chatterjee, S. and Mahata, P. (2009). Time-delayed absorber for controlling friction-driven vibration. *Journal of sound and vibration*, 322(1-2):39–59.

Chen, D., Smith, M., and LaPierre, S. (2003). Advanced drillstring dynamics system integrates real-time modeling and measurements. *SPE Latin American and Caribbean Petroleum Engineering Conference*.

Cheney, M. and Isaacson, D. (1992). Distinguishability in impedance imaging. *IEEE Transactions on Biomedical Engineering*, 39(8):852–860.

Christoforou, A. P. and Yigit, A. S. (2003). Fully coupled vibrations of actively controlled drillstrings. *Journal of sound and vibration*, 267(5):1029–1045.

Clausen, J. R., Schen, A. E., Forster, I., and Prill, J. (2014). Drilling With Induced Vibrations Improves ROP and Mitigates Stick/Slip in Vertical and Directional Wells. *IADC/SPE Drilling Conference*.

Clayer, F., Vandiver, J. K., and Lee, H. Y. (1990). The Effect of Surface and Downhole Boundary Conditions on the Vibration of Drillstrings. In *SPE Annual Technical Conference and Exhibition*. Society of Petroleum Engineers.

Coe, J. and Brandenberg, S. J. (2010). P-wave reflection imaging of submerged soil models using ultrasound. *J. Geotech. Geoenviron. Eng.*

Dareing, D. W. and Livesay, B. J. (1968). Longitudinal and Angular Drill-String Vibrations With Damping. *Journal of Engineering for Industry*, 90(4):671–679.

Dashevskiy, D., Dubinsky, V., and Macpherson, J. D. (1999). Application of neural networks for predictive control in drilling dynamics. *SPE Annual Technical Conference and Exposition*.

Deily, F. H., Dareing, D. W., Paff, G. H., Ortloff, J. E., and Lynn, R. D. (1968). Downhole Measurements of Drill String Forces and Motions. *Journal of Engineering for Industry*, 90(2):217–225.

Den Hartog, J. P. (2013). *Mechanical Vibrations*. Read Books Ltd.

Depouhon, A. and Detournay, E. (2014). Journal of Sound and Vibration. *Journal of sound and vibration*, 333(7):2019–2039.

Desmette, S., Will, J., Coudyzer, C., and Le, P. (2005). Isubs: A New Generation of Autonomous Instrumented Downhole Tool. *SPE/IADC Drilling Conference*.

Drinkwater, B. W. and Wilcox, P. D. (2006). Ultrasonic arrays for non-destructive evaluation: A review. *NDT and E International*, 39(7):525–541.

Drumheller, D. S. (1989). Acoustical properties of drill strings. *The Journal of the Acoustical Society of America*, 85(3):1048.

Drumheller, D. S. (1993). Coupled extensional and bending motion in elastic waveguides. *Wave Motion*, 17(4):319–327.

Drumheller, D. S. (2002). Wave impedances of drill strings and other periodic media. *The Journal of the Acoustical Society of America*, 112(6):2527–13.

Drumheller, D. S. and Knudsen, S. D. (1995). The propagation of sound waves in drill strings. *The Journal of the Acoustical Society of America*, 97(4):2116–2125.

Dunayevsky, V. A., Judzis, A., and Mills, W. H. (1984). *Onset of Drillstring Precession in a Directional Borehole*. Society of Petroleum Engineers.

Dwars, S. (2015). Recent Advances in Soft Torque Rotary Systems. *SPE/IADC Drilling Conference and Exhibition*.

Dwars, S., Stulemeijer, I., and Runia, J. J. (2013). A brief history of the Shell" Soft Torque Rotary System" and some recent case studies. *SPE/IADC Drilling Conference*.

Dykstra, M. W. (1996). *Nonlinear Drillstring Dynamics*. PhD thesis, University of Tulsa.

Dykstra, M. W., Chen, D., and Warren, T. M. (1994). Experimental evaluations of drill bit and drill string dynamics. *SPE Annual Technical Conference and Exposition*.

Dykstra, M. W., Chen, D., Warren, T. M., and Azar, J. J. (1995). Drillstring component mass imbalance: a major source of downhole vibrations. *SPE Drilling Conference*.

Dykstra, M. W., Neubert, M., Hanson, J. M., and Meiners, M. J. (2001). Improving drilling performance by applying advanced dynamics models. *paper SPE*.

Ertas, D., Bailey, J. R., Wang, L., and Pastusek, P. E. (2013). Drillstring mechanics model for surveillance, root cause analysis, and mitigation of torsional and axial vibrations. *SPE/IADC Drilling Conference*.

Esmaeili, A., Elahifar, B., and Fruhwirth, R. K. (2012). Laboratory Scale Control of Drilling Parameters to Enhance Rate of Penetration and Reduce Drill String Vibration. *SPE Saudi Arabia Section Technical Symposium and Exhibition*.

Falodun, S., Kellas, M., and Ehrunmwunsee, K. (2005). Optimal Horizontal Wellbore Placement Using New Drilling Technology In the Niger Delta-Bonga Field Case Study. *18th World Petroleum Conference*.

Finnie, I. and Bailey, J. J. (1960). An Experimental Study of Drill-String Vibration. *Journal of Engineering for Industry*, 82(2):129–135.

Forster, I. (2011). Axial Excitation as a Means of Stick Slip Mitigation-Small Scale Rig Testing and Full Scale Field Testing. *SPE/IADC Drilling Conference and Exhibition*.

Gazdag, J. (1978). Wave equation migration with the phase-shift method. *Geophysics*, 43(7):1342–1351.

Gee, R., Forster, I., Clausen, J. R., and Prill, J. (2014). Drilling With Induced Vibrations Improves ROP and Mitigates Stick/Slip in Vertical and Directional Wells. *IADC/SPE Drilling Conference*.

Gee, R., Hanley, C., Hussain, R., and Canuel, L. (2015). Axial Oscillation Tools vs. Lateral Vibration Tools for Friction Reduction–What's the Best Way to Shake the Pipe? *SPE/IADC Drilling Conference*.

Germay, C., Van de Wouw, N., Nijmeijer, H., and Sepulchre, R. (2009). Nonlinear Drillstring Dynamics Analysis. *SIAM Journal on Applied Dynamical Systems*, 8(2):527–553.

Ghasemloonia, A., Rideout, D. G., and Butt, S. D. (2014). Analysis of multimode nonlinear coupled axial-transverse drillstring vibration in vibration assisted rotary drilling. *Journal of Petroleum Science and Engineering*, 116(C):36–49.

Ghayesh, M. H. (2012). Journal of Sound and Vibration. *Journal of sound and vibration*, 331(23):5107–5124.

Ghayesh, M. H., Kafiabad, H. A., and Reid, T. (2012). International Journal of Solids and Structures. *International Journal of Solids and Structures*, 49(1):227–243.

Gibbs, S. G. (1975). Computing gearbox torque and motor loading for beam pumping units with consideration of inertia effects. *Journal of Petroleum Technology*, 27(09):1153–1159.

Gillan, C., Boone, S. G., Leblanc, M. G., Picard, R. P., and Fox, R. T. (2011). Applying Computer Based Precision Drill Pipe Rotation and Oscillation to Automate Slide Drilling Steering Control. In *Canadian Unconventional Resources Conference*. Society of Petroleum Engineers.

Green, P. L. and Worden, K. (2014). Bayesian System Identification of Nonlinear Systems: Informative Training Data through Experimental Design. In *Proceedings of IMAC XXXII*.

Hakimi, H. and Moradi, S. (2010). Drillstring vibration analysis using differential quadrature method. *Journal of Petroleum Science and Engineering*, 70(3-4):235–242.

Halsey, G. W., Kyllingstad, A., Aarrestad, T. V., and Lysne, D. (1986). *Drillstring Torsional Vibrations: Comparison Between Theory and Experiment on a Full-Scale Research Drilling Rig*. Society of Petroleum Engineers.

Han, J.-H., Kim, Y.-J., and Karkoub, M. (2013). Modeling of wave propagation in drill strings using vibration transfer matrix methods. *The Journal of the Acoustical Society of America*, 134(3):1920–12.

Heisig, G. and Neubert, M. (2000). *Lateral Drillstring Vibrations in Extended-Reach Wells*. Society of Petroleum Engineers.

Ho, H. S. (1986). *General Formulation of Drillstring Under Large Deformation and Its Use in BHA Analysis*. Society of Petroleum Engineers.

Hoffmann, O. J., Jain, J. R., Spencer, R. W., and Makkar, N. (2012). Drilling dynamics measurements at the drill bit to address today's challenges. *2012 IEEE International Instrumentation and Measurement Technology Conference (I2MTC)*, pages 443–448.

Hohl, A., Tergeist, M., Oueslati, H., and Herbig, C. (2016). Prediction and Mitigation of Torsional Vibrations in Drilling Systems. *IADC/SPE Drilling Conference*.

Hopf, K. and Co, J. H. F. (2011). Agitator for a drill and related methods. US Patent Office.

Hu, Y., Di, Q., Zhu, W., Chen, Z., and Wang, W. (2012). Dynamic characteristics analysis of drillstring in the ultra-deep well with spatial curved beam finite element. *Journal of Petroleum Science and Engineering*, 82-83:166–173.

Ishida, Y. (1994). Nonlinear vibrations and chaos in rotordynamics. *JSME international journal Ser C*.

Jadric, I. (1998). *Modeling and control of a synchronous generator with electronic load*. PhD thesis, Virginia Polytechnic Institute and State University.

Jain, J. R., Oueslati, H., Hohl, A., and Reckmann, H. (2014). High-Frequency Torsional Dynamics of Drilling Systems: An Analysis of the Bit-System Interaction. *IADC/SPE Drilling Conference*.

Jansen, J. D. (1991). Non-linear rotor dynamics as applied to oilwell drillstring vibrations. *Journal of sound and vibration*, 147(1):115–135.

Janwadkar, S. S., Fortenberry, D. G., and Roberts, G. K. (2006). BHA and Drillstring Modeling Maximizes Drilling Performance in Lateral Wells of Barnett Shale Gas Field of N. Texas. *SPE Gas Technology ....*

Johancsik, C. A., Friesen, D. B., and Dawson, R. (1984). Torque and Drag in Directional Wells-Prediction and Measurement. *Journal of Petroleum Technology*, 36(06):987–992.

Kalsi, M. S., Wang, J. K., and Chandra, U. (1987). Transient dynamic analysis of the drillstring under jarring operations by the fem. *SPE Drilling Engineering*.

Khan, K. Z. (1986). Longitudinal and Torsional Vibration of Drill Strings.

Khulief, Y. A. and Al-Naser, H. (2005). Finite element dynamic analysis of drillstrings. *Finite Elements in Analysis and Design*, 41(13):1270–1288.

Khulief, Y. A., Al-Sulaiman, F. A., and Bashmal, S. (2007). Vibration analysis of drillstrings with self-excited stick–slip oscillations. *Journal of sound and vibration*, 299(3):540–558.

Kieschnick, M., Kieschnick, M. L., Jacob, T., James, B., Karuppiah, V., and Hamilton, R. (2013). *Pre-Job Modeling/Resulting Integrated BHA System Solution Sets Multiple ROP Records, North Field Qatar*. Society of Petroleum Engineers.

Kovalyshen, Y. (2013). Journal of Sound and Vibration. *Journal of sound and vibration*, 332(24):6321–6334.

Kreisle, L. F. and Vance, J. M. (1970). Mathematical Analysis of the Effect of a Shock Sub on the Longitudinal Vibrations of an Oilwell Drill String. *Society of Petroleum Engineers Journal*, 10(04):349–356.

Kreuzer, E. and Steidl, M. (2010). A Wave-Based Approach to Adaptively Control Self-Excited Vibrations in Drill-Strings. *PAMM*, 10(1):509–510.

Kriesels, P. C., Keultjes, W., Dumont, P., and Huneidi, I. (1999). Cost savings through an integrated approach to drillstring vibration control. *SPE/IADC Middle East ...*.

Kyllingstad, A. and Nessjøen, P. J. (2009). A New Stick-Slip Prevention System. In *SPE/IADC Drilling Conference and Exhibition*. Society of Petroleum Engineers.

Kyllingstad, A. and Nessjøen, P. J. (2010). Hardware-in-the-Loop Simulations Used as a Cost-Efficient Tool for Developing an Advanced Stick-Slip Prevention System. *IADC/SPE Drilling Conference and ...*.

Ledgerwood III, L. W. and Tergeist, M. (2014). High-Frequency Torsional Dynamics of Drilling Systems: An Analysis of the Bit-System Interaction. *IADC/SPE Drilling Conference*.

Lee, H. Y. (1991). *Drillstring axial vibration and wave propagation in boreholes*. PhD thesis, Massachussetts Institute of Technology.

Lee, J.-S. and Santamarina, J. C. (2005). P-wave reflection imaging. *Geotechnical testing journal*, 28(2):12595.

Leine, R. I., van Campen, D. H., and Keultjes, W. J. G. (2002). Stick-slip Whirl Interaction in Drillstring Dynamics. *Journal of Vibration and Acoustics*, 124(2):209.

Liao, C.-M., Vlajic, N., Karki, H., and Balachandran, B. (2012). International Journal of Mechanical Sciences. *International Journal of Mechanical Sciences*, 54(1):260–268.

Macpherson, J. D., Mason, J. S., and Kingman, J. (1993). Surface measurement and analysis of drillstring vibrations while drilling. *SPE/IADC Drilling Conference*.

Maidla, E. E., Haci, M., and Wright, D. (2009). Case History Summary: Horizontal Drilling Performance Improvement Due to Torque Rocking on 800 Horizontal Land Wells Drilled for Unconventional Gas Resources. In *SPE Annual Technical Conference and Exhibition*. Society of Petroleum Engineers.

Makkar, N., Oueslati, H., Schwefe, T., and Hohl, A. (2014). The Need for High Frequency Vibration Measurement Along With Dynamics Modeling to Understand the Genesis of PDC Bit Damage. *IADC/SPE Drilling Conference*.

McCann, D. M. and Forde, M. C. (2001). Review of NDT methods in the assessment of concrete and masonry structures. *NDT and E International*, 34(2):71–84.

McCarthy, J. P., Stanes, B., and Rebellon, J. E. (2009). A step change in drilling efficiency: Quantifying the effects of adding an axial oscillation tool within challenging wellbore environments. *SPE/IADC Drilling Conference*.

McCormick, J. E. and Chiu, T. (2011). *The Practice and Evolution of Torque and Drag Reduction: Theory and Field Results, paper SPE 147100 presented at the SPE Annual Technical ....* Denver.

Mihajlović, N., Wouw, N. v. d., Rosielle, P. C. J. N., and Nijmeijer, H. (2007). Interaction between torsional and lateral vibrations in flexible rotor systems with discontinuous friction. *Nonlinear Dynamics*, 50(3):679–699.

Nandakumar, K. and Wiercigroch, M. (2013). Stability analysis of a state dependent delayed, coupled two DOF model of drill-stringvibration. *Journal of sound and vibration*, 332(10):2575–2592.

Navarro-Lopez, E. M. (2009). An alternative characterization of bit-sticking phenomena in a multi-degree-of-freedom controlled drillstring. *Nonlinear Analysis: Real World Applications*, 10(5):3162–3174.

Navarro-López, E. M. and Cortés, D. (2007). Avoiding harmful oscillations in a drillstring through dynamical analysis. *Journal of sound and vibration*, 307(1-2):152–171.

Navarro-Lopez, E. M. and Cortes, D. (2007). Sliding-mode control of a multi-DOF oilwell drillstring with stick-slip oscillations. In *American Control Conference, 2007. ACC '07*, pages 3837–3842. IEEE.

Navarro-Lopez, E. M. and Licéaga-Castro, E. (2009). Non-desired transitions and sliding-mode control of a multi-DOF mechanical system with stick-slip oscillations. *Chaos, Solitons and Fractals*, 41(4):2035–2044.

Nessjøen, P. J., Kyllingstad, A., and Dambrosio, P. (2011). Field Experience with an Active Stick-Slip Prevention System. *SPE/IADC Drilling Conference*.

Newman, K. R., Burnett, T. G., Pursell, J. C., and Gouasmia, O. (2009). Modeling the Affect of a Downhole Vibrator. In *SPE/ICoTA Coiled Tubing and Well Intervention Conference and Exhibition*.

Newton, R. G. (1981). Inversion of reflection data for layered media: a review of exact methods. *Geophysical Journal International*, 65(1):191–215.

Nicholson, J. W. (1986). Drill String Dynamics Interim Report: The Trilobed Bottomhole Pattern and Resulting Bit Bouncing and Kelly Bouncing,. Technical report, Shell Development Ballaire Research Center, Houston.

Oppenheim, A. V. and Schafer, R. W. (2009). *Dscrete-Time Signal Processing*. Prentice Hall.

Oueslati, H., Jain, J. R., and Reckmann, H. (2013a). New Insights Into Drilling Dynamics Through High-Frequency Vibration Measurement and Modeling. *SPE Annual Technical Conference and Exposition*.

Oueslati, H., Jain, J. R., and Reckmann, H. (2013b). New Insights Into Drilling Dynamics Through High-Frequency Vibration Measurement and Modeling. *SPE Annual Technical Conference and Exposition*.

Ozkentli, E. (2012). *High Frequency Effects of Variable Frequency Drives (VFD) on Electrical Submersible Pump (ESP) Systems*. PhD thesis, Texas A&M University.

Parfitt, S. and Abbassian, F. (1995). A model for shock sub performance qualification. *SPE/IADC Drilling Conference*.

Paslay, P. R. and Bogy, D. B. (1963). Drill String Vibrations Due to Intermittent Contact of Bit Teeth. *Journal of Engineering for Industry*, 85(2):187–194.

Patil, P. A. and Teodoriu, C. (2013). A comparative review of modelling and controlling torsional vibrations and experimentation using laboratory setups. *Journal of Petroleum Science and Engineering*.

Perneder, L., Detournay, E., and Downton, G. (2012). International Journal ofRock Mechanics & Mining Sciences. *International Journal of Rock Mechanics and Mining Sciences*, 51(c):81–90.

Rao, V. (1991). Acoustic transmission through fluid-filled pipes in boreholes.

Rasmussen, C. E. and Williams, C. K. I. (2006). *Gaussian Processes for Machine Learning*. Mit Press.

Reckmann, H., Jogi, P., and Herbig, C. (2007). Using Dynamics Measurements While Drilling to Detect Lithology Changes and to Model Drilling Dynamics. *ASME 2007 ....*

Reid, D. and Rabia, H. (1995). Analysis of Drillstring Failures. In *SPE/IADC Drilling Conference*. Society of Petroleum Engineers.

Richard, T., Germay, C., and Detournay, E. (2007). A simplified model to explore the root cause of stick–slip vibrations in drilling systems with drag bits. *Journal of sound and vibration*, 305(3):432–456.

Ritto, T. G., Soize, C., and Sampaio, R. (2009). International Journal of Non-Linear Mechanics. *International Journal of Non-Linear Mechanics*, 44(8):865–876.

Robertson, L., Mason, C. J., Sherwood, A. S., and Newman, K. R. (2004). Dynamic Excitation Tool: Developmental Testing and CTD Field Case Histories. In *SPE/ICoTA Coiled Tubing Conference and Exhibition*. Society of Petroleum Engineers.

Robinson, L. (2010). *Drill Bit Nozzle Pressure Loss*. American Association of Drilling Engineers.

Rudat, J., Dmitriy Dashevskiy, J. R. L. P., Dashevskiy, D., and Pohle, L. (2011). Model-based stability analysis of torsional drillstring oscillations. *Control Applications (CCA)*.

Sahebkar, S. M., Ghazavi, M. R., Khadem, S. E., and Ghayesh, M. H. (2011). Nonlinear vibration analysis of an axially moving drillstring system with time dependent axial load and axial velocity in inclined well. *MAMT*, 46(5):743–760.

Saldivar, B. and Mondié, S. (2013). Drilling vibration reduction via attractive ellipsoid method. *Journal of the Franklin Institute*, 350(3):485–502.

Sananikone, P., Kamoshima, O., and White, D. B. (1992). A field method for controlling drillstring torsional vibrations. *SPE/IADC Drilling Conference*.

Santos, H., Placido, J., and Wolter, C. (1999). Consequences and relevance of drillstring vibration on wellbore stability. *SPE/IADC Drilling Conference*.

Santosa, F. and Vogelius, M. (1990). A backprojection algorithm for electrical impedance imaging. *SIAM Journal on Applied Mathematics*, 50(1):216–243.

Sawaryn, S. J. and Thorogood, J. L. (2005). A Compendium of Directional Calculations Based on the Minimum Curvature Method. *SPE Drilling & Completion*, 20(01):24–36.

Seutter, D., Radmanovich, D. J., and 1473706 Alberta Ltd. (2012). System, method and apparatus for drilling agitator. US Patent Office.

Shen, C. C., Chou, Y. H., and Li, P. C. (2005). Pulse inversion techniques in ultrasonic nonlinear imaging. *Journal of Medical Ultrasound*, 13(1):3–17.

Sheppard, M. C., Wick, C., and Burgess, T. (1987). Designing Well Paths To Reduce Drag and Torque. *SPE Drilling Engineering*, 2(04):344–350.

Shor, R. J., Dykstra, M. W., Hoffmann, O. J., and Coming, M. (2015a). *For Better or Worse: Applications of the Transfer Matrix Approach for Analyzing Axial and Torsional Vibration*. Society of Petroleum Engineers.

Shor, R. J., Pehlivanturk, C., Acikmese, B., and van Oort, E. (2015b). Propagation of Torsional Vibrations in Drillstrings: How Borehole Geometry Affects Transmission and Implications on Mitigation Techniques. In *International Conference on Engineering Vibration*, Lubljana, Slovenia.

Shor, R. J., Pryor, M., and van Oort, E. (2014). Drillstring Vibration Observation, Modeling and Prevention in the Oil and Gas Industry. *ASME 2014 Dynamic Systems and Control Conference*.

Skaugen, E. (1987). The Effects of Quasi-Random Drill Bit Vibrations Upon Drillstring Dynamic Behavior. In *SPE Annual Technical Conference and Exhibition*.

Skaugen, E. and Kyllingstad, A. (1986). Performance Testing of Shock Absorbers. In *SPE Annual Technical Conference and Exhibition*. Society of Petroleum Engineers.

Skeem, M. R., Friedman, M. B., and Walker, B. H. (1979). Drillstring Dynamics During Jar Operation. *Journal of Petroleum Technology*, 31(11):1381–1386.

Smith, N. and Webb, A. G. (2011). Introduction to Medical Imaging.

Stroud, D., Coveney, V., and Lines, L. A. (2013). Torsional Resonance-An Understanding Based on Field and Laboratory Tests with Latest Generation Point-the-Bit Rotary Steerable System. *SPE/IADC Drilling Conference*.

Swanson, E., Powell, C. D., and Weissman, S. (2005). A practical review of rotating machinery critical speeds and modes. *Sound and Vibration*.

Thomson, W. (1996). *Theory of Vibration with Applications*. CRC Press.

Tikhonov, V., Valiullin, K., Nurgaleev, A., Ring, L., Gandikota, R., Chaguine, P., and Cheatham, C. (2014). Dynamic Model for Stiff-String Torque and Drag (see associated supplementary discussion). *SPE Drilling & Completion*, 29(03):279–294.

Tikhonov, V. S. and Safronov, A. I. (2002). Investigation of Drillstring Transverse Vibrations at Rotary Drilling of Inclined Wells. *ASME 2002 . . .*, pages 305–315.

Tonneson, H. A., Berg, B., Kvalvaag, T., and Pedersen, S. (1995). Tonneson - Integrated Drilling System. *Petroleum Computer Conference*, pages 1–7.

Trindade, M. A., Wolter, C., and Sampaio, R. (2005). Karhunen–Loève decomposition of coupled axial/bending vibrations of beams subject to impacts. *Journal of sound and vibration*, 279(3-5):1015–1036.

van Oort, E., Ugueto, G. A., and Gradishar, J. R. (2013). Setting Free The Bear: The Challenges And Lessons Of The Ursa A-10 Deepwater ERD Well. *SPE/IADC Drilling Conference*.

Vandiver, K. J., Nicholson, J. W., and Shyu, R. J. (1990). Case studies of the bending vibration and whirling motion of drill collars. *SPE Drilling Engineering*, 5(4).

Viguié, R., Kerschen, G., Golinval, J. C., McFarland, D. M., Bergman, L. A., Vakakis, A. F., and Van de Wouw, N. (2009). Using passive nonlinear

targeted energy transfer to stabilize drill-string systems. *Mechanical Systems and Signal Processing*, 23(1):148–169.

Warren, T. W., Oster, J. H., Sinor, L. A., and Chen, D. C. K. (1998). Shock Sub Performance Tests. In *IADC/SPE Drilling Conference*. Society of Petroleum Engineers.

Wilcox, P. D. (2003). A rapid signal processing technique to remove the effect of dispersion from guided wave signals. *IEEE Transactions on Ultrasonics, Ferroelectrics and Frequency Control*, 50(4):419–427.

Wolf, S. F., Zacksenhouse, M., and Arian, A. (1985). *Field Measurements of Downhole Drillstring Vibrations*. Society of Petroleum Engineers.

Yigit, A. S. and Christoforou, A. P. (1996). Coupled axial and transverse vibrations of oilwell drillstrings. *Journal of sound and vibration*.

Yigit, A. S. and Christoforou, A. P. (2000). Coupled torsional and bending vibrations of actively controlled drillstrings. *Journal of sound and vibration*.

Yilmaz, M., Mujeeb, S., and Dhansri, N. R. (2013). A H-infinity Control Approach for Oil Drilling Processes. *Procedia - Procedia Computer Science*, 20:134–139.

Young, F. S. (1969). Computerized Drilling Control. *Journal of Petroleum Technology*, pages 1–14.

Zamanian, M., Khadem, S. E., and Ghazavi, M. R. (2007). Stick-slip oscillations of drag bits by considering damping of drilling mud and active damping system. *Journal of Petroleum Science and Engineering*, 59(3-4):289–299.

Zamudio, C. A., Tlusty, J. L., and Dareing, D. W. (1987). Self-Excited Vibrations in Drillstrings. In *SPE Annual Technical Conference and Exhibition*. Society of Petroleum Engineers.

Vita

Roman J. Shor graduated from West High School in Salt Lake City, Utah, in 2004 and subsequently matriculated at the University of Pennsylvania in Philadelphia. He received a Bachelor of Arts in Mathematics and a Bachelor of Science in Engineering in Computer Science and Engineering in 2009 and a Master of Science in Engineering in Computer and Information Science in 2010. In the fall of 2011, he entered the Graduate School at the University of Texas at Austin and earned a Master of Science in Engineering in Petroleum Engineering in 2014.

Permanent address: roman.shor@utexas.edu

This dissertation was typeset with LaTeX[†] by the author.

[†]LaTeX is a document preparation system developed by Leslie Lamport as a special version of Donald Knuth's TeX Program.